

Chapter 7

Aeroelastic Stability in Forward Flight

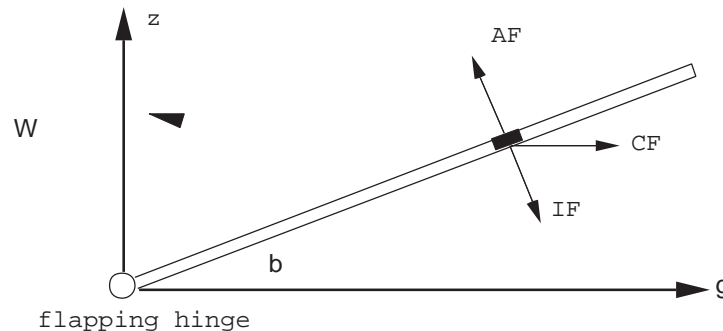
The forward flight condition introduces an extra dimension of complexity to the rotorcraft aeroelastic stability and response problems. The airflow on the disk is asymmetric, and also a part of the region is in either stalled flow or in reversed flow condition. The complexity is caused by the blade aerodynamic forces which are very much involved.

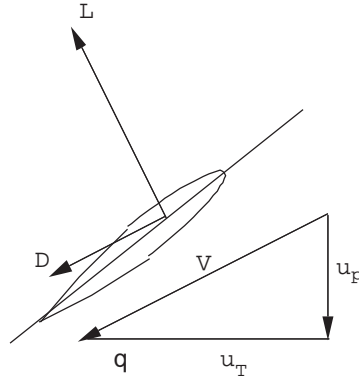
The equations of blade motion in forward flight contain many periodic terms and therefore one has to develop special mathematical tools to solve these equations. One possible way of solving these equations is to write the blade equations in the fixed reference frame using Fourier coordinate transformation, and then solve these equations approximately either neglecting altogether periodic terms or using the harmonic balance method on the periodic terms. The other involved method is to use Floquet theory in the fixed reference frame. The second approach is to keep the blade equations in the rotating reference frame and solve these using the Floquet or time integration technique or harmonic balance method. With the dynamic inflow modeling, it is more appropriate to use the first approach and solve the equations in the fixed reference frame.

To understand the fundamentals of forward flight, we shall start with a simple blade model undergoing rigid flap motion. Later on a two-degree-of-motion, flap and lag, will be investigated for aeroelastic stability in forward flight.

7.1 Flap Motion in forward flight

The blade is assumed rigid and it undergoes a single degree of motion, rigid flap, about the flap hinge. The blade is exposed to forward flight environment.





The equation of motion of a blade is

$$\beta^{**} + \nu_\beta^2 \beta = \gamma \overline{M}_\beta$$

where ν_β is the rotating flap frequency and γ is the Lock number. The \overline{M}_β represents the aerodynamic moment about the flap hinge

$$\overline{M}_\beta = \frac{1}{\rho a c \Omega^2 R^4} \int_0^L r F_z dr$$

$$F_z \approx L$$

$$= \frac{1}{2} \rho V^2 c a \left(\theta - \frac{u_p}{u_T} \right)$$

$$= \frac{1}{2} \rho c a (u_T^2 \theta - u_p u_T)$$

The flow components are

$$\frac{u_T}{\Omega R} = \mu \sin \psi + x$$

$$\frac{u_p}{\Omega R} = x \dot{\beta} + \lambda + \beta \mu \cos \psi$$

where $x = \frac{r}{R}$ and λ is the induced inflow. The μ is the advance ratio,

$$\mu = \frac{v \cos \alpha}{\Omega R} \approx \frac{V}{\Omega R} \quad (\alpha \text{ is tilt of TPP})$$

$$\overline{M}_\beta = \frac{1}{2} \int_0^1 x \left[\left(\frac{u_T}{\Omega R} \right)^2 \theta - \frac{u_p}{\Omega R} \frac{u_T}{\Omega R} \right] dx$$

Assuming θ is uniform along the blade length. It is also assumed that the induced inflow λ is uniform on the disk.

$$\begin{aligned} \overline{M}_\beta &= \left(\frac{1}{8} + \frac{\mu}{3} \sin \psi + \frac{\mu^2}{4} \sin^2 \psi \right) \theta - \left(\frac{1}{8} + \frac{\mu}{6} \sin \psi \right) \beta^* \\ &\quad - \left(\frac{1}{6} + \frac{\mu}{4} \sin \psi \right) \lambda - \mu \cos \psi \left(\frac{1}{6} + \frac{\mu}{4} \sin \psi \right) \beta \end{aligned}$$

The flap equation becomes

$$\beta^{**} + \left(\frac{1}{8} + \frac{\mu}{6} \sin \psi \right) \beta^* + \left[\nu_\beta^2 + \gamma \mu \cos \psi \left(\frac{1}{6} + \frac{\mu}{4} \sin \psi \right) \right] \beta$$

$$\begin{aligned}
&= \gamma \left(\frac{1}{8} + \frac{\mu}{3} \sin \psi + \frac{\mu^2}{4} \sin^2 \psi \right) \theta \\
&\quad - \gamma \left(\frac{1}{6} + \frac{\mu}{4} \sin \psi \right) \lambda
\end{aligned} \tag{7.1}$$

This is a linear differential equation containing periodic coefficients. If the effect of pitch-flap coupling $k_{p\beta}$ is also to be introduced, then replace θ by $\theta - k_{p\beta}$ in the above equation.

$$\begin{aligned}
&\beta^{**} + \gamma \left(\frac{1}{8} + \frac{\mu}{6} \sin \psi \right) \beta^* + \left[\nu_\beta^2 + \gamma \mu \cos \psi \left(\frac{1}{6} + \frac{\mu}{4} \sin \psi \right) \right. \\
&\quad \left. + \gamma \left(\frac{1}{8} + \frac{\mu}{3} \sin \psi + \frac{\mu^2}{4} \sin^2 \psi \right) k_{p\beta} \right] \beta \\
&= \gamma \left(\frac{1}{8} + \frac{\mu}{3} \sin \psi + \frac{\mu^2}{4} \sin^2 \psi \right) \theta - \gamma \left(\frac{1}{6} + \frac{\mu}{4} \sin \psi \right) \lambda
\end{aligned} \tag{7.2}$$

7.2 Hover Stability Roots

Let us first examine hover flight case ($\mu = 0$). The blade equation becomes

$$\beta^{**} + \frac{\gamma}{8} \beta^* + \left(\nu_\beta^2 + \frac{\gamma}{8} k_{p\beta} \right) \beta = \frac{\gamma \theta}{8} - \frac{\gamma \lambda}{6}$$

The stability of the system can be examined from the eigenvalues of this equation.

$$s = -\frac{\gamma}{16} \pm i \sqrt{\nu_\beta^2 + k_{p\beta} \frac{\gamma}{8} - \left(\frac{\gamma}{16} \right)^2}$$

This is a complex pair i.e., two eigenvalues. The real part of the eigenvalue represents the damping of the flap mode and the imaginary part represents the frequency of the flap mode.

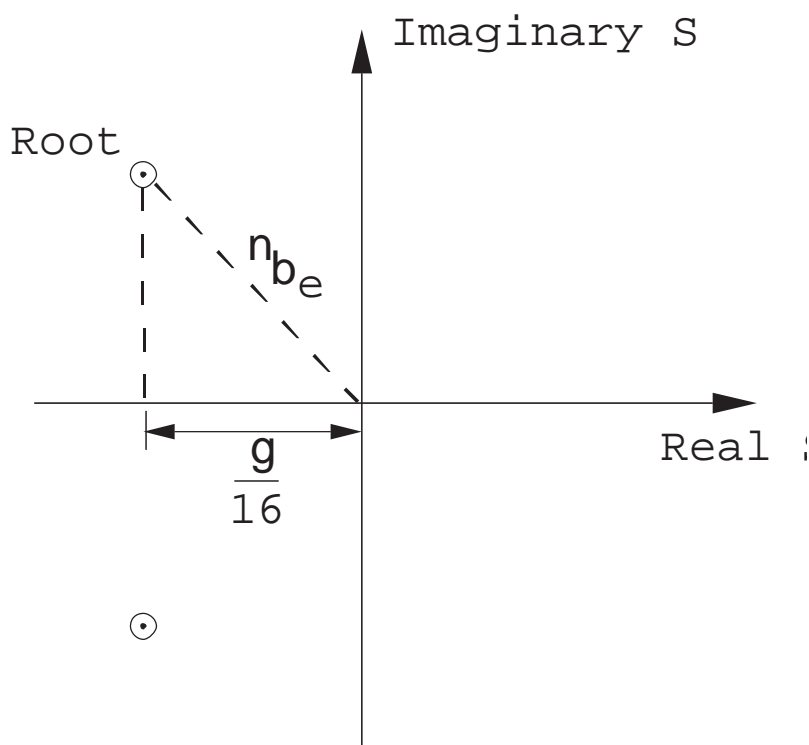
$$\text{Frequency of damped oscillations } \omega_d = \sqrt{\nu_\beta^2 + k_{p\beta} \frac{\gamma}{8} - \left(\frac{\gamma}{16} \right)^2}$$

$$\text{Natural frequency } \nu_{\beta e} = \sqrt{\nu_\beta^2 + k_{p\beta} \frac{\gamma}{8}}$$

$$\text{Damping ratio } \zeta = -\frac{\text{Real } s}{|s|}$$

$$= \frac{\gamma}{16\nu_{\beta e}}$$

Thus, the damping of the flap mode depends on the Lock number and is always a positive number. This shows that there is no likelihood of instability of the flap mode. In fact, for a typical Lock number of 8, the damping ratio is about 50%, a very high number. This damping is due to aerodynamic force caused by the flapping motion. For a 4-bladed rotor, there will be four identical pairs. Let us plot roots for a blade in a complex plane



The roots will always lie in the left half of the plane on a semi-circular arc.

7.3 Forward Flight Stability Roots

The equation of motion for a blade in forward flight (Eq. 7.2) contains periodic coefficients. This equation is expressed in the rotating reference frame. One way is to solve numerically this equation using the Floquet theory. For hover case ($\mu = 0$), the roots are complex conjugate pairs and the magnitude of the root depends on ν_β , Y and $k_{p\beta}$. For forward flight the roots, in addition, also depend on the advance ratio, μ . For low μ , the forward flight roots behavior is influenced by hover roots. Let us consider these blade cases with $k_{p\beta} = 0$.

I. $\nu_\beta = 1$ and $\gamma = 12$ (Articulated)

$$s_{\text{hover}} = -\frac{12}{16} \pm i\sqrt{1 - \left(\frac{12}{16}\right)^2}$$

$$= -\frac{3}{4} \pm i\sqrt{\frac{7}{16}}$$

Frequency of oscillation close to 1/2 per rev.

II. $\nu_\beta = 1.15$ and $\gamma = 6$ (Hingeless)

$$s_{\text{hover}} = -\frac{3}{8} \pm i\sqrt{(1.15)^2 - \frac{9}{64}}$$

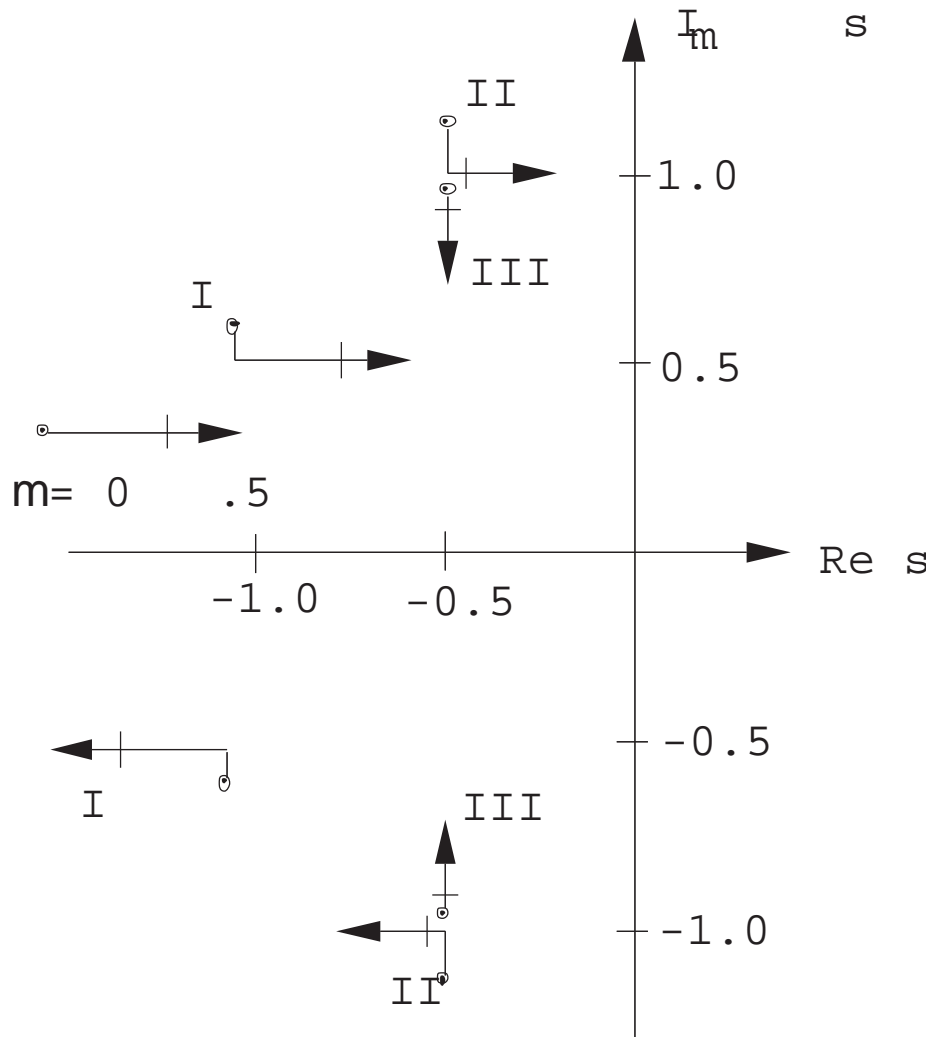
Frequency of oscillation close to 1 per rev.

III. $\nu_\beta = 1.0$ and $\gamma = 6$ (Articulated)

$$s_{\text{hover}} = -\frac{3}{8} \pm i\sqrt{1 - \frac{9}{64}}$$

Frequency of oscillation not close to 1/2 per rev. or 1 per rev.

Let us examine the behavior of roots for change of μ from 0 to 0.5.



For values of γ and ν_β such that the hover frequency ($I_m s$) is not close to a multiple of $1/2/\text{rev}$. (Case III), the roots for low μ only exhibit a second order (μ^2) change in frequency and the damping remains unchanged.

For values of γ and ν_β such that the hover frequency ($I_m s$) is close to a multiple of $1/2/\text{rev}$. (Case I), the roots for low μ exhibit a first order (μ) change. There can occur a degradation of stability, perhaps even an instability, an important characteristic of the periodic system.

For values of γ and ν_β such that the hover frequency ($I_m s$) is close to $1/\text{rev}$. (Case II), the roots exhibit similar behavior like Case I. For both cases one finds that the frequency $I_m s$ decreases while damping Real s remains constant until an integer multiple of $1/2/\text{rev}$. is reached. A further increase of μ results in a change of damping, a decrease for the upper root and an increase for the lower root, and the frequency stays constant. For larger μ , one needs to include the effect of reversed flow as well as higher modes.

7.3.1 Stability Roots in Rotating Coordinates

7.3.2 Stability Roots in Fixed Coordinates

Let us examine the flapping dynamics in the fixed reference frame. The equation of motion for the blade flapping in the rotating frame (Eq. 7.2) is converted to the fixed reference frame using the Fourier coordinate transformation.

Let us consider a 3-bladed rotor, $n = 1$

$$\beta^{(m)} = \beta_0 + \beta_{1c} \cos \psi_m + \beta_{1s} \sin \psi_m$$

Using

$$\frac{1}{N} \sum_{m=1}^N (de) = 0$$

$$\frac{2}{N} \sum_{m=1}^N (de) \cos \psi_m = 0$$

$$\frac{2}{N} \sum_{m=1}^N (de) \sin \psi_m = 0$$

results in

$$\begin{bmatrix} \beta_0^{**} \\ \beta_{1c}^{**} \\ \beta_{1s}^{**} \end{bmatrix} = \begin{bmatrix} \frac{\gamma}{8} & 0 & \frac{\mu\gamma}{12} \\ 0 & \frac{\gamma}{8} + \frac{\mu\gamma}{12} \sin 3\psi & 2 - \frac{\mu\gamma}{12} \cos 3\psi \\ \frac{\mu\gamma}{6} & -2 - \frac{\mu\gamma}{12} \cos 3\psi & \frac{\gamma}{8} - \frac{\mu\gamma}{12} \sin 3\psi \end{bmatrix} \begin{bmatrix} \beta_0^* \\ \beta_{1c}^* \\ \beta_{1s}^* \end{bmatrix} + \begin{bmatrix} \nu_\beta^2 & \frac{\mu^2\gamma}{16} \sin 3\psi & -\frac{\mu^2\gamma}{16} \cos 3\psi \\ \frac{\mu\gamma}{6} + \frac{\mu^2\gamma}{8} \sin 3\psi & \nu_\beta^2 - 1 + \frac{\mu\gamma}{6} \cos 3\psi & \frac{\gamma}{8} + \frac{\mu\gamma}{6} \sin 3\psi + \frac{\mu^2\gamma}{16} \\ -\frac{\mu^2\gamma}{8} \cos 3\psi & -\frac{\gamma}{8} + \frac{\mu^2\gamma}{16} + \frac{\mu\gamma}{6} \sin 3\psi & \nu_\beta^2 - 1 - \frac{\mu\gamma}{6} \cos 3\psi \end{bmatrix} \begin{bmatrix} \beta_0 \\ \beta_{1c} \\ \beta_{1s} \end{bmatrix} \quad (7.3)$$

Similarly for a 4-bladed rotor

$$\beta^{(m)} = \beta_0 + \beta_{1c} \cos \psi_m + \beta_{1s} \sin \psi_m + \beta_2 (-1)^{(m)}$$

results in

$$\begin{bmatrix} \beta_0^{**} \\ \beta_{1c}^{**} \\ \beta_{1s}^{**} \\ \beta_2^{**} \end{bmatrix} = \begin{bmatrix} \frac{\gamma}{8} & 0 & \frac{\mu\gamma}{12} & 0 \\ 0 & \frac{\gamma}{8} & 2 & \frac{\mu\gamma}{6} \sin 2\psi \\ -\frac{\mu\gamma}{16} & -2 & \frac{\gamma}{8} & -\frac{\mu\gamma}{6} \cos 2\psi \\ 0 & \frac{\mu\gamma}{12} \sin 2\psi & -\frac{\mu\gamma}{12} \cos 2\psi & \frac{\gamma}{8} \end{bmatrix} \begin{bmatrix} \beta_0^* \\ \beta_{1c}^* \\ \beta_{1s}^* \\ \beta_2^* \end{bmatrix} + \begin{bmatrix} \nu_\beta^2 & 0 & 0 & \frac{\mu^2\gamma}{8} \sin 2\psi \\ \frac{\mu\gamma}{6} & \nu_\beta^2 - 1 + \frac{\mu^2\gamma}{16} \sin 4\psi & \frac{\gamma}{8} + \frac{\gamma}{16} \mu^2 - \frac{\gamma}{16} \mu^2 \cos 4\psi & \frac{\mu\gamma}{6} \cos 2\psi \\ 0 & -\frac{\gamma}{8} + \frac{\gamma}{16} \mu^2 - \frac{\gamma}{16} \mu^2 \cos 4\psi & \nu_\beta^2 - 1 - \mu^2 \frac{\gamma}{16} \sin 4\psi & \frac{\mu\gamma}{8} \sin 2\psi \\ \frac{\mu^2\gamma}{8} \sin 2\psi & \frac{\mu\gamma}{6} \cos 2\psi & \frac{\mu\gamma}{6} \sin 2\psi & \nu^2 \beta \end{bmatrix} \begin{bmatrix} \beta_0 \\ \beta_{1c} \\ \beta_{1s} \\ \beta_2 \end{bmatrix} \quad (7.4)$$

It is important to note that the 3-bladed rotor equations in the fixed system contain periodic terms of 3ψ only. For a 4-bladed rotor, the equations contain periodic terms of 4ψ as well as 2ψ . Therefore, in the fixed system, the vibratory forces take place at N/rev for an odd bladed rotor and N/rev and $\frac{N}{2}/\text{rev}$ for an even bladed rotor where N is the total number of blades.

Let us examine an example of an articulated 3-bladed rotor with $\nu_\beta = 1$ and $\gamma = 12$. In the rotating frame there are three identical roots

$$s_R = -\frac{3}{4} \pm \sqrt{\frac{7}{16}}$$

and in the fixed systems, again there are three roots;

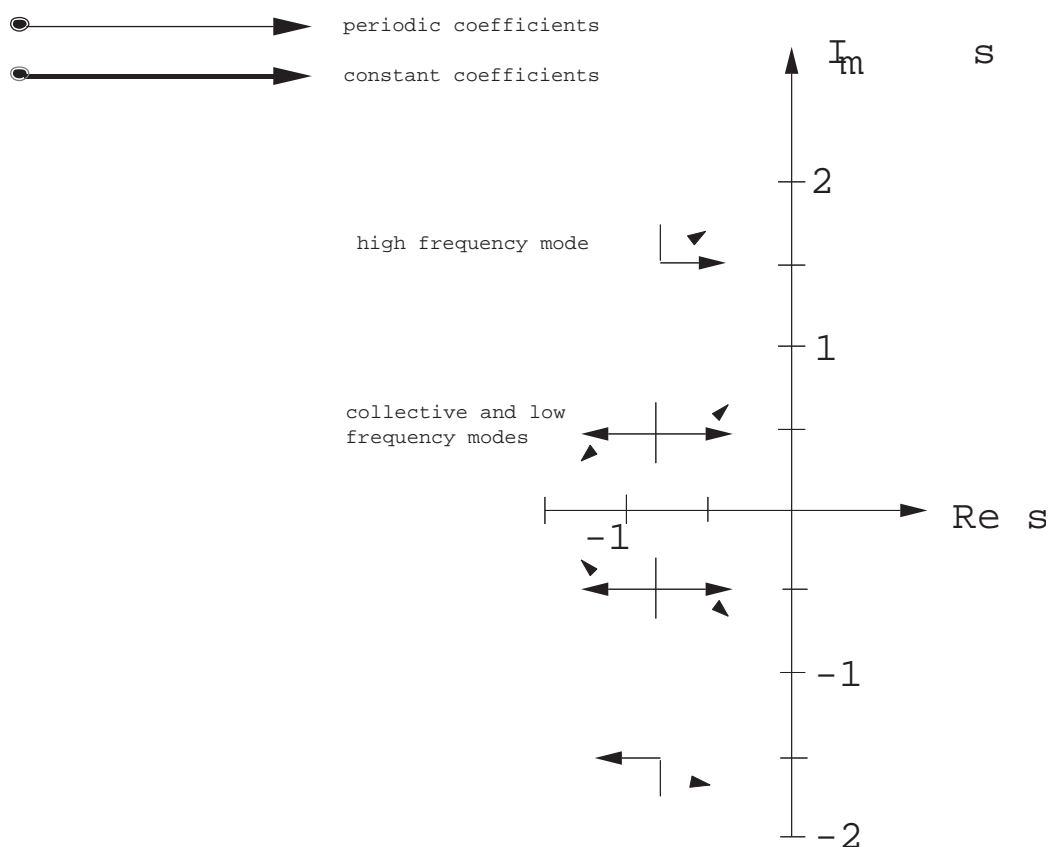
coning $s = s_R$

high frequency $s = s_R + i$

low frequency $s = s_R - i$

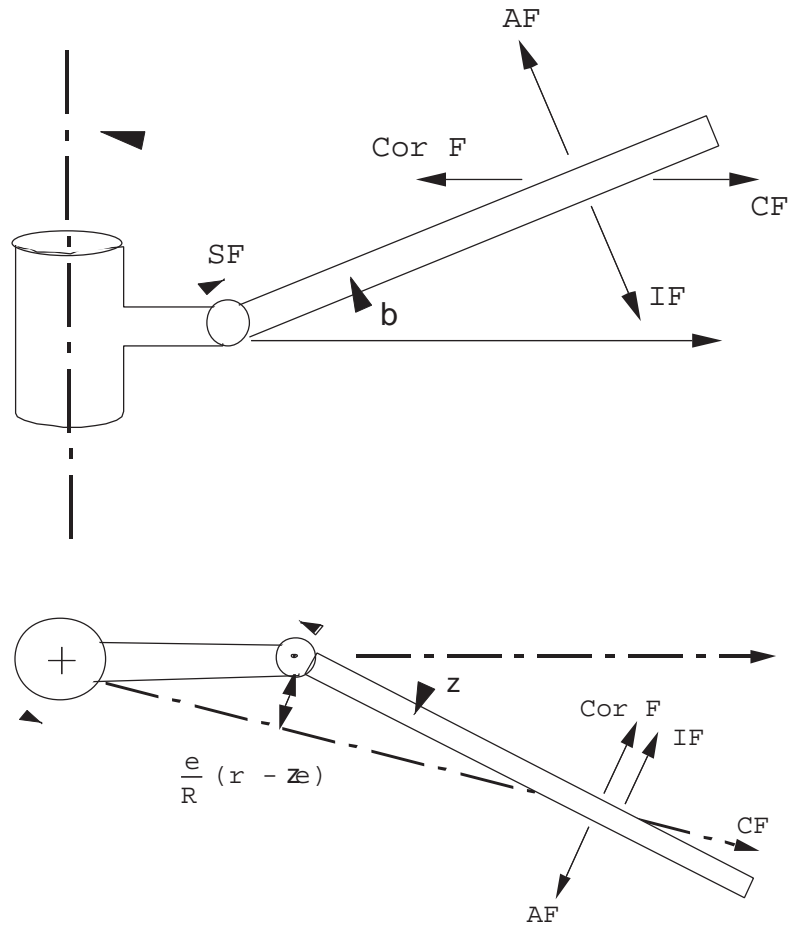
For forward flight condition, the roots of the equations can be obtained for different μ . One simple approach is to neglect all periodic terms in the fixed system equations and solve these as constant coefficient equations. The results are quite satisfactory for low advance ratios ($\mu < 0.5$), especially for the low frequency mode. One should keep in mind that this type of approximation won't work in the rotating frame. The second method is to solve the fixed frame equations numerically using the Floquet theory. Another way is to use the harmonic balance method in the fixed frame. In the figure, results are obtained using the Floquet theory and constant coefficient approximation.

The stability behavior will be identical whether the rotating reference frame or the fixed reference frame are used.



7.4 Flap-lag Stability in Forward Flight

The blade is assumed rigid and it undergoes two degrees of motion, flap and lag motions about hinges. There are bending springs at the hinges to obtain desired flap and lag frequencies.



The equations of motion become

Flap Eq.:

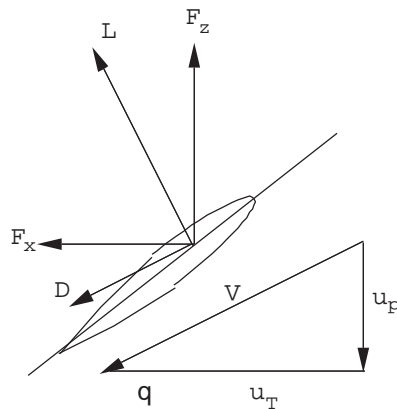
$$\beta^{**} + \nu_{\beta}^2 \beta - 2\beta \zeta^* = \gamma \overline{M}_{\beta} + \frac{\omega_{\beta_0}^2}{\Omega^2} \beta_p$$

Lag Eq.:

$$\zeta^{**} + \nu_{\zeta}^2 \zeta + 2\frac{\omega_{\zeta_0}}{\Omega} \zeta_L \zeta^* + \beta \beta^* = \gamma \overline{M}_{\zeta}$$

(7.5)

where ν_{β} and ν_{ζ} are rotating flap and lag frequencies and ζ_L is the structural damping coefficient in the lag mode. The ω_{β_0} and ω_{ζ_0} are the nonrotating flap and lag frequencies.



Quasisteady aerodynamics is used to obtain the aerodynamic forces on the blade. The reversed flow effects are neglected.

$$F_z \approx L = \frac{1}{2} \rho a c (u_T^2 \theta - u_p u_T)$$

$$F_x \approx L \frac{u_p}{u_T} + D = \frac{1}{2} \rho a c \left(\frac{c_d}{a} u_T^2 + u_p u_T \theta - u_p^2 \right)$$

Perturbation forces are

$$\delta F_z = \frac{1}{2} \rho a c [\delta u_T (2u_T \theta - u_p) - \delta u_p (u_T) + \delta \theta u_T^2]$$

$$\delta F_x = \frac{1}{2} \rho a c \left[\delta u_T \left(2u_T \frac{c_d}{a} + u_p \theta \right) + \delta u_p (u_T \theta - 2u_p) + \delta \theta (u_p u_T) \right]$$

For making analysis simple, the effect of radial force is neglected.

The flow components are

Steady:

$$\begin{aligned} \frac{u_T}{\Omega R} &= x + \mu \sin \psi \\ \frac{u_p}{\Omega R} &= \lambda + x \dot{\beta} + \beta \mu \cos \psi \end{aligned} \quad (7.6)$$

Perturbation:

$$\begin{aligned} \frac{\delta u_T}{\Omega R} &= -x \dot{\zeta} - \mu \zeta \cos \psi \\ \frac{\delta u_p}{\Omega R} &= x \dot{\beta} + \mu \beta \cos \psi \end{aligned} \quad (7.7)$$

The solution of the governing equation (7.6) consists of two major steps.

- (a) Calculation of trim.
- (b) Calculation of perturbation stability.

7.4.1 Perturbation Stability Solution

It is assumed that the flutter motion is a small perturbation about the steady trim solution.

$$(\beta)_{\text{Total}} = (\beta)_{\text{trim}} + (\beta)_{\text{perturbation}}$$

$$(\zeta)_{\text{Total}} = (\zeta)_{\text{perturbation}}$$

This is because $(\zeta)_{\text{trim}}$ trim is neglected. The trim values of β are calculated as

$$(\beta)_{\text{trim}} = -\beta_{1c} \sin \psi + \beta_{1s} \sin \psi = \beta_T$$

$$(\beta)_{\text{trim}}^* = \beta_0 + \beta_{1c} \cos \psi + \beta_{1s} \cos \psi = \beta_T^*$$

Let us remove the perturbation word from β and ζ . Substituting this in the governing equation (7.5), and also including the perturbation aerodynamic moment expressions, and keeping linear terms in perturbation motion components one gets,

$$\begin{bmatrix} ** \\ \beta \\ ** \\ \zeta \end{bmatrix} + [C(\psi)] \begin{bmatrix} * \\ \beta \\ * \\ \zeta \end{bmatrix} + [K(\psi)] \begin{bmatrix} \beta \\ \zeta \end{bmatrix} = 0 \quad (7.8)$$

These are matrices of order two, and the various terms are

$$c_{11}(\psi) = \frac{\gamma}{8} \left(1 + \frac{4}{3} \mu \sin \psi \right)$$

$$\begin{aligned}
c_{12}(\psi) &= \frac{\gamma}{8} \left(\frac{4}{3}\lambda + \frac{4}{3}\mu\beta_T \cos \psi + \beta_T^* \right) \\
&\quad - \frac{\gamma}{4}\theta \left(1 + \frac{4}{3}\mu \sin \psi \right) + 2\beta_T \\
c_{21}(\psi) &= -\frac{\gamma}{4} \left(\frac{4}{3}\lambda + \frac{4}{3}\mu\beta_T \cos \psi - \beta_T^* \right) \\
&\quad + \frac{\gamma}{8}\theta \left(1 + \frac{4}{3}\mu \sin \psi \right) - 2\beta_T \\
c_{22}(\psi) &= \frac{\gamma}{8}\theta \left(\frac{4}{3}\lambda + \frac{4}{3}\mu \cos \psi \beta_T + \beta_T^* \right) \\
&\quad + \frac{c_{d0}}{a} \frac{\gamma}{4} \left(1 + \frac{4}{3}\mu \sin \psi \right) - 2\beta_T \beta_T^* \\
k_{11}(\psi) &= \nu_\beta^2 + \frac{\gamma}{8} \left(\frac{4}{3}\mu \cos \psi + 2\mu^2 \sin \psi \cos \psi \right) \\
&\quad - \frac{\gamma}{8}k_{p\beta} \left(1 + \frac{8}{3}\mu \sin \psi + 2\mu^2 \sin^2 \psi \right) \\
k_{12}(\psi) &= \frac{\gamma}{8}\mu \cos \psi \left(2\lambda + \frac{4}{3}\beta_T^* \right) - \frac{\gamma}{4}\theta \left(\frac{4}{3}\mu \cos \psi + 2\mu^2 \sin \psi \cos \psi \right) \\
&\quad - \frac{\gamma}{4}\beta_T \left(\mu^2 \cos 2\psi - \frac{2}{3}\mu \sin \psi \right) \\
&\quad - \frac{\gamma}{8}k_{p\beta} \left(1 + \frac{8}{3}\mu \sin \psi + 2\mu^2 \sin^2 \psi \right) \\
k_{21}(\psi) &= -\frac{\gamma}{4}\mu \cos \psi \left(2\lambda + \frac{4}{3}\beta_T^* \right) + \frac{\gamma}{8}\theta \left(\frac{4}{3}\mu \cos \psi + \mu^2 \sin 2\psi \right) \\
&\quad - \frac{\gamma}{2}\beta_T \mu^2 \cos^2 \psi + \frac{\gamma}{8}k_{p\beta} \left[\frac{4}{3}\lambda \left(1 + \frac{3}{2}\mu \sin \psi \right) \right. \\
&\quad \left. + \beta_T^* \left(1 + \frac{8}{3}\mu \sin \psi \right) + \beta_T \left(\frac{4}{3}\mu \cos \psi + \mu^2 \sin 2\psi \right) \right] \\
k_{22}(\psi) &= \nu_\zeta^2 + \frac{\gamma}{8} \left[2\frac{c_{d0}}{a} \left(\frac{4}{3}\mu \cos \psi + \psi^2 \sin 2\psi \right) \right. \\
&\quad \left. + \mu \cos \psi \theta \left(2\lambda + \frac{4}{3}\beta_T^* \right) - \beta_T \theta \left(\frac{4}{3}\mu \sin \psi - 2\mu^2 \cos \psi \right) \right. \\
&\quad \left. + 2\mu\beta_T \sin \psi \left(2\lambda + \frac{4}{3}\beta_T^* + 2\mu\beta_T \cos \psi \right) \right] \\
&\quad + \frac{\gamma}{8}k_{p\beta} \left[\frac{4}{3}\lambda \left(1 + \frac{3}{2}\mu \sin \psi \right) + \beta_T \left(\frac{4}{3}\mu \cos \psi + \mu^2 \sin 2\psi \right) \right. \\
&\quad \left. + \beta_T^* \left(1 + \frac{4}{3}\mu \sin \psi \right) \right]
\end{aligned}$$

In the above expressions

$$\theta = \theta_0 + \theta_{1c} \cos \psi + \theta_{1s} \sin \psi$$

The stability of the system is calculated from the solution of the perturbation equations (7.8). There are many methods to solve these equations. Two possible approaches are discussed here

- (a) Constant coefficient approximation.
- (b) Floquet Theory.

7.4.2 Constant Coefficient Approximation

The coefficients of the matrices (\tilde{c}, \tilde{k}) contain periodic terms, and these are approximated as constant terms by taking average values over a period of 2π . For example,

$$(c_{ij})_{\text{new}} = \frac{1}{2\pi} \int_0^{2\pi} c_{ij}(\psi) d\psi$$

$$(k_{ij})_{\text{new}} = \frac{1}{2\pi} \int_0^{2\pi} k_{ij}(\psi) d\psi$$

and this results in

$$c_{11} = \frac{\gamma}{8}$$

$$c_{12} = 2\beta_0 + \frac{\gamma}{8} \left(\frac{4}{3}\lambda + \frac{2}{3}\mu\beta_{1c} \right) - \frac{\gamma}{4} \left(\theta_0 + \frac{2}{3}\mu\theta_{1s} \right)$$

$$c_{21} = -2\beta_0 - \frac{\gamma}{4} \left(\frac{4}{3}\lambda + \frac{2}{3}\mu\beta_{1c} \right) + \frac{\gamma}{8} \left(\theta_0 + \frac{2}{3}\mu\theta_{1s} \right)$$

$$c_{22} = \frac{\gamma}{8} \left[2\frac{c_{d_0}}{a} + \frac{1}{2}\theta_{1c}\beta_{1s} - \frac{1}{2}\theta_{1s}\beta_{1c} + \frac{2}{3}\mu\theta_{1c} + \frac{2}{3}\mu\theta_{1c}\beta_0 \right. \\ \left. + \theta_0 \left(\frac{4}{3}\lambda + \frac{2}{3}\mu\beta_{1c} \right) \right]$$

$$k_{11} = \nu_\beta^2 - \frac{\gamma}{8}k_{p_\beta}(1 + \mu^2)$$

$$k_{12} = -\frac{\gamma}{8}k_{p_\zeta}(1 + \mu^2) - \frac{\gamma}{6}\mu\theta_{1c}$$

$$k_{21} = \frac{\gamma}{6}\lambda k_{p_\zeta} + \frac{\gamma}{8}\mu \left(\frac{2}{3}\theta_{1c} - \frac{4}{3}\beta_{1c} - 2\mu\beta_0 \right)$$

$$k_{22} = \frac{\gamma}{8} \left[\mu\lambda\theta_{1c} - \frac{2}{3}\mu\beta_0\theta_{1s} - \frac{4}{3}\mu\beta_0\beta_{1c} + 2\mu\lambda\beta_{1s} \right] \frac{\gamma}{6}k_{p_\zeta}\lambda$$

The perturbation equations (7.8) become constant coefficient equations and these can be solved as a standard eigenvalue problem.

7.4.3 Floquet Theory

The perturbation equations (7.8) contain periodic terms and the stability of these equations can be calculated using Floquet theory. As a first step, the Floquet transition matrix is to be calculated. For this purpose, the equations (7.8) are transformed to first order form.

$$\{\dot{q}^*\} = [A(\psi)]\{q\} \tag{7.9}$$

where

$$\{q\} = \begin{bmatrix} \beta \\ \zeta \\ * \\ \beta \\ * \\ \zeta \end{bmatrix}$$

$$[A] = \begin{bmatrix} \tilde{O} & \tilde{I} \\ -\tilde{k} & -\tilde{c} \end{bmatrix}$$

To obtain the Floquet transition matrix $[Q]$, the equations (7.9) are solved numerically using some standard time integration technique (say Runge-Kutta) with unity initial conditions. The solution at $\psi = 2\pi$ gives the elements of transition matrix. For example,

$$\begin{bmatrix} \beta \\ \zeta \\ * \\ \beta \\ * \\ \zeta \end{bmatrix} = \begin{bmatrix} 1 \\ 0 \\ 0 \\ 0 \end{bmatrix}_{Ic} \Rightarrow \begin{bmatrix} Q_{11} \\ Q_{21} \\ Q_{31} \\ Q_{41} \end{bmatrix} \quad (\text{solution at } \psi = 2\pi)$$

After the transition matrix is evaluated, the next step is to obtain its eigenvalue.

$$\lambda\{q\} = [Q]\{q\}$$

If the absolute value of any of the eigenvalue (λ) is greater than one, the system is unstable.

The numerical results are obtained for a typical rotor configuration with the following characteristics

$$\begin{aligned} \nu_\beta &= 1.15 & \gamma &= 1.15 & \frac{c_T}{\sigma} &= .2 & \sigma &= .05 \\ \nu_\zeta &= 1.4 & k_{p\beta} &= k_{p\zeta} = 0 & \beta_p &= 0 & f/A &= 0.01 \\ c_{d0} &= .01 & a &= 2\pi & \frac{h}{R} &= .2 \\ x_{cg} &= y_{cg} = 0 & c_{m_{xF}} &= c_{m_{yF}} = 0 \end{aligned}$$

Earlier, the trim is calculated for this configuration. These results are plotted for various values of advance ratio μ .

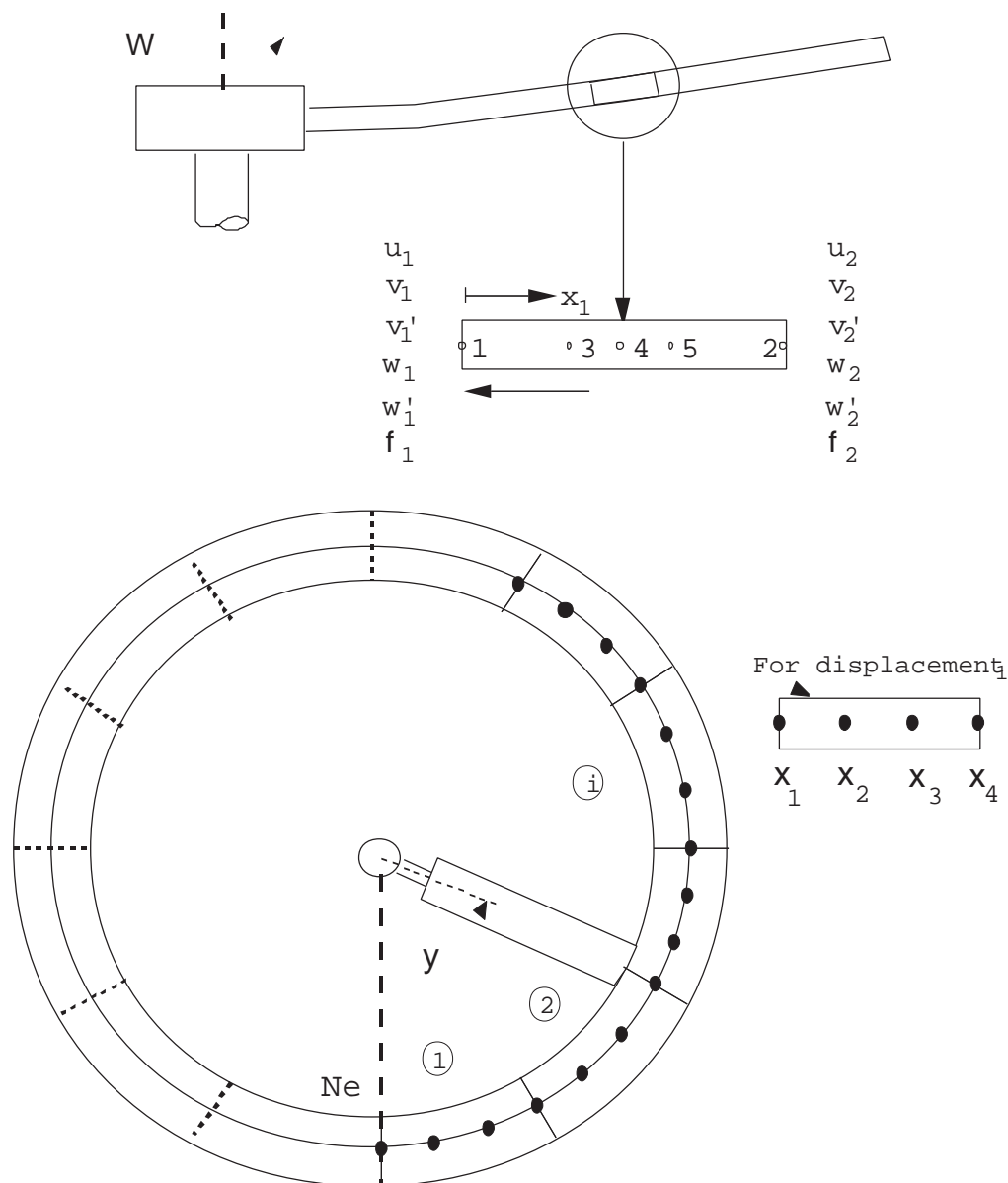
Conclusions:

1. The constant coefficient approximation in the rotating system gives satisfactory results for low advance ratio ($\mu < 0.1$).
2. The flap-lag stability in forward flight is very sensitive to the trim solution. For example, the propulsive trim results are quite different from moment trim results.
3. For large advance ratio ($\mu > 0.1$), the inflow is affected appreciably by the helicopter drag term (f/A).
4. The implicit periodic coefficients (due to β_{1c} , β_{1s} , θ_{1c} , θ_{1s}) and the explicit periodic coefficients ($\mu \sin \psi$, $\mu \cos \psi$) are important for flap-lag stability analysis.
5. The torsion degree of motion has a considerable influence on blade stability if torsional frequency is small.

References

1. Johnson, W., Helicopter Theory, Princeton University Press, 1980, Chapter 12.
2. Biggers, J. C., "Some Approximations to the Flapping Stability of Helicopter Rotors," Journal of the American Helicopter Society, Vol. 19, No. 4, Oct. 1974.
3. Friedman, P. P. and Kattapalli, S. B. R., "Coupled Flap-Lag-Torsional Dynamics of Hingeless Rotor Blades in Forward Flight," Journal of the American Helicopter Society, Vol. 24, No. 4, Oct. 1982, pp. 28-36.

4. Peters, D. A., "Flap-Lag Stability of Helicopter Rotor Blades in Forward Flight," Journal of the American Helicopter Society, Vol. 20, No. 4, Oct. 1975, pp. 2-13.
5. Panda, B. and Chopra, I., "Flap-Lag-Torsion Stability in Forward Flight," Presented at the Second Decennial Specialists' Meeting on Rotorcraft Dynamics at Ames Research Center, Moffett Field, Calif., Nov. 1984.
6. Panda, B. and Chopra, I., "Dynamic Stability of Hingeless and Bearingless Rotors in Forward Flight," Presented at the International Conference on Rotorcraft Basic Research, Research Triangle Park, North Carolina, Feb. 1985.



COUPLED TRIM ANALYSIS

- Uncoupled Vehicle Trim (Propulsive)
 - Control Settings and Vehicle Attitude
 - Initial Guess for Iteration Process

- Blade Steady Response
 - Determination of Time Dependent Blade Deflections Using Finite Element Method in Time
 - Normal Mode Equations
- Coupled Trim Solution
 - Update Control Settings and Vehicle Attitude
 - Satisfy Nonlinear Vehicle Equilibrium Equations
 - Vehicle Trim and Blade Response Calculated Iteratively as One Coupled Solution Using Modified Newton Method

Chapter 8

Trailing Edge Flaps and Tabs

This chapter deals with the dynamics of trailing edge flaps. Smart material based actuators can be used to activate on-blade trailing edge flaps. The aeroelastic response of the flaps can be used to effectively change the airload distribution on the rotor blades. In general, active surfaces like trailing edge flaps can be used for – 1. vibration control, 2. loads control, and 3. swash-plateless primary control. Trailing edge flaps have also been studied for purposes of rotor noise control.

Flaps on rotor blades operate under high centrifugal loads. Present smart actuators have been demonstrated to produce $\pm 10^\circ$ of flap deflections in vacuum, and $\pm 4^\circ$ with wind on. To obtain such values of flap deflection, the actuator deformations are amplified using mechanical, electrical, or aerodynamic means. Mechanical and electrical amplifications are widely used. Aerodynamic amplification, e.g. in form of servo tabs, is still in the exploratory phase for rotary wing applications [1].

To avoid confusion with blade flap, the trailing edge flap will be termed aileron.

8.1 Flap-Torsion-Aileron Dynamics of a Wing Section

First a classical 2 degree-of-freedom flap torsion model is shown. Then a 3 degree-of-freedom model including aileron dynamics is studied.

8.1.1 Flap-Torsion dynamics

First consider a case without aileron. In order to maintain classical notations (used in bending-torsion flutter studies) let h be the heave motion positive downwards, and θ be the nose up twist. The heave motion h is the translational motion of the shear center, i.e. elastic axis. The twist θ is ofcourse same about all points. The heave equation is obtained by balancing the net force. The moment equation is obtained by balancing the net moments about the shear center. Balancing moments about the shear center prevents the calculation of the reaction forces occuring at that point.

The moment equilibrium gives

$$\begin{aligned} I_{cg}\ddot{\theta} + mx_I^2\ddot{\theta} + mx_I\ddot{h} + k_\theta\theta &= M_{ea} \\ I_\theta\ddot{\theta} + S_\theta\ddot{h} + k_\theta\theta &= M_{ea} \end{aligned} \tag{8.1}$$

The force equilibrium gives

$$\begin{aligned} m\ddot{h} + mx_I\ddot{\theta} + k_h h &= -L \\ S_\theta\ddot{\theta} + m\ddot{h} + k_h h &= -L \end{aligned} \tag{8.2}$$

8.1.2 Flap-torsion-aileron dynamics: Force method

A coupled flap-torsion-aileron model for a wing is developed using force method (Newton). The derivation of the governing equations are simpler using the energy method. The energy method is shown in the next subsection. The force balance method is used here to illustrate the force transfer mechanism from the aileron to the wing.

Consider the free body diagram of the aileron alone. The downward acceleration of the aileron c.g. and its angular acceleration are given by

$$\ddot{h} + \{b(a+c) + y_I\} \ddot{\theta} + y_I \ddot{\delta}$$

and

$$\ddot{\theta} + \ddot{\delta}$$

Balancing moments about the aileron hinge gives

$$\begin{aligned} I_{cg\delta}(\ddot{\theta} + \ddot{\delta}) + m\delta \left[\ddot{h} + \{b(a+c) + y_I\} \ddot{\theta} + y_I \ddot{\delta} \right] y_I + k_\delta \delta &= M_2 \\ I_\delta \ddot{\delta} + I_\theta \ddot{\theta} + S_\delta \ddot{h} + S_\delta b(a+c) \ddot{\theta} + k_\delta \delta &= M_2 \\ I_\delta \ddot{\delta} + [I_\delta + S_\delta b(a+c)] \ddot{\theta} + S_\delta \ddot{h} + k_\delta \delta &= M_2 \end{aligned} \quad (8.3)$$

The effect of flap is felt on the wing via the reaction force R at the flap hinge. R is obtained by balancing forces on the aileron

$$\begin{aligned} L_2 + R + m\delta \left[\ddot{h} + \{b(a+c) + y_I\} \ddot{\theta} + y_I \ddot{\delta} \right] &= 0 \\ R = -L_2 - m\delta \left[\ddot{h} + \{b(a+c) + y_I\} \ddot{\theta} + y_I \ddot{\delta} \right] \end{aligned} \quad (8.4)$$

Now consider the free body diagram of the wing alone. Using force balance the wing heave equation becomes

$$\begin{aligned} m\ddot{h} + mx_I \ddot{\theta} + k_h h - R &= -L_1 \\ M\ddot{h} + S\ddot{\theta} + S_\delta \ddot{\delta} + k_h h &= -L \end{aligned} \quad (8.5)$$

where

$$\begin{aligned} M &= m + m_\delta \\ L &= L_1 + L_2 \\ S &= S_\theta + m_\delta [b(a+c) + y_I] \end{aligned}$$

Thus the parameters involved in the heave equation contain properties pertaining to the entire section including the aileron. Now use the moment balance equation

$$I_\theta \ddot{\theta} + S_\theta \ddot{h} + k_\theta \theta - k_\delta \delta - Rb(a+c) = M_1$$

Replace $k_\delta \delta$ from equation 8.3 and R from equation 8.4 to obtain

$$I\ddot{\theta} + S\ddot{h} + [I_\delta + S_\delta b(a+c)] \ddot{\delta} = M_{ea} \quad (8.6)$$

where

$$\begin{aligned} I &= I_\theta + b^2(a+c)^2 m_\delta + 2S_\delta b(a+c) + I_\delta \\ &= I_\theta + \int_{ail} [b(a+c) + s]^2 dm_\delta \\ S &= S_\theta + S_\delta + b(a+c)m_\delta \\ M_{ea} &= M_1 + M_2 - L_2 b(a+c) \end{aligned}$$

Note that

$$\begin{aligned}
S_\theta &= \text{wing moment about wing e.a.} \\
S_\delta &= \text{aileron moment about aileron e.a.} \\
S_\delta + m_\delta b(a+c) &= \text{aileron moment about wing e.a.} \\
S &= \text{section moment about wing e.a.} \\
I_\theta &= \text{inertia of wing about wing e.a.} \\
I_\delta &= \text{inertia of aileron about aileron e.a.} \\
I_\delta + b^2(a+c)^2 m_\delta + 2S_\delta b(a+c) &= \text{inertia of aileron about wing e.a.} \\
I &= \text{inertia of section about wing e.a.}
\end{aligned} \tag{8.7}$$

All the above quantities are defined per unit span. The units for m , S , and I are kg/m , $kg-m/m$, and $kg-m^2/m$. Alternatively they can be treated as kg , $kg-m$, and $kg-m^2$ while keeping in mind they pertain to unit span of the wing.

8.1.3 Flap-torsion-Aileron dynamics: Energy method

The same equations as above are now rederived using the energy method (Euler–Lagrange). This derivation is given in Lanczos [2]. Let T be the kinetic energy of the system, U be the potential energy of the system and δW the virtual work. Then the Euler–Lagrange equations of motion are given by

$$\frac{d}{dt} \left(\frac{\partial T}{\partial \dot{q}} \right) - \frac{\partial T}{\partial q} + \frac{\partial U}{\partial q} = Q \tag{8.8}$$

where q are the degrees of freedom, here h , θ , and δ . Q is such that

$$\delta W = \int Q \delta q$$

$$\begin{aligned}
T &= T_w + T_a \\
T_w &= \int_w dT_w \\
&= \frac{1}{2} \int_w [\dot{h} + r\dot{\theta}]^2 dm \\
&= \frac{1}{2} m \dot{h}^2 + \frac{1}{2} I_\theta \dot{\theta}^2 + \dot{h} \dot{\theta} S_\theta \\
T_a &= \int_a dT_a \\
&= \frac{1}{2} \int_a [\dot{h} + \{b(a+c) + s\} \dot{\theta} + s\dot{\delta}]^2 dm_\delta \\
&= \frac{1}{2} m_\delta \dot{h}^2 + \frac{1}{2} [I_\delta + b^2(a+c)^2 m_\delta + 2b(a+c)S_\delta] \dot{\theta}^2 \\
&\quad I_\delta \dot{\delta}^2 + 2\dot{h} \dot{\theta} [b(a+c)m_\delta + S_\delta] + 2\dot{\delta} \dot{\theta} [b(a+c)S_\delta + I_\delta] + 2\dot{h} \dot{\delta} S_\delta
\end{aligned}$$

Therefore

$$T = \frac{1}{2} M \dot{h}^2 + \frac{1}{2} I \dot{\delta}^2 + \dot{h} \dot{\theta} S + \frac{1}{2} I_\delta \dot{\delta}^2 + \dot{h} \dot{\delta} S_\delta + \frac{1}{2} [b(a+c)S_\delta + I_\delta] \dot{\delta} \dot{\theta}$$

The potential energy is

$$U = \frac{1}{2} k_h h^2 + \frac{1}{2} k_\theta \theta^2 + \frac{1}{2} k_\delta \delta^2$$

The virtual work is

$$\begin{aligned}\delta W &= -L_1\delta h - L_2b(a+c)\delta\theta - L_2\delta h + M_1\delta\theta + M_2(\delta\theta + \delta\delta) \\ &= -(L_1 + L_2)\delta h + \{M_1 + M_2 - L_2b(a+c)\}\delta\theta + M_2\delta\delta \\ &= L\delta h + M_{ea}\delta\theta + M_2\delta\delta\end{aligned}$$

Now apply the Lagrange equations for h , θ , and δ separately to obtain the same equations as before

$$M\ddot{h} + S\ddot{\theta} + S_\delta\ddot{\delta} + k_h h = -L \quad (8.9)$$

$$I\ddot{\theta} + S\ddot{h} + [I_\delta + S_\delta b(a+c)]\ddot{\delta} = M_{ea} \quad (8.10)$$

$$I_\delta\ddot{\delta} + [I_\delta + S_\delta b(a+c)]\ddot{\theta} + S_\delta\ddot{h} + k_\delta\delta = M_2 \quad (8.11)$$

8.2 Flap-Torsion-Aileron-Tab Dynamics of a Rotor Blade

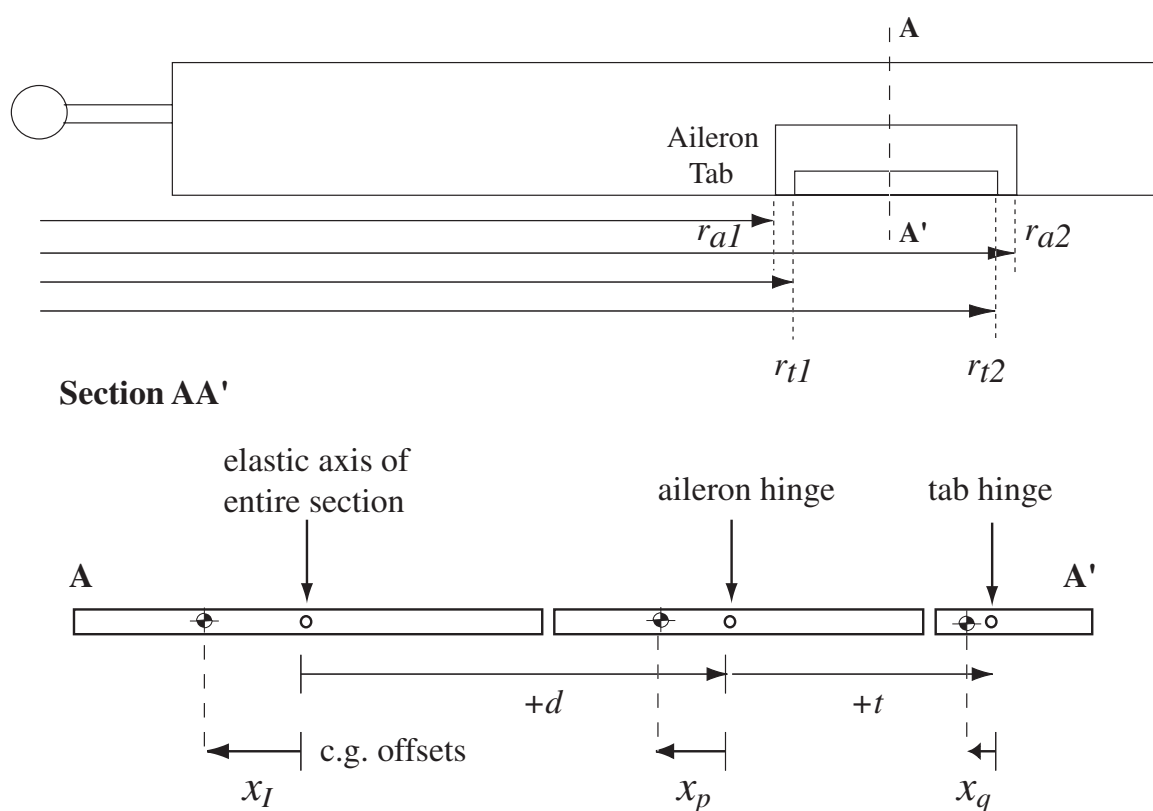


Figure 8.1: Airfoil with aileron and tab; geometry, pitch axes offsets and center of gravity offsets

8.2.1 Governing equations

Hamilton's variational principle is the general principle from which the Euler-Lagrange differential equation, and the Newton's Laws of motion can be deduced. For a conservative system, Hamilton's principle states that the true motion of a system, between prescribed initial conditions at time t_1 and final conditions at time t_2 , is that particular motion for which the time integral of the difference between the potential and kinetic energies is a minimum. For an aeroelastic system, there are non-conservative forces which are not derivable from a potential function. The generalized Hamilton's

principle, applicable to nonconservative systems, is expressed as

$$\begin{aligned}\delta\pi &= \delta \int_{t_1}^{t_2} (U - T - W)dt = 0 \quad \text{or} \\ \delta\pi &= \int_{t_1}^{t_2} (\delta U - \delta T - \delta W)dt = 0\end{aligned}\tag{8.12}$$

In order to prevent confusion between the aileron deflection δ and the variational δ , let the aileron and tab deflections be p , and q radians. The flap and torsion deflections are β and θ as before. Let the aileron span be from r_{a1} to r_{a2} . Let the tab span be from r_{t1} to r_{t2} .

A general blade section extends from the leading edge LE_b to the trailing edge TE_b . On the composite section spanning across the aileron it extends from the LE_b to a shorter trailing edge upto the aileron TE_{ba} . Similarly the aileron extends from LE_a to TE_a , except over the tab span, where it extends from LE_a to TE_{at} . TE_{at} denotes trailing edge of the aileron over the tab span. The tab extends from LE_t to the TE_t . Note that in general, TE_t or TE_a need not be the same as TE_b .

Let us define the following structural properties. η is a general local coordinate along the blade section, aileron, or tab.

Blade properties:

$$\begin{aligned}\rho &= \text{area density } kg/m^2 \\ \int_{LE_b}^{TE_b} \rho d\eta &= m_b \quad \text{mass per unit span } kg/m \\ \int_{LE_b}^{TE_b} \eta \rho d\eta &= x_I m_b = s_\theta \quad \text{first moment of mass per unit span } kg - m/m \\ \int_{LE_b}^{TE_b} \eta^2 \rho d\eta &= i_\theta \quad \text{second moment of mass per unit span } kg - m^2/m\end{aligned}\tag{8.13}$$

For each we have the following radial moments

$$\begin{aligned}\int_e^R m_b dr &= M_b \quad \text{zero-th radial moment} = \text{blade mass } kg \\ \int_e^R (r - e) m_b dr &= S_\beta \quad \text{first radial moment} = \text{first flap moment } kg - m \\ \int_e^R (r - e)^2 m_b dr &= I_\beta \quad \text{second radial moment} = \text{flap moment of inertia } kg - m^2\end{aligned}\tag{8.14}$$

Then

$$\begin{aligned}\int_e^R s_\theta dr &= \int_e^R x_I m_b dr = S_\theta \quad \text{zero-th radial moment } kg - m \\ \int_e^R (r - e) s_\theta dr &= \int_e^R (r - e) x_I m_b dr = \bar{S}_\theta \quad \text{first radial moment } kg - m^2 \\ \int_e^R (r - e)^2 s_\theta dr &= \int_e^R (r - e)^2 x_I m_b dr = \bar{\bar{S}}_\theta \quad \text{second radial moment } kg - m^2\end{aligned}\tag{8.15}$$

And finally

$$\begin{aligned}
 \int_e^R i_\theta dr &= I_\theta \quad \text{zero-th radial moment} \quad kg - m \\
 \int_e^R (r - e)i_\theta dr &= \bar{I}_\theta \quad \text{first radial moment} \quad kg - m^2 \\
 \int_e^R (r - e)^2 i_\theta dr &= \bar{\bar{I}}_\theta \quad \text{second radial moment} \quad kg - m^2
 \end{aligned} \tag{8.16}$$

Aileron properties:

$$\begin{aligned}
 \int_{LE_a}^{TE_a} \rho d\eta &= m_a \quad \text{mass per unit span} \quad kg/m \\
 \int_{LE_a}^{TE_a} \eta \rho d\eta &= x_p m_a = s_a \quad \text{first moment of mass per unit span} \quad kg - m/m \\
 \int_{LE_a}^{TE_a} \eta^2 \rho d\eta &= i_a \quad \text{second moment of mass per unit span} \quad kg - m^2/m
 \end{aligned} \tag{8.17}$$

For each we have the following radial moments

$$\begin{aligned}
 \int_{r_{a1}}^{r_{a2}} m_a dr &= M_a \quad \text{zero-th radial moment} = \text{aileron mass} \quad kg \\
 \int_{r_{a1}}^{r_{a2}} (r - e)m_a dr &= S_{\beta a} \quad \text{first radial moment} \quad kg - m \\
 \int_{r_{a1}}^{r_{a2}} (r - e)^2 m_a dr &= I_{\beta a} \quad \text{second radial moment} \quad kg - m^2
 \end{aligned} \tag{8.18}$$

Then

$$\begin{aligned}
 \int_{r_{a1}}^{r_{a2}} s_a dr &= \int_{r_{a1}}^{r_{a2}} x_p m_a dr = S_a \quad \text{zero-th radial moment} \quad kg - m \\
 \int_{r_{a1}}^{r_{a2}} (r - e)s_a dr &= \int_{r_{a1}}^{r_{a2}} (r - e)x_p m_a dr = \bar{S}_a \quad \text{first radial moment} \quad kg - m^2 \\
 \int_{r_{a1}}^{r_{a2}} (r - e)^2 s_a dr &= \int_{r_{a1}}^{r_{a2}} (r - e)^2 x_p m_a dr = \bar{\bar{S}}_a \quad \text{second radial moment} \quad kg - m^2
 \end{aligned} \tag{8.19}$$

And finally

$$\begin{aligned}
 \int_{r_{a1}}^{r_{a2}} i_a dr &= I_a \quad \text{zero-th radial moment} \quad kg - m \\
 \int_{r_{a1}}^{r_{a2}} (r - e)i_a dr &= \bar{I}_a \quad \text{first radial moment} \quad kg - m^2 \\
 \int_{r_{a1}}^{r_{a2}} (r - e)^2 i_a dr &= \bar{\bar{I}}_a \quad \text{second radial moment} \quad kg - m^2
 \end{aligned} \tag{8.20}$$

Tab properties:

$$\begin{aligned}
\int_{LE_t}^{TE_t} \rho d\eta &= m_t \quad \text{mass per unit span} \quad kg/m \\
\int_{LE_t}^{TE_t} \eta \rho d\eta &= x_q m_t = s_t \quad \text{first moment of mass per unit span} \quad kg - m/m \\
\int_{LE_t}^{TE_t} \eta^2 \rho d\eta &= i_t \quad \text{second moment of mass per unit span} \quad kg - m^2/m
\end{aligned} \tag{8.21}$$

For each we have the following radial moments

$$\begin{aligned}
\int_{r_{t1}}^{r_{t2}} m_t dr &= M_t \quad \text{zero-th radial moment} = \text{tab mass} \quad kg \\
\int_{r_{t1}}^{r_{t2}} (r - e) m_t dr &= S_{\beta t} \quad \text{first radial moment} \quad kg - m \\
\int_{r_{t1}}^{r_{t2}} (r - e)^2 m_t dr &= I_{\beta t} \quad \text{second radial moment} \quad kg - m^2
\end{aligned} \tag{8.22}$$

Then

$$\begin{aligned}
\int_{r_{t1}}^{r_{t2}} s_t dr &= \int_{r_{t1}}^{r_{t2}} x_q m_t dr = S_t \quad \text{zero-th radial moment} \quad kg - m \\
\int_{r_{t1}}^{r_{t2}} (r - e) s_t dr &= \int_{r_{t1}}^{r_{t1}} r x_q m_t dr = \bar{S}_t \quad \text{first radial moment} \quad kg - m^2 \\
\int_{r_{t1}}^{r_{t2}} (r - e)^2 s_a dr &= \int_{r_{t1}}^{r_{t2}} r^2 x_q m_t dr = \bar{\bar{S}}_t \quad \text{second radial moment} \quad kg - m^2
\end{aligned} \tag{8.23}$$

And finally

$$\begin{aligned}
\int_{r_{t1}}^{r_{t2}} i_t dr &= I_t \quad \text{zero-th radial moment} \quad kg - m \\
\int_{r_{t1}}^{r_{t2}} (r - e) i_t dr &= \bar{I}_t \quad \text{first radial moment} \quad kg - m^2 \\
\int_{r_{t1}}^{r_{t2}} (r - e)^2 i_t dr &= \bar{\bar{I}}_t \quad \text{second radial moment} \quad kg - m^2
\end{aligned} \tag{8.24}$$

The total potential energy and its variation is given by

$$\begin{aligned}
U &= \frac{1}{2} (k_\beta \beta^2 + k_\theta \theta^2 + k_p p^2 + k_q q^2) \\
\delta U &= k_\beta \delta \beta + k_\theta \delta \theta + k_p \delta p + k_q \delta q
\end{aligned} \tag{8.25}$$

The virtual work is given by

$$\delta W = M_\beta \delta \beta + M_\theta \delta \theta + M_p \delta p + M_q \delta q \tag{8.26}$$

where M_β is the aerodynamic flap hinge moment, M_θ is the aerodynamic twist moment about the blade rotation axis, M_p is the aerodynamic twist moment about the aileron rotation axis (aileron hinge), and M_q is the aerodynamic twist moment about the tab rotation axis (tab hinge).

The total kinetic energy and its variation is contributed by the blade, aileron, and the flap. Let the velocity of a point on the blade be v_b , that of a point on the aileron be v_a , and that of a point on the tab be v_t . The total kinetic energy and its variation can be expressed as

$$\begin{aligned}
T &= \frac{1}{2} \int_b \rho_b v_b^2 + \frac{1}{2} \int_a \rho_a v_a^2 + \frac{1}{2} \int_t \rho_t v_t^2 \\
\delta T &= \int_b \rho_b \bar{\mathbf{v}}_b \cdot \delta \bar{\mathbf{v}}_b + \int_a \rho_a \bar{\mathbf{v}}_a \cdot \delta \bar{\mathbf{v}}_a + \int_t \rho_t \bar{\mathbf{v}}_t \cdot \delta \bar{\mathbf{v}}_t
\end{aligned} \tag{8.27}$$

To obtain these velocities and variations, consider the following coordinate transformations:

$$\begin{Bmatrix} \hat{i}_2 \\ \hat{j}_2 \\ \hat{k}_2 \end{Bmatrix} = \begin{bmatrix} c\beta & 0 & s\beta \\ 0 & 1 & 0 \\ -s\beta & 0 & c\beta \end{bmatrix} \begin{Bmatrix} \hat{i}_1 \\ \hat{j}_1 \\ \hat{k}_1 \end{Bmatrix} \quad \text{undeformed to flap} \quad (8.28)$$

$$\begin{Bmatrix} \hat{i}_3 \\ \hat{j}_3 \\ \hat{k}_3 \end{Bmatrix} = \begin{bmatrix} 1 & 0 & 0 \\ 0 & c\theta & s\theta \\ 0 & -s\theta & c\theta \end{bmatrix} \begin{Bmatrix} \hat{i}_2 \\ \hat{j}_2 \\ \hat{k}_2 \end{Bmatrix} \quad \text{flap to torsion} \quad (8.29)$$

$$\begin{Bmatrix} \hat{i}_4 \\ \hat{j}_4 \\ \hat{k}_4 \end{Bmatrix} = \begin{bmatrix} 1 & 0 & 0 \\ 0 & c(\theta+p) & s(\theta+p) \\ 0 & -s(\theta+p) & c(\theta+p) \end{bmatrix} \begin{Bmatrix} \hat{i}_2 \\ \hat{j}_2 \\ \hat{k}_2 \end{Bmatrix} \quad \text{flap to aileron} \quad (8.30)$$

$$\begin{Bmatrix} \hat{i}_5 \\ \hat{j}_5 \\ \hat{k}_5 \end{Bmatrix} = \begin{bmatrix} 1 & 0 & 0 \\ 0 & c(\theta+p+q) & s(\theta+p+q) \\ 0 & -s(\theta+p+q) & c(\theta+p+q) \end{bmatrix} \begin{Bmatrix} \hat{i}_2 \\ \hat{j}_2 \\ \hat{k}_2 \end{Bmatrix} \quad \text{flap to tab} \quad (8.31)$$

The position of a generic point on the deformed blade can be expressed as

$$\mathbf{r} = x_1 \hat{i}_1 + y_1 \hat{j}_1 + z_1 \hat{k}_1 \quad (8.32)$$

The angular velocity vector is given by

$$\boldsymbol{\Omega} = \Omega \hat{k}_1 \quad (8.33)$$

Thus the velocity of a generic point on the deformed blade, can be expressed as

$$\begin{aligned} \mathbf{v} &= \frac{\partial \mathbf{r}}{\partial t} + \bar{\boldsymbol{\Omega}} \times \mathbf{r} \\ &= \dot{\mathbf{r}} + \boldsymbol{\Omega} \times \mathbf{r} \\ &= (\dot{x}_1 - \Omega x_1) \hat{i}_1 + (\dot{y}_1 + \Omega y_1) \hat{j}_1 + \dot{z}_1 \hat{k}_1 \end{aligned} \quad (8.34)$$

The variation is given by

$$\bar{\mathbf{v}} = (\delta \dot{x}_1 - \Omega \delta x_1) \hat{i}_1 + (\delta \dot{y}_1 + \Omega \delta y_1) \hat{j}_1 + \delta \dot{z}_1 \hat{k}_1 \quad (8.35)$$

From where it follows

$$\bar{\mathbf{v}} \cdot \delta \bar{\mathbf{v}} = (\dot{x}_1 - \Omega x_1)(\delta \dot{x}_1 - \Omega \delta x_1) + (\dot{y}_1 + \Omega y_1)(\delta \dot{y}_1 + \Omega \delta y_1) + \dot{z}_1 \delta \dot{z}_1 \quad (8.36)$$

Anticipating integration over time as in equation 8.12 we note that

$$\begin{aligned} \int_{t_1}^{t_2} \dot{x} \delta x &= \dot{x} \delta x \Big|_{t_1}^{t_2} - \int_{t_1}^{t_2} \ddot{x} \delta x \\ &= 0 + \int_{t_1}^{t_2} \ddot{x} \delta x \end{aligned}$$

Using the above, $\dot{x}_1 \delta x_1$ can be replaced with $-\ddot{x}_1 \delta x_1$, $x_1 \delta \dot{x}_1$ can be replaced with $-\dot{x}_1 \delta x_1$, etc. Thus, because

$$\begin{aligned} \int_{t_1}^{t_2} \bar{\mathbf{v}} \cdot \delta \bar{\mathbf{v}} &= \int_{t_1}^{t_2} (\dot{x}_1 - \Omega x_1)(\delta \dot{x}_1 - \Omega \delta x_1) + (\dot{y}_1 + \Omega y_1)(\delta \dot{y}_1 + \Omega \delta y_1) + \dot{z}_1 \delta \dot{z}_1 \\ &= \int_{t_1}^{t_2} (-\ddot{x}_1 + \Omega^2 x_1) \delta x_1 + (-\dot{y}_1 + \Omega^2 y_1) \delta y_1 - \dot{z}_1 \delta z_1 \end{aligned}$$

the variational expression 8.36 can be re-written as

$$\bar{\mathbf{v}} \cdot \delta \bar{\mathbf{v}} = (-\ddot{x}_1 + \Omega^2 x_1) \delta x_1 + (-\ddot{y}_1 + \Omega^2 y_1) \delta y_1 - \ddot{z}_1 \delta z_1 \quad (8.37)$$

Now we have all the tools to derive the governing equations. First, consider a generic point on the blade

$$\mathbf{r} = e \hat{i}_1 + (r - e) \hat{i}_2 + \eta \hat{j}_3$$

where η is the local chordwise coordinate. Using the transformations 8.31 and 8.28 above we have

$$\mathbf{r} = x_1 \hat{i}_1 + y_1 \hat{j}_1 + z_1 \hat{k}_1$$

where

$$\begin{aligned} x_1 &= e + (r - e) c \beta - \eta s \theta s \beta \\ y_1 &= \eta c \theta \\ z_1 &= (r - e) s \beta + \eta s \theta c \beta \end{aligned}$$

Then

$$\begin{aligned} \dot{x}_1 &= -(r - e) s \beta \dot{\beta} - \eta s \theta c \beta \dot{\beta} - \eta c \theta s \beta \dot{\theta} \\ \dot{y}_1 &= -\eta s \theta \dot{\theta} \\ \dot{z}_1 &= (r - e) c \beta \dot{\beta} - \eta s \theta s \beta \dot{\beta} + \eta c \theta c \beta \dot{\theta} \end{aligned} \quad (8.38)$$

$$\begin{aligned} \delta x_1 &= -(r - e) s \beta \delta \beta - \eta s \theta c \beta \delta \beta - \eta c \theta s \beta \delta \theta \\ \delta y_1 &= -\eta s \theta \delta \theta \\ \delta z_1 &= (r - e) c \beta \delta \beta - \eta s \theta s \beta \delta \beta + \eta c \theta c \beta \delta \theta \end{aligned}$$

Use small angle assumption and neglect non-linear terms to obtain

$$\begin{aligned} x_1 &= r \\ y_1 &= \eta \\ z_1 &= (r - e) \beta + \eta \theta \end{aligned} \quad (8.39)$$

$$\begin{aligned} \delta x_1 &= -(r - e) \beta \delta \beta - \eta \theta \delta \beta - \eta \beta \delta \theta \\ \delta y_1 &= -\eta \theta \delta \theta \\ \delta z_1 &= (r - e) \delta \beta - \eta \delta \theta \end{aligned} \quad (8.40)$$

$$\begin{aligned} \dot{x}_1 &= 0 \\ \dot{y}_1 &= 0 \\ \dot{z}_1 &= (r - e) \dot{\beta} + \eta \dot{\theta} \end{aligned} \quad (8.41)$$

Differentiating equations 8.38, making small angle assumption, and neglecting non-linear terms yield

$$\begin{aligned} \ddot{x}_1 &= 0 \\ \ddot{y}_1 &= 0 \\ \ddot{z}_1 &= (r - e) \ddot{\beta} + \eta \ddot{\theta} \end{aligned} \quad (8.42)$$

The variation in kinetic energy then becomes

$$\delta T_b = \int_{span} \int_{chord} [\mathbf{v} \cdot \delta \mathbf{v}]_b \rho d\eta dr \quad (8.43)$$

where the limit of integration for the blade, without the aileron, is

$$\int_{span} \int_{chord} = \int_e^{r_{a1}} \int_{TE_b}^{LE_b} + \int_{r_{a1}}^{r_{a2}} \int_{TE_b}^{LE_b} + \int_{r_{a2}}^R \int_{TE_b}^{LE_b} \quad (8.44)$$

$\mathbf{v} \cdot \delta \mathbf{v}$ is given by equation 8.37. Using equations 8.39 to 8.42 we have

$$\begin{aligned} (\mathbf{v} \cdot \delta \mathbf{v})_b &= \Omega^2 r [- (r - e) \beta \delta \beta - \eta \theta \delta \beta - \eta \beta \delta \theta] \\ &\quad + \Omega^2 \eta (-\eta \theta \delta \theta) \\ &\quad - \left[(r - e) \ddot{\beta} + \eta \ddot{\theta} \right] [(r - e) \delta \beta + \eta \delta \theta] \end{aligned} \quad (8.45)$$

Group the variational terms

$$\begin{aligned} (\mathbf{v} \cdot \delta \mathbf{v})_b &= \left[-\Omega^2 r (r - e) \beta - \Omega^2 r \eta \theta - (r - e)^2 \ddot{\beta} - \eta (r - e) \ddot{\theta} \right] \delta \beta \\ &\quad + \left[-\Omega^2 \eta r \beta - \Omega^2 \eta^2 \theta - \eta (r - e) \ddot{\beta} - \eta^2 \ddot{\theta} \right] \delta \theta \end{aligned} \quad (8.46)$$

Replace r with $(r - e) + e$ to have

$$\begin{aligned} (\mathbf{v} \cdot \delta \mathbf{v})_b &= \left[-\Omega^2 (r - e)^2 \beta - \Omega^2 e (r - e) \beta - \Omega^2 (r - e) \eta \theta - \Omega^2 e \eta \theta - (r - e)^2 \ddot{\beta} - \eta (r - e) \ddot{\theta} \right] \delta \beta \\ &\quad + \left[-\Omega^2 \eta (r - e) \beta - \Omega^2 \eta e \beta - \Omega^2 \eta^2 \theta - \eta (r - e) \ddot{\beta} - \eta^2 \ddot{\theta} \right] \delta \theta \end{aligned} \quad (8.47)$$

Equation 8.47 would help express the variation of kinetic energy of a point on the blade in terms of variations of flap and torsion degrees of freedom. Let us now proceed to obtain a similar expression for a point on the aileron in terms of variations of flap, torsion, and aileron degrees of freedom. The procedure is same as above, and the notations used will be same.

For a generic point on the aileron we have

$$\mathbf{r} = e \hat{i}_1 + (r - e) \hat{i}_2 - d \hat{j}_3 + \eta \hat{j}_4$$

where d is the distance of the aileron hinge lying behind the elastic axis or the center of rotation of the blade section. d is positive behind the blade. η is the local chordwise coordinate of the aileron along direction \hat{j}_4 . Thus η is zero at the aileron hinge, and positive forward to it. Using the coordinate transformations given above, small angle assumption on the degrees of freedom, and neglecting the non-linear terms we have

$$\begin{aligned} x_1 &= r \\ y_1 &= -d + \eta \\ z_1 &= (r - e) \beta + (\eta - d) \theta + \eta p \end{aligned} \quad (8.48)$$

$$\begin{aligned} \delta x_1 &= -(r - e) \beta \delta \beta - \eta \theta \delta \beta - \eta \beta \delta \theta \\ \delta y_1 &= -\eta \theta \delta \theta \\ \delta z_1 &= (r - e) \delta \beta - \eta \delta \theta \end{aligned} \quad (8.49)$$

$$\begin{aligned} \dot{x}_1 &= 0 \\ \dot{y}_1 &= 0 \\ \dot{z}_1 &= (r - e) \dot{\beta} - d \dot{\theta} + \eta \dot{\theta} + \eta \dot{p} \end{aligned} \quad (8.50)$$

$$\begin{aligned} \ddot{x}_1 &= 0 \\ \ddot{y}_1 &= 0 \\ \ddot{z}_1 &= (r - e) \ddot{\beta} - d \ddot{\theta} + \eta \ddot{\theta} + \eta \ddot{p} \end{aligned} \quad (8.51)$$

The variation in kinetic energy is

$$\delta T_a = \int_{span} \int_{chord} [\mathbf{v} \cdot \delta \mathbf{v}]_a \rho d\eta dr \quad (8.52)$$

where the limit of integration is given by

$$\int_{r_{a1}}^{r_{t1}} \int_{TE_a}^{LE_a} + \int_{r_{t1}}^{r_{t2}} \int_{TE_{at}}^{LE_a} + \int_{r_{t2}}^{r_{a2}} \int_{TE_a}^{LE_a} \quad (8.53)$$

and

$$\begin{aligned} (\mathbf{v} \cdot \delta \mathbf{v})_a = & \left[-\Omega^2 r(r-e)\beta + \Omega^2 r d\theta - \Omega^2 r\theta\eta - \Omega^2 r\eta p - (r-e)^2 \ddot{\beta} \right. \\ & \left. + d(r-e)\ddot{\theta} - \eta(r-e)\ddot{\theta} - \eta(r-e)\ddot{p} \right] \delta\beta \\ & \left[\Omega^2 r d\beta - \Omega^2 r\eta\beta + \Omega^2(\eta-d)d\theta - \Omega^2(\eta-d)\eta\theta - \Omega^2(\eta-d)\eta p \right. \\ & \left. - (\eta-d)(r-e)\ddot{\beta} + (\eta-d)d\ddot{\theta} - (\eta-d)\eta\ddot{\theta} - (\eta-d)\eta\ddot{p} \right] \delta\theta \\ & \left[-\Omega^2 r\eta\beta - \Omega^2(\eta-d)\eta p - \Omega^2(\eta-d)\eta\theta \right. \\ & \left. - \eta(r-e)\ddot{\beta} + \eta d\ddot{\theta} - \eta^2\ddot{\theta} - \eta^2\ddot{p} \right] \delta p \end{aligned} \quad (8.54)$$

Equation 8.54 would help express the variation of kinetic energy of a point on the aileron in terms of variations of flap, torsion, and aileron degrees of freedom. Let us now proceed to obtain a similar expression for a point on the tab in terms of variations of flap, torsion, aileron, and tab degrees of freedom. The procedure is same as above, and the notations used will be same.

For a generic point on the tab we have

$$\mathbf{r} = e\hat{i}_1 + (r-e)\hat{i}_2 - d\hat{j}_3 - t\hat{j}_4 + \eta\hat{j}_4$$

where t is the distance of the tab hinge lying behind the aileron hinge. t is positive behind the aileron. η is the local chordwise coordinate of the tab along direction \hat{j}_5 . Thus η is zero at the tab hinge, and positive forward to it. Using the coordinate transformations given above, small angle assumption on the degrees of freedom, and neglecting the non-linear terms we have

$$\begin{aligned} x_1 &= r \\ y_1 &= -t - d + \eta \\ z_1 &= (r-e)\beta + (\eta-d-t)\theta + (\eta-t)p + \eta q \end{aligned} \quad (8.55)$$

$$\begin{aligned} \delta x_1 &= [-(r-e)\beta + (d+t-\eta)\theta + (t-\eta)p - \eta q] \delta\beta \\ & \quad [(d+t-\eta)\beta] \delta\theta + [(t-\eta)\beta] \delta p \\ \delta y_1 &= [(d+t-\eta)\theta + (t-\eta)p - \eta q] \delta\theta \\ & \quad [(t-\eta)\theta + (t-\eta)p - \eta q] \delta p + [-\eta(\theta+p)] \delta q \\ \delta z_1 &= (r-e)\delta\beta - (d+t-\eta)\delta\theta - (t-\eta)\delta p + \eta\delta q \end{aligned} \quad (8.56)$$

$$\begin{aligned} \dot{x}_1 &= 0 \\ \dot{y}_1 &= 0 \\ \dot{z}_1 &= (r-e)\dot{\beta} + (\eta-d-t)\dot{\theta} + (\eta-t)\dot{p} + \eta\dot{q} \end{aligned} \quad (8.57)$$

$$\begin{aligned} \ddot{x}_1 &= 0 \\ \ddot{y}_1 &= 0 \\ \ddot{z}_1 &= (r-e)\ddot{\beta} - d\ddot{\theta} + \eta\ddot{\theta} + \eta\ddot{p} \end{aligned} \quad (8.58)$$

The variation in kinetic energy is

$$\delta T_a = \int_{span} \int_{chord} [\mathbf{v} \cdot \delta \mathbf{v}]_t \rho d\eta dr \quad (8.59)$$

where the limit of integration is given by

$$\int_{span} \int_{chord} = \int_{r_{t1}}^{r_{t2}} \int_{TE_t}^{LE_t} \quad (8.60)$$

and

$$\begin{aligned} (\mathbf{v} \cdot \delta \mathbf{v})_t = & \left[-\Omega^2 r(r-e)\beta - \Omega^2 r(\eta-d-t)\theta - \Omega^2 r(\eta-t)p - \Omega^2 r\eta q \right. \\ & \left. - (r-e)^2 \ddot{\beta} - (r-e)(\eta-d-t)\ddot{\theta} - (r-e)(\eta-t)\ddot{p} - \eta(r-e)\ddot{q} \right] \delta\beta \\ & \left[-\Omega^2 r(\eta-d-t)\beta - \Omega^2(\eta-d-t)^2\theta - \Omega^2(\eta-d-t)(\eta-t)p - \Omega^2\eta(\eta-d-t) \right. \\ & \left. - (r-e)(\eta-d-t)\ddot{\beta} - (\eta-d-t)^2\ddot{\theta} - (\eta-d-t)(\eta-t)\ddot{p} - \eta(\eta-d-t)\ddot{q} \right] \delta\theta \\ & \left[-\Omega^2 r(\eta-t)\beta - \Omega^2(\eta-t-d)(\eta-t)\theta \right. \\ & \left. - \Omega^2(\eta-t-d)(\eta-t)p - \Omega^2\eta(\eta-d-t)q \right. \\ & \left. - (r-e)(\eta-t)\ddot{\beta} - (\eta-t)(\eta-d-t)\ddot{\theta} - (\eta-t)^2\ddot{p} - \eta(\eta-t)\ddot{q} \right] \delta p \\ & \left[-\Omega^2 r\eta\beta - \Omega^2\eta(\eta-d-t)(\theta+p+q) \right. \\ & \left. - (r-e)\eta\ddot{\beta} - (\eta-d-t)\eta\ddot{\theta} - \eta(\eta-t)\ddot{p} - \eta^2\ddot{q} \right] \delta q \end{aligned} \quad (8.61)$$

Using equations 8.25, 8.26, and the integrated forms of equations 8.47, 8.54, and 8.61, equation 8.12 can be brought to the following form

$$\pi = \int_{t_1}^{t_2} [(\dots)\delta\beta + (\dots)\delta\theta + (\dots)\delta p + (\dots)\delta q] = 0$$

Putting the terms (...) = 0 generates the four governing equations for flap, torsion, aileron deflection, and tab deflection.

Tab equation:

The tab equation is found by collecting the terms associated with δq and setting them to zero. The kinetic energy terms are obtained from 8.59, 8.60, and eq: 8.61 as follows

$$-\Omega^2 \bar{S}_t \beta - \Omega^2 S_{te} \beta - \Omega^2 I_t (\theta + p + q) + \Omega^2 (d+t) S_t (\theta + p + q) - \bar{S}_t \ddot{\beta} - I_t \ddot{\theta} + (d+t) S_t \ddot{\theta} - I_t \ddot{p} + t S_t \ddot{p} - I_t \ddot{q}$$

Together with $-k_t$ and $-M_q$ from the potential energy and virtual work terms from equations 8.25 and 8.26 we have the equation for tab dynamics as follows

$$\begin{aligned} & \bar{S}_t \ddot{\beta} + \Omega^2 \bar{S}_t \left(1 + \frac{e S_t}{\bar{S}_t} \right) \beta \\ & + [I_t - (d+t) S_t] \ddot{\theta} + \Omega^2 I_t \left[1 - \frac{(d+t) S_t}{I_t} \right] \theta \\ & + (I_t - t S_t) \ddot{p} + \Omega^2 I_t \left[1 - \frac{(d+t) S_t}{I_t} \right] p \\ & + I_t \ddot{q} + \Omega^2 I_t \left[1 - \frac{(d+t) S_t}{I_t} + \frac{k_t}{I_t \Omega^2} \right] q = M_q \end{aligned} \quad (8.62)$$

Aileron equation:

Care must be taken while gathering the terms (...) corresponding to δp . The terms occurring in the potential energy variation, and virtual work are trivial. Consider the kinetic energy terms. Terms associated with δp occur only in equations 8.54 and 8.61. Let us write down the variation in kinetic energy

$$\begin{aligned}
& \int_{r_{a1}}^{r_{t1}} \int_{TE_a}^{LE_a} [-\Omega^2 r \eta \beta - \Omega^2 (\eta - d) \eta p - \Omega^2 (\eta - d) \eta \theta \\
& \quad - \eta (r - e) \ddot{\beta} + \eta d \ddot{\theta} - \eta^2 \ddot{\theta} - \eta^2 \ddot{p}] \\
& \int_{r_{t1}}^{r_{t2}} \int_{TE_{at}}^{LE_a} [-\Omega^2 r \eta \beta - \Omega^2 (\eta - d) \eta p - \Omega^2 (\eta - d) \eta \theta \\
& \quad - \eta (r - e) \ddot{\beta} + \eta d \ddot{\theta} - \eta^2 \ddot{\theta} - \eta^2 \ddot{p}] \\
& \int_{r_{t2}}^{r_{a2}} \int_{TE_a}^{LE_a} [-\Omega^2 r \eta \beta - \Omega^2 (\eta - d) \eta p - \Omega^2 (\eta - d) \eta \theta \\
& \quad - \eta (r - e) \ddot{\beta} + \eta d \ddot{\theta} - \eta^2 \ddot{\theta} - \eta^2 \ddot{p}] \\
& + \\
& \int_{r_{t1}}^{r_{t2}} \int_{TE_t}^{LE_t} [-\Omega^2 r (\eta - t) \beta - \Omega^2 (\eta - t - d) (\eta - t) \theta \\
& \quad - \Omega^2 (\eta - t - d) (\eta - t) p - \Omega^2 \eta (\eta - d - t) q \\
& \quad - (r - e) (\eta - t) \ddot{\beta} - (\eta - t) (\eta - d - t) \ddot{\theta} - (\eta - t)^2 \ddot{p} - \eta (\eta - t) \ddot{q}]
\end{aligned}$$

The first three integrals are contributions from aileron motion $[\mathbf{v} \cdot \delta \mathbf{v}]_a$. The fourth is a contribution from tab motion $[\mathbf{v} \cdot \delta \mathbf{v}]_t$. In the first three integrals, η , the local coordinate of integration, is the distance from aileron hinge (positive forward), say η_a . In the fourth, η , the local coordinate of integration, is the distance from the tab hinge (positive forward), say η_t . Thus, $\eta_t - t = \eta_a$. Note the second integral. It extends chord-wise over that part of the aileron which excludes the tab. Note the last integral, it extends chord-wise only over the tab. The underlined integrands of this integral are identical to those occurring in the second integral. Thus these terms can be considered together with the second integral, with the lower limit of integration for the second integral now changed from TE_{at} to TE_t . Thus the sectional properties here would now refer to the sectional properties as a whole, not excluding the tab properties. Thus, the kinetic energy terms can be re-organized as follows

$$\begin{aligned}
& \int_{r_{a1}}^{r_{t1}} \int_{TE_a}^{LE_a} [-\Omega^2 r \eta \beta - \Omega^2 (\eta - d) \eta p - \Omega^2 (\eta - d) \eta \theta \\
& \quad - \eta (r - e) \ddot{\beta} + \eta d \ddot{\theta} - \eta^2 \ddot{\theta} - \eta^2 \ddot{p}] \\
& \int_{r_{t1}}^{r_{t2}} \int_{TE_a}^{LE_a} [-\Omega^2 r \eta \beta - \Omega^2 (\eta - d) \eta p - \Omega^2 (\eta - d) \eta \theta \\
& \quad - \eta (r - e) \ddot{\beta} + \eta d \ddot{\theta} - \eta^2 \ddot{\theta} - \eta^2 \ddot{p}] \\
& \int_{r_{t2}}^{r_{a2}} \int_{TE_a}^{LE_a} [-\Omega^2 r \eta \beta - \Omega^2 (\eta - d) \eta p - \Omega^2 (\eta - d) \eta \theta \\
& \quad - \eta (r - e) \ddot{\beta} + \eta d \ddot{\theta} - \eta^2 \ddot{\theta} - \eta^2 \ddot{p}] \\
& + \\
& \int_{r_{t1}}^{r_{t2}} \int_{TE_t}^{LE_t} [-\Omega^2 \eta (\eta - d - t) q - \eta (\eta - t) \ddot{q}]
\end{aligned}$$

where the first three integrals have now the same limits of integration for the second integral. Thus the expression becomes

$$\begin{aligned} & \int_{r_{a1}}^{r_{a2}} \int_{TE_a}^{LE_a} [-\Omega^2 r \eta \beta - \Omega^2 (\eta - d) \eta p - \Omega^2 (\eta - d) \eta \theta \\ & - \eta (r - e) \ddot{\beta} + \eta d \ddot{\theta} - \eta^2 \ddot{\theta} - \eta^2 \ddot{p}] \\ & + \\ & \int_{r_{t1}}^{r_{t2}} \int_{TE_t}^{LE_t} [-\Omega^2 \eta (\eta - d - t) q - \eta (\eta - t) \ddot{q}] \end{aligned}$$

where, note that the limits of the first integral extends across the entire span of the aileron from r_{a1} to r_{a2} . The above expression equals

$$\begin{aligned} & -\Omega^2 \bar{S}_a \beta - \Omega^2 e S_a \beta + \Omega^2 d S_a p - \Omega^2 I_a p + \Omega^2 d S_a \theta - \Omega^2 I_a \theta - \\ & \bar{S}_a \ddot{\beta} + S_a d \ddot{\theta} - I_a \ddot{\theta} - I_a \ddot{p} \\ & - I_t \ddot{q} + t S_t \ddot{q} - \Omega^2 I_t q + \Omega^2 S_t (d + t) q \end{aligned}$$

Adding the potential energy and virtual work contributions, the equation for aileron dynamics becomes

$$\begin{aligned} & \bar{S}_a \ddot{\beta} + \Omega^2 \bar{S}_a \left(1 + \frac{e S_a}{\bar{S}_a} \right) \beta \\ & + [I_a - d S_a] \ddot{\theta} + \Omega^2 I_a \left[1 - \frac{d S_a}{I_a} \right] \theta \\ & + I_a \ddot{p} + \Omega^2 I_a \left[1 - \frac{d S_a}{I_a} + \frac{k_a}{I_a \Omega^2} \right] p \\ & + (I_t - t S_t) \ddot{q} + \Omega^2 I_t \left[1 - \frac{(d + t) S_t}{I_t} \right] q = M_p \end{aligned} \tag{8.63}$$

Proceeding similarly, we obtain the torsion and flapping equations as follows

Torsion equation:

$$\begin{aligned} & \bar{S}_\theta \ddot{\beta} + \Omega^2 \bar{S}_\theta \left(1 + \frac{e S_\theta}{\bar{S}_\theta} \right) \beta \\ & + I_\theta \ddot{\theta} + \Omega^2 I_\theta \left[1 + \frac{k_\theta}{I_\theta \Omega^2} \right] \theta \\ & + [I_a - d S_a] \ddot{p} + \Omega^2 I_a \left[1 - \frac{d S_a}{I_a} \right] p \\ & + (I_t - (d + t) S_t) \ddot{q} + \Omega^2 I_t \left[1 - \frac{(d + t) S_t}{I_t} \right] q = M_\theta \end{aligned} \tag{8.64}$$

Flap equation:

$$\begin{aligned}
& I_\beta \ddot{\beta} + \Omega^2 I_\beta \left[1 + \frac{eS_\beta}{I_\beta} + \frac{k_\beta}{I_\beta \Omega^2} \right] \beta \\
& + \bar{S}_\theta \ddot{\theta} + \Omega^2 \bar{S}_\theta \left(1 + \frac{eS_\theta}{\bar{S}_\theta} \right) \theta \\
& + \bar{S}_a \ddot{p} + \Omega^2 \bar{S}_a \left(1 + \frac{eS_a}{\bar{S}_a} \right) p \\
& + \bar{S}_t \ddot{q} + \Omega^2 \bar{S}_t \left(1 + \frac{eS_t}{\bar{S}_t} \right) q = M_\beta
\end{aligned} \tag{8.65}$$

8.2.2 Hinge Moments

The tab hinge moment is simply $k_t q$. From the tab equation 8.62 we have the following.

$$\begin{aligned}
k_t q &= M_q - \bar{S}_t \ddot{\beta} - \Omega^2 \bar{S}_t \left(1 + \frac{eS_t}{\bar{S}_t} \right) \beta \\
& - [I_t - (d+t)S_t] \ddot{\theta} - \Omega^2 I_t \left[1 - \frac{(d+t)S_t}{I_t} \right] \theta \\
& - (I_t - tS_t) \ddot{p} - \Omega^2 I_t \left[1 - \frac{(d+t)S_t}{I_t} \right] p \\
& - I_t \ddot{q} - \Omega^2 I_t \left[1 - \frac{(d+t)S_t}{I_t} \right] q
\end{aligned} \tag{8.66}$$

The right hand side of the above expression is useful when the tab deflection is prescribed. Similarly the aileron hinge moment is obtained from equation 8.63

$$\begin{aligned}
k_a p &= M_p - \bar{S}_a \ddot{\beta} - \Omega^2 \bar{S}_a \left(1 + \frac{eS_a}{\bar{S}_a} \right) \beta \\
& - [I_a - dS_a] \ddot{\theta} - \Omega^2 I_a \left[1 - \frac{dS_a}{I_a} \right] \theta \\
& - I_a \ddot{p} - \Omega^2 I_a \left[1 - \frac{dS_a}{I_a} \right] p \\
& - (I_t - tS_t) \ddot{q} - \Omega^2 I_t \left[1 - \frac{(d+t)S_t}{I_t} \right] q = M_p
\end{aligned} \tag{8.67}$$

The torsion and flap hinge moments at the blade root can also be easily obtained from equations 8.75 and 8.65 and is left to the reader.

8.2.3 Initial condition response

For initial condition response set M_β , M_θ , M_a , and M_t to zero and solve for β , θ , p , q with initial conditions $\beta(0)$, $\theta(0)$, $p(0)$, $q(0)$ and $\dot{\beta}(0)$, $\dot{\theta}(0)$, $\dot{p}(0)$, $\dot{q}(0)$.

8.2.4 Response with prescribed tab deflections

When $q(t)$ is prescribed, the tab equation is removed, and the flap, torsion and aileron equations take the following forms.

Flap equation:

$$\begin{aligned}
& I_\beta \ddot{\beta} + \Omega^2 I_\beta \left[1 + \frac{eS_\beta}{I_\beta} + \frac{k_\beta}{I_\beta \Omega^2} \right] \beta \\
& + \bar{S}_\theta \ddot{\theta} + \Omega^2 \bar{S}_\theta \left(1 + \frac{eS_\theta}{\bar{S}_\theta} \right) \theta \\
& + \bar{S}_a \ddot{p} + \Omega^2 \bar{S}_a \left(1 + \frac{eS_a}{\bar{S}_a} \right) p \\
& = M_\beta - \bar{S}_t \ddot{q} - \Omega^2 \bar{S}_t \left(1 + \frac{eS_t}{\bar{S}_t} \right) q
\end{aligned} \tag{8.68}$$

Torsion equation:

$$\begin{aligned}
& \bar{S}_\theta \ddot{\beta} + \Omega^2 \bar{S}_\theta \left(1 + \frac{eS_\theta}{\bar{S}_\theta} \right) \beta \\
& + I_\theta \ddot{\theta} + \Omega^2 I_\theta \left[1 + \frac{k_\theta}{I_\theta \Omega^2} \right] \theta \\
& + [I_a - dS_a] \ddot{p} + \Omega^2 I_a \left[1 - \frac{dS_a}{I_a} \right] p \\
& = M_\theta - (I_t - (d+t)S_t) \ddot{q} - \Omega^2 I_t \left[1 - \frac{(d+t)S_t}{I_t} \right] q
\end{aligned} \tag{8.69}$$

Aileron equation:

$$\begin{aligned}
& \bar{S}_a \ddot{\beta} + \Omega^2 \bar{S}_a \left(1 + \frac{eS_a}{\bar{S}_a} \right) \beta \\
& + [I_a - dS_a] \ddot{\theta} + \Omega^2 I_a \left[1 - \frac{dS_a}{I_a} \right] \theta \\
& + I_a \ddot{p} + \Omega^2 I_a \left[1 - \frac{dS_a}{I_a} + \frac{k_a}{I_a \Omega^2} \right] p \\
& = M_a - (I_t - tS_t) \ddot{q} - \Omega^2 I_t \left[1 - \frac{(d+t)S_t}{I_t} \right] q
\end{aligned} \tag{8.70}$$

8.2.5 Flap-Torsion-Aileron Dynamics for a Rotor Blade

The coupled flap-torsion-aileron dynamics follows from the flap-torsion-aileron-tab dynamics derived in the previous section, by simply removing the the tab degree of freedom $q(t)$. Thus we have

Flap equation:

$$\begin{aligned}
& I_\beta \ddot{\beta} + \Omega^2 I_\beta \left[1 + \frac{eS_\beta}{I_\beta} + \frac{k_\beta}{I_\beta \Omega^2} \right] \beta \\
& + \bar{S}_\theta \ddot{\theta} + \Omega^2 \bar{S}_\theta \left(1 + \frac{eS_\theta}{\bar{S}_\theta} \right) \theta \\
& + \bar{S}_a \ddot{p} + \Omega^2 \bar{S}_a \left(1 + \frac{eS_a}{\bar{S}_a} \right) p = M_\beta
\end{aligned} \tag{8.71}$$

Torsion equation:

$$\begin{aligned}
& \bar{S}_\theta \ddot{\beta} + \Omega^2 \bar{S}_\theta \left(1 + \frac{eS_\theta}{\bar{S}_\theta} \right) \beta \\
& + I_\theta \ddot{\theta} + \Omega^2 I_\theta \left[1 + \frac{k_\theta}{I_\theta \Omega^2} \right] \theta \\
& + [I_a - dS_a] \ddot{p} + \Omega^2 I_a \left[1 - \frac{dS_a}{I_a} \right] p = M_\theta
\end{aligned} \tag{8.72}$$

Aileron equation:

$$\begin{aligned}
& \bar{S}_a \ddot{\beta} + \Omega^2 \bar{S}_a \left(1 + \frac{eS_a}{\bar{S}_a} \right) \beta \\
& + [I_a - dS_a] \ddot{\theta} + \Omega^2 I_a \left[1 - \frac{dS_a}{I_a} \right] \theta \\
& + I_a \ddot{p} + \Omega^2 I_a \left[1 - \frac{dS_a}{I_a} + \frac{k_a}{I_a \Omega^2} \right] p = M_a
\end{aligned} \tag{8.73}$$

8.2.6 Response using prescribed aileron deflections

If the aileron deflections $p(t)$ are prescribed then the equations become

Flap equation:

$$\begin{aligned}
& I_\beta \ddot{\beta} + \Omega^2 I_\beta \left[1 + \frac{eS_\beta}{I_\beta} + \frac{k_\beta}{I_\beta \Omega^2} \right] \beta \\
& + \bar{S}_\theta \ddot{\theta} + \Omega^2 \bar{S}_\theta \left(1 + \frac{eS_\theta}{\bar{S}_\theta} \right) \theta \\
& = M_\beta - \bar{S}_a \ddot{p} - \Omega^2 \bar{S}_a \left(1 + \frac{eS_a}{\bar{S}_a} \right) p
\end{aligned} \tag{8.74}$$

Torsion equation:

$$\begin{aligned}
& \bar{S}_\theta \ddot{\beta} + \Omega^2 \bar{S}_\theta \left(1 + \frac{eS_\theta}{\bar{S}_\theta} \right) \beta \\
& + I_\theta \ddot{\theta} + \Omega^2 I_\theta \left[1 + \frac{k_\theta}{I_\theta \Omega^2} \right] \theta \\
& = M_\theta - [I_a - dS_a] \ddot{p} - \Omega^2 I_a \left[1 - \frac{dS_a}{I_a} \right] p
\end{aligned} \tag{8.75}$$

8.2.7 Flap-Torsion-Aileron-Tab equations in non-dimensional form

The coupled blade-torsion-trailing flap-tab equations are non-dimensionalized by dividing them by $I_b \Omega^2$. Thus we obtain the following

Flap equation:

$$\begin{aligned}
& \beta^{**} + \left[1 + \frac{eS_\beta}{I_\beta} + \frac{k_\beta}{I_\beta \Omega^2} \right] \beta \\
& + \frac{\bar{S}_\theta}{I_b} \theta^{**} + \frac{\bar{S}_\theta}{I_b} \left(1 + \frac{eS_\theta}{\bar{S}_\theta} \right) \theta \\
& + \frac{\bar{S}_a}{I_b} p^{**} + \frac{\bar{S}_a}{I_b} \left(1 + \frac{eS_a}{\bar{S}_a} \right) p \\
& + \frac{\bar{S}_t}{I_b} q^{**} + \frac{\bar{S}_t}{I_b} \left(1 + \frac{eS_t}{\bar{S}_t} \right) q = \gamma \bar{M}_\beta
\end{aligned} \tag{8.76}$$

where γ is the lock number, and

$$\begin{aligned}
\bar{M}_\beta &= \frac{1}{2} \int_0^1 y \bar{C}_l u_t^2 dy \\
y &= \frac{r}{R} \\
\bar{C}_l &= \frac{C_l}{a} \quad \text{where } a \text{ is a reference lift curve slope used to calculate } \gamma \\
u_t &= \frac{U_T}{\Omega R}
\end{aligned}$$

Torsion equation:

$$\begin{aligned}
& \frac{\bar{S}_\theta}{I_b} \beta^{**} + \frac{\bar{S}_\theta}{I_b} \left(1 + \frac{eS_\theta}{\bar{S}_\theta} \right) \beta \\
& + \frac{I_\theta}{I_b} \theta^{**} + \frac{I_\theta}{I_b} \left[1 + \frac{k_\theta}{I_\theta \Omega^2} \right] \theta \\
& + \left(\frac{I_a - dS_a}{I_b} \right) p^{**} + \frac{I_a}{I_b} \left[1 - \frac{dS_a}{I_a} \right] p \\
& + \left[\frac{I_t - (d+t)S_t}{I_b} \right] q^{**} + \frac{I_t}{I_b} \left[1 - \frac{(d+t)S_t}{I_t} \right] q = \gamma \bar{M}_\theta
\end{aligned} \tag{8.77}$$

$$\begin{aligned}
\bar{M}_\theta &= \frac{1}{2} \int_0^1 \bar{C}_{mea} \bar{c} u_t^2 dy \\
\bar{c} &= \frac{c}{R}
\end{aligned}$$

Aileron equation:

$$\begin{aligned}
& \frac{\bar{S}_a}{I_b} \beta^{**} + \frac{\bar{S}_a}{I_b} \left(1 + \frac{eS_a}{\bar{S}_a} \right) \beta \\
& + \left(\frac{I_a - dS_a}{I_b} \right) \theta^{**} + \frac{I_a}{I_b} \left[1 - \frac{dS_a}{I_a} \right] \theta \\
& + \frac{I_a}{I_b} p^{**} + \frac{I_a}{I_b} \left[1 - \frac{dS_a}{I_a} + \frac{k_a}{I_a \Omega^2} \right] p \\
& + \left(\frac{I_t - tS_t}{I_b} \right) q^{**} + \frac{I_t}{I_b} \left[1 - \frac{(d+t)S_t}{I_t} \right] q = \gamma \bar{M}_p
\end{aligned} \tag{8.78}$$

$$\bar{M}_p = \frac{1}{2} \int_0^1 \bar{C}_{mp} \bar{c} u_t^2 dy$$

Tab equation:

$$\begin{aligned} & \frac{\bar{S}_t}{I_b} \beta^{**} + \frac{\bar{S}_t}{I_b} \left(1 + \frac{eS_t}{\bar{S}_t}\right) \beta \\ & + \left[\frac{I_t - (d+t)S_t}{I_b} \right] \theta^{**} + \frac{I_t}{I_b} \left[1 - \frac{(d+t)S_t}{I_t}\right] \theta \\ & + \left(\frac{I_t - tS_t}{I_b} \right) p^{**} + \frac{I_t}{I_b} \left[1 - \frac{(d+t)S_t}{I_t}\right] p \\ & + \frac{I_t}{I_b} q^{**} + \frac{I_t}{I_b} \left[1 - \frac{(d+t)S_t}{I_t} + \frac{k_t}{I_t \Omega^2}\right] q = \gamma \bar{M}_q \end{aligned} \quad (8.79)$$

$$\bar{M}_q = \frac{1}{2} \int_0^1 \bar{C}_{mq} \bar{c} u_t^2 dy$$

8.3 Aerodynamic Model

The foundation of flap-torsion-aileron-tab aerodynamics was laid by Theodorsen and Garrick in 1942 [3]. It was developed to study flutter of fixed wing aircraft tails with control surfaces, including servo tabs.

8.3.1 Theodorsen model for aileron

Consider a section with flap. The section extends from $x = -b$ to $x = +b$, where b is half-chord. The pitch axis of the main part of the blade (elastic axis of the entire section) is located at $x = x_a$. The main blade ends at $x = x_c$. The pitch axis of the aileron is at the same point, i.e. there is no aerodynamic overhang.

The effective angle of attack of a 2-dimensional wing section (without aileron or tab) undergoing pitch and plunge motion is calculated at the 3/4 chord location. This is done so that the expression obtained for the sectional lift coefficient, C_l is consistent with thin airfoil theory.

$$\alpha_e = \alpha + \frac{\dot{h}}{U} + \left(\frac{1}{2} - x_a\right) b \frac{\dot{\alpha}}{U} \quad (8.80)$$

For a section with an aileron, the effective angle of attack can be extended to include the effect of aileron deflection

$$\alpha_{ep} = \alpha_e + \frac{1}{\pi} T_{10}^c p + \frac{1}{2\pi} T_{11}^c \frac{b\dot{p}}{U} \quad (8.81)$$

where T 's are geometric constants given later. Define

$$Q = U \alpha_{ep} \quad (8.82)$$

Then the lift, pitching moment, and aileron hinge moment are given as follows. The circulatory components are

$$\begin{aligned} L &= 2\pi\rho U b Q C(k) \\ M_a &= 2\pi\rho U b^2 \left[\left(x_a + \frac{1}{2}\right) C(k) - \frac{1}{2} \right] Q \\ M_p &= -\rho U b^2 [T_{12}^c C(k) - T_4] Q \end{aligned} \quad (8.83)$$

$C(k)$ is the unsteady Theodorsen constant accounting for the shed wake. The circulatory components have terms both associated with the shed wake and those not associated with the shed wake. The noncirculatory components are

$$\begin{aligned}
L &= \rho b^2 \left(\pi U \dot{\alpha} + \pi \dot{h} - \pi b a \ddot{a} - U T_4^c \dot{p} - b T_1^c \ddot{p} \right) \\
M_a &= -\rho b^2 \left[\underline{-\pi U^2 \alpha} + \pi \left(\frac{1}{8} + x_a^2 \right) b^2 \ddot{\alpha} + U^2 T_4^c p + \{ T_1^c - T_8^c - (x_c - x_a) T_4^c \} b U \dot{p} \right. \\
&\quad \left. - \{ T_7^c + (c - a) T_1^c \} b^2 \ddot{p} - \pi a b \ddot{h} - \underline{\pi U \dot{h}} \right] \\
M_p &= -\rho b^2 \left[\underline{U^2 T_4^c \alpha} + \underline{T_4^c U \dot{h}} - (2T_9^c + T_1^c) b U \dot{\alpha} + 2T_{13}^c b^2 \ddot{\alpha} + \frac{1}{\pi} T_5^c U^2 p - \frac{1}{\pi} b^2 T_3^c \ddot{p} - T_1^c b \ddot{h} \right]
\end{aligned} \tag{8.84}$$

The underlined terms in the noncirculatory components cancel with the non-shed wake related terms in the circulatory components. Grouped into shed wake related and non shed wake related terms the final expressions after addition become

$$\begin{aligned}
L &= 2\pi \rho U b Q C(k) + \rho b^2 \left(\pi U \dot{\alpha} + \pi \dot{h} - \pi b a \ddot{a} - U T_4^c \dot{p} - b T_1^c \ddot{p} \right) \\
M_a &= 2\pi \rho U b^2 \left(x_a + \frac{1}{2} \right) Q C(k) - \rho b^2 \left[\underline{\pi U b \left(\frac{1}{2} - x_a \right) \dot{\alpha}} + \pi \left(\frac{1}{8} + x_a^2 \right) b^2 \ddot{\alpha} \right. \\
&\quad \left. + U^2 (T_{10}^c + T_4^c) p + \left\{ T_1^c - T_8^c - (x_c - x_a) T_4^c + \frac{b}{2} T_{11}^c \right\} b U \dot{p} \right. \\
&\quad \left. - \{ T_7^c + (c - a) T_1^c \} b^2 \ddot{p} - \pi a b \ddot{h} \right] \\
M_p &= -\rho U b^2 T_{12}^c Q C(k) - \rho b^2 \left[- \left\{ 2T_9^c + T_1^c + T_4^c \left(\frac{1}{2} - x_a \right) \right\} b U \dot{\alpha} + 2T_{13}^c b^2 \ddot{\alpha} \right. \\
&\quad \left. + \frac{1}{\pi} (T_5^c - \underline{T_4^c T_{10}^c}) U^2 p - \underline{-\frac{1}{2\pi} b T_4^c T_{11}^c U \dot{p}} - \frac{1}{\pi} b^2 T_3^c \ddot{p} - T_1^c b \ddot{h} \right]
\end{aligned} \tag{8.85}$$

where the underlined terms are circulatory terms not related to shed wake effects. The nondimensional lift and moment coefficients are then simply

$$\begin{aligned}
C_l &= \frac{L}{\frac{1}{2} \rho U^2 (2b)} \\
C_{ma} &= \frac{M_a}{\frac{1}{2} \rho U^2 (2b)^2} \\
C_{mp} &= \frac{M_p}{\frac{1}{2} \rho U^2 (2b)^2}
\end{aligned} \tag{8.86}$$

8.3.2 Theodorsen and Garrick model for aileron and tab

Here a general airfoil section with an aileron and a tab with aerodynamic overhangs for both are considered, see Fig. 8.2. As shown in the figure, the entire section extends from $x = -b$ to $x = +b$, where b is half-chord. The pitch axis of the main part of the blade (elastic axis of the entire section) is located at $x = x_a$. The main blade ends at $x = x_c$. The pitch axis of the aileron is at $x = x_e$. The distance between x_c and x_e is the aerodynamic overhang of the aileron, l , where $l = x_e - x_c$. The aileron ends at $x = x_d$. The pitch axis of the tab is at $x = x_f$. The distance between x_f and x_d is the aerodynamic overhang of the tab, m , where $m = x_f - x_d$. The analysis assumes no leak of fluid in the gaps between the wing and the aileron, and between the aileron and the tab. These gaps are considered sealed.

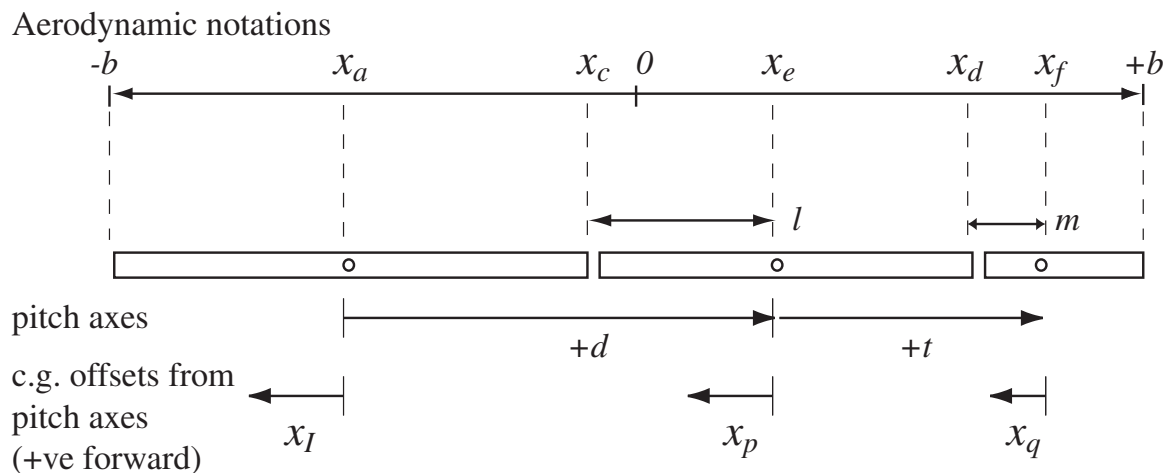


Figure 8.2: Airfoil with aileron and tab; aerodynamic notations

For a section with flap and tab the effective angle of attack can be extended to include the effect of aileron and tab deflections, p , and q .

$$\alpha_{epq} = \alpha_e + \frac{1}{\pi}(T_{10}^c - lT_{21}^c)p + \frac{1}{2\pi}(T_{11}^c - 2lT_{10}^c)\frac{b\dot{p}}{U} + \frac{1}{\pi}(T_{10}^d - mT_{21}^d)q + \frac{1}{2\pi}(T_{11}^d - 2lT_{10}^d)\frac{b\dot{q}}{U} \quad (8.87)$$

where T 's are geometric constants given later. Define Q is the same way as before

$$Q = U\alpha_{epq} \quad (8.88)$$

The final expressions for sectional lift, pitching moment and the aileron and tab hinges can be organized into shed wake and non shed wake terms are as follows

$$\begin{aligned} L &= 2\pi\rho UbQC(k) - \rho bU^2(T_{l1} + lT_{l2} + mT_{l3}) + L_I \\ M_a &= 2\pi\rho Ub^2\left(x_a + \frac{1}{2}\right)C(k)Q - \rho b^2U^2(T_{a1} + lT_{a2} + mT_{a3}) + M_{aI} \\ M_p &= -\rho Ub^2(T_{12}^c - 2lT_{20}^c)C(k)Q - \rho b^2U^2(T_{p1} + lT_{p2} + l^2T_{p3} + mT_{p4} + lmT_{p5}) + M_{pI} \\ M_q &= -\rho Ub^2(T_{12}^d - 2mT_{20}^d)C(k)Q - \rho b^2U^2(T_{q1} + mT_{q2} + m^2T_{q3} + lT_{q4} + lmT_{q5}) + M_{qI} \end{aligned} \quad (8.89)$$

$C(k)$ is the unsteady Theodorsen constant accounting for the the shed wake. L_I , M_{aI} , M_{pI} , and M_{qI} are the inertial (or acceleration) terms. In coefficient form we have

$$\begin{aligned} C_l &= \frac{L}{\frac{1}{2}\rho U^2(2b)} \\ C_{ma} &= \frac{M_a}{\frac{1}{2}\rho U^2(2b)^2} \\ C_{mp} &= \frac{M_p}{\frac{1}{2}\rho U^2(2b)^2} \\ C_{mq} &= \frac{M_q}{\frac{1}{2}\rho U^2(2b)^2} \end{aligned} \quad (8.90)$$

Using equations 8.89 and 8.90 we obtain the non-dimensional coefficients as

$$\begin{aligned}
C_l &= 2\pi \frac{Q}{U} C(k) - \frac{1}{2} T_l + C_{li} \\
C_{ma} &= 2\pi \frac{1}{2} \left(x_a + \frac{1}{2} \right) \frac{Q}{U} C(k) - \frac{1}{2} T_{ma} + C_{mai} \\
C_{mp} &= -\frac{1}{2} \frac{Q}{U} (T_{12}^c - 2lT_{20}^c) C(k) - \frac{1}{2} T_{mp} + C_{mpi} \\
C_{mq} &= -\frac{1}{2} \frac{Q}{U} (T_{12}^d - 2mT_{20}^d) C(k) - \frac{1}{2} T_{mq} + C_{mqi}
\end{aligned} \tag{8.91}$$

where Q/U is the effective angle of attack α_{epq} of the section calculated at the 3/4 chord location. T_l , T_{ma} , T_{mp} , and T_{mq} are defined as follows.

$$\begin{aligned}
T_l &= T_{l1} + lT_{l2} + mT_{l3} \\
T_{ma} &= T_{a1} + lT_{a2} + mT_{a3} \\
T_{mp} &= T_{p1} + lT_{p2} + l^2T_{p3} + mT_{p4} + lmT_{p5} \\
T_{mq} &= T_{q1} + mT_{q2} + m^2T_{q3} + lT_{q4} + lmT_{q5}
\end{aligned} \tag{8.92}$$

where

$$\begin{aligned}
T_{l1} &= \pi \frac{b\dot{\alpha}}{U} - T_4^c \frac{b\dot{p}}{U} - T_4^d \frac{b\dot{q}}{U} \\
T_{l2} &= -2 \frac{b\dot{p}}{U} \sqrt{1-x_c^2} \\
T_{l3} &= -2 \frac{b\dot{q}}{U} \sqrt{1-x_d^2}
\end{aligned} \tag{8.93}$$

and

$$\begin{aligned}
T_{a1} &= \pi \left(\frac{1}{2} - a \right) \frac{b\dot{\alpha}}{U} + T_{15}^c p + T_{16}^c \frac{b\dot{p}}{U} + T_{15}^d q + T_{16}^d \frac{b\dot{q}}{U} \\
T_{a2} &= T_{22}^c p + T_{23}^c \frac{b\dot{p}}{U} \\
T_{a3} &= T_{22}^d q + T_{23}^d \frac{b\dot{q}}{U}
\end{aligned} \tag{8.94}$$

and

$$\begin{aligned}
T_{p1} &= T_{17}^c \frac{b\dot{\alpha}}{U} + \frac{1}{\pi} T_{18}^c p + \frac{1}{\pi} T_{19}^c \frac{b\dot{p}}{U} + \frac{1}{\pi} Y_{9q} + \frac{1}{\pi} Y_{10} \frac{b\dot{q}}{U} \\
T_{p2} &= T_{25}^c \frac{b\dot{\alpha}}{U} + \frac{1}{\pi} T_{26}^c p + \frac{1}{\pi} T_{27}^c \frac{b\dot{p}}{U} + \frac{1}{\pi} Y_{11q} + \frac{1}{\pi} Y_{12} \frac{b\dot{q}}{U} \\
T_{p3} &= \frac{1}{\pi} T_{28} p + \frac{1}{\pi} T_{29} \frac{b\dot{p}}{U} \\
T_{p4} &= \frac{1}{\pi} Y_{13q} + \frac{1}{\pi} Y_{14} \frac{b\dot{q}}{U} \\
T_{p5} &= \frac{1}{\pi} Y_{15q} + \frac{1}{\pi} Y_{16} \frac{b\dot{q}}{U}
\end{aligned} \tag{8.95}$$

and

$$\begin{aligned}
T_{q1} &= T_{17}^d \frac{b\dot{\alpha}}{U} + \frac{1}{\pi} Y_{17} p + \frac{1}{\pi} Y_{13} \frac{b\dot{p}}{U} + \frac{1}{\pi} T_{18}^d q + \frac{1}{\pi} T_{19}^d \frac{b\dot{q}}{U} \\
T_{q2} &= T_{25}^d \frac{b\dot{\alpha}}{U} + \frac{1}{\pi} Y_{19} p + \frac{1}{\pi} Y_{20} \frac{b\dot{p}}{U} + \frac{1}{\pi} T_{26}^d q + \frac{1}{\pi} T_{27}^d \frac{b\dot{q}}{U} \\
T_{q3} &= \frac{1}{\pi} T_{28}^d p + \frac{1}{\pi} T_{29} \frac{b\dot{p}}{U} \\
T_{q4} &= \frac{1}{\pi} Y_{21} q + \frac{1}{\pi} Y_{22} \frac{b\dot{q}}{U} \\
T_{q5} &= \frac{1}{\pi} Y_{23} q + \frac{1}{\pi} Y_{24} \frac{b\dot{q}}{U}
\end{aligned} \tag{8.96}$$

The inertial terms L_I , M_{aI} , M_{pI} , and M_{qI} as given in equation 8.89 are as follows.

$$\begin{aligned}
L_I &= -\rho b \left(\pi b \ddot{h} - \pi b a \ddot{\alpha} - T_1^c b \ddot{p} - T_1^d b \ddot{q} \right) \\
&\quad - \rho b l \left(b^2 T_4^c \ddot{p} \right) - \rho b m \left(b^2 T_4^d \ddot{q} \right) \\
M_{aI} &= -\rho b^2 \left[\pi a h \ddot{h} + \pi b^2 \left(\frac{1}{8} + a^2 \right) \ddot{\alpha} + 2T_{13}^c b^2 \ddot{p} + 2T_{13}^d b^2 \ddot{q} \right] \\
&\quad - \rho b^2 l \left(T_{24}^c b^2 \ddot{p} \right) - \rho b^2 m \left(T_{24}^d b^2 \ddot{q} \right) \\
M_{pI} &= -\rho b^2 \left(-T_1^c b \ddot{h} + 2T_{13}^c b^2 \ddot{\alpha} - \frac{1}{\pi} T_3^c b^2 \ddot{p} - \frac{1}{\pi} Y_6 b^2 \ddot{q} \right) \\
&\quad - \rho b^2 l \left(T_4^c b \ddot{h} + T_{24}^c b^2 \ddot{\alpha} + \frac{2}{\pi} T_2^c b^2 \ddot{p} + \frac{1}{\pi} Y_3 b^2 \ddot{q} \right) \\
&\quad - \rho b^2 l^2 \left(-\frac{1}{\pi} T_5^c b^2 \ddot{p} \right) - \rho b^2 m \left(\frac{1}{\pi} Y_4 b^2 \ddot{q} \right) - \rho b^2 l m \left(-\frac{1}{\pi} Y_1 b^2 \ddot{q} \right) \\
M_{qI} &= -\rho b^2 \left(-T_1^d b \ddot{h} + 2T_{13}^d b^2 \ddot{\alpha} - \frac{1}{\pi} Y_6 b^2 \ddot{p} - \frac{1}{\pi} T_3^d b^2 \ddot{q} \right) \\
&\quad - \rho b^2 m \left(T_4^d b \ddot{h} + T_{24}^d b^2 \ddot{\alpha} + \frac{1}{\pi} Y_4 b^2 \ddot{p} + \frac{2}{\pi} T_2^d b^2 \ddot{q} \right) \\
&\quad - \rho b^2 m^2 \left(-\frac{1}{\pi} T_5^d b^2 \ddot{p} \right) - \rho b^2 l \left(\frac{1}{\pi} Y_3 b^2 \ddot{p} \right) - \rho b^2 l m \left(-\frac{1}{\pi} Y_1 b^2 \ddot{p} \right)
\end{aligned} \tag{8.97}$$

The nondimensional forms used in equations 8.91 are obtained by simply dividing the above expressions by $\rho U^2 b$ and $2\rho U^2 b^2$, for lift and moments respectively, as given in equations 8.90.

The constants are provided below.

$$\begin{aligned}
T_1^c &= -\frac{1}{3}(2+x_c^2)\sqrt{1-x_c^2}+x_c\cos^{-1}x_c \\
T_2^c &= x_c(1-x_c^2)-(1+x_c^2)\sqrt{1-x_c^2}\cos^{-1}x_c+x_c(\cos^{-1}x_c)^2 \\
T_3^c &= -\frac{1}{8}(1-x_c^2)(5x_c^2+4)+\frac{1}{4}x_c(7+2x_c^2)\sqrt{1-x_c^2}\cos^{-1}x_c-\left(\frac{1}{8}+x_c^2\right)(\cos^{-1}x_c)^2 \\
T_4^c &= x_c\sqrt{1-x_c^2}-\cos^{-1}x_c \\
T_5^c &= -(1-x_c^2)+2x_c\sqrt{1-x_c^2}\cos^{-1}x_c-(\cos^{-1}x_c)^2 \\
T_8^c &= -\frac{1}{3}(1-x_c^2)^{3/2}-x_cT_4 \\
T_9^c &= \frac{1}{2}\left[\frac{1}{3}(1-x_c^2)^{3/2}+x_aT_4\right] \\
T_{10}^c &= \sqrt{1-x_c^2}+\cos^{-1}x_c \\
T_{11}^c &= (2-x_c)\sqrt{1-x_c^2}+(1-2x_c)\cos^{-1}x_c \\
T_{12}^c &= (2+x_c)\sqrt{1-x_c^2}-(1+2x_c)\cos^{-1}x_c \\
T_{15}^c &= T_4^c+T_{10}^c \\
T_{16}^c &= T_1^c-T_8^c-(x_c-x_a)T_4^c+\frac{1}{2}T_{11}^c \\
T_{17}^c &= -2T_9^c-T_1^c+\left(x_a-\frac{1}{2}\right)T_4^c \\
T_{18}^c &= T_5^c-T_4^cT_{10}^c \\
T_{19}^c &= -\frac{1}{2}T_4^cT_{11}^c
\end{aligned} \tag{8.98}$$

$$\begin{aligned}
T_{20}^c &= -\sqrt{1-x_c^2}+\cos^{-1}x_c \\
T_{21}^c &= \sqrt{\frac{1+x_c}{1-x_c}} \\
T_{22}^c &= 2\sqrt{1-x_c^2}-\sqrt{\frac{1+x_c}{1-x_c}} \\
T_{23}^c &= (-1-2x_c+2x_a)\sqrt{1-x_c^2} \\
T_{25}^c &= T_4^c-(1-x_c)\sqrt{1-x_c^2} \\
T_{26}^c &= 2\sqrt{1-x_c^2}T_{20}^c+T_4^c\sqrt{\frac{1+x_c}{1-x_c}} \\
T_{27}^c &= T_4^cT_{10}^c-\sqrt{1-x_c^2}T_{11}^c \\
N_{c,c'} &= \left|\frac{1-x'_cx_c-\sqrt{1-x_c'^2}\sqrt{1-x_c^2}}{x_c-x'_c}\right| \\
T_{28}^c &= 2(1+x_c+\log_{10}N_{c,c'}) \\
T_{29}^c &= 2\sqrt{1-x_c^2}T_{10}^c
\end{aligned} \tag{8.99}$$

x'_c denotes the beginning coordinate of the aileron. x_c denotes the ending coordinate of the main blade. Thus x'_c-x_c denotes the gap between the main blade and the aileron. Note that the expressions for T^d are obtained by simply replacing x_c with x_d in the above expressions. Similarly, $N_{c,d}$ is obtained by replacing x'_c with x_d in the expression for $N_{c,c'}$. $N_{d,d'}$ is obtained by replacing

x_c with x_d , and x'_c with x'_d . x'_d is the beginning coordinate of the tab. x_d is the ending coordinate of the aileron. Thus, as in the case of aileron, $x'_d - x_d$ denotes the gap between the aileron and the tab. Define the following constants.

$$\begin{aligned} q_c &= \sqrt{1 - x_c^2} \\ q_d &= \sqrt{1 - x_d^2} \\ q_{cd} &= q_c q_d \\ a_c &= \cos^{-1} x_c \\ a_d &= \cos^{-1} x_d \end{aligned}$$

The Y terms are functions of both x_c and x_d . The T terms are understood to be associated with x_c when no explicit variable is indicated. For example, T_4 in Y_9 means T_4^c .

$$\begin{aligned} Y_1 &= -q_{cd} - a_c a_d + x_d q_d a_c + x_c q_c a_d - (x_d - x_c)^2 \log_{10} N_{c,d} \\ Y_2 &= 2q_d a_c - 2(x_d - x_c) \log_{10} N_{c,d} \\ Y_3 &= \frac{1}{3}(x_c + 2x_d)q_c q_d + x_d a_c a_d - \frac{1}{3}q_d a_c (2 + x_d^2) - \frac{1}{3}q_c a_d (1 + 3x_c x_d - x_c^2) + \\ &\quad \frac{1}{3}(x_d - x_c)^3 \log_{10} N_{c,d} \\ Y_4 &= \frac{1}{3}(x_d + 2x_c)q_d q_c + x_c a_c a_d - \frac{1}{3}q_c a_d (2 + x_c^2) - \\ &\quad \frac{1}{3}q_d a_c (1 + 3x_d x_c - x_d^2) + \frac{1}{3}(x_c - x_d)^3 \log_{10} N_{c,d} \\ Y_5 &= -q_{cd} + (2x_c - x_d)q_d a_c + (x_d - x_c)^2 \log_{10} N_{c,d} \\ Y_6 &= -q_{cd} \left(1 + \frac{x_c^2}{6} + \frac{x_d^2}{6} + \frac{11}{12}x_c x_d \right) - a_c a_d \left(\frac{1}{8} + x_d x_c \right) \\ &\quad + \frac{1}{3}a_c q_d \left[\left(\frac{5}{2} - x_d^2 \right) \frac{x_d}{4} + x_c (2 + x_d^2) \right] \\ &\quad + \frac{1}{3}a_d q_c \left[\left(\frac{5}{2} - x_c^2 \right) \frac{x_c}{4} + x_d (2 + x_c^2) \right] + \frac{1}{12}(x_d - x_c)^4 \log_{10} N_{c,d} \end{aligned} \tag{8.100}$$

$$\begin{aligned}
Y_7 &= 2q_c a_c - 2(x_c - x_d) \log_{10} N_{c,d} \\
Y_8 &= -q_{cd} + (2x_d - x_c)q_c a_d + (x_c - x_d)^2 \log_{10} N_{c,d} \\
Y_9 &= Y_1 - T_4 T_{10} \\
Y_{10} &= Y_3 - Y_4 - \frac{1}{2} T_4 T_{11} \\
Y_{11} &= Y_7 - 2q_c T_{10} \\
Y_{12} &= Y_1 - Y_8 - q_c T_{11} \\
Y_{13} &= Y_2 + T_4 T_{21} \\
Y_{14} &= Y_5 - Y_9 \\
Y_{15} &= 2q_c T_{21} + 2 \log_{10} N_{c,d} \\
Y_{16} &= Y_2 - Y_7 + 2q_c T_{10} \\
Y_{17} &= Y_1 - T_4 T_{10} \\
Y_{18} &= Y_4 - Y_3 - \frac{1}{2} T_4 T_{11} \\
Y_{19} &= Y_2 - 2q_d T_{10} \\
Y_{20} &= Y_1 - Y_5 - q_d T_{11} \\
Y_{21} &= Y_7 + T_4 T_{21} \\
Y_{22} &= -Y_1 + Y_8 + T_{10} T_4 \\
Y_{23} &= 2q_d T_{21} + 2 \log_{10} N_{c,d} \\
Y_{24} &= Y_7 - Y_2 + 2q_d T_{10}
\end{aligned} \tag{8.101}$$

8.3.3 2D airfoil data

The expressions given earlier are valid for flat plate airfoils with sealed gaps and for inviscid and incompressible flows. In real applications air control surfaces are slotted. They generate hinge gaps and protrude into the flow when deflected. The flow is characterized by compressibility effects and stall at high angles of attack or deflections. Airfoil properties obtained from steady wind tunnel tests can be used to refine the steady part of the aerodynamic modeling. Calculated properties from 2D CFD analyses can be incorporated in the same manner. Let us understand which parts of the theory can be replaced with refined values. To this end we shall re-organize the coefficients given in equation 8.91 using equations 8.87 and 8.88. First consider the lift coefficient C_l . Keeping only the steady terms we can write

$$\begin{aligned}
C_l &= 2\pi \left[\alpha + \frac{1}{\pi} (T_{10}^c - lT_{21}^c) p + \frac{1}{\pi} (T_{10}^d - mT_{21}^d) q \right] \\
&= 2\pi\alpha + 2(T_{10}^c - lT_{21}^c) p + 2(T_{10}^d - mT_{21}^d) q
\end{aligned} \tag{8.102}$$

The above can be written in general as

$$C_l = C_0 + C_1 \alpha + C_{lp} p + C_{lq} q \tag{8.103}$$

where $C_0 = C_l(\alpha = 0, p = 0, q = 0)$ and C_1 is the lift curve slope. In the case of thin airfoil theory we had $C_0 = 0$, $C_1 = 2\pi$, $C_{lp} = 2(T_{10}^c - lT_{21}^c)$ and $C_{lq} = (T_{10}^d - mT_{21}^d)$. But these coefficients can in general be replaced with real airfoil properties. $C_{lp} p$ is an increment in lift brought about by the aileron deflection. It can be written as $(\Delta C_l)_p$. $C_{lq} q$ is an increment in lift brought about by the tab deflection. It can be written as $(\Delta C_l)_q$. $C_0 + C_1 \alpha$ is the baseline airfoil C_l . It can be written as $(C_l)_{af}$. Thus C_l can be written as

$$C_l = (C_l)_{af} + (\Delta C_l)_p + (\Delta C_l)_q \tag{8.104}$$

To use equation 8.103 the airfoil tables should be used to extract the coefficients C_0 , C_1 , C_{lp} , and C_{lq} . The coefficients must be extracted locally however depending on α , p and q specially in the stall regions. Alternatively, equation 8.104 can be used and incremental contributions can be read off directly from the tables.

Now consider the moments. Let the moment about any point a be C_{ma} . It can be related to the moment about any other point ac by

$$C_{ma} = C_{mac} + C_l \frac{1}{2} (x_a - x_{ac}) \quad (8.105)$$

where x_a and x_{ac} are the coordinates of the two points. The above equation simply relates the moment about any two general points. If x_{ac} is chosen as the aerodynamic center C_{mac} will be the moment about the aerodynamic center with the property that it is independant of angle of attack. Thin airfoil theory gives $x_{ac} = 1/4c$ and $C_{mac} = 0$, which gives back the expression in equation 8.91. In general for cambered airfoils x_{ac} is not at quarter chord and C_{mac} is not zero so that the above general expression should be used. x_{ac} and C_{mac} can be extracted from the airfoil property data where the moments are often measured about any convenient location. For example assume that the moments are available about the quarter chord. In equation 8.105 choose a to be at $1/4c$, which in our convention gives $x_a = -1/2$ to obtain

$$C_{m25} = C_{mac} - C_l \frac{1}{2} \left(\frac{1}{2} + x_{ac} \right) \quad (8.106)$$

Use C_{mac} from the above equation 8.106 and substitute in equation 8.105 to obtain

$$C_{ma} = C_{m25} + C_l \frac{1}{2} \left(x_a + \frac{1}{2} \right) \quad (8.107)$$

Note that the above equation 8.107 could have been directly obtained from equation 8.105 by choosing ac as the quarter chord. The above is a general expression valid for all airfoils. Expand C_l and C_{m25} as follows

$$C_l = C_0 + C_1 \alpha + C_{lp} p + C_{lq} q$$

$$C_{m25} = C_{m250} + \frac{\partial C_{m25}}{\partial \alpha} \alpha + \frac{\partial C_{m25}}{\partial p} p + \frac{\partial C_{m25}}{\partial q} q$$

where from equation 8.106 we have

$$\frac{\partial C_{m25}}{\partial \alpha} = \frac{\partial C_{mac}}{\partial \alpha} - C_l \frac{1}{2} \left(\frac{1}{2} + x_{ac} \right) = 0 - C_l \frac{1}{2} \left(\frac{1}{2} + x_{ac} \right) \quad (8.108)$$

Thus equation 8.107 becomes

$$C_{ma} = C_{m250} + C_0 \frac{1}{2} (x_a - x_{ac}) + C_1 \frac{1}{2} (x_a - x_{ac}) \alpha$$

$$+ \left[\frac{\partial C_{m25}}{\partial p} + C_{lp} \frac{1}{2} \left(x_a + \frac{1}{2} \right) \right] p + \left[\frac{\partial C_{m25}}{\partial q} + C_{lq} \frac{1}{2} \left(x_a + \frac{1}{2} \right) \right] q \quad (8.109)$$

which using equation 8.107 can be seen to be of a general form

$$C_{ma} = C_{ma0} + \frac{\partial C_{ma}}{\partial \alpha} \alpha + \frac{\partial C_{ma}}{\partial p} p + \frac{\partial C_{ma}}{\partial q} q \quad (8.110)$$

The coefficients in the above equation 8.110 can be determined from airfoil property tables via the expressions given in equation 8.109. The C_{m25} , C_0 and C_1 can be obtained from the baseline

airfoil tables with undeflected aileron and tab. The factors C_{lp} , C_{lq} , $\partial C_{m25}/\partial p$ and $\partial C_{m25}/\partial q$ can be obtained from aileron and tab tables. Let us explore the values provided by thin airfoil theory. This helps us understand which parts of the thin airfoil theory are being refined by the use of airfoil tables. The thin airfoil theory expression was

$$C_{ma} = 2\pi \left[\alpha + \frac{1}{\pi}(T_{10}^c - lT_{21}^c)p + \frac{1}{\pi}(T_{10}^d - mT_{21}^d)q \right] \frac{1}{2} \left(x_a + \frac{1}{2} \right) - \frac{1}{2} \left(T_{15}^c + lT_{22}^c + mT_{22}^d \right) p - \frac{1}{2} T_{15}^d q \quad (8.111)$$

Comparing equations 8.109 and 8.111 we have

$$\begin{aligned} C_{m250} &= 0 \\ C_0 &= 0 \\ C_1 &= 2\pi \\ C_{lp} &= 2(T_{10}^c - lT_{21}^c) \\ C_{lq} &= 2(T_{10}^d - mT_{21}^d) \\ \frac{\partial C_{m25}}{\partial p} &= -\frac{1}{2} \left(T_{15}^c + lT_{22}^c + mT_{22}^d \right) \\ \frac{\partial C_{m25}}{\partial q} &= -\frac{1}{2} T_{15}^d \end{aligned}$$

An alternative expression to equation 8.110 can be obtained by recognizing

$$\begin{aligned} C_{m250} + C_0 \frac{1}{2}(x_a - x_{ac}) + C_1 \frac{1}{2}(x_a - x_{ac})\alpha &= (C_{m25})_{af} + (C_l)_{af} \frac{1}{2} \left(x_a + \frac{1}{2} \right) \\ \frac{\partial C_{m25}}{\partial p} p &= (\Delta C_{m25})_p \quad \text{change in moment due to aileron} \\ \frac{\partial C_{m25}}{\partial q} q &= (\Delta C_{m25})_q \quad \text{change in moment due to tab} \\ C_{lp} p &= (\Delta C_l)_p \quad \text{change in lift due to aileron} \\ C_{lq} q &= (\Delta C_l)_q \quad \text{change in lift due to tab} \end{aligned}$$

Thus the expression 8.109 can be written as

$$\begin{aligned} C_{ma} &= (C_{m25})_{af} + (C_l)_{af} \frac{1}{2} \left(x_a + \frac{1}{2} \right) \\ &+ \left[(\Delta C_{m25})_p + \frac{1}{2} \left(x_a + \frac{1}{2} \right) (\Delta C_l)_p \right] + \left[(\Delta C_{m25})_q + \frac{1}{2} \left(x_a + \frac{1}{2} \right) (\Delta C_l)_q \right] \end{aligned} \quad (8.112)$$

where the quantities can be read off directly from the airfoil tables. For lift we had equations 8.103 and 8.104. For moment about the pitch axis we have equations 8.110 and 8.112.

The hinge moments for the aileron and tab can also be obtained in a similar manner. Thus for the airfoil hinge moment we have

$$\begin{aligned} C_{mp} &= C_{mp0} + \frac{\partial C_{mp}}{\partial \alpha} \alpha + \frac{\partial C_{mp}}{\partial p} p + \frac{\partial C_{mp}}{\partial q} q \\ &= (C_{mp})_{af} + \frac{\partial C_{mp}}{\partial p} p + \frac{\partial C_{mp}}{\partial q} q \\ &= (C_{mp})_{af} + (\Delta C_{mp})_p + (\Delta C_{mp})_q \end{aligned} \quad (8.113)$$

Similarly for the tab hinge moment

$$\begin{aligned}
C_{mq} &= C_{mq0} + \frac{\partial C_{mq}}{\partial \alpha} \alpha + \frac{\partial C_{mq}}{\partial p} p + \frac{\partial C_{mq}}{\partial q} q \\
&= (C_{mq})_{af} + \frac{\partial C_{mq}}{\partial p} p + \frac{\partial C_{mq}}{\partial q} q \\
&= (C_{mq})_{af} + (\Delta C_{mq})_p + (\Delta C_{mq})_q
\end{aligned} \tag{8.114}$$

As an example, figure 8.3 shows the baseline airfoil properties for a NACA 0009 airfoil. Figures 8.3(a) and 8.3(b) show the airfoil $(C_l)_{af}$ and $(C_{m25})_{af}$ variation with angle of attack. Figures 8.3(d) and (f) show the aileron and tab hinge moments of the airfoil with undeflected aileron and tab angles. These are $(C_{mp})_{af}$ and $(C_{mq})_{af}$. Figures 8.3(c) and (e) are the local lifts on the aileron and tab obtained by integrating the pressure distributions only around the aileron and the tab. The test data presented here is from Ref. [4]. The properties have been nondimensionalized in a slightly different manner compared to the analysis given earlier and are denoted with bars. The lift and pitching moment coefficients are the same. The local lift and hinge moments are nondimensionalized with respect to the local chord of the control surface.

$$\begin{aligned}
(\bar{C}_l)_p &= \frac{N_p}{\frac{1}{2}\rho U^2 c_p} \\
(\bar{C}_l)_q &= \frac{N_q}{\frac{1}{2}\rho U^2 c_q} \\
\bar{C}_{mp} &= \frac{M_p}{\frac{1}{2}\rho U^2 c_p^2} = C_{mp} \left(\frac{c}{c_p}\right)^2 \\
\bar{C}_{mq} &= \frac{M_q}{\frac{1}{2}\rho U^2 c_q^2} = C_{mq} \left(\frac{c}{c_q}\right)^2
\end{aligned}$$

Consider now an angle of attack $\alpha = 1/2^\circ$. The flap and tab are now deflected. Figure 8.4 shows the increments in lift, quarter chord pitching moment, local control surface lifts, and hinge moments brought about by the deflection. The increments are plotted versus aileron deflection over a range of tab angles. The values at zero tab angle can be assumed to correspond to an aileron only case with the aileron size of 30% chord. Figure 8.5 replots the same data with the properties now varying with tab angle over a range of aileron angle. The values at zero aileron angle can be assumed to correspond to an aileron only case with the aileron size of 9% chord.

The general expressions for lift, pitching moment and hinge moments given earlier in equations 8.103, 8.110, 8.113 and 8.114 can be extended for the unsteady case to increase sensitivity terms for the angular rates and accelerations. This form is useful for aeroelastic stability analyses as it identifies the aerodynamic damping and stiffness associated with the flap and tab deflections. Thus we have

$$C_l = C_0 + C_{l\dot{h}} \dot{h} + C_{l\ddot{h}} \ddot{h} + C_{l\alpha} \alpha + C_{lp} p + C_{lq} q + C_{l\dot{\alpha}} \dot{\alpha} + C_{l\dot{p}} \dot{p} + C_{l\dot{q}} \dot{q} + C_{l\ddot{\alpha}} \ddot{\alpha} + C_{l\ddot{p}} \ddot{p} + C_{l\ddot{q}} \ddot{q} \tag{8.115}$$

8.4 Flexible blade equations

The rotor blade is assumed flexible. The aileron and the tab are still single degrees of freedom. The flexibility of the control surface along the span is neglected. The axial extension u_e equation remains unchanged.

Elastic extension equation u_e :

$$\begin{aligned} & \left[EAu'_e + EAK_A^2 \left(\theta' \hat{\phi}' + \theta' w' v'' + \frac{\hat{\phi}'^2}{2} \right) \right. \\ & \left. - EAe_A v'' (\cos \theta - \hat{\phi} \sin \theta) + EA w'' (\sin \theta + \hat{\phi} \cos \theta) \right]' \\ & + m(\ddot{u}_e - u_e - x - 2\dot{v}) = L_u \end{aligned} \quad (8.116)$$

Chord bending equation v :

$$\begin{aligned} & [v''(EI_Z \cos^2 \theta + EI_Y \sin^2 \theta) + w''(EI_Z - EI_Y) \cos \theta \sin \theta \\ & - v'' \hat{\phi} \sin 2\theta (EI_Z - EI_Y) + w'' \hat{\phi} \cos 2\theta (EI_Z - EI_Y) \\ & - v'' \hat{\phi}^2 \cos 2\theta (EI_Z - EI_Y) - w'' \hat{\phi}^2 \sin 2\theta (EI_Z - EI_Y) \\ & - EB_2 \theta' \hat{\phi}' \cos \theta - EAe_A u'_e (\cos \theta - \hat{\phi} \sin \theta) + EAK_A^2 u'_e w' \theta' \\ & + (GJ + EB_1 \theta'^2) \hat{\phi}' w' - EC_2 \hat{\phi}'' \sin \theta]'' \\ & - m \left[-\ddot{v} + e_g \ddot{\theta} \sin \theta + e_g \cos \theta + v - \hat{\phi} \sin \theta + 2\dot{v} \beta_p + 2e_g \dot{v}' \cos \theta \right. \\ & \left. + 2e_g \dot{w}' \sin \theta + \ddot{\phi} e_g \sin \theta - 2\dot{u}_e + 2 \int_0^x (v' \dot{v}' + w' \dot{w}') dx \right] \\ & - me_g \left(x \cos \theta - \hat{\phi} x \sin \theta + 2\dot{v} \cos \theta \right)' + \left\{ mv' \int_x^1 (-\ddot{u}_e + u_e + x + 2\dot{v}) \right\}' \\ & - m_p e_p \left(\ddot{p} \sin \theta + p \ddot{\theta} \cos \theta + 2\dot{\theta} \dot{p} \cos \theta - p \dot{\theta}^2 \sin \theta - p \sin \theta \right) - m_p e_p p (x \sin \theta)' \\ & - m_q e_q \left(\ddot{q} \sin \theta + 2\dot{q} \dot{\theta} \cos \theta - q \sin \theta + q \ddot{\theta} \cos \theta - q \dot{\theta}^2 \sin \theta \right) = L_v \end{aligned} \quad (8.117)$$

Flap bending equation w :

$$\begin{aligned} & [w''(EI_Z \sin^2 \theta + EI_Y \cos^2 \theta) + v''(EI_Z - EI_Y) \cos \theta \sin \theta \\ & + w'' \hat{\phi} \sin 2\theta (EI_Z - EI_Y) + v'' \hat{\phi} \cos 2\theta (EI_Z - EI_Y) \\ & + w'' \hat{\phi}^2 \cos 2\theta (EI_Z - EI_Y) - v'' \hat{\phi}^2 \sin 2\theta (EI_Z - EI_Y) \\ & - EAe_A u'_e (\sin \theta + \hat{\phi} \cos \theta) - EB_2 \hat{\phi}' \theta' \sin \theta + EC_2 \hat{\phi}'' \cos \theta]'' \\ & - m \left(-\ddot{w} - e_g \ddot{\theta} \cos \theta - e_g \ddot{\phi} \cos \theta - 2\dot{v} \beta_p - x \beta_p \right) \\ & - me_g \left(x \sin \theta + \hat{\phi} x \cos \theta + 2\dot{v} \sin \theta \right)' + \left\{ mw' \int_x^1 (-\ddot{u}_e + u_e + x + 2\dot{v}) \right\}' \\ & - m_p e_p \left(-\ddot{p} \cos \theta + p \ddot{\theta} \sin \theta + 2\dot{\theta} \dot{p} \sin \theta + p \dot{\theta}^2 \cos \theta \right) - m_p e_p p (x \cos \theta)' \\ & - m_q e_q \left(-\ddot{q} \cos \theta - 2\dot{q} \dot{\theta} \sin \theta + q \ddot{\theta} \sin \theta + q \dot{\theta}^2 \cos \theta \right) = L_w \end{aligned} \quad (8.118)$$

Torsion equation $\hat{\phi}$:

$$\begin{aligned}
& (w''^2 - v''^2) \cos \theta \sin \theta (EI_Z - EI_Y) + v'' w'' \cos 2\theta \\
& \hat{\phi} (w''^2 - v''^2) \cos 2\theta (EI_Z - EI_Y) - 2\hat{\phi} v'' w'' \sin 2\theta \\
& + \left[GJ(\hat{\phi}' + w' v'') + EAK_A^2(\theta' + \phi') u'_e \right. \\
& \left. + EB_1 \theta'^2 \hat{\phi}' - EB_2 \theta' (v'' \cos \theta + w'' \sin \theta) \right]' \\
& - \left[-k_m^2 \hat{\phi} - \hat{\phi} (k_{m_2}^2 - k_{m_1}^2) \cos 2\theta - (k_{m_2}^2 - k_{m_1}^2) \cos \theta \sin \theta - x \beta_p e_g \cos \theta \right. \\
& \left. - v e_g \sin \theta + x v' e_g \sin \theta - x w' e_g \cos \theta + \ddot{v} e_g \sin \theta - \ddot{w} e_g \cos \theta - k_m^2 \ddot{\theta} \right] \\
& + m_p k_p^2 \ddot{p} - m_p e_p (d\ddot{p} + dp \cos 2\theta) \\
& + m_q k_q^2 \ddot{q} - m_q e_q [(t+d)\ddot{q} + (t+d)q \cos 2\theta] = L_{\hat{\phi}}
\end{aligned} \tag{8.119}$$

Aileron equation p :

$$\begin{aligned}
& m_p k_p^2 \left[-\ddot{\phi} - \ddot{p} - \ddot{\theta} - 2\dot{w}' \sin^2 \theta - (1 + 2\dot{v}') \sin \theta \cos \theta - (p + \hat{\phi}) \cos 2\theta \right] \\
& + m_p e_p \left[-\ddot{w} \cos \theta + \ddot{v} \sin \theta + d(\ddot{\phi} + \ddot{\theta}) + 2d\dot{w}' \sin^2 \theta + 2d\dot{v}' \sin \theta \cos \theta - v \sin \theta \right. \\
& \left. + x v' \sin \theta - x w' \cos \theta + d\hat{\phi} \cos 2\theta + dp \cos^2 \theta + d \cos \theta \sin \theta + dp\dot{\theta}^2 \right] \\
& + m_q k_q^2 \left[-\ddot{\phi} - \ddot{p} - \ddot{q} - \ddot{\theta} - 2\dot{w}' \sin^2 \theta - (1 + 2\dot{v}') \sin \theta \cos \theta \right. \\
& \left. - (p + q + \hat{\phi}) \cos 2\theta \right] \\
& m_q e_q \left[(t+d) (\ddot{\phi} + \ddot{\theta}) + (1 + 2\dot{v}') (t+d) \sin \theta \cos \theta + \right. \\
& \left. + (t+d)(p+q) \cos^2 \theta - tq\dot{\theta}^2 \cos^2 \theta + (t+d)\hat{\phi} \cos^2 \theta \right. \\
& \left. + (2\dot{w}' - 1)(t+d) \sin^2 \theta + (\ddot{v} - v + x v') \sin \theta + t(\ddot{p} + \ddot{q}) + (t+d)q\dot{\theta}^2 \right. \\
& \left. + (-\ddot{w} - x w' - x \beta_p) \cos \theta \right] \\
& + k_p p = M_p
\end{aligned} \tag{8.120}$$

Tab equation q :

$$\begin{aligned}
& m_q k_q^2 \left[-\ddot{\phi} - \ddot{p} - \ddot{q} - \ddot{\theta} - 2\dot{w}' \sin^2 \theta - (1 + 2\dot{v}') \sin \theta \cos \theta - (p + q + \hat{\phi}) \cos 2\theta \right] \\
& + m_q e_q \left[(t+d) (\ddot{\phi} + \ddot{\theta}) + t\ddot{p} - (t+d)\dot{\theta}^2 \sin \theta \cos \theta + (1 + 2\dot{v}') (t+d) \sin \theta \cos \theta \right. \\
& \left. + (t+d)(p+q+\hat{\phi}) \cos^2 \theta - tp \sin^2 \theta + 2(t+d)\dot{w}' \sin^2 \theta - (t+d)\hat{\phi} \sin^2 \theta + \right. \\
& \left. + (\ddot{v} - v + x v') \sin \theta + (-\ddot{w} - x w' + x \beta_p) \cos \theta \right] \\
& + k_q q = M_q
\end{aligned} \tag{8.121}$$

The sectional properties are defined as follows. The blade properties include the aileron and tab. They are assumed to remain nominally constant in presence of aileron and tab deflections. The aileron properties include the tab. They are assumed to remain nominally constant in presence of tab deflections. The blade properties are as follows.

$$\begin{aligned}
\int \int_A d\eta d\zeta &= A \\
\int \int_A \eta d\eta d\zeta &= Ae_A \\
\int \int_A \zeta d\eta d\zeta &= 0 \\
\int \int_A \lambda_T d\eta d\zeta &= 0 \\
\int \int_A (\eta^2 + \zeta^2) d\eta d\zeta &= AK_A^2 \\
\int \int_A (\eta^2 + \zeta^2)^2 d\eta d\zeta &= B_1 \\
\int \int_A \eta(\eta^2 + \zeta^2)^2 d\eta d\zeta &= B_2 \\
\int \int_A \eta^2 d\eta d\zeta &= I_Z \\
\int \int_A \zeta^2 d\eta d\zeta &= I_Y \\
\int \int_A \lambda_T^2 d\eta d\zeta &= EC_1 \\
\int \int_A \zeta \lambda_T d\eta d\zeta &= EC_2 \\
\int \int_A \rho d\eta d\zeta &= m \\
\int \int_A \rho \eta d\eta d\zeta &= me_g \\
\int \int_A \rho \zeta^2 d\eta d\zeta &= mk_{m_1}^2 \\
\int \int_A \rho \eta^2 d\eta d\zeta &= mk_{m_2}^2 \\
\int \int_A \rho(\eta^2 + \zeta^2) d\eta d\zeta &= mk_m^2 \\
\int \int_A \rho \zeta d\eta d\zeta &= 0 \\
\int \int_A \rho \eta \zeta d\eta d\zeta &= 0 \\
\int \int_A \rho \lambda_T d\eta d\zeta &= 0
\end{aligned} \tag{8.122}$$

were A is the sectional area, e_A is the tension axis offset positive in front of the elastic axis, E is the Young's modulus of the blade material, m is mass per unit span, e_g is the center of gravity offset positive in front of the elastic axis, and k_m , k_{m_1} and k_{m_2} are the radii of gyration.

The aileron and tab properties are as follows. They are the same, aileron properties are denoted with the subscript p , the tab properties with q .

$$\begin{aligned}
\int \int_{A_q} \rho d\eta d\zeta &= m_q & \int \int_{A_p} \rho d\eta d\zeta &= m_p \\
\int \int_{A_q} \rho \eta d\eta d\zeta &= me_q & \int \int_{A_p} \rho \eta d\eta d\zeta &= me_p \\
\int \int_{A_q} \rho(\eta^2 + \zeta^2) d\eta d\zeta &= m_p k_q^2 & \int \int_{A_p} \rho(\eta^2 + \zeta^2) d\eta d\zeta &= m_p k_p^2
\end{aligned} \tag{8.123}$$

m_p and m_q are the aileron and tab mass per unit span, k_p and k_q are the radii of gyration and e_p and e_q are the local c.g. offsets with respect to aileron and tab hinge axes. The c.g. offsets are positive forward.

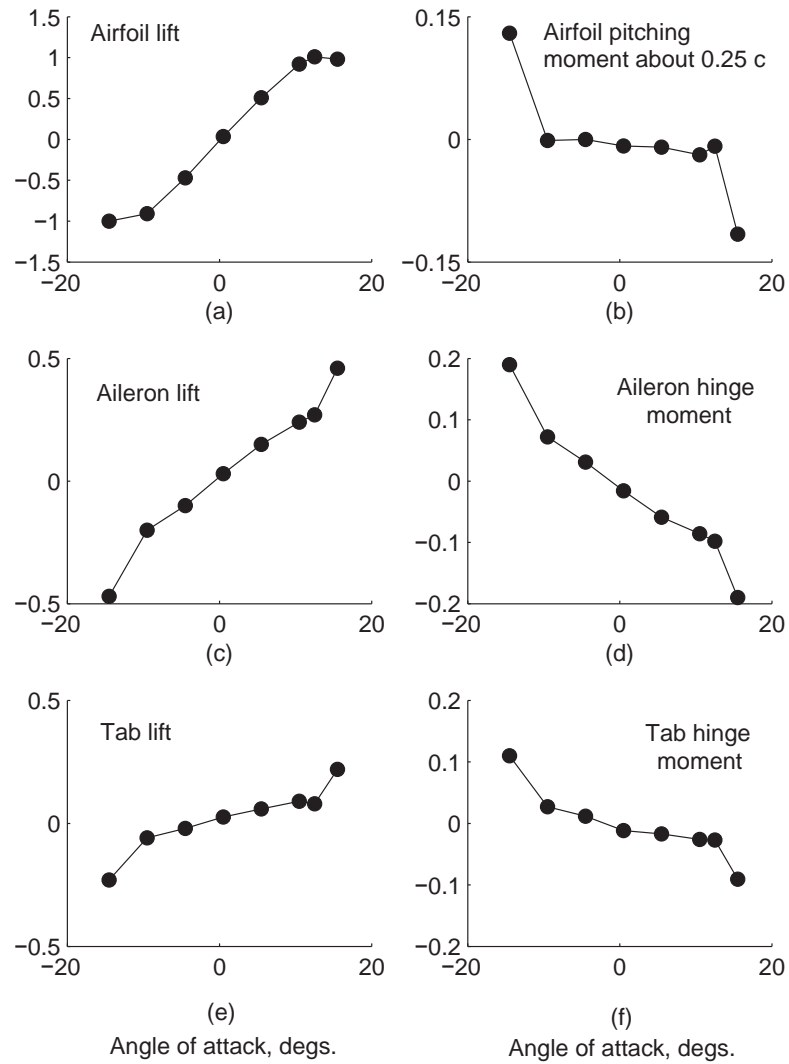


Figure 8.3: NACA 0009 airfoil property variations with section angle of attack α ; undeflected aileron and tab of size $c_p = 21\%c$, $c_q = 9\%c$, zero overhang; (a) airfoil C_l (b) airfoil $C_{m_{25}}$ (c) aileron lift $(\bar{C}_l)_p$ (d) aileron hinge moment \bar{C}_{m_p} (e) tab lift $(\bar{C}_l)_q$ (f) tab hinge moment \bar{C}_{m_q}

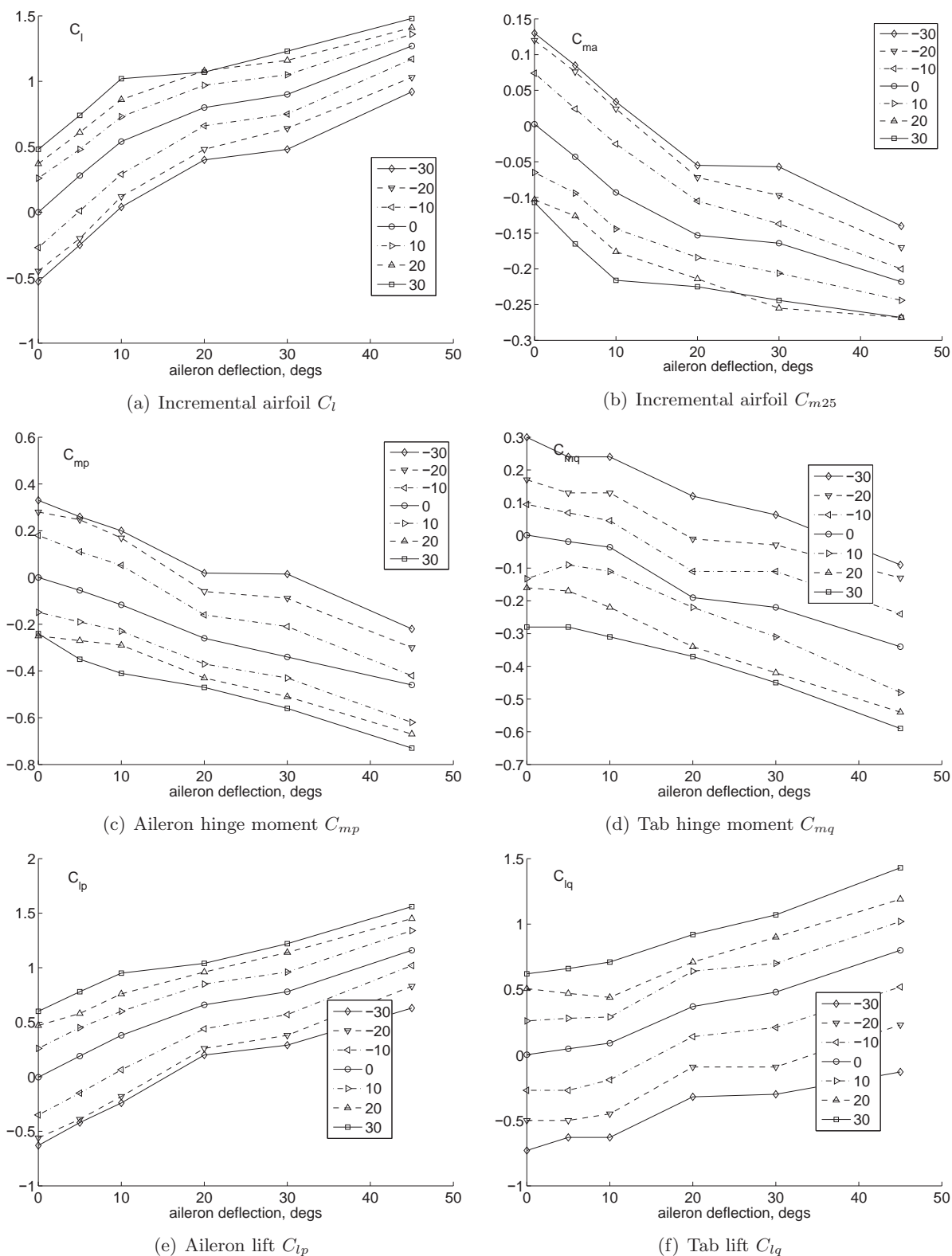


Figure 8.4: Measured properties of a NACA 0009 airfoil varying with aileron deflections at fixed tab settings; aileron and tab are 21% and 9% of total chord with zero overhang; airfoil angle of attack $1/2^\circ$

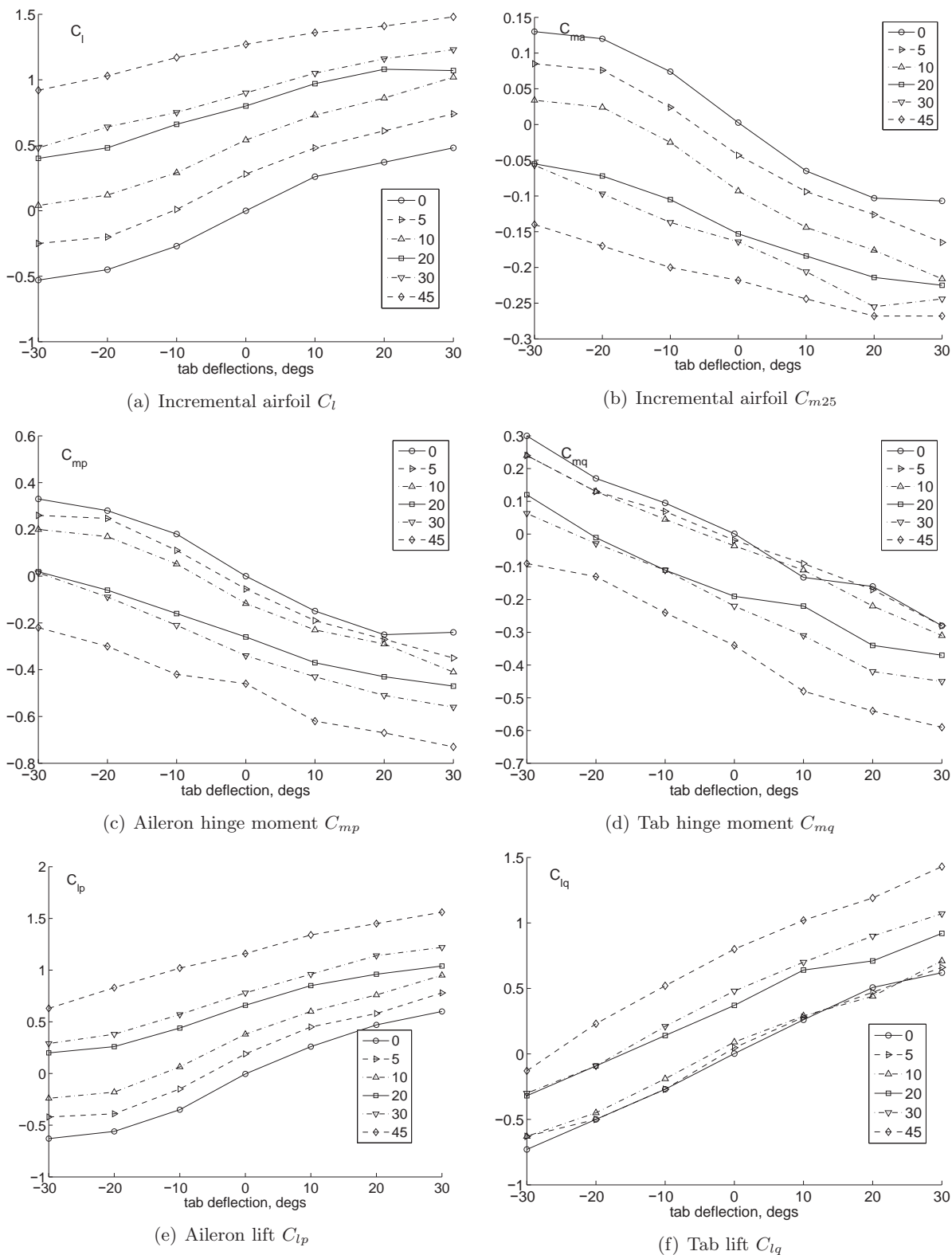


Figure 8.5: Measured properties of a NACA 0009 airfoil varying with tab deflections at fixed aileron settings; aileron and tab are 21% and 9% of total chord with zero overhang; airfoil angle of attack $1/2^\circ$

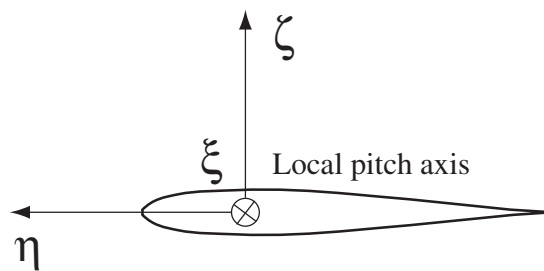


Figure 8.6: Local coordinates of a general element; blade, aileron, or the tab

Bibliography

- [1] Falls, J., Datta, A., and Chopra, I., "Integrated Servo-tabs and Trailing Edge Flaps for Helicopter Primary Control," 62nd Annual Forum of the American Helicopter Society, Phoenix, AZ, May 28-31, 2006.
- [2] Lanczos, C., *The Variational Principles of Mechanics*, Dover Publications, Inc., New York, NY, 1970.
- [3] Theodorsen, T., and Garrick, I. E., "Nonstationary Flow About a Wing-Aileron-Tab Combination Including Aerodynamic Balance," NACA Report No. 736, 1942.
- [4] Ames, M. B. and Sears, R. I., "Pressure-Distribution Investigation of an N.A.C.A. 0009 Airfoil With a 30-Percent-Chord Plain Flap and Three Tabs," NACA Technical Notes No. 759, Washington, May 1940.

Chapter 9

CFD for Rotors

This chapter describes Computational Fluid Dynamics (CFD) methods as applied to rotary wing flows.

9.1 Isentropic Flow Relations

The second law of thermodynamics states that the net rise in internal energy of a system is contributed partly by the heat added and partly by the work done on the system

$$\delta q + \delta w = de \quad (9.1)$$

The assumption is that there is no friction or dissipation losses. The work done on the system is given by $\delta w = -pdv$. p is the pressure and v is the specific volume. Thus

$$\delta q = de + pdv \quad (9.2)$$

The enthalpy h is defined as follows

$$\begin{aligned} h &= e + pv \\ &= e + RT \end{aligned}$$

where $pv = RT$ for a perfect gas. Therefore we have

$$\begin{aligned} dh &= de + pdv + vdp \\ de &= dh - pdv - vdp \end{aligned}$$

Using the above in equation 9.2 we have another expression for δq .

$$\delta q = dh - vdp \quad (9.3)$$

When heat δq is added to a system its temperature T rises. The amount of heat needed for unit rise in temperature is defined as specific heat. During the process of heat addition the volume of the system can be kept constant. Alternatively the volume may be allowed to change so as to keep its pressure constant. The specific heat value differs in the two cases. Thus there are two definitions of specific heat.

$$C_v = \left(\frac{\delta q}{dT} \right)_{\text{constant } v} \quad C_p = \left(\frac{\delta q}{dT} \right)_{\text{constant } p} \quad (9.4)$$

Using the above expressions and equations 9.2 and 9.3 it follows

$$\delta q = C_v dT \quad (9.5)$$

$$de + 0 = C_v dT \quad (9.6)$$

$$e = C_v T \quad (9.7)$$

Similarly

$$\delta q = C_p dT \quad (9.8)$$

$$dh + 0 = C_p dT \quad (9.9)$$

$$h = C_p T \quad (9.10)$$

where the assumption is that $e = 0$ and $h = 0$ at $T = 0$. Even though the above expressions have been obtained considering constant pressure and constant volume processes, the relations hold in general for any process for a perfect gas. A perfect gas is where there are no intermolecular forces. Thermodynamics is related to compressible aerodynamics through the assumption of isentropic flow. Consider the following definitions

Adiabatic process : $\delta q = 0$

Reversible process : no friction or dissipation

Isentropic process : adiabatic + reversible

For an isentropic process, set equation 9.2 to zero and use equation 9.5

$$\begin{aligned} \delta q = de + pdv &= 0 \\ -pdv &= de \\ -pdv &= C_v dT \end{aligned} \quad (9.11)$$

Similarly set equation 9.3 to zero and use equation 9.8 we have

$$\begin{aligned} \delta q = dh - vdp &= 0 \\ vdp &= dh \\ vdp &= C_p dT \end{aligned} \quad (9.12)$$

Dividing one by the other we have

$$\begin{aligned} \frac{-pdv}{vdp} &= \frac{C_v}{C_p} \\ \frac{dp}{p} &= -\gamma \frac{dv}{v} \end{aligned}$$

where $\gamma = C_p/C_v$ is the ratio of specific heats. Integration between states 1 and 2 gives

$$\frac{p_2}{p_1} = \left(\frac{v_2}{v_1} \right)^{-\gamma}$$

As $\rho = 1/v$ it follows

$$\frac{p_2}{p_1} = \left(\frac{v_2}{v_1} \right)^{-\gamma} = \left(\frac{\rho_2}{\rho_1} \right)^{\gamma}$$

Using the gas law $\rho = p/RT$

$$\frac{p_2}{p_1} = \left(\frac{T_2}{T_1} \right)^{\frac{\gamma}{\gamma-1}}$$

Thus, finally we have

$$\frac{p_2}{p_1} = \left(\frac{\rho_2}{\rho_1}\right)^\gamma = \left(\frac{T_2}{T_1}\right)^{\frac{\gamma}{\gamma-1}} \quad (9.13)$$

Further, we have

$$\begin{aligned} \frac{p}{\rho^\gamma} &= \text{constant } C \\ p &= C\rho^\gamma \\ \frac{dp}{d\rho} &= C\gamma\rho^{\gamma-1} = \left(\frac{p}{\rho^\gamma}\right)\gamma\rho^{\gamma-1} = \frac{\gamma p}{\rho} \end{aligned}$$

Relating the speed of sound to $dp/d\rho$ we have

$$\begin{aligned} a^2 &= \frac{dp}{d\rho} \\ a^2 &= \frac{\gamma p}{\rho} = \gamma RT \\ a &= \sqrt{\frac{\gamma p}{\rho}} = \sqrt{\gamma RT} \end{aligned} \quad (9.14)$$

9.1.1 Unsteady Bernoulli's Equation

Recall that the unsteady Bernoulli's equation (or the Kelvin's equation) is given by

$$\phi_t + \frac{1}{2}(V^2 - U_\infty^2) + \int_{p_\infty}^p \frac{dp}{\rho} = 0$$

where ϕ is the velocity potential. Using

$$\begin{aligned} p &= C\rho^\gamma \\ dp &= C\gamma\rho^{\gamma-1}d\rho \\ \frac{dp}{\rho} &= C\gamma\rho^{\gamma-2}d\rho \end{aligned}$$

we obtain

$$\begin{aligned} \int_{p_\infty}^p \frac{dp}{\rho} &= C\gamma \int_{p_\infty}^p \rho^{\gamma-2}d\rho \\ &= \frac{C\gamma}{\gamma-1} (\rho^{\gamma-1} - \rho_\infty^{\gamma-1}) \\ &= \frac{1}{\gamma-1} \left[\frac{\gamma(C\rho^\gamma)}{\rho} - \frac{\gamma(C\rho_\infty^\gamma)}{\rho_\infty} \right] \\ &= \frac{1}{\gamma-1} (a^2 - a_\infty^2) \end{aligned} \quad (9.15)$$

Thus the unsteady Bernoulli's equation takes the following form

$$\begin{aligned} a^2 &= a_\infty^2 - (\gamma-1) \left(\phi_t + \frac{1}{2}V^2 - \frac{1}{2}U_\infty^2 \right) \\ \frac{a^2}{a_\infty^2} &= 1 - \frac{\gamma-1}{a_\infty^2} \left(\phi_t + \frac{1}{2}V^2 - \frac{1}{2}U_\infty^2 \right) \end{aligned} \quad (9.16)$$

From the isentropic relation given in equation 9.13 we have

$$\frac{p}{p_\infty} = \left(\frac{\rho}{\rho_\infty}\right)^\gamma = \left(\frac{\gamma RT}{\gamma RT_\infty}\right)^{\frac{\gamma}{\gamma-1}} = \left(\frac{a^2}{a_\infty^2}\right)^{\frac{\gamma}{\gamma-1}} \quad (9.17)$$

The following two forms follow

$$\frac{p}{p_\infty} = \left[1 - \frac{\gamma-1}{a_\infty^2} \left(\phi_t + \frac{1}{2}V^2 - \frac{1}{2}U_\infty^2\right)\right]^{\frac{\gamma}{\gamma-1}} \quad (9.18)$$

$$\frac{\rho}{\rho_\infty} = \left[1 - \frac{\gamma-1}{a_\infty^2} \left(\phi_t + \frac{1}{2}V^2 - \frac{1}{2}U_\infty^2\right)\right]^{\frac{1}{\gamma-1}} \quad (9.19)$$

For potential flow at rest at infinity $U_\infty = 0$.

9.1.2 Pressure coefficient

From equation 9.18 we have

$$\frac{p-p_\infty}{p_\infty} = \left[1 - \frac{\gamma-1}{a_\infty^2} \left(\phi_t + \frac{1}{2}V^2 - \frac{1}{2}U_\infty^2\right)\right]^{\frac{\gamma}{\gamma-1}} - 1 \quad (9.20)$$

Now

$$\frac{p-p_\infty}{p_\infty} = \frac{p-p_\infty}{\rho_\infty} \frac{\rho_\infty}{p_\infty} = \frac{p-p_\infty}{\rho_\infty} \frac{a_\infty^2}{\gamma}$$

Using equation 9.20 we obtain

$$\frac{p-p_\infty}{\rho_\infty} = \frac{1}{\gamma} \left\{ \left[1 - \frac{\gamma-1}{a_\infty^2} \left(\phi_t + \frac{1}{2}V^2 - \frac{1}{2}U_\infty^2\right)\right]^{\frac{\gamma}{\gamma-1}} - 1 \right\}$$

Thus the pressure coefficient is given by

$$C_p = \frac{p-p_\infty}{\frac{1}{2}\rho_\infty U_\infty^2} = \frac{2}{\gamma M_\infty^2} \left\{ \left[1 - \frac{\gamma-1}{a_\infty^2} \left(\phi_t + \frac{1}{2}V^2 - \frac{1}{2}U_\infty^2\right)\right]^{\frac{\gamma}{\gamma-1}} - 1 \right\} \quad (9.21)$$

9.2 Potential equation in the non-conservation form

Recall that under potential flow assumptions, the non-conservative form of the Euler equations reduce to

$$a^2 \nabla^2 \phi = \phi_{tt} + \frac{\partial}{\partial t} V^2 + V \cdot \nabla \frac{V^2}{2}$$

where $V = \nabla \phi$. Expressed only in terms of the velocity potential, the above equation becomes

$$a^2 \nabla^2 \phi = \phi_{tt} + \frac{\partial}{\partial t} (\nabla \phi)^2 + \nabla \phi \cdot \nabla \left[\frac{1}{2} (\nabla \phi)^2 \right] \quad (9.22)$$

where a^2 is obtained from the Bernoulli's equation. From equation 9.16 we have

$$a^2 = a_\infty^2 - (\gamma-1) \left[\phi_t + \frac{1}{2} (\nabla \phi)^2 \right] \quad (9.23)$$

where U_∞ has been set to zero. Thus the velocity potential ϕ is defined with respect to a fluid at rest at infinity. The above two equations completely define the problem. It can be expanded in any coordinate system as long as the boundary conditions are correctly imposed. For rotor problems the surface boundary condition is easily incorporated using a blade fixed rotating coordinate system. This transformation is described next.

9.2.1 Blade fixed moving frame

Using a blade fixed coordinate influences the equations and boundary conditions. The definition of ϕ remains the same as before, i.e. a velocity potential with respect to fluid at rest. This statement means that the derivative of ϕ along the chosen coordinate directions still yields velocities along those coordinate directions, but still with respect to the fluid at rest. Let (x, y, z) , with unit vectors (i, j, k) be the fixed coordinates. (x', y', z') , with unit vectors (i', j', k') , translates and rotates with respect to the fixed coordinates. Let the translational velocity be V in the (x, y) plane at an angle α with the x axis. The velocities along the x and y axes are then $V \cos \alpha$ and $V \sin \alpha$. Define $V \cos \alpha / \Omega R = \mu$. Then $V \sin \alpha / \Omega R$ becomes equal to $\mu \tan \alpha$. The translational velocity is then $-\mu \Omega R i + 0j + \mu \Omega R \tan \alpha k$. The rotational velocity is $\Omega k = \Omega k'$. The coordinate directions (i', j', k') can be expressed along (i, j, k) at any instant using the following relation

$$\begin{Bmatrix} i \\ j \\ k \end{Bmatrix} = \begin{bmatrix} \sin \psi & \cos \psi & 0 \\ -\cos \psi & \sin \psi & 0 \\ 0 & 0 & 1 \end{bmatrix} \begin{Bmatrix} i' \\ j' \\ k' \end{Bmatrix} = R \begin{Bmatrix} i' \\ j' \\ k' \end{Bmatrix} \quad (9.24)$$

where $\psi = \Omega t$ and $R = R(t)$ is the rotation matrix. Consider a point P on the rotating blade. Let the coordinates of P be given by

$$\begin{Bmatrix} x' \\ y' \\ z' \end{Bmatrix}^T \begin{Bmatrix} i' \\ j' \\ k' \end{Bmatrix}$$

in the rotating frame and

$$\begin{Bmatrix} x \\ y \\ z \end{Bmatrix}^T \begin{Bmatrix} i \\ j \\ k \end{Bmatrix}$$

in the fixed frame. Then we have

$$\begin{aligned} \begin{Bmatrix} x \\ y \\ z \end{Bmatrix}^T \begin{Bmatrix} i \\ j \\ k \end{Bmatrix} &= \begin{Bmatrix} -\mu \Omega R \\ 0 \\ \mu \Omega R \tan \alpha \end{Bmatrix}^T \begin{Bmatrix} i \\ j \\ k \end{Bmatrix} t + \begin{Bmatrix} x' \\ y' \\ z' \end{Bmatrix}^T \begin{Bmatrix} i' \\ j' \\ k' \end{Bmatrix} \\ &= t \begin{Bmatrix} -\mu \Omega R \\ 0 \\ \mu \Omega R \tan \alpha \end{Bmatrix}^T \begin{Bmatrix} i \\ j \\ k \end{Bmatrix} + \begin{Bmatrix} x' \\ y' \\ z' \end{Bmatrix}^T R^T \begin{Bmatrix} i \\ j \\ k \end{Bmatrix} \end{aligned}$$

Transpose both sides to re-write

$$\begin{Bmatrix} i \\ j \\ k \end{Bmatrix}^T \begin{Bmatrix} x \\ y \\ z \end{Bmatrix} = t \begin{Bmatrix} i \\ j \\ k \end{Bmatrix}^T \begin{Bmatrix} -\mu \Omega R \\ 0 \\ \mu \Omega R \tan \alpha \end{Bmatrix} + \begin{Bmatrix} i \\ j \\ k \end{Bmatrix}^T R \begin{Bmatrix} x' \\ y' \\ z' \end{Bmatrix}$$

which can be written as

$$\mathbf{r} = \mu \mathbf{t} + \mathbf{R}(\mathbf{t}) \mathbf{r}'$$

where \mathbf{r} is the position vector in the fixed frame and \mathbf{r}' is the position vector in the rotating frame. The rotating frame coordinates are (x, y, z, t) . The fixed frame coordinates are (x', y', z', t') .

9.2.2 Velocity and acceleration in the moving frame

We saw how the position vector in the rotating frame is related to the position vector in the fixed frame. Let us determine the velocity and acceleration in the rotating frame.

Let O be the origin in the fixed frame. Let O' be the origin of the moving frame. O' translates with respect to O . Consider a point P . $O'P$ is the vector \mathbf{r}' . The rate of change of this vector is the rate at which P changes its position with respect to O' . This is denoted by $\partial\mathbf{r}'/\partial\mathbf{t}$. When measured by an observer in the moving frame this rate can be denoted by $(\partial\mathbf{r}'/\partial\mathbf{t})_{x'y'z'}$. When measured by an observer in the fixed frame this rate can be denoted by $(\partial\mathbf{r}'/\partial\mathbf{t})_{xyz}$. We know

$$\begin{aligned} \left(\frac{\partial\mathbf{r}'}{\partial\mathbf{t}}\right)_{xyz} &= \left(\frac{\partial\mathbf{r}'}{\partial\mathbf{t}}\right)_{x'y'z'} + \Omega \times \mathbf{r}' \\ &= (V_P)_{x'y'z'} + \Omega \times \mathbf{r}' \end{aligned}$$

The velocity of P in the fixed frame is $(V_P)_{xyz}$. Let the translational velocity of O' with respect to O is \dot{R} . Then,

$$\begin{aligned} (V_P)_{xyz} &= \dot{R} + \left(\frac{\partial\mathbf{r}'}{\partial\mathbf{t}}\right)_{xyz} \\ &= \dot{R} + (V_P)_{x'y'z'} + \Omega \times \mathbf{r}' \end{aligned}$$

Note that $\dot{R} = (V'_O)_{xyz}$. Therefore $(V_P)_{xyz} - (V'_O)_{xyz}$ is the rate at which P changes its position with respect to O' as measured by an observer in the fixed frame. This is $(\partial\mathbf{r}'/\partial\mathbf{t})_{xyz}$, hence we get back the first equation. Similarly consider the accelerations.

$$\begin{aligned} (a_P)_{xyz} &= \ddot{R} + \frac{d}{dt} \left[\left(\frac{\partial\mathbf{r}'}{\partial\mathbf{t}}\right)_{xyz} \right]_{xyz} \\ &= \ddot{R} + \frac{d}{dt} \left[\left(\frac{\partial\mathbf{r}'}{\partial\mathbf{t}}\right)_{x'y'z'} + \Omega \times \mathbf{r}' \right]_{xyz} \\ &= \ddot{R} + \frac{d}{dt} \left[\left(\frac{\partial\mathbf{r}'}{\partial\mathbf{t}}\right)_{x'y'z'} \right]_{x'y'z'} + \Omega \times \left(\frac{\partial\mathbf{r}'}{\partial\mathbf{t}}\right)_{x'y'z'} + \frac{d}{dt} (\Omega \times \mathbf{r}')_{x'y'z'} + \Omega \times \Omega \times \mathbf{r}' \\ &= \ddot{R} + (a_P)_{x'y'z'} + 2\Omega \times (V_P)_{x'y'z'} + \dot{\Omega} \times (V_P)_{x'y'z'} + \Omega \times \Omega \times \mathbf{r}' \end{aligned}$$

Thus to summarize we have

$$(V_P)_{xyz} = \dot{R} + (V_P)_{x'y'z'} + \Omega \times \mathbf{r}' \quad (9.25)$$

$$(a_P)_{xyz} = \ddot{R} + (a_P)_{x'y'z'} + 2\Omega \times (V_P)_{x'y'z'} + \dot{\Omega} \times (V_P)_{x'y'z'} + \Omega \times \Omega \times \mathbf{r}' \quad (9.26)$$

For the rotor in steady flight we have

$$\begin{aligned} \dot{R} &= \mu \\ \ddot{R} &= 0 \\ \dot{\Omega} &= 0 \\ (V_P)_{x'y'z'} &= V \\ (a_P)_{x'y'z'} &= V_t \end{aligned} \quad (9.27)$$

Using the above in equations 9.25 and 9.26 it follows

$$\begin{aligned} V &= -\Omega \times \mathbf{r}' - \mu \\ V_t &= -2\Omega \times V - \Omega \times \Omega \times \mathbf{r}' \end{aligned} \quad (9.28)$$

We have for the rotor

$$\begin{aligned}\Omega &= \Omega k' \\ \mathbf{r}' &= \mathbf{x}'\mathbf{i}' + \mathbf{y}'\mathbf{j}' + \mathbf{z}'\mathbf{k}' \\ \mu &= (-\mu\Omega\mathbf{R})\mathbf{i} + \mathbf{0}\mathbf{j} + (\mu\Omega\mathbf{R} \tan \alpha)\mathbf{k}\end{aligned}$$

Put the above expressions in equations 9.28 and use the transformation given in equation 9.24 to obtain the following.

$$\begin{aligned}V &= \begin{pmatrix} \Omega y' + \mu\Omega R \sin \psi \\ -\Omega x' + \mu\Omega R \cos \psi \\ -\mu\Omega R \tan \alpha \end{pmatrix}^T \begin{pmatrix} i' \\ j' \\ k' \end{pmatrix} = \begin{pmatrix} V_1 \\ V_2 \\ V_3 \end{pmatrix}^T \begin{pmatrix} i' \\ j' \\ k' \end{pmatrix} \\ V_t &= \begin{pmatrix} \Omega^2 x' + 2\Omega V_2 \\ \Omega^2 y' - 2\Omega V_1 \\ 0 \end{pmatrix}^T \begin{pmatrix} i' \\ j' \\ k' \end{pmatrix}\end{aligned}\tag{9.29}$$

Henceforth all analysis will be done in the moving frame using the expressions given in equations (9.29). The dashes (') can be dropped for convenience.

9.2.3 Derivatives in the moving frame

We now need the derivatives - one spatial derivative (the gradient), and two time derivatives (velocity and acceleration).

The gradient is frame invariant.

$$\nabla = \nabla'$$

This can be shown as follows.

$$\begin{aligned}\nabla' &= \frac{\partial}{\partial x'}i' + \frac{\partial}{\partial y'}j' + \frac{\partial}{\partial z'}k' \\ &= \begin{pmatrix} i' \\ j' \\ k' \end{pmatrix}^T \begin{pmatrix} \frac{\partial}{\partial x} \frac{\partial x}{\partial x'} + \frac{\partial}{\partial y} \frac{\partial y}{\partial x'} + \frac{\partial}{\partial z} \frac{\partial z}{\partial x'} \\ \frac{\partial}{\partial x} \frac{\partial x}{\partial y'} + \frac{\partial}{\partial y} \frac{\partial y}{\partial y'} + \frac{\partial}{\partial z} \frac{\partial z}{\partial y'} \\ \frac{\partial}{\partial x} \frac{\partial x}{\partial z'} + \frac{\partial}{\partial y} \frac{\partial y}{\partial z'} + \frac{\partial}{\partial z} \frac{\partial z}{\partial z'} \end{pmatrix} \\ &= \begin{pmatrix} i \\ j \\ k \end{pmatrix}^T R \begin{pmatrix} \frac{\partial}{\partial x} \frac{\partial x}{\partial x'} + \frac{\partial}{\partial y} \frac{\partial y}{\partial x'} + \frac{\partial}{\partial z} \frac{\partial z}{\partial x'} \\ \frac{\partial}{\partial x} \frac{\partial x}{\partial y'} + \frac{\partial}{\partial y} \frac{\partial y}{\partial y'} + \frac{\partial}{\partial z} \frac{\partial z}{\partial y'} \\ \frac{\partial}{\partial x} \frac{\partial x}{\partial z'} + \frac{\partial}{\partial y} \frac{\partial y}{\partial z'} + \frac{\partial}{\partial z} \frac{\partial z}{\partial z'} \end{pmatrix} \\ &= \begin{pmatrix} i \\ j \\ k \end{pmatrix}^T \begin{bmatrix} \sin \psi & \cos \psi & 0 \\ -\cos \psi & \sin \psi & 0 \\ 0 & 0 & 1 \end{bmatrix} \begin{pmatrix} \sin \psi \frac{\partial}{\partial x} - \cos \psi \frac{\partial}{\partial y} \\ \sin \psi \frac{\partial}{\partial y} + \cos \psi \frac{\partial}{\partial x} \\ \frac{\partial}{\partial z} \end{pmatrix} \\ &= \frac{\partial}{\partial x}i + \frac{\partial}{\partial y}j + \frac{\partial}{\partial z}k \\ &= \nabla\end{aligned}$$

Now consider the time derivative.

$$\begin{aligned}\frac{\partial}{\partial t} &= \frac{\partial}{\partial t'} \frac{\partial t'}{\partial t} + \frac{\partial}{\partial x'} \frac{\partial x'}{\partial t} + \frac{\partial}{\partial y'} \frac{\partial y'}{\partial t} + \frac{\partial}{\partial z'} \frac{\partial z'}{\partial t} \\ &= \frac{\partial}{\partial t'} + V_1 \frac{\partial}{\partial x'} + v_2 \frac{\partial}{\partial y'} + V_3 \frac{\partial}{\partial z'} \\ &= \frac{\partial}{\partial t'} + \mathbf{V} \cdot \nabla'\end{aligned}$$

where V is the velocity in the moving frame. Thus

$$\phi_t = \phi_{t'} + V \cdot \nabla' \phi \quad (9.30)$$

The second derivative with respect to time can be taken in a similar manner

$$\begin{aligned} \phi_{tt} &= \frac{\partial \phi_t}{\partial t} \\ &= \frac{\partial}{\partial t'} (\phi_t) + V \cdot \nabla' \phi_t \\ &= \frac{\partial}{\partial t'} (\phi_{t'} + V \cdot \nabla' \phi) + V \cdot \nabla' (\phi_{t'} + V \cdot \nabla' \phi) \\ &= \phi_{t't'} + V \cdot \nabla' \phi_{t'} + \nabla' \phi \cdot V_{t'} + V \cdot \nabla' \phi_{t'} + V \cdot \nabla' (V \cdot \nabla' \phi) \end{aligned}$$

Thus the second derivative of ϕ with respect to time is given by

$$\phi_{tt} = \phi_{t't'} + 2V \cdot \nabla' \phi_{t'} + \nabla' \phi \cdot V_{t'} + (V \cdot \nabla') (V \cdot \nabla' \phi) \quad (9.31)$$

9.2.4 Full Potential Equations

Use equations 9.30 and 9.31 to reduce equations 9.22 and 9.23 to the moving frame. Note that

$$\begin{aligned} \frac{\partial}{\partial t} (\nabla \phi)^2 &= \frac{\partial}{\partial t'} (\nabla \phi)^2 + V \cdot \nabla' (\nabla \phi)^2 \\ &= 2\nabla' \phi \cdot \nabla \phi_{t'} + V \cdot \nabla' (\nabla \phi)^2 \end{aligned}$$

After substitution, the dashes ($'$) can be removed. The potential and the Bernoulli equations then take the following form

$$\begin{aligned} a^2 \nabla^2 \phi &= \phi_{tt} + 2V \cdot \nabla \phi_t + \nabla \phi \cdot V_t + (V \cdot \nabla) (V \cdot \nabla \phi) + \\ &\quad 2\nabla \phi \cdot \nabla \phi_t + V \cdot \nabla (\nabla \phi)^2 + \nabla \phi \cdot \left[\frac{1}{2} (\nabla \phi)^2 \right] \\ a^2 &= a_\infty^2 - (\gamma - 1) \left[\phi_t + V \cdot \nabla \phi + \frac{1}{2} (\nabla \phi)^2 \right] \end{aligned} \quad (9.32)$$

Velocity V and acceleration V_t are given by equations 9.29. Solve for ϕ and obtain the fluid velocities ϕ_x , ϕ_y and ϕ_z directly in the moving frame.

For physical insight, the above equations can be expanded using the following.

$$\begin{aligned} V \cdot \nabla \phi &= V_1 \phi_x + V_2 \phi_y + V_3 \phi_z \\ \frac{1}{2} (\nabla \phi)^2 &= \frac{1}{2} (\phi_x^2 + \phi_y^2 + \phi_z^2) \end{aligned}$$

The Bernoulli equation then becomes

$$a^2 = a_\infty^2 - (\gamma - 1) \left[\phi_t + V_1 \phi_x + V_2 \phi_y + V_3 \phi_z + \frac{1}{2} (\phi_x^2 + \phi_y^2 + \phi_z^2) \right] \quad (9.33)$$

To expand the potential equation use the following

$$\begin{aligned}
2V \cdot \nabla \phi_t &= 2V_1 \phi_{xt} + 2V_2 \phi_{yt} + 2V_3 \phi_{zt} \\
\nabla (V \cdot \nabla \phi) &= \frac{\partial}{\partial x} (V_1 \phi_x + V_2 \phi_y + V_3 \phi_z) i + \frac{\partial}{\partial y} (V_1 \phi_x + V_2 \phi_y + V_3 \phi_z) j \\
&\quad + \frac{\partial}{\partial z} (V_1 \phi_x + V_2 \phi_y + V_3 \phi_z) k \\
&= (V_1 \phi_{xx} + V_2 \phi_{yx} - \Omega \phi_y + V_3 \phi_{zx}) i \\
&\quad + (V_1 \phi_{xy} + \Omega \phi_x + V_2 \phi_{yy} + V_3 \phi_{zy}) j \\
&\quad + (V_1 \phi_{xz} + V_2 \phi_{yz} + V_3 \phi_{zz}) k \\
(V \cdot \nabla) (V \cdot \nabla \phi) &= V_1^2 \phi_{xx} + V_2^2 \phi_{yy} + V_3^2 \phi_{zz} \\
&\quad + 2V_1 V_2 \phi_{yx} + 2V_2 V_3 \phi_{yz} + 2V_3 V_1 \phi_{xz} - V_1 \Omega \phi_y + V_2 \Omega \phi_x \\
\nabla \phi \cdot V_t &= (\Omega^2 x + 2\Omega V_2) \phi_x + (\Omega^2 y - 2\Omega V_1) \phi_y \\
2\nabla \phi \cdot \nabla \phi_t &= 2\phi_x \phi_{xt} + 2\phi_y \phi_{yt} + 2\phi_z \phi_{zt} \\
(\nabla \phi)^2 &= \phi_x^2 + \phi_y^2 + \phi_z^2 \\
V \cdot (\nabla \phi)^2 &= (2\phi_x \phi_{xx} + 2\phi_y \phi_{yx} + 2\phi_z \phi_{zx}) V_1 \\
&\quad (2\phi_x \phi_{xy} + 2\phi_y \phi_{yy} + 2\phi_z \phi_{zy}) V_2 \\
&\quad (2\phi_x \phi_{xz} + 2\phi_y \phi_{yz} + 2\phi_z \phi_{zz}) V_3 \\
\nabla \phi \cdot \nabla \left[\frac{1}{2} (\nabla \phi)^2 \right] &= (\phi_x \phi_{xx} + \phi_y \phi_{yx} + \phi_z \phi_{zx}) \phi_x \\
&\quad (\phi_x \phi_{xy} + \phi_y \phi_{yy} + \phi_z \phi_{zy}) \phi_y \\
&\quad (\phi_x \phi_{xz} + \phi_y \phi_{yz} + \phi_z \phi_{zz}) \phi_z
\end{aligned}$$

Now define the total velocities as

$$\begin{aligned}
q_1 &= \phi_x + V_1 \\
q_2 &= \phi_y + V_2 \\
q_3 &= \phi_z + V_3
\end{aligned}$$

Then the potential equation takes the following form

$$\begin{aligned}
a^2 (\phi_{xx} + \phi_{yy} + \phi_{zz}) &= \phi_{tt} + 2q_1 \phi_{xt} + 2q_2 \phi_{yt} + 2q_3 \phi_{zt} \\
&\quad q_1^2 \phi_{xx} + q_2^2 \phi_{yy} + q_3^2 \phi_{zz} + 2q_1 q_2 \phi_{xy} + 2q_2 q_3 \phi_{yz} + 2q_3 q_1 \phi_{zx} \\
&\quad \phi_x (\Omega^2 x + 2\Omega V_2) + \phi_y (\Omega^2 y - 2\Omega V_1)
\end{aligned} \tag{9.34}$$

In Einstein notation equations 9.33 and 9.34 are also expressible as

$$\begin{aligned}
a^2 \nabla^2 \phi &= \phi_{tt} + 2q_i \phi_{tx_i} + \dot{V}_i \phi_{x_i} + q_i q_j \phi_{x_i x_j} \\
a^2 &= a_\infty^2 - (\gamma - 1) \left[\phi_t + V_j \phi_{x_j} + \frac{1}{2} \phi_{x_j} \phi_{x_j} \right]
\end{aligned} \tag{9.35}$$

where the pressure is related to velocity of sound as

$$\frac{p}{p_\infty} = \left(\frac{a^2}{a_\infty^2} \right)^{\frac{\gamma}{\gamma-1}}$$

9.2.5 Boundary conditions

The near field boundary conditions are that the flow is tangential to the blade. Let the blade surface be given by

$$F(x, y, z, t) = 0 \quad (9.36)$$

then the flow tangency condition is that the substantial derivative $DF/Dt = 0$.

$$\frac{\partial F}{\partial t} + q \cdot \nabla F = 0 \quad (9.37)$$

where q is the total velocity as given in the previous section. The blade surface description can be recast as

$$F(x, y, z, t) = z - g(x, y, t) \quad (9.38)$$

Then from 9.37

$$\begin{aligned} -g_t + q \cdot (-g_x i - g_y j + k) &= 0 \\ -g_t + (-q_x g_x - q_y g_y + q_z) &= 0 \end{aligned} \quad (9.39)$$

which reduces to

$$q_z = g_t + q_x g_x + q_y g_y \quad (9.40)$$

on the surface $z = g(x, y, t)$. Expanding the q 's and ignoring the second order terms, the linearized boundary conditions are given by

$$\begin{aligned} \phi_z + V_3 &= g_t + (V_1 + \phi_x) g_x + (V_2 + \phi_y) g_y \\ \phi_z &= g_t + V_1 g_x + V_2 g_y - V_3 \end{aligned} \quad (9.41)$$

The wake boundary condition is implemented in the following manner. The wake is a vortex surface which allows a tangential velocity jump but not a normal velocity jump. Similarly it allows a tangential pressure jump but not a normal pressure jump. The normal velocity jump is Δv_n where Δ signifies the difference between the upper and lower surfaces v_u and v_l . Thus

$$v_u - v_l = \Delta v_n = 0$$

$$\Delta p = 0$$

Consider a two dimensional airfoil wake. It follows from Kelvin's equation

$$\left(\phi_t + \frac{1}{2} v^2 \right)_u = \left(\phi_t + \frac{1}{2} v^2 \right)_l$$

or

$$\Delta \phi_t + \frac{1}{2} (v_u - v_l)(v_u + v_l) = 0$$

or

$$\Delta \phi_t + \frac{\Delta \phi}{\Delta x} v_w = 0$$

where $(v_u + v_l)/2$ has been defined as the wake velocity. The above expression can be written in general for a 3-dimensional flow

$$\Delta \phi_t + v_w \cdot \nabla (\Delta \phi) = 0$$

$$\frac{D\Delta\phi}{Dt} = 0$$

This states that the potential difference $\Delta\phi$ is constant for a point on the wake surface that is convected with the wake velocity. The wake velocity is taken as the mean of the upper and lower velocities at each point on the vortex sheet. The wake is treated as a planar surface without accounting for its curvature. The tip vortices from previous blades can be incorporated into the computational domain as additional potential jump.

The far field boundary conditions are

$$\phi_t = 0$$

$$\nabla\phi = 0$$

They can be imposed as a Neumann condition. The time derivatives of the velocity potential along the characteristics of the flow equation vanish for each spanwise plane.

$$\phi_t + v_a \cdot \nabla\phi = 0$$

9.2.6 Small disturbance equations for subsonic and transonic flows

The small disturbance assumption helps to understand the essential character of the flow. In earlier days they were attractive due to their reduced computational requirements. The unsteady compressible potential flow equations for the rotor are given by 9.35. The Laplace operator on the left hand side of the first equation is

$$\nabla^2\phi = \phi_{x_i}\phi_{x_j}\delta_{ij} \quad (9.42)$$

Equation 9.35 has no assumptions for the disturbance. The following scaling parameters are used to make small disturbance assumptions under subsonic and transonic flow conditions. The assumptions are made so that the essential features of the equation under each condition are maintained.

$$\phi = \Omega Rc \delta$$

$$g(x, y) = c \tau$$

Subsonic

For subsonic flow we make the following assumption

$$a^2 \approx a_\infty^2 \quad (9.43)$$

This is because

$$V_i \ll a_\infty \quad (9.44)$$

Recall that the total velocity at a point in the flow field q_i is the sum of V_i and ϕ_x , where i are the coordinate directions, V_i is the local free stream corresponding to the translation and rotation of the rotor in these directions, and ϕ_i is the potential of the additional velocity induced by the rotor blades. The later is assumed to be small compared to the free stream under subsonic flow conditions. The second order terms in ϕ_i are neglected.

$$\begin{aligned} q_i q_j &= V_i V_j + \phi_{x_i} V_j + \phi_{x_j} V_i + \phi_{x_i} \phi_{x_j} \\ &\approx V_i V_j + \phi_{x_i} V_j + \phi_{x_j} V_i \end{aligned} \quad (9.45)$$

Use assumptions 9.43 and 9.45, and the notation 9.42 to reduce the potential equation 9.35 to the following form. The potential equation reduces to

$$(a_\infty^2 \delta_{ij} - V_i V_j) \phi_{x_i} \phi_{x_j} = \phi_{tt} + 2V_i \phi_{tx_i} + \dot{V}_i \phi_{x_i} \quad (9.46)$$

Expanding in cartesian coordinates

$$\begin{aligned} a_\infty^2 (\phi_{xx} + \phi_{yy} + \phi_{zz}) - V_1^2 \phi_{xx} - 2V_1 V_2 \phi_{xy} - 2V_1 V_3 \phi_{xz} - V_2^2 \phi_{yy} - V_3^2 \phi_{zz} - 2V_2 V_3 \phi_{xz} \\ = \phi_{tt} + 2V_1 \phi_{xt} + 2V_2 \phi_{yt} + 2V_3 \phi_{zt} + (\Omega^2 x + 2\Omega V_2) \phi_x + (\Omega^2 y - 2\Omega V_1) \phi_y \end{aligned} \quad (9.47)$$

The equation can be further simplified by making the following assumptions. For a small tip path plane tilt,

$$V_3 \approx 0 \quad (9.48)$$

. For subsonic flow we have

$$(\Omega^2 x + 2\Omega V_2) \phi_x + (\Omega^2 y - 2\Omega V_1) \phi_y \ll a_\infty^2 \phi_{xx} \quad (9.49)$$

With these assumptions equation 9.47 becomes

$$\begin{aligned} (a_\infty^2 - V_1^2) \phi_{xx} - 2V_1 V_2 \phi_{xy} + (a_\infty^2 - V_2^2) \phi_{yy} + a_\infty^2 \phi_{zz} \\ = \phi_{tt} + 2V_1 \phi_{xt} + 2V_2 \phi_{yt} \end{aligned} \quad (9.50)$$

For quasi-steady assumption, e.g. for small 1/rev flapping, the right hand side of equation 9.50 is set to zero.

$$(a_\infty^2 - V_1^2) \phi_{xx} - 2V_1 V_2 \phi_{xy} + (a_\infty^2 - V_2^2) \phi_{yy} + a_\infty^2 \phi_{zz} = 0 \quad (9.51)$$

Note that even though the time derivatives of the perturbation potential have been set to zero, the effect of rotation is still included via the $\sin \psi$ and $\cos \psi$ terms within V_1 and V_2 . Similarly the boundary conditions also retain a time dependance by being a function of blade azimuth. Hence the assumption is called quasi-steady.

Transonic flow

Here the assumption $a^2 \approx a_\infty^2$ as given by equation 9.43 is no longer valid. In the transonic range V_1 is of the same order as a_∞^2 . However the square of the potential is still negligible with respect to the square of the speed of sound.

$$\phi^2 \ll a^2 \quad (9.52)$$

With this assumption, the Bernoulli's equation in 9.35 becomes

$$a^2 = a_\infty^2 - (\gamma - 1) [\phi_t + V_j \phi_{x_j}]$$

Keep the assumption given by equation 9.48.

$$V_3 \approx 0$$

With the above two assumptions the potential equation 9.35 becomes

$$\begin{aligned} (\phi_{xx} + \phi_{yy} + \phi_{zz}) [a_\infty^2 - (\gamma - 1) (\phi_t + V_1 \phi_x + V_2 \phi_y)] = \\ \phi_{tt} + 2V_1 \phi_{xt} + 2V_2 \phi_{yt} + \phi_{xx} (V_1^2 + 2\phi_x V_1) + \phi_{yy} (V_2^2 + 2\phi_y V_2) \\ 2\phi_{xy} (V_1 \phi_y + V_2 \phi_x + V_1 V_2) + 2\phi_{yz} V_2 \phi_z + 2\phi_{zx} V_1 \phi_z \\ \phi_x (\Omega^2 x + 2\Omega V_2) + \phi_y (\Omega^2 y - 2\Omega V_1) \end{aligned} \quad (9.53)$$

For 3D flows ϕ_{xx} and ϕ_{yy} are of the same order of magnitude. The chordwise flow gradient is of the same order as the spanwise flow gradient. The following terms can be neglected.

$$\begin{aligned}\phi_{xz}\phi_z &\approx 0 \\ \phi_{yz}\phi_z &\approx 0\end{aligned}\tag{9.54}$$

Then equation 9.53 takes the following form.

$$\begin{aligned}\phi_{xx} [a_\infty^2 - V_1^2 - (\gamma + 1)V_1\phi_x - (\gamma - 1)V_2\phi_y] \\ \phi_{yy} [a_\infty^2 - V_2^2 - (\gamma - 1)V_1\phi_x - (\gamma + 1)V_2\phi_y] \\ \phi_{zz} [a_\infty^2 - (\gamma - 1)V_1\phi_x - (\gamma - 1)V_2\phi_y] \\ - 2\phi_{xy} (V_1V_2 + V_1\phi_y + V_2\phi_x) \\ = 2V_1\phi_{xt} + 2V_2\phi_{yt} + \phi_x (\Omega^2x + 2\Omega V_2) + \phi_y (\Omega^2y - 2\Omega V_1)\end{aligned}\tag{9.55}$$

Equation 9.55 is the non-conservative transonic small perturbation equation.

9.2.7 Literature

Non-conservative small disturbance

1. Caradonna, F. X. and Isom, M. P., "Subsonic and Transonic Potential Flow Over Helicopter Rotor Blades," AIAA Journal, Vol. 10, Dec. 1972, pp. 1606-1612. Steady-state formulation.
2. Caradonna, F. X. and Isom, M. P., "Numerical Calculation of Unsteady Transonic Potential Flow Over Helicopter Rotor Blades," AIAA Journal, Vol. 14, April 1976, pp. 482-488. Unsteady formulation. Forward flight. Spanwise freestream velocity component due to changing blade position was assumed to be small and was incompletely modeled.
3. Grant, J. "Calculation of the Supercritical Flow Over the Tip Region of Non-Lifting Rotor Blade at Arbitrary Azimuth," Royal Aircraft Establishment Tech. Rept. 77180, Dec. 1977. Included all free stream terms. However, quasi-steady formation.

Non-conservative full potential

1. Jameson, A. and Caughey, D. A., "Numerical Calculation of Transonic Flow Past a Swept Wing," Courant Institute of Mathematical Sciences, New York University, New York, C00-3077-140, June 1977. Fixed wing code FLO22. Non-conservative with respect to mass flux.
2. Arieli, R. and Tauber, M. E., "Computation of Transonic Flow About Helicopter Rotor Blades," AIAA Journal, Vol. 24, No. 5, May 1986, pp. 722-727. Quasi-steady. Exact boundary conditions, not small disturbance.
3. Chang, I-Chung and Tung, C., "Computation of Subsonic and Transonic Flow about Lifting Rotor Blades," AIAA Paper 79-1667, Aug. 1979.

9.3 Potential equation in conservation form

The potential equation in conservation form is the continuity equation in conservation form.

9.3.1 Full potential equation

The full potential equation is obtained by replacing the velocities in the continuity equation with derivatives of the potential function.

$$\frac{\partial \rho}{\partial t} + \frac{\partial}{\partial x} (\rho \Phi_x) + \frac{\partial}{\partial y} (\rho \Phi_y) + \frac{\partial}{\partial z} (\rho \Phi_z) = 0 \quad (9.56)$$

where Φ is the potential of the total velocity. The density is obtained from the unsteady Bernoulli's equation 9.19. The velocity potential is defined with respect to fluid at rest, hence U_∞ is set to zero. $V^2 = (\nabla \phi)^2 = \phi_x^2 + \phi_y^2 + \phi_z^2$.

$$\frac{\rho}{\rho_\infty} = \left[1 - \frac{\gamma - 1}{a_\infty^2} \left(\Phi_t + \frac{1}{2} \Phi_x^2 + \frac{1}{2} \Phi_y^2 + \frac{1}{2} \Phi_z^2 \right) \right]^{\frac{1}{\gamma - 1}} \quad (9.57)$$

The equations can be non-dimensionalized as follows :

$$\Phi = \bar{\Phi} a_\infty c$$

where c is a characteristic length, e.g. blade mean chord. Similarly Φ_y and Φ_z .

$$x = \bar{x} c \quad y = \bar{y} c \quad z = \bar{z} c$$

$$t = \bar{t} (c/a_\infty)$$

Then

$$\frac{\partial \Phi}{\partial x} = \frac{\partial \bar{\Phi} a_\infty c}{\partial \bar{x} c} = a_\infty \frac{\partial \bar{\Phi}}{\partial \bar{x}}$$

$$\frac{\partial \Phi}{\partial t} = \frac{\partial \bar{\Phi} a_\infty c}{\partial \bar{t} (c/a_\infty)} = a_\infty^2 \frac{\partial \bar{\Phi}}{\partial \bar{t}}$$

$$\rho = \bar{\rho} \rho_\infty$$

Thus the equations reduce to the following non-dimensional form

$$\begin{aligned} \frac{\partial \rho}{\partial \bar{t}} + \frac{\partial}{\partial \bar{x}} (\rho \Phi_x) + \frac{\partial}{\partial \bar{y}} (\rho \Phi_y) + \frac{\partial}{\partial \bar{z}} (\rho \Phi_z) &= 0 \\ \rho &= \left[1 - \frac{\gamma - 1}{2} (2\Phi_t + \Phi_x^2 + \Phi_y^2 + \Phi_z^2) \right]^{\frac{1}{\gamma - 1}} \end{aligned} \quad (9.58)$$

where the bars ($\bar{\quad}$) have been dropped for convenience.

9.3.2 Generalized coordinate transformation

A generalized transformation can be used to map an arbitrary body surface like a rotor blade to a rectangular coordinate surface in a transformed plane. Boundary conditions on the body can be accurately treated. The grids can be clustered as desired. Transformation to rectangular coordinates is needed only for a finite difference discretization of the governing equations. The finite difference discretization is usually used in conjunction with structured grids. The transformation is given by

$$\begin{aligned} \xi &= \xi(x, y, z, t) \\ \eta &= \eta(x, y, z, t) \\ \zeta &= \zeta(x, y, z, t) \\ \tau &= t \end{aligned} \quad (9.59)$$

The Bernoulli's equation transforms as follows.

$$\begin{aligned}\Phi_t &= \Phi_\tau + \Phi_\xi \xi_t + \Phi_\eta \eta_t + \Phi_\zeta \zeta_t \\ \Phi_x &= \Phi_\xi \xi_x + \Phi_\eta \eta_x + \Phi_\zeta \zeta_x \\ \Phi_y &= \Phi_\xi \xi_y + \Phi_\eta \eta_y + \Phi_\zeta \zeta_y \\ \Phi_z &= \Phi_\xi \xi_z + \Phi_\eta \eta_z + \Phi_\zeta \zeta_z\end{aligned}$$

It follows

$$\Phi_x^2 + \Phi_y^2 + \Phi_z^2 = A_1 \Phi_\xi^2 + A_2 \Phi_\eta^2 + A_3 \Phi_\zeta^2 + 2A_4 \Phi_\xi \phi_\eta + 2A_5 \Phi_\eta \Phi_\zeta + 2A_6 \Phi_\zeta \phi_\xi$$

where

$$\begin{aligned}A_1 &= \xi_x^2 + \xi_y^2 + \xi_z^2 \\ A_2 &= \eta_x^2 + \eta_y^2 + \eta_z^2 \\ A_3 &= \zeta_x^2 + \zeta_y^2 + \zeta_z^2 \\ A_4 &= \xi_x \eta_x + \xi_y \eta_y + \xi_z \eta_z \\ A_5 &= \eta_x \zeta_x + \eta_y \zeta_y + \eta_z \zeta_z \\ A_6 &= \zeta_x \xi_x + \zeta_y \xi_y + \zeta_z \xi_z\end{aligned}$$

Therefore

$$\begin{aligned}2\Phi_t + \Phi_x^2 + \Phi_y^2 + \Phi_z^2 &= 2\Phi_\tau + 2\Phi_\xi \xi_t + 2\Phi_\eta \eta_t + 2\Phi_\zeta \zeta_t + A_1 \Phi_\xi^2 + A_2 \Phi_\eta^2 + A_3 \Phi_\zeta^2 \\ &\quad + 2A_4 \Phi_\xi \phi_\eta + 2A_5 \Phi_\eta \Phi_\zeta + 2A_6 \Phi_\zeta \phi_\xi \\ &= 2\Phi_\tau + \Phi_\xi (2\xi_t + A_1 \Phi_\xi + 2A_4 \Phi_\eta + 2A_6 \Phi_\zeta) \\ &\quad + \Phi_\eta (2\eta_t + A_2 \Phi_\eta + 2A_5 \Phi_\zeta) \\ &\quad + \Phi_\zeta (2\zeta_t + A_3 \Phi_\zeta) \\ &= 2\Phi_\tau + \Phi_\xi (2\xi_t + A_1 \Phi_\xi + A_4 \Phi_\eta + A_6 \Phi_\zeta) \\ &\quad + \Phi_\eta (2\eta_t + A_4 \Phi_\xi + A_2 \Phi_\eta + A_5 \Phi_\zeta) \\ &\quad + \Phi_\zeta (2\zeta_t + A_6 \Phi_\xi + A_5 \Phi_\eta + A_3 \Phi_\zeta) \\ &= \Phi_\xi (\xi_t + U) + \Phi_\eta (\eta_t + V) + \Phi_\zeta (\zeta_t + W)\end{aligned}$$

where

$$\begin{aligned}U &= \xi_t + A_1 \Phi_\xi + A_4 \Phi_\eta + A_6 \Phi_\zeta \\ V &= \eta_t + A_4 \Phi_\xi + A_2 \Phi_\eta + A_5 \Phi_\zeta \\ W &= \zeta_t + A_6 \Phi_\xi + A_5 \Phi_\eta + A_3 \Phi_\zeta\end{aligned}$$

The Bernoulli's equation then becomes

$$\rho = \left\{ 1 - \frac{\gamma - 1}{2} [2\Phi_\tau + (\xi_t + U) \Phi_\xi + (\eta_t + V) \Phi_\eta + (\zeta_t + W) \Phi_\zeta] \right\}^{\frac{1}{\gamma - 1}} \quad (9.60)$$

U , V , and W defined as above are called the contravariant velocities along the ξ , η , and ζ coordinate directions. Now consider the transformation of the potential equation 9.56. The transformed potential equation is given as follows.

$$\frac{\partial}{\partial \tau} \left(\frac{\rho}{J} \right) + \frac{\partial}{\partial \xi} \left(\frac{\rho U}{J} \right) + \frac{\partial}{\partial \eta} \left(\frac{\rho V}{J} \right) + \frac{\partial}{\partial \zeta} \left(\frac{\rho W}{J} \right) = 0 \quad (9.61)$$

where J is the jacobian of the transformation.

$$J = \begin{bmatrix} \xi_x & \eta_x & \zeta_x \\ \xi_y & \eta_y & \zeta_y \\ \xi_z & \eta_z & \zeta_z \end{bmatrix}$$

The details of the derivation will be described later.

9.3.3 Literature

Conservative small disturbance

1. Caradonna, F. X. and Phillippe, J. J., "The Flow Over a Helicopter Blade Tip in the Transonic Regime," *Vertica*, Vol. 2, April 1978, pp. 43-60.
2. Phillippe, J. J. and Chattot, J. J., "Experimental and Theoretical Studies on Helicopter Blade Tips at ONERA," Sixth European Rotorcraft Forum, Bristol, England, Paper 46, Sept. 1980, pp. 16-19.

Conservative Full Potential

1. Bridgeman, J. O., Steger, J. L., and Caradonna, F. X., "A Conservative Finite-Difference Algorithm for the Unsteady Transonic Potential Equation in Generalized Coordinates," AIAA Paper 82-1388, Aug. 1982. Fixed wing.
2. Sankar, L. N. and Prichard, D., "Solution of Transonic Flow Past Rotor Blades Using the Conservative Full Potential Equation," AIAA Paper 85-5012, Oct. 1985.
3. Strawn, R. C., and Caradonna, F. X., "Conservative Full-Potential Model for Unsteady Transonic Rotor Flows," AIAA Journal, Vol. 25, No.2, Feb. 1987.

9.4 Euler and Navier-Stokes equations

The governing equations are again transformed into a body-fitted coordinate system. This transformation is necessary only for structured grids. It was given by equation 9.59 where the coordinates x, y, z, t were transformed to $\xi, \eta, \zeta,$ and τ . The meaning of body-fitted coordinates is that the body surface is completely described by constant ξ, η and ζ lines. Thus the body surface can be simply and accurately treated. In addition, as previously mentioned the transformation can be used to cluster grids in regions of the flow with high gradients. It is important to understand certain features of this transformation.

9.4.1 Review of Curvilinear coordinates

Consider a vector \vec{r} in a three dimensional space. It can be represented in different ways. One way is the cartesian representation that we are familiar with. Here, three rectilinear coordinate directions are chosen which are mutually orthogonal. The vector is projected along the coordinate directions. The projected lengths are then multiplied with tangent vectors along the directions to complete the representation of the vector. The tangent vectors are called base vectors. For example, if the coordinate directions are $(x_1x_2x_3)$ then the tangent vector, or base vector, along x_1 would be

$$\lim_{\Delta x_1 \rightarrow 0} \frac{\vec{r}(x_1 + \Delta x_1) - \vec{r}(x_1)}{\Delta x_1} = \frac{\Delta x_1 i}{\Delta x_1} = i$$

where i is an unit vector along x_1 . Similarly the tangent vectors along x_2 and x_3 may be denoted by j and k . A differential increment of the position vector, $d\vec{r}$, can be represented by adding the differential increments along the coordinate directions multiplied by tangent vectors along those

directions.

$$\begin{aligned}\vec{dr} &= \begin{Bmatrix} dx_1 \\ dx_2 \\ dx_3 \end{Bmatrix}^T \begin{Bmatrix} i \\ j \\ k \end{Bmatrix} \\ &= \begin{Bmatrix} 1 \\ 0 \\ 0 \end{Bmatrix}^T \begin{Bmatrix} i \\ j \\ k \end{Bmatrix} dx_1 + \begin{Bmatrix} 0 \\ 1 \\ 0 \end{Bmatrix}^T \begin{Bmatrix} i \\ j \\ k \end{Bmatrix} dx_2 + \begin{Bmatrix} 0 \\ 0 \\ 1 \end{Bmatrix}^T \begin{Bmatrix} i \\ j \\ k \end{Bmatrix} dx_3\end{aligned}$$

or in vector notation

$$\vec{dr} = \begin{Bmatrix} dx_1 \\ dx_2 \\ dx_3 \end{Bmatrix} = dx_1 \begin{Bmatrix} 1 \\ 0 \\ 0 \end{Bmatrix} + dx_2 \begin{Bmatrix} 0 \\ 1 \\ 0 \end{Bmatrix} + dx_3 \begin{Bmatrix} 0 \\ 0 \\ 1 \end{Bmatrix} \quad (9.62)$$

Instead of $(x_1x_2x_3)$ the vector \underline{r} can also be represented using a set of generalized curvilinear coordinate directions $(\xi_1\xi_2\xi_3)$. The base vectors can be chosen as before, i.e., along the tangent directions. For example, the base vector along ξ_1 , would be the tangent vector given by

$$\lim_{\Delta\xi_1 \rightarrow 0} \frac{\vec{r}(\xi_1 + \Delta\xi_1) - \vec{r}(\xi_1)}{\Delta\xi_1} = \frac{\Delta\xi_1 \underline{a}_1}{\Delta\xi_1} = \underline{a}_1$$

where \underline{a}_1 is now a unit vector tangent to ξ_1 . Similarly in the other directions the base vectors would be \underline{a}_2 and \underline{a}_3 . Thus in a curvilinear coordinate system the differential increment expression 9.62 takes the following form

$$\underline{dr} = \underline{a}_1 d\xi_1 + \underline{a}_2 d\xi_2 + \underline{a}_3 d\xi_3 \quad (9.63)$$

A tangential system of base vectors, as described above, are called covariant base vectors. A perpendicular system of base vectors is called contravariant base vectors. In the later case the base vectors are chosen perpendicular to the coordinate directions.

The differential increment expression 9.63 leads to the definition of the fundamental metric tensor.

Fundamental metric tensor

The magnitude of the differential increment is given by

$$\begin{aligned}(\text{arc length } ds)^2 &= \underline{dr} \cdot \underline{dr} \\ &= \sum_i \sum_j \underline{a}_i \cdot \underline{a}_j d\xi_i d\xi_j \\ &= \sum_i \sum_j g_{ij} d\xi_i d\xi_j\end{aligned} \quad (9.64)$$

where $g_{ij} = \underline{a}_i \cdot \underline{a}_j$ are the nine covariant metric tensor components.

Incremental arc length

An incremental arc length along ξ_1 direction is given by

$$ds_1 = |\underline{a}_1| d\xi_1 = \sqrt{g_{11}} d\xi_1 \quad (9.65)$$

To generalize

$$ds_i = |\underline{a}_i| d\xi_i = \sqrt{g_{ii}} d\xi_i \quad i = 1, 2, 3 \quad (9.66)$$

Incremental area

An incremental area on a coordinate surface of constant ξ_i is given by

$$dS_i = |\underline{a}_j \times \underline{a}_k| d\xi_j d\xi_k$$

$$|\underline{a}_j \times \underline{a}_k|^2 = (\underline{a}_j \cdot \underline{a}_j)(\underline{a}_k \cdot \underline{a}_k) - (\underline{a}_k \cdot \underline{a}_j)^2 = g_{jj}g_{kk} - g_{jk}^2$$

Therefore

$$dS_i = \sqrt{g_{jj}g_{kk} - g_{jk}^2} d\xi_j d\xi_k \quad (i,j,k) = (1,2,3) \text{ in a cyclic manner} \quad (9.67)$$

Incremental volume

An incremental volume enclosed by the three coordinate directions is given by

$$dV = \underline{a}_1 \cdot (\underline{a}_2 \times \underline{a}_3) d\xi_1 d\xi_2 d\xi_3 \quad (9.68)$$

Use the following

$$(A \times B)(C \times D) = (A \cdot C)(B \cdot D) - (A \cdot D)(B \cdot C)$$

or

$$(A \cdot D)(B \cdot C) = (A \cdot C)(B \cdot D) - (A \times B)(C \times D)$$

Now

$$\begin{aligned} \left[\underline{a}_1 \cdot (\underline{a}_2 \times \underline{a}_3) \right]^2 &= \left[\underline{a}_1 \cdot (\underline{a}_2 \times \underline{a}_3) \right] \left[(\underline{a}_2 \times \underline{a}_3) \cdot \underline{a}_1 \right] \\ &= (\underline{a}_1 \cdot \underline{a}_1) \left[(\underline{a}_2 \times \underline{a}_3) \cdot (\underline{a}_2 \times \underline{a}_3) \right] - |\underline{a}_1 \times (\underline{a}_2 \times \underline{a}_3)|^2 \\ &= (\underline{a}_1 \cdot \underline{a}_1) \left[(\underline{a}_2 \cdot \underline{a}_2)(\underline{a}_3 \cdot \underline{a}_3) - (\underline{a}_2 \cdot \underline{a}_3)^2 \right] - |\underline{a}_1 \times (\underline{a}_2 \times \underline{a}_3)|^2 \end{aligned}$$

Now use

$$A \times (B \times C) = (A \cdot C)B - (A \cdot B)C$$

to obtain

$$\begin{aligned} \left[\underline{a}_1 \cdot (\underline{a}_2 \times \underline{a}_3) \right]^2 &= g_{11}(g_{22}g_{33} - g_{23}^2) - (g_{13}a_2 - g_{12}a_3)^2 \\ &= \Delta(g_{ij}) \\ &= g \end{aligned}$$

where $\Delta(g_{ij}) = g$ is the determinant of the nine element covariant symmetric metric tensor. Thus equation (9.68) can be written as

$$dV = \sqrt{g} d\xi_1 d\xi_2 d\xi_3 \quad (9.69)$$

9.4.2 Generalized coordinate transformation

Consider again the transformation 9.59. This is the forward transformation, if x, y, z, t are known, ξ, η, ζ , and τ can be determined. The jacobian of the transformation J is given as follows.

$$\begin{pmatrix} d\xi \\ d\eta \\ d\zeta \end{pmatrix} = \begin{bmatrix} \xi_x & \eta_x & \zeta_x \\ \xi_y & \eta_y & \zeta_y \\ \xi_z & \eta_z & \zeta_z \end{bmatrix} \begin{pmatrix} dx \\ dy \\ dz \end{pmatrix} + \begin{pmatrix} \xi_t \\ \eta_t \\ \zeta_t \end{pmatrix} dt = J \begin{pmatrix} dx \\ dy \\ dz \end{pmatrix} + \begin{pmatrix} \xi_t \\ \eta_t \\ \zeta_t \end{pmatrix} dt \quad (9.70)$$

The jacobian also relates the partial derivatives.

$$\begin{pmatrix} \frac{\partial}{\partial x} \\ \frac{\partial}{\partial y} \\ \frac{\partial}{\partial z} \end{pmatrix} = \begin{bmatrix} \xi_x & \eta_x & \zeta_x \\ \xi_y & \eta_y & \zeta_y \\ \xi_z & \eta_z & \zeta_z \end{bmatrix} \begin{pmatrix} \frac{\partial}{\partial \xi} \\ \frac{\partial}{\partial \eta} \\ \frac{\partial}{\partial \zeta} \end{pmatrix} = J \begin{pmatrix} \frac{\partial}{\partial \xi} \\ \frac{\partial}{\partial \eta} \\ \frac{\partial}{\partial \zeta} \end{pmatrix} \quad (9.71)$$

We have

$$\begin{aligned} \begin{pmatrix} \frac{\partial}{\partial x} \\ \frac{\partial}{\partial y} \\ \frac{\partial}{\partial z} \end{pmatrix} &= \begin{bmatrix} \xi_x & \eta_x & \zeta_x \\ \xi_y & \eta_y & \zeta_y \\ \xi_z & \eta_z & \zeta_z \end{bmatrix} \begin{pmatrix} \frac{\partial}{\partial \xi} \\ \frac{\partial}{\partial \eta} \\ \frac{\partial}{\partial \zeta} \end{pmatrix} \\ &= \begin{bmatrix} \xi_x & \eta_x & \zeta_x \\ \xi_y & \eta_y & \zeta_y \\ \xi_z & \eta_z & \zeta_z \end{bmatrix} \begin{bmatrix} x_\xi & y_\xi & z_\xi \\ x_\eta & y_\eta & z_\eta \\ x_\zeta & y_\zeta & z_\zeta \end{bmatrix} \begin{pmatrix} \frac{\partial}{\partial \xi} \\ \frac{\partial}{\partial \eta} \\ \frac{\partial}{\partial \zeta} \end{pmatrix} \end{aligned} \quad (9.72)$$

It follows

$$\begin{bmatrix} \xi_x & \eta_x & \zeta_x \\ \xi_y & \eta_y & \zeta_y \\ \xi_z & \eta_z & \zeta_z \end{bmatrix} \begin{bmatrix} x_\xi & y_\xi & z_\xi \\ x_\eta & y_\eta & z_\eta \\ x_\zeta & y_\zeta & z_\zeta \end{bmatrix} = I \quad (9.73)$$

From the above equation 9.73 we have

$$\begin{bmatrix} x_\xi & y_\xi & z_\xi \\ x_\eta & y_\eta & z_\eta \\ x_\zeta & y_\zeta & z_\zeta \end{bmatrix} = \begin{bmatrix} \xi_x & \eta_x & \zeta_x \\ \xi_y & \eta_y & \zeta_y \\ \xi_z & \eta_z & \zeta_z \end{bmatrix}^{-1} = J^{-1} \quad (9.74)$$

Thus

$$J^{-1} = x_\xi(y_\eta z_\zeta - z_\eta y_\zeta) + y_\xi(x_\zeta z_\eta - z_\zeta x_\eta) + z_\xi(x_\eta y_\zeta - x_\zeta y_\eta) \quad (9.75)$$

Before we go any further, let us study the transformation. At any instant of time, which is the same in both coordinates as $\tau = t$, we have (x, y, z) as the cartesian coordinates, and (ξ, η, ζ) as the curvilinear coordinates. A differential increment of a position vector \underline{dr} in the cartesian coordinates is given by $[dx dy dz]^T$, where dx, dy , and dz are increments along the cartesian axes. These can be expressed in terms of increments along the curvilinear axes using the chain rule.

$$\begin{aligned} dx &= x_\xi d\xi + x_\eta d\eta + x_\zeta d\zeta \\ dy &= y_\xi d\xi + y_\eta d\eta + y_\zeta d\zeta \\ dz &= z_\xi d\xi + z_\eta d\eta + z_\zeta d\zeta \end{aligned}$$

The above is in the same form as equation 9.63. ξ_1 is now ξ , ξ_2 is now η and ξ_3 is now ζ . The differential increment \underline{dr} is

$$\underline{dr} = \begin{pmatrix} dx \\ dy \\ dz \end{pmatrix} = d\xi \begin{pmatrix} x_\xi \\ x_\eta \\ x_\zeta \end{pmatrix} + d\eta \begin{pmatrix} y_\xi \\ y_\eta \\ y_\zeta \end{pmatrix} + d\zeta \begin{pmatrix} z_\xi \\ z_\eta \\ z_\zeta \end{pmatrix} \quad (9.76)$$

and the covariant base vectors in the curvilinear coordinates are

$$\underline{a}_1 = \begin{Bmatrix} x_\xi \\ x_\eta \\ x_\zeta \end{Bmatrix} \quad \underline{a}_2 = \begin{Bmatrix} y_\xi \\ y_\eta \\ y_\zeta \end{Bmatrix} \quad \underline{a}_3 = \begin{Bmatrix} z_\xi \\ z_\eta \\ z_\zeta \end{Bmatrix} \quad (9.77)$$

Thus x_ξ, y_ξ , etc are called the covariants of the transformation. They are tangents to the curvilinear coordinate directions. Note that they are obtained by taking partial derivatives from the inverse transformation. The inverse transformation is as follows.

$$\begin{aligned} x &= x(\xi, \eta, \zeta, \tau) \\ y &= y(\xi, \eta, \zeta, \tau) \\ z &= z(\xi, \eta, \zeta, \tau) \\ t &= \tau \end{aligned} \quad (9.78)$$

From equation 9.73 we have

$$\begin{bmatrix} \xi_x & \eta_x & \zeta_x \\ \xi_y & \eta_y & \zeta_y \\ \xi_z & \eta_z & \zeta_z \end{bmatrix} = \begin{bmatrix} x_\xi & y_\xi & z_\xi \\ x_\eta & y_\eta & z_\eta \\ x_\zeta & y_\zeta & z_\zeta \end{bmatrix}^{-1} = \frac{\text{cofactor of entry } x_{ji}}{J^{-1}} \quad (9.79)$$

The metrics of the transformation ξ_x, ξ_y , etc are thus related to the covariants x_ξ, x_η by the following expression.

$$\begin{aligned} \xi_x &= J(y_\eta z_\zeta - y_\zeta z_\eta) \\ \eta_x &= J(y_\zeta z_\xi - y_\xi z_\zeta) \\ \zeta_x &= J(y_\xi z_\eta - y_\eta z_\xi) \\ \\ \xi_y &= J(x_\zeta z_\eta - x_\eta z_\zeta) \\ \eta_y &= J(x_\xi z_\zeta - x_\zeta z_\xi) \\ \zeta_y &= J(x_\eta z_\xi - x_\xi z_\eta) \\ \\ \xi_z &= J(x_\eta y_\zeta - x_\zeta y_\eta) \\ \eta_z &= J(x_\zeta y_\xi - x_\xi y_\zeta) \\ \zeta_z &= J(x_\xi y_\eta - x_\eta y_\xi) \end{aligned} \quad (9.80)$$

9.4.3 Euler equation in generalized coordinates

The Euler equation in cartesian form is given as

$$\frac{\partial q}{\partial t} + \frac{\partial F}{\partial x} + \frac{\partial G}{\partial y} + \frac{\partial H}{\partial z} = 0 \quad (9.81)$$

where

$$q = \begin{Bmatrix} \rho \\ \rho u \\ \rho v \\ \rho w \\ \rho E \end{Bmatrix} \quad F = \begin{Bmatrix} \rho u \\ \rho u^2 + p \\ \rho uv \\ \rho uw \\ \rho u(E + p) \end{Bmatrix} \quad G = \begin{Bmatrix} \rho v \\ \rho vu \\ \rho v^2 + p \\ \rho vw \\ \rho v(E + p) \end{Bmatrix} \quad H = \begin{Bmatrix} \rho w \\ \rho wu \\ \rho wv \\ \rho w^2 + p \\ \rho w(E + p) \end{Bmatrix} \quad (9.82)$$

Note that the convective fluxes F, G, H were earlier denoted as F_x, F_y, F_z in chapter 4. The pressure p and temperature T can be determined from the total energy per unit mass E as follows. The internal energy by unit mass is $e = E - 0.5(u^2 + v^2 + w^2) = C_v T$. Thus

$$T = \frac{1}{C_v} \left[E - \frac{1}{2}(u^2 + v^2 + w^2) \right] \quad (9.83)$$

Now $p = \rho RT$. Therefore

$$\begin{aligned} p &= \frac{\rho R}{C_v} \left[E - \frac{1}{2}(u^2 + v^2 + w^2) \right] \\ &= \frac{\rho RT}{C_v T} \left[E - \frac{1}{2}(u^2 + v^2 + w^2) \right] \\ &= \frac{\rho(h - e)}{C_v T} \left[E - \frac{1}{2}(u^2 + v^2 + w^2) \right] \\ &= \frac{\rho(C_p - C_v)T}{C_v T} \left[E - \frac{1}{2}(u^2 + v^2 + w^2) \right] \\ &= (\gamma - 1)\rho \left[E - \frac{1}{2}(u^2 + v^2 + w^2) \right] \end{aligned} \quad (9.84)$$

The generalized coordinate transformation preserves the conservation form of the equations. First pre-multiply equation (9.81) by J^{-1} . Now, consider the terms one by one. First the time derivative.

$$\begin{aligned} J^{-1} \frac{\partial q}{\partial t} &= J^{-1} \left(\frac{\partial q}{\partial \tau} + \xi_t \frac{\partial q}{\partial \xi} + \eta_t \frac{\partial q}{\partial \eta} + \zeta_t \frac{\partial q}{\partial \zeta} \right) \\ &= \frac{\partial}{\partial \tau} (J^{-1}q) + \frac{\partial}{\partial \xi} (J^{-1}\xi_t q) + \frac{\partial}{\partial \eta} (J^{-1}\eta_t q) + \frac{\partial}{\partial \zeta} (J^{-1}\zeta_t q) \\ &\quad - q \left[\frac{\partial}{\partial \tau} (J^{-1}) + \frac{\partial}{\partial \xi} (J^{-1}\xi_t) + \frac{\partial}{\partial \eta} (J^{-1}\eta_t) + \frac{\partial}{\partial \zeta} (J^{-1}\zeta_t) \right] \end{aligned} \quad (9.85)$$

Now consider the spatial derivatives

$$\begin{aligned} &J^{-1} \left(\frac{\partial F}{\partial x} + \frac{\partial G}{\partial y} + \frac{\partial H}{\partial z} \right) \\ &= J^{-1} \left[\xi_x \frac{\partial F}{\partial \xi} + \eta_x \frac{\partial F}{\partial \eta} + \zeta_x \frac{\partial F}{\partial \zeta} + \xi_y \frac{\partial G}{\partial \xi} + \eta_y \frac{\partial G}{\partial \eta} + \zeta_y \frac{\partial G}{\partial \zeta} + \xi_z \frac{\partial H}{\partial \xi} + \eta_z \frac{\partial H}{\partial \eta} + \zeta_z \frac{\partial H}{\partial \zeta} \right] \\ &= J^{-1} \left[\xi_x \frac{\partial F}{\partial \xi} + \eta_x \frac{\partial F}{\partial \eta} + \zeta_x \frac{\partial F}{\partial \zeta} + \xi_y \frac{\partial G}{\partial \xi} + \eta_y \frac{\partial G}{\partial \eta} + \zeta_y \frac{\partial G}{\partial \zeta} + \xi_z \frac{\partial H}{\partial \xi} + \eta_z \frac{\partial H}{\partial \eta} + \zeta_z \frac{\partial H}{\partial \zeta} \right] \\ &= (y_\eta z_\zeta - y_\zeta z_\eta) F_\xi + (x_\zeta z_\eta - x_\eta z_\zeta) G_\xi + (x_\eta y_\zeta - x_\zeta y_\eta) H_\xi + \\ &\quad (y_\zeta z_\xi - z_\zeta y_\xi) F_\eta + (x_\xi z_\zeta - x_\zeta z_\xi) G_\eta + (x_\zeta y_\xi - x_\xi y_\zeta) H_\eta + \\ &\quad (y_\xi z_\eta - y_\eta z_\xi) F_\zeta + (x_\eta z_\xi - x_\xi z_\eta) G_\zeta + (x_\xi y_\eta - x_\eta y_\xi) H_\zeta \end{aligned} \quad (9.86)$$

Use equations 9.80 to rewrite the above expression as

$$\begin{aligned}
& [(y_\eta z_\zeta - y_\zeta z_\eta)F]_\xi - \underline{F(y_\eta z_\zeta - y_\zeta z_\eta)_\xi} \\
& [(x_\zeta z_\eta - x_\eta z_\zeta)G]_\xi - \underline{G(x_\zeta z_\eta - x_\eta z_\zeta)_\xi} \\
& [(x_\eta y_\zeta - x_\zeta y_\eta)H]_\xi - \underline{H(x_\eta y_\zeta - x_\zeta y_\eta)_\xi} \\
& [(y_\zeta z_\xi - z_\zeta y_\xi)F]_\eta - \underline{F(y_\zeta z_\xi - z_\zeta y_\xi)_\eta} \\
& [(x_\xi z_\zeta - x_\zeta z_\xi)G]_\eta - \underline{G(x_\xi z_\zeta - x_\zeta z_\xi)_\eta} \\
& [(x_\zeta y_\xi - x_\xi y_\zeta)H]_\eta - \underline{H(x_\zeta y_\xi - x_\xi y_\zeta)_\eta} \\
& [(y_\xi z_\eta - y_\eta z_\xi)F]_\zeta - \underline{F(y_\xi z_\eta - y_\eta z_\xi)_\zeta} \\
& [(x_\eta z_\xi - x_\xi z_\eta)G]_\zeta - \underline{G(x_\eta z_\xi - x_\xi z_\eta)_\zeta} \\
& [(x_\xi y_\eta - x_\eta y_\xi)H]_\zeta - \underline{H(x_\xi y_\eta - x_\eta y_\xi)_\zeta}
\end{aligned} \tag{9.87}$$

The underlined expressions, when expanded, assuming necessary smoothness of the transformation cancel out to zero. Thus the transformed equation becomes

$$\begin{aligned}
\frac{\partial}{\partial \tau} \left(\frac{q}{J} \right) &+ \frac{\partial}{\partial \xi} \left(\frac{\xi_t q + \xi_x F + \xi_y G + \xi_z H}{J} \right) \\
&+ \frac{\partial}{\partial \eta} \left(\frac{\eta_t q + \eta_x F + \eta_y G + \eta_z H}{J} \right) \\
&+ \frac{\partial}{\partial \zeta} \left(\frac{\zeta_t q + \zeta_x F + \zeta_y G + \zeta_z H}{J} \right) \\
&- q \left[\frac{\partial}{\partial \tau} \left(\frac{1}{J} \right) + \frac{\partial}{\partial \xi} \left(\frac{\xi_t}{J} \right) + \frac{\partial}{\partial \eta} \left(\frac{\eta_t}{J} \right) + \frac{\partial}{\partial \zeta} \left(\frac{\zeta_t}{J} \right) \right]
\end{aligned}$$

The above equation is in the following strong conservation form

$$\hat{q}_\tau + \hat{F}_\xi + \hat{G}_\eta + \hat{H}_\zeta = 0 \tag{9.88}$$

provided the expression multiplied with q vanishes.

$$\frac{\partial}{\partial \tau} \left(\frac{1}{J} \right) + \frac{\partial}{\partial \xi} \left(\frac{\xi_t}{J} \right) + \frac{\partial}{\partial \eta} \left(\frac{\eta_t}{J} \right) + \frac{\partial}{\partial \zeta} \left(\frac{\zeta_t}{J} \right) = 0 \tag{9.89}$$

The above equation 9.89 is called the geometric conservation law. The expression was suggested by Thomas and Lombard in 1970 and states that the rate at which the volume of a discretized mesh element changes with time must be same as the rate at which its six faces sweep the domain. It is important to satisfy this relationship in order to avoid spurious production of mass, momentum, and energy within the computational mesh elements.

Thus the flow equations 9.88 is solved along with the geometric conservation law 9.89. It is also necessary to prescribe a physically consistent set of boundary conditions on all the solid and fluid boundaries in the computational domain. We shall discuss boundary conditions later. Consider equation 9.88. This equation has exactly the same form as the original equation 9.81 in the cartesian

domain. Now consider the expression \hat{F} in equation (9.88).

$$\hat{F}_\xi = J^{-1} [\xi_t q + \xi_x F + \xi_y G + \xi_z H] \quad (9.90)$$

$$= J^{-1} \begin{bmatrix} \xi_t \rho + \xi_x \rho u + \xi_y \rho v + \xi_z \rho w \\ \xi_t \rho u + \xi_x \rho u u + \xi_x p + \xi_y \rho v u + \xi_z \rho w u \\ \xi_t \rho v + \xi_x \rho u v + \xi_y \rho v v + \xi_y p + \xi_z \rho w v \\ \xi_t \rho w + \xi_x \rho u w + \xi_y \rho v w + \xi_z \rho w w + \xi_z p \\ \xi_t (E + p) - \xi_t p + \xi_x \rho u (E + p) + \xi_y \rho v (E + p) + \xi_z \rho w (E + p) \end{bmatrix} \quad (9.91)$$

$$= J^{-1} \begin{bmatrix} \rho U \\ \rho u U + \xi_x p \\ \rho v U + \xi_y p \\ \rho w U + \xi_z p \\ (E + p)U - \xi_t p \end{bmatrix} \quad (9.92)$$

where

$$U = \xi_t + \xi_x u + \xi_y v + \xi_z w \quad (9.93)$$

Similarly \hat{F} and \hat{G} can be expressed as

$$\hat{F} = J^{-1} \begin{bmatrix} \rho V \\ \rho u V + \eta_x p \\ \rho v V + \eta_y p \\ \rho w V + \eta_z p \\ (E + p)V - \eta_t p \end{bmatrix} \quad \hat{G} = J^{-1} \begin{bmatrix} \rho W \\ \rho u W + \zeta_x p \\ \rho v W + \zeta_y p \\ \rho w W + \zeta_z p \\ (E + p)W - \zeta_t p \end{bmatrix} \quad (9.94)$$

where

$$V = \eta_t + \eta_x u + \eta_y v + \eta_z w \quad (9.95)$$

$$W = \zeta_t + \zeta_x u + \zeta_y v + \zeta_z w \quad (9.96)$$

U, V, W are the contravariant velocities along ξ, η, ζ directions. ξ_t, η_t, ζ_t incorporate the effect of grid motion. ξ, η, ζ do not depend on τ . Therefore we have

$$\begin{aligned} \xi_\tau = 0 &= \xi_t + \xi_x x_\tau + \xi_y y_\tau + \xi_z z_\tau \\ \eta_\tau = 0 &= \eta_t + \eta_x x_\tau + \eta_y y_\tau + \eta_z z_\tau \\ \zeta_\tau = 0 &= \zeta_t + \zeta_x x_\tau + \zeta_y y_\tau + \zeta_z z_\tau \end{aligned} \quad (9.97)$$

Thus

$$\begin{aligned} \xi_t &= -x_\tau \xi_x - y_\tau \xi_y + z_\tau \xi_z \\ \eta_t &= -x_\tau \eta_x - y_\tau \eta_y + z_\tau \eta_z \\ \zeta_t &= -x_\tau \zeta_x - y_\tau \zeta_y + z_\tau \zeta_z \end{aligned} \quad (9.98)$$

The above expressions are used to account for the unsteady motion of the grid. Using the above expressions, U, V, W can also be written in the following form.

$$\begin{aligned} U &= (u - x_\tau) \xi_x + (v - y_\tau) \xi_y + (w - z_\tau) \xi_z \\ V &= (u - x_\tau) \eta_x + (v - y_\tau) \eta_y + (w - z_\tau) \eta_z \\ W &= (u - x_\tau) \zeta_x + (v - y_\tau) \zeta_y + (w - z_\tau) \zeta_z \end{aligned} \quad (9.99)$$

9.4.4 Thomas and Lombard's Geometric Conservation Law

Consider a cell volume Δv_i where i is the cell number. It has j surfaces denoted by S_{ij} . The time variation of cell volume is related to the areas, orientations, and velocities of cell faces.

$$\frac{d}{dt} \int_{\Delta v_i} dv = \sum_j \int_{S_{ij}} W_s \cdot ds$$

W_S is the local velocity of boundary surface S . For an entire flow domain R

$$\frac{d}{dt} \int_{\Delta v} dv = \int_s W_s \cdot ds \quad (9.100)$$

Note that the above equation is very similar to the mass conservation law in integral form. In fact it can be deduced straight away from the mass conservation law by replacing ρ with 1, and setting the fluid velocity to zero. Recall that the integral statement of the law of mass conservation for a spatial region R of volume v bounded by a closed surface s and fluid velocity V is given by

$$\frac{d}{dt} \int_{\Delta v_i} \rho dv + \int_s \rho(V - W_s) \cdot ds$$

Using the above mentioned substitution, it reduces to equation (9.100). The integral form of the geometric conservation law (9.100) can be recast into a differential form. Consider the computation domain. Consider now the transformation ξ, η, ζ . The incremental volume in the cartesian coordinates is $dx dy dz$. Use equation (9.68) and the definitions (9.77) and (9.75) to obtain

$$dv = dx dy dz = J^{-1} d\xi d\eta d\zeta \quad (9.101)$$

Therefore equation (9.100) is transformed into

$$\frac{d}{d\tau} \int_{\Delta v} J^{-1} d\xi d\eta d\zeta = \int_s W_s \cdot J^{-1} d\xi d\eta d\zeta \quad (9.102)$$

The transformation ξ, η, ζ generates a boundary conforming curvilinear coordinates. Boundary conforming means that the boundary s of the body is composed only of segments of the form $\xi = \text{constant}$, $\eta = \text{constant}$, and $\zeta = \text{constant}$. In the cartesian coordinates, the velocities at any point on the boundary is given by $W_s = (x_\tau, y_\tau, z_\tau)$. In general the transformation defines a velocity field $W = (x_\tau, y_\tau, z_\tau)$ throughout a region R that coincides with W_s in the boundary. Thus the divergence theorem can be applied to reduce the surface integral to a volume integral.

$$\frac{d}{d\tau} \int_{\Delta v} J^{-1} d\xi d\eta d\zeta = \int_v (\nabla \cdot W) J^{-1} d\xi d\eta d\zeta \quad (9.103)$$

Consider the expressions on the right hand side first. We have

$$\begin{aligned} \nabla \cdot W &= (W_1)_x + (W_2)_y + (W_3)_z \\ &= \xi_x(W_1)_\xi + \eta_x(W_1)_\eta + \zeta_x(W_1)_\zeta + \\ &\quad \xi_y(W_2)_\xi + \eta_y(W_2)_\eta + \zeta_y(W_2)_\zeta + \\ &\quad \xi_z(W_3)_\xi + \eta_z(W_3)_\eta + \zeta_z(W_3)_\zeta \\ &= \nabla \xi \cdot W_\xi + \nabla \eta \cdot W_\eta + \nabla \zeta \cdot W_\zeta \end{aligned}$$

Therefore

$$\begin{aligned} J^{-1}(\nabla \cdot W) &= (J^{-1} \nabla \xi \cdot W)_\xi + (J^{-1} \nabla \eta \cdot W)_\eta + (J^{-1} \nabla \zeta \cdot W)_\zeta \\ &\quad - [(J^{-1} \nabla \xi)_\xi + (J^{-1} \nabla \eta)_\eta + (J^{-1} \nabla \zeta)_\zeta] \cdot W \end{aligned}$$

Now we have

$$\begin{aligned}\xi_\tau = 0 &= \xi_t + \xi_x x_\tau + \xi_y y_\tau + \xi_z z_\tau \\ &= \xi_t + \nabla \xi \cdot W\end{aligned}$$

Hence

$$\begin{aligned}\xi_t &= -\nabla \xi \cdot W \\ \eta_t &= -\nabla \eta \cdot W \\ \zeta_t &= -\nabla \zeta \cdot W\end{aligned}$$

and

$$\begin{aligned}J^{-1}(\nabla \cdot W) &= -(J^{-1}\xi_t)_\xi - (J^{-1}\eta_t)_\eta - (J^{-1}\zeta_t)_\zeta \\ &\quad - W \cdot [(J^{-1}\nabla \xi)_\xi + (J^{-1}\nabla \eta)_\eta + (J^{-1}\nabla \zeta)_\zeta] \\ &= \underline{(J^{-1}\xi_t)_\xi} - (J^{-1}\eta_t)_\eta - (J^{-1}\zeta_t)_\zeta \\ &\quad - x_\tau \underline{[(J^{-1}\xi_x)_\xi + (J^{-1}\eta_x)_\eta + (J^{-1}\zeta_x)_\zeta]} \\ &\quad - y_\tau \underline{[(J^{-1}\xi_y)_\xi + (J^{-1}\eta_y)_\eta + (J^{-1}\zeta_y)_\zeta]} \\ &\quad - z_\tau \underline{[(J^{-1}\xi_z)_\xi + (J^{-1}\eta_z)_\eta + (J^{-1}\zeta_z)_\zeta]}\end{aligned}$$

Each of the underlined expressions cancel to zero. For example,

$$\begin{aligned}(J^{-1}\xi_y)_\xi + (J^{-1}\eta_y)_\eta + (J^{-1}\zeta_y)_\zeta &= [J^{-1}J(y_\eta z_\zeta - y_\zeta z_\eta)]_\xi + \\ &\quad [J^{-1}J(y_\zeta z_\xi - y_\xi z_\zeta)]_\eta + \\ &\quad [J^{-1}J(y_\xi z_\eta - y_\eta z_\xi)]_\eta \\ &= 0\end{aligned}$$

Now consider the left hand side of equation (9.103). Because ξ, η, ζ are boundary-confirming, the surface s and volume v are fixed in time τ . Hence the operator $\partial/\partial\tau$ can be moved inside the integral. Thus, equation (9.103) finally reduces to

$$\int_v [(J^{-1})_\tau + (J^{-1}\xi_t)_\xi + (J^{-1}\eta_t)_\eta + (J^{-1}\zeta_t)_\zeta] d\xi d\eta d\zeta = 0 \quad (9.104)$$

As v is fixed in time τ the above reduces to equation (9.89) which is the differential statement of the geometric conservation law. Again, it can be verified that we can obtain the same expression from the mass conservation equation, which is the first component of the vector equation (9.88) by putting $\rho = 1$ and $u, v, w = 0$.

9.4.5 Navier-Stokes equations in generalized coordinates

The Navier-Stokes equations in cartesian form is given by

$$\frac{\partial q}{\partial t} + \frac{\partial(F - F_v)}{\partial x} + \frac{\partial(G - G_v)}{\partial y} + \frac{\partial(H - H_v)}{\partial z} = 0 \quad (9.105)$$

where F, G, H are same as in the Euler equations. F_v, G_v, H_v are the additional diffusive fluxes. Recall from chapter 4 that they are given by

$$F_v = \begin{Bmatrix} 0 \\ \tau_{xx} \\ \tau_{yx} \\ \tau_{zx} \\ \beta_x \end{Bmatrix} \quad G_v = \begin{Bmatrix} 0 \\ \tau_{xy} \\ \tau_{yy} \\ \tau_{zy} \\ \beta_y \end{Bmatrix} \quad H_v = \begin{Bmatrix} 0 \\ \tau_{xz} \\ \tau_{yz} \\ \tau_{zz} \\ \beta_z \end{Bmatrix} \quad \begin{aligned} \beta_x &= u\tau_{xx} + v\tau_{xy} + w\tau_{xz} + q_x \\ \beta_y &= u\tau_{yx} + v\tau_{yy} + w\tau_{yz} + q_y \\ \beta_z &= u\tau_{zx} + v\tau_{zy} + w\tau_{zz} + q_z \end{aligned} \quad (9.106)$$

where τ 's are the shear stresses and q 's the heat fluxes. The pressure and temperature are again related to the internal energy per unit mass E and the flow velocities u, v, w via equations (9.84) and (9.83).

The transformed equation in body-conforming curvilinear coordinates is similar to equation (9.88) with the additional terms F_v, G_v, H_v .

$$\hat{q}_\tau + (\hat{F} - \hat{F}_v)_\xi + (\hat{G} - \hat{G}_v)_\eta + (\hat{H} - \hat{H}_v)_\zeta = 0 \quad (9.107)$$

where

$$\hat{F}_v = J^{-1} \left\{ \begin{array}{c} 0 \\ \xi_x \tau_{xx} + \xi_y \tau_{xy} + \xi_z \tau_{xz} \\ \xi_x \tau_{yx} + \xi_y \tau_{yy} + \xi_z \tau_{yz} \\ \xi_x \tau_{zx} + \xi_y \tau_{zy} + \xi_z \tau_{zz} \\ \xi_x \beta_x + \xi_y \beta_y + \xi_z \beta_z \end{array} \right\} \quad (9.108)$$

$$\hat{G}_v = J^{-1} \left\{ \begin{array}{c} 0 \\ \eta_x \tau_{xx} + \eta_y \tau_{xy} + \eta_z \tau_{xz} \\ \eta_x \tau_{yx} + \eta_y \tau_{yy} + \eta_z \tau_{yz} \\ \eta_x \tau_{zx} + \eta_y \tau_{zy} + \eta_z \tau_{zz} \\ \eta_x \beta_x + \eta_y \beta_y + \eta_z \beta_z \end{array} \right\} \quad (9.109)$$

$$\hat{H}_v = J^{-1} \left\{ \begin{array}{c} 0 \\ \zeta_x \tau_{xx} + \zeta_y \tau_{xy} + \zeta_z \tau_{xz} \\ \zeta_x \tau_{yx} + \zeta_y \tau_{yy} + \zeta_z \tau_{yz} \\ \zeta_x \tau_{zx} + \zeta_y \tau_{zy} + \zeta_z \tau_{zz} \\ \zeta_x \beta_x + \zeta_y \beta_y + \zeta_z \beta_z \end{array} \right\} \quad (9.110)$$

The geometric conservation law remains same as equation (9.89).

Thin layer approximation

Capturing the viscous gradients near the body is difficult for high Reynolds number flows. Often the gradients perpendicular to the body are targeted for accurate calculation, the gradients along the body are neglected. In the case of body-conforming grids the body surface is mapped onto a $\zeta = \text{constant}$ line. In this case all viscous derivatives along the ξ and η directions are neglected.

$$\hat{q}_\tau + \hat{F}_\xi + \hat{G}_\eta + \hat{H}_\zeta = \hat{H}_v \zeta \quad (9.111)$$

The velocity derivatives are

$$u_x = \zeta_x u_\zeta$$

$$u_y = \zeta_y u_\zeta$$

$$u_z = \zeta_z u_\zeta$$

$$v_x = \zeta_x v_\zeta$$

$$v_y = \zeta_y v_\zeta$$

$$v_z = \zeta_z v_\zeta$$

$$(9.112)$$

$$w_x = \zeta_x w_\zeta$$

$$w_y = \zeta_y w_\zeta$$

$$w_z = \zeta_z w_\zeta$$

9.4.6 Surface Boundary Conditions

From equations (9.93) and (9.95) we have

$$\begin{Bmatrix} U - \xi_t \\ V - \eta_t \\ W - \zeta_t \end{Bmatrix} = \begin{bmatrix} \xi_x & \xi_y & \xi_z \\ \eta_x & \eta_y & \eta_z \\ \zeta_x & \zeta_y & \zeta_z \end{bmatrix} \begin{Bmatrix} u \\ v \\ w \end{Bmatrix} \quad (9.113)$$

Inverting, we have

$$\begin{aligned} \begin{Bmatrix} u \\ v \\ w \end{Bmatrix} &= \begin{bmatrix} \xi_x & \xi_y & \xi_z \\ \eta_x & \eta_y & \eta_z \\ \zeta_x & \zeta_y & \zeta_z \end{bmatrix}^{-1} \begin{Bmatrix} U - \xi_t \\ V - \eta_t \\ W - \zeta_t \end{Bmatrix} \\ &= J^{-1} \begin{bmatrix} (\eta_y \zeta_z - \eta_z \zeta_y) & -(\xi_y \zeta_z - \zeta_y \xi_z) & (\xi_y \eta_z - \eta_y \xi_z) \\ -(\eta_x \zeta_z - \eta_z \zeta_x) & (\xi_x \zeta_z - \xi_z \zeta_x) & -(\xi_x \eta_z - \xi_z \eta_x) \\ (\eta_x \zeta_y - \eta_y \zeta_x) & -(\xi_x \zeta_y - \xi_y \zeta_x) & (\xi_x \eta_y - \xi_y \eta_x) \end{bmatrix} \begin{Bmatrix} U - \xi_t \\ V - \eta_t \\ W - \zeta_t \end{Bmatrix} \end{aligned} \quad (9.114)$$

For inviscid flow, as in the case of Euler equations, the boundary condition is

$$W = 0$$

The corresponding u, v, w are obtained from equation (9.114). For viscous flow, as in the case of Navier-Stokes equations, the boundary conditions are

$$U = V = W = 0$$

Chapter 10

Helicopter Vibration

Vibration in helicopters is only one of the many major problems. Helicopter vibration is the unsteady acceleration of any given location inside the fuselage, e.g. at the pilot seat, co-pilot seat or at a given crew or passenger station measured along three mutually orthogonal axes (as a fraction of acceleration due to gravity, g). Vibration not only effects the ride quality but also influences the fatigue life of the various components. The prime source of helicopter vibration is the main rotor. In this chapter we shall concentrate mainly on the vibration caused by the main rotor.

10.1 Measure of Helicopter Vibration

The basic measure of helicopter vibration, as given in the Aeronautical Design Standard (released in 1986 as ADS-27 by the U.S. Army Aviation Systems Command, AVSCOM), is the Intrusion Index (II) [1]. This is computed by normalizing triaxial accelerometer data for the four largest spectral peaks up to 60 Hz. The four largest spectral peaks generally correspond to multiples of the rotor RPM (Revolutions Per Minute) e.g. 1/rev (once per revolution, same as the rotor RPM), 2/rev, 3/rev etc, indicating that they arise from main rotor loads. For conventional helicopter rotors, the RPM corresponds to around 4 to 4.5 Hz. The ADS-27 measure does not include the 1/rev vibration. This is to emphasize the special importance of this harmonic. The 1/rev vibration arises in the fuselage if the blades are out of track - i.e, when all the blades do not follow the same trajectory in space. For tracked and identical rotor blades, the frequencies, in /rev, transmitted to the fuselage via the rotor hub are integral multiples of blade number. For example for a 4-bladed helicopter like the UH-60A, 4/rev, 8/rev, 12/rev and so on are transmitted to the fuselage. The frequency corresponding to the blade number, 4/rev in this case, is called the blade passage frequency. Non-integral multiples are transmitted only in the case of non-identical (damaged or dissimilar) or out of track blades.

The four largest harmonics are measured along each axis and their norm is used to obtain the intrusion index. This produces a single scalar quantity as a measure of vibration which combines 12 harmonics (four each in three axes). The three axes are weighted differently, the vertical vibrations are weighted most heavily, the lateral vibrations have a 0.75 weight relative to the vertical and the longitudinal vibrations have a 0.50 weight relative to the vertical. This is done to allow designers the freedom to trade off between directions and frequency within the confines of a single scalar measure of vibration.

The ADS-27 relaxed the fuselage vibration levels compared to original standards set by the Utility Tactical Transport Aircraft System (UTTAS) and Advanced Attack Helicopter (AAH) developmental programs [2]. None of the helicopter designs even came close to those original specifications. The revised ADS-27 standards are still too stringent. For example, for the UH-60A Black Hawk helicopter with an articulated 4 bladed main rotor system, the vibration levels can be 100% higher in forward flight compared to the ADS-27 requirements [3], see Fig. 10.1.

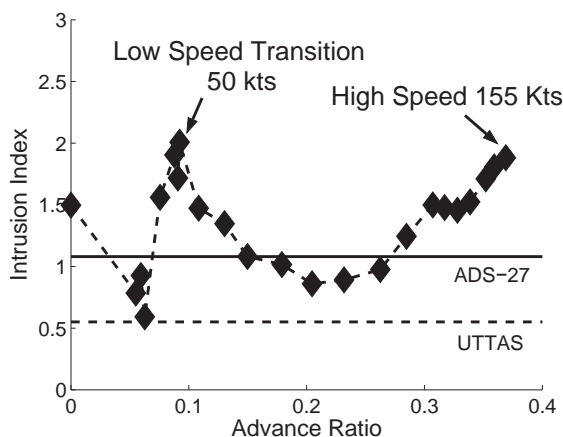


Figure 10.1: Measured Vibration at Pilot Seat of the UH-60A in Steady Level Flight, take off weight 16,500 lbs; Bousman 1999

The intrusion index at the pilot floor for the UH-60A at transition speed of around 40 kts is about 2.1 (ADS-27 level is about 1.1). 4/rev and 8/rev harmonics account for 91% of this number. At high speed of about 155 kts, 4 and 8/rev contribute to around 67% of the index. 2/rev and 6/rev contribute to 19% and 5% of the index. This shows that frequencies corresponding to non-integer multiples of blade number can contribute significantly to fuselage vibration at certain flight conditions.

Currently, vibration reduction devices, active and passive, are used to meet these requirements. Their cost and weight penalty has been excessive in part because of inadequate vibration prediction capability. Accurate prediction capability at an early design stage may enable the design of low vibration helicopter systems.

10.2 Sources of Helicopter Vibration

The prime source of helicopter vibration is the main rotor. The frequency of vibration caused by the main rotor is at integer multiples of the rotor RPM - 1 per revolution (1/rev) is the rotor RPM, then 2/rev, 3/rev and so on. In addition to the main rotor, other sources of vibration are - the engine/fan system, the main rotor transmission/drive-shaft/gear system, the tail rotor and its transmission system and loose components that are a regular or external part of the aircraft. Examples are out of balance rotor blades, loose tail fins, loose engine shaft mounts, unsecured canopy, landing gear system or external weapons or cargo systems.

As shown in Fig. 10.1, the vibration level is generally low in hover and it increases with higher forward speeds. One encounters large vibration amplitudes at a low forward speed, i.e. at the transition flight speed, and then at very high speeds. Therefore, there are two regimes: low speed flight (transition) and high speed flight, where the vibration levels are critical. The rotor flow field in the first regime is characterized by wake induced loadings in the first and fourth quadrants. The rotor flow field in the second regime is characterized by tip compressibility effects between the first and second quadrants. The mechanisms behind vibratory loads at low speed is the intertwining of tip vortices which lie close to the rotor disk [4]. As the speed increases, the disk tilts forward and the vortex wake is swept away from the disk plane and the wake-induced vibrations become smaller. At still higher speeds, the vibration level starts to increase again. The mechanism of vibratory loads at high speed is the large elastic twist deformation of the rotor blades due to unsteady transonic pitching moments occurring near the blade tips (80% R to tip). The wake has a secondary role at the relatively inboard stations (60%–80% R) [5, 6].

If there is a slight dissimilarity between the blades, there is a likelihood of 1/rev hub forces and moments which can cause a large 1/rev vibration in the airframe. This is the reason that a major effort is made in the rotorcraft industry to manufacture an identical set of blades. Then, whatever small differences of structural and aerodynamic properties for different blades exist, they are covered during the tracking and balancing operations. The dissimilarity of the inertial unbalance is corrected by suitably placing a small balancing weight at the tip of the blade. The aerodynamic dissimilarity is corrected by adjusting the trim tab as well as the pitch link.

The fuselage vibration at any station depends not only on the external loadings but also on the fuselage dynamic characteristics. The fuselage dynamic characteristics are in general coupled with the dynamics of other component structures. For example, the main rotor loads are transmitted to the fuselage via the rotor hub. The fuselage dynamic response feeds back into the blade motions via the hub and pylon assembly.

In addition to dynamic coupling, a significant amount of aerodynamic interference or coupling exists between the main rotor, airframe and tail rotor structures. The flow around the fuselage affect the aerodynamics of the main rotor and the tail rotor. The downwash from the main rotor changes the aerodynamics of the fuselage, tail rotor and horizontal tail and stabilizers. Under certain low speed conditions, the vortex wake from the main rotor impinges directly on the tail boom that gives rise to fuselage vibration at the blade passage frequency.

10.3 Analysis of Helicopter Vibration

For accurate prediction of helicopter vibration at any fuselage station, the following physical mechanisms must be modeled.

1. Structural dynamics of the main rotor with non-linear inertial couplings, moderately large deformations, boundary conditions with multiple load paths, pitch link and damper properties at the root, advanced geometry blades with sweep, droop and pre-twist and rotor-airframe coupling terms.
2. Aerodynamics of the main rotor which accounts for time varying unsteady effects, attached flow, stalled flow, dynamic stall, free or prescribed rotor wake, a lifting-line or lifting-surface model for calculating the blade airloads compatible with airfoil property data.
3. Aerodynamic and structural dynamic model of the airframe or fuselage which includes a tail rotor model, properties of the vertical and horizontal tail and fuselage center of gravity location. A detailed structural model of the flexible fuselage would include rotor-body coupling terms and modeling of rotor hub, pylon, tail boom and other difficult components.
4. Rotor-fuselage aerodynamic interaction effects. The downwash from the rotor and the upwash from the fuselage affect the fuselage and rotor airflows respectively as well as coupling their aerodynamic characteristics.
5. A vehicle trim model using a isolated rotor wind tunnel trim, or a free flight propulsive trim under steady level or steady maneuvering conditions.
6. Computation Fluid Dynamic models can be used to replace - from parts of the aerodynamic modeling of the main rotor, to the full rotor system to the entire rotor-fuselage-tail rotor flow field, depending on the level of details sought, scope of analysis and resources available.
7. Active on-blade components like trailing edge flaps, actuators and blade to blade structural and aerodynamic dissimilarities and damage.

The above models can be combined together to synthesize a comprehensive analysis to predict helicopter performance, airloads, blade loads and fuselage vibration. Detailed modeling of all the above mechanisms are prohibitive in terms of computational and modeling costs and cannot be routinely used for design purposes. Nor is it necessary for preliminary design. Depending on the level of accuracy and type of results sought from the analysis, simplifying assumptions can be made which focuses on the key mechanisms. For example, for calculation of basic rotor performance, blade airloads are more important than rotor-fuselage aerodynamic interactions. For calculation of blade airloads at low thrust conditions, dynamic stall models need not be used. For calculation of bending moments, flexible blade modes are more important than fuselage dynamics. At low speed transition flight, a free wake model is more important than transonic effects. At a high speed, transonic effects are more important than free wake. Thus, if the underlying key mechanisms of a particular flight condition are understood and modeled, reasonably accurate solutions can be obtained from a simplified analysis. In general, for accurate prediction of fuselage vibration at all flight conditions, all the above mechanisms need to be modeled.

10.4 Rotor Vibratory Loads

For accurate prediction of fuselage vibration, the dynamics and aerodynamics of all components - main rotor, airframe, tail rotor etc and their mutual interactions must be modeled accurately. However, the most significant contribution to fuselage vibration is the loads of the main rotor system. Because only the harmonics of the blade passage frequency are dominantly transferred to the fuselage, main rotor loads which generate those harmonics are termed vibratory loads. In addition to the vibratory loads, oscillatory blade loads arising out of blade dynamics are also critical. They are important for the design of blades, control linkages, hub attachments as well as rotor performance.

As discussed above, the dominant contributor to fuselage vibration is the main rotor - the oscillatory loads that are transmitted to the airframe via the rotor hub and pylon assembly. The oscillatory and vibratory blade loads originate due to : (1) unsteady aerodynamic environment and (2) dynamic response of the flexible rotor blades. The dynamic response of the blades are determined by non-linear inertial couplings between flap, lag, elastic torsion and axial degrees of motion, moderately large deformations, large pitch angles required for rotor trim, damper properties, material non-linearities and rotor-fuselage dynamic interactions.

The problem of rotor loads and vibration has been the focus of dynamics research since the beginning of the industry. The aerodynamics of a rotor blade differ from that of a fixed wing due to the following phenomenon.

- Rotor inflow, generated by high RPM of the blades (around 250 for conventional main rotors), necessary for vertical flight.
- Cyclic variation of blade pitch angle, necessary for control.
- Time varying, asymmetric flow in forward flight with large variations of angle of attack in the advancing and retreating sides.
- Enormous compressibility effects including shocks on the advancing side and stalled flow on the retreating side.
- The complex, unsteady wake structure of each blade interacting with following blades.

Because of rotation, the outboard span stations of the blades generate more lift and trail strong tip vortices. The tip vortices are the dominant features of the wake and in general contribute to non-uniform inflow variation around the rotor disk. Unlike airplane wings, these vortices remain in the vicinity of the rotor disk and interact with the following blades.

A fixed wing aircraft uses wings for lift, control surfaces for vehicle control and thrusters for propulsion. On the other hand, in a rotary wing aircraft, the main rotor performs all three functions at the same time. The rotor disk angle is controlled by time varying 1/rev pitch inputs to the blades (using swash-plate). The rotor thrust is controlled by steady pitch input to the blades (collective angle). This generates steady and 1/rev air loads at each blade section which collectively determine the magnitude and orientation of the rotor thrust.

In forward flight, the asymmetric velocity variation around the rotor disk together with cyclic pitch angles and complex inflow distribution generate higher harmonic air loads, 3/rev and higher. For example, a velocity variation of zero and 1/rev creates a zero, 1 and 2/rev variation in the square of velocity, which when multiplied with 1/rev cyclic angles generates zero, 1, 2 and 3/rev airloads. The steady components are used to trim the vehicle, the 1/rev components are required for control, the higher harmonics give rise to rotor vibration. At certain flight conditions, significant higher harmonic air loads are generated creating severe rotor vibration - e.g., tip vortex induced airloads in transition flight, dynamic stall air loads in high thrust flight, unsteady transonic air loads at high speed flights and a combination of all in maneuvering flight.

The long slender rotor blades are highly flexible. As a result significant elastic bending deformations occur in flap, lag and twist in response to airloads. Because they are equi-spaced from one another in azimuth angle, and identical, their aerodynamic loading and structural dynamic response is expected to differ only in phase. And because they are all joined at the hub, the individual blade loads at the hub add up to cancel the non-integral harmonics of blade passage frequency. For example, as mentioned before, in the case of a 4 bladed rotor system like the UH-60A Black Hawk, only steady, 4/rev, 8/rev, 12/rev, i.e., in general pN_b/rev , where p is an integer, are transmitted from the rotor system to the hub. Dissimilarities or damage of the blades make them non-identical and generate non pN_b/rev loads.

For identical blades, only integral harmonics are transmitted. Because of simple trigonometry, the integral blade number harmonics in the fixed hub system are generated by the adjoining harmonics in the rotating blades. Thus, (3/4/5)/rev blade loads in the rotating frame generate 4/rev hub loads in the fixed frame, (7/8/9)/rev blade loads generate 8/rev hub loads and in general $(p+1)N_b$, pN_b , $(p-1)N_b/\text{rev}$ blade loads in the rotating frame generate pN_b/rev hub loads in the fixed frame. All harmonics of blade loads are important for blade design, but only blade passage harmonics (and multiples) and their adjoining harmonics have the potential for hub and fuselage vibration. The large deflection response of the rotor blades feeds back to the air loads which generate time varying aerodynamic stiffness and damping matrices. The damping of the rotor system comes primarily from aerodynamics. The structural response of the rotor blades are therefore aeroelastic in nature and governed by the periodic stiffness, damping and forcing functions. In addition, the moderate to large flap, lag and elastic torsion deformations of the blades form a nonlinear coupled system with complex boundary conditions and multiple load paths at the root.

Accurate prediction of rotor loads is key to advanced rotorcraft design. Attractive and radical low noise, high performance (range and endurance) rotor designs may be evaluated quickly and at low cost using reliable analyses methods. For a reliable analysis, it is necessary to understand and model the physics of structural dynamics and aerodynamics accurately. Such a capability does not exist today (discussed later). Designers rely on costly and time consuming wind tunnel and flight tests. Rotor aeromechanics is at the heart of the helicopter system and any modification in existing design cannot be undertaken unless its impact on blade loads, control loads and vibration are clearly ascertained. Prediction of control loads is important for designing more agile and maneuverable rotor systems. While the peak magnitudes are important for sizing and design of the control system components, the phase of the response is important for implementing control algorithms.

Apart from degraded ride quality, high vibration directly increases maintenance and operating costs because of frequent replacement schedules of critical fatigued components. The maintenance, and direct operating cost of a helicopter is the greatest hindrance toward its becoming a serious

candidate for civilian short haul flight. A helicopter with its unique vertical take off and landing capability offers the most promising solution for reducing airport and air traffic congestion. Vibration is one of the major hindrances to fulfilling this potential.

Smart structure actuated on-blade active control mechanisms show enormous potential for reducing and controlling rotor vibration [7, 8, 9, 10]. The actuator requirements and control limits can be reliably designed and tested, without expensive wind tunnel or flight tests, provided the mechanisms of helicopter vibration are well understood and predicted. Passive vibration reduction techniques, using composite tailoring [11] and structural optimization, can be devised and tested with confidence without expensive wind tunnel tests. A detailed discussion on smart structures technology can be found in Chopra [12].

10.4.1 Periodic Blade Forcing

In forward flight, the blade is exposed to periodic aerodynamic forcing consisting of many harmonics. Consider a simple example of a lift force occurring at a radial station r from the rotation axis.

$$L = \frac{1}{2}\rho V^2 c_a \alpha \quad \text{where } c_l = a\alpha$$

We have for small angles of attack

$$V^2 \approx U_T^2$$

$$\alpha \approx \theta - \frac{U_P}{U_T}$$

The lift force is then

$$L \approx \frac{1}{2}\rho a c (U_T^2 \theta - U_P U_T)$$

In forward flight we have

$$\theta = \theta_C(\psi) + \phi(\psi) = \theta_0 + \theta_{1C} \cos \psi + \theta_{1S} \sin \psi + \phi(\psi)$$

$$U_T = \Omega r + \mu \Omega R \sin \psi$$

$$U_P = \lambda \Omega R + r \dot{\beta} + \mu \beta \Omega R \cos \psi$$

$$\lambda = \lambda_0 + \lambda_{1C} \cos \psi + \lambda_{1S} \sin \psi + \lambda_{2C} \cos 2\psi + \lambda_{2S} \sin 2\psi \dots$$

The general steady state flap and twist responses are given by

$$\beta(\psi) = \beta_0 + \beta_{1C} \cos \psi + \beta_{1S} \sin \psi + \beta_{2C} \cos 2\psi + \beta_{2S} \sin 2\psi + \dots$$

$$\phi(\psi) = \phi_0 + \phi_{1C} \cos \psi + \phi_{1S} \sin \psi + \phi_{2C} \cos 2\psi + \phi_{2S} \sin 2\psi + \dots$$

The lift becomes

$$L = \frac{1}{2}\rho a c [(\Omega r + \mu \Omega R \sin \psi)^2 (\theta_0 + \theta_{1C} \cos \psi + \theta_{1S} \sin \psi + \phi_0 + \phi_{1C} \cos \psi + \phi_{1S} \sin \psi + \dots) - (\lambda_0 \Omega R + \lambda_{1C} \Omega R \cos \psi + \lambda_{1S} \Omega R \sin \psi + \lambda_{2C} \Omega R \cos 2\psi + \lambda_{2S} \Omega R \sin 2\psi + \dots - r \beta_{1C} \sin \psi + r \beta_{1S} \cos \psi - 2r \beta_{2C} \sin 2\psi + \dots) (\Omega r + \mu \Omega R \sin \psi)]$$

Thus

$$L = L(r, \sin \psi, \cos \psi, \sin 2\psi, \cos 2\psi, \sin 3\psi, \cos 3\psi, \sin 4\psi, \cos 4\psi, \dots)$$

Thus, the blade section lift is a function of radial position and consists of many harmonics. In a similar way, the other aerodynamic forces and moments acting on the blade are also periodic and consist of many harmonics. Typically, the magnitude of harmonics higher than 5/rev become smaller and are less important for the prediction of vibration.

10.4.2 Hub Loads in Rotating Frame

The aeroelastic response of the blades are determined using the aerodynamic forcing. The sectional blade loads can then be obtained using either the response (curvature method) or a combination of response and forcing (force summation). The sectional blade loads at the root are called the root loads or reaction forces at the blade root. The root loads can then be transferred to the hub. These are the hub loads in the rotating frame. The hub loads in the rotating frame can be denoted by f_x, f_y, f_z , (shear loads) and m_x, m_y, m_z (moments). For a physical feel, consider the case of a hingeless rotor, or an articulated rotor with zero hinge offset. Then the hub loads in the rotating frame are simply the blade root shears and bending moments

$$f_x(\psi) = s_x = \text{Drag shear load}$$

$$f_y(\psi) = s_r = \text{Radial shear load}$$

$$f_z(\psi) = s_z = \text{Vertical shear load}$$

$$m_x(\psi) = n_f = \text{Flap bending moment}$$

$$m_y(\psi) = n_t = \text{Torsion moment}$$

$$m_z(\psi) = -n_l = - \text{Lag bending moment}$$

Consider the general form of the blade root loads. Let ψ_m denote the azimuthal position of the m -th blade, where $m = 1, 2, \dots, N$. Then, the vertical shear load at the root of the m -th blade can be written as

$$\begin{aligned} s_z^{(m)} &= s_{z_0} + s_{z_{1C}} \cos \psi_m + s_{z_{1S}} \sin \psi_m + s_{z_{2C}} \cos 2\psi_m + s_{z_{2S}} \sin 2\psi_m + \\ &\quad s_{z_{3C}} \cos 3\psi_m + s_{z_{3S}} \sin 3\psi_m + \dots \quad m = 1, 2, \dots, N \\ &= s_{z_0} + \sum_{n=1}^{\infty} (s_{z_{nC}} \cos n\psi_m + s_{z_{nS}} \sin n\psi_m) \end{aligned} \quad (10.1)$$

Similarly the radial shear and drag shear loads can be written as

$$s_r^{(m)} = s_{r_0} + \sum_{n=1}^{\infty} (s_{r_{nC}} \cos n\psi_m + s_{r_{nS}} \sin n\psi_m) \quad m = 1, 2, \dots, N \quad (10.2)$$

$$s_x^{(m)} = s_{x_0} + \sum_{n=1}^{\infty} (s_{x_{nC}} \cos n\psi_m + s_{x_{nS}} \sin n\psi_m) \quad m = 1, 2, \dots, N \quad (10.3)$$

The flap, lag, and torsion moments can be written as

$$n_f^{(m)} = n_{f_0} + \sum_{n=1}^{\infty} (n_{f_{nC}} \cos n\psi_m + n_{f_{nS}} \sin n\psi_m) \quad m = 1, 2, \dots, N \quad (10.4)$$

$$n_l^{(m)} = n_{l_0} + \sum_{n=1}^{\infty} (n_{l_{nC}} \cos n\psi_m + n_{l_{nS}} \sin n\psi_m) \quad m = 1, 2, \dots, N \quad (10.5)$$

$$n_t^{(m)} = n_{t_0} + \sum_{n=1}^{\infty} (n_{t_{nC}} \cos n\psi_m + n_{t_{nS}} \sin n\psi_m) \quad m = 1, 2, \dots, N \quad (10.6)$$

10.4.3 Hub Loads in Fixed Frame

The hub loads in fixed frame are obtained by summation of the loads from all the blades. For a tracked rotor, this procedure cancels out many harmonics of the hub loads in the rotating frame. The hub loads in the fixed frame are

$$\begin{aligned}
 T = \text{Thrust} &= \sum_{m=1}^N s_z^{(m)} \\
 H = \text{Drag force} &= \sum_{m=1}^N (s_r^{(m)} \cos \psi_m + s_x^{(m)} \sin \psi_m) \\
 Y = \text{Side force} &= \sum_{m=1}^N (s_r^{(m)} \sin \psi_m - s_x^{(m)} \cos \psi_m) \\
 M_x = \text{Rolling moment} &= \sum_{m=1}^N n_f^{(m)} \sin \psi_m \\
 M_y = \text{Pitching moment} &= - \sum_{m=1}^N n_f^{(m)} \cos \psi_m \\
 Q = \text{Torque} &= \sum_{m=1}^N n_t^{(m)}
 \end{aligned} \tag{10.7}$$

For a tracked rotor, the thrust becomes

$$\begin{aligned}
 T &= N s_{z_0} + \sum_{m=1}^N \left[\sum_{n=1}^{\infty} (s_{z_{nC}} \cos n\psi_m + s_{z_{nS}} \sin n\psi_m) \right] \\
 &= N s_{z_0} + \sum_{n=1}^{\infty} \left[\sum_{m=1}^N (s_{z_{nC}} \cos n\psi_m + s_{z_{nS}} \sin n\psi_m) \right]
 \end{aligned} \tag{10.8}$$

Using

$$\begin{aligned}
 \frac{1}{N} \sum_{m=1}^N \cos n\psi_m &= f_n \cos n\psi \\
 \frac{1}{N} \sum_{m=1}^N \sin n\psi_m &= f_n \sin n\psi
 \end{aligned} \tag{10.9}$$

where

$$\begin{aligned}
 f_n &= 1 & \text{if } n = pN & \quad p \text{ integer} \\
 f_n &= 0 & \text{otherwise}
 \end{aligned} \tag{10.10}$$

and $p\psi$ is the azimuthal location of the first blade, the thrust becomes

$$T = N s_{z_0} + N \sum_{p=1}^{\infty} (s_{z_{pNC}} \cos pN\psi_m + s_{z_{pNS}} \sin pN\psi_m) \tag{10.11}$$

The first component is the steady thrust. The other components are all pN/rev harmonics. The rest of the harmonics get cancelled at the hub. Note that the pN -th harmonic of the thrust is

caused by the pN -th harmonic of the blade root shear. Consider the rotor drag force. Again, assume a tracked rotor.

$$\begin{aligned}
 H &= \sum_{m=1}^N \left[s_{r_0} + \sum_{n=1}^{\infty} (s_{r_{nC}} \cos n\psi_m + s_{r_{nS}} \sin n\psi_m) \right] \cos \psi_m \\
 &\quad \sum_{m=1}^N \left[s_{x_0} + \sum_{n=1}^{\infty} (s_{x_{nC}} \cos n\psi_m + s_{x_{nS}} \sin n\psi_m) \right] \sin \psi_m \\
 &= \sum_{m=1}^N [s_{r_0} \cos \psi_m + s_{x_0} \sin \psi_m] + \frac{1}{2} \sum_{m=1}^N \sum_{n=1}^{\infty} \{s_{r_{nC}} [\cos(n+1)\psi_m + \cos(n-1)\psi_m] \\
 &\quad + s_{r_{nS}} [\sin(n+1)\psi_m + \sin(n-1)\psi_m] + s_{x_{nC}} [\sin(n+1)\psi_m - \sin(n-1)\psi_m] \\
 &\quad + s_{x_{nS}} [\cos(n-1)\psi_m - \cos(n+1)\psi_m]\}
 \end{aligned} \tag{10.12}$$

Note that

$$\begin{aligned}
 \sum_{m=1}^N \cos \psi_m &= \sum_{m=1}^N \sin \psi_m = 0 \\
 \frac{1}{N} \sum_{m=1}^N \cos(n+1)\psi_m &= \cos(n+1)\psi, \quad \text{for } n = pN - 1, \quad p \text{ integer} \\
 \frac{1}{N} \sum_{m=1}^N \cos(n-1)\psi_m &= \cos(n-1)\psi, \quad \text{for } n = pN + 1, \quad p \text{ integer}
 \end{aligned}$$

Therefore the following terms can be written as

$$\begin{aligned}
 \sum_{m=1}^N \sum_{n=1}^{\infty} s_{r_{nC}} \cos(n+1)\psi_m &= \sum_{n=1}^{\infty} \sum_{m=1}^N s_{r_{nC}} \cos(n+1)\psi_m = \sum_{n=1}^{\infty} N s_{r_{(pN-1)C}} \cos pN\psi \\
 \sum_{m=1}^N \sum_{n=1}^{\infty} s_{r_{nC}} \cos(n-1)\psi_m &= \sum_{n=1}^{\infty} \sum_{m=1}^N s_{r_{nC}} \cos(n-1)\psi_m = \sum_{n=1}^{\infty} N s_{r_{(pN+1)C}} \cos pN\psi
 \end{aligned}$$

The final expression for rotor drag then becomes

$$\begin{aligned}
 H &= \frac{N}{2} \sum_{p=1}^{\infty} \left[(s_{r_{(pN-1)C}} - s_{x_{(pN-1)S}}) \cos pN\psi + (s_{r_{(pN-1)S}} + s_{x_{(pN-1)C}}) \sin pN\psi \right] \\
 &\quad \frac{N}{2} \sum_{p=1}^{\infty} \left[(s_{r_{(pN+1)C}} + s_{x_{(pN+1)S}}) \cos pN\psi + (s_{r_{(pN+1)S}} - s_{x_{(pN+1)C}}) \sin pN\psi \right]
 \end{aligned} \tag{10.13}$$

Similarly the side force is

$$\begin{aligned}
 Y &= \frac{N}{2} \sum_{p=1}^{\infty} \left[- (s_{r_{(pN-1)S}} + s_{x_{(pN-1)C}}) \cos pN\psi + (s_{r_{(pN-1)C}} - s_{x_{(pN-1)S}}) \sin pN\psi \right] \\
 &\quad + \frac{N}{2} \sum_{p=1}^{\infty} \left[(s_{r_{(pN+1)S}} - s_{x_{(pN+1)C}}) \cos pN\psi - (s_{r_{(pN+1)C}} + s_{x_{(pN+1)S}}) \sin pN\psi \right]
 \end{aligned} \tag{10.14}$$

Again, the inplane hub loads H and Y consists of harmonics which are multiples of N/rev . Note that unlike the thrust T , the pN/rev harmonics here are caused by the $pN + 1$ and $pN - 1/\text{rev}$

harmonics of blade inplane shears in the rotating frame. The hub roll moment is

$$\begin{aligned}
 M_x &= \sum_{m=1}^N \left[n_{f_0} + \sum_{n=1}^{\infty} (n_{f_{nC}} \cos n\psi_m + n_{f_{nS}} \sin n\psi_m) \right] \sin \psi_m \\
 &= \sum_{m=1}^N n_{f_0} \sin \psi_m + \frac{1}{2} \sum_{m=1}^N \sum_{n=1}^{\infty} \{ n_{f_{nC}} [\sin(n+1)\psi_m - \sin(n-1)\psi_m] \\
 &\quad + n_{f_{nS}} [\cos(n-1)\psi_m - \cos(n+1)\psi_m] \} \\
 &= \frac{N}{2} \sum_{p=1}^{\infty} \left[-n_{f_{(pN-1)C}} \sin pN\psi - n_{f_{(pN-1)S}} \cos pN\psi \right] \\
 &\quad + \frac{N}{2} \sum_{p=1}^{\infty} \left[-n_{f_{(pN+1)C}} \sin pN\psi + n_{f_{(pN+1)S}} \cos pN\psi \right]
 \end{aligned} \tag{10.15}$$

Similarly the hub pitch moment is

$$\begin{aligned}
 M_y &= -\frac{N}{2} \sum_{p=1}^{\infty} \left[n_{f_{(pN-1)C}} \cos pN\psi + n_{f_{(pN-1)S}} \sin pN\psi \right] \\
 &\quad - \frac{N}{2} \sum_{p=1}^{\infty} \left[n_{f_{(pN+1)C}} \cos pN\psi + n_{f_{(pN+1)S}} \sin pN\psi \right]
 \end{aligned} \tag{10.16}$$

Thus the pN/rev harmonics of the rotor roll and pitch moments are caused by the $pN+1$ and $pN-1/\text{rev}$ harmonics of the flap bending moments. The hub loads in the fixed frame for 2, 3, and 4 bladed rotors are summarized in the following tables.

Table 10.1: Vertical Loads Transmitted by Blades to Hub

Vertical Shear at Blade Root s_z Harmonics	Hub Load T in Fixed Frame		
	2-Bladed Rotor	3-Bladed Rotor	4-Bladed Rotor
s_{z_0}	$2s_{z_0}$	$3s_{z_0}$	$4s_{z_0}$
$s_{z_{1c}} \cos \psi_m$	0	0	0
$s_{z_{1s}} \sin \psi_m$	0	0	0
$s_{z_{2c}} \cos 2\psi_m$	$2s_{z_{2c}} \cos 2\psi$	0	0
$s_{z_{2s}} \sin 2\psi_m$	$2s_{z_{2s}} \sin 2\psi$	0	0
$s_{z_{3c}} \cos 3\psi_m$	0	$2s_{z_{3c}} \cos 3\psi$	0
$s_{z_{3s}} \sin 3\psi_m$	0	$2s_{z_{3s}} \sin 3\psi$	0
$s_{z_{4c}} \cos 4\psi_m$	$2s_{z_{4c}} \cos 4\psi$	0	$4s_{z_{4c}} \cos 4\psi$
$s_{z_{4s}} \sin 4\psi_m$	$2s_{z_{4s}} \sin 4\psi$	0	$4s_{z_{4s}} \sin 4\psi$
$s_{z_{5c}} \cos 5\psi_m$	0	0	0
$s_{z_{5s}} \sin 5\psi_m$	0	0	0
$s_{z_{6c}} \cos 6\psi_m$	$2s_{z_{6c}} \cos 6\psi$	$3s_{z_{6c}} \cos 6\psi$	0
$s_{z_{6s}} \sin 6\psi_m$	$2s_{z_{6s}} \sin 6\psi$	$3s_{z_{6s}} \sin 6\psi$	0

10.5 Vibration Control

For purposes of a simple illustration the helicopter can be thought of as a system of springs, dampers and masses connected to each other, which are being forced by external vibratory forces. There

are many natural frequencies and so one expects a complex response. If we can assume that all the blades are identical, structurally and aerodynamically (a tracked rotor case), then the vibration in the fixed system is simplified. The periodic blade loads in the rotating system are transmitted to the body in the fixed frame at a dominant frequency of $N\Omega$ rad/s, where N is the number of blades and Ω is the rotational speed. Sometimes, the higher multiple harmonics of this frequency, $2N\Omega$ and $3N\Omega$, are also important. The rotor acts as a big filter and transmits only pN/rev harmonics to the body, where p is an integer, and all other harmonics cancel themselves at the rotor hub.

The pN hub vertical force and yaw moment (torque) in the fixed frame are caused by vertical shear and lag moments in the rotating system at the same frequency (pN/rev). This is because the excitation forces are symmetric and there is no change of frequency due to the transformation from one frame to another reference frame. However, the pN/rev inplane hub forces and pitch and roll moments in the fixed frame are caused by the blade oscillatory lag shear and flapwise moments at two frequencies of $pN \pm 1/\text{rev}$ in the rotating frame. This makes vibration reduction easier since only selected harmonics are to be suppressed.

There are two methods to reduce vibration.

1. Design Process
2. Suppression Devices

In the Design Process, the structural and aerodynamic characteristics of the blade are tailored to achieve reduction in vibration. This requires an optimization procedure during during. The key parameters like disk loading, tip speed, solidity and blade chord are not designed based on vibration requirements, but they influence vibration. The selection of other parameters like blade twist and tip shape can be made to reduce vibration. An important requirement is to avoid resonances with excitation harmonics. But suitable use of composite materials and application of structural optimization techniques on the blade and blade, vibration can be reduced by a significant amount.

The Suppression Devices can be of many types. Broadly, they are classified into two categories:

1. Passive control devices
2. Active control devices

In passive control devices the vibration source is either isolated or diffused. When the vibration source is isolated the device is called an isolator. When the vibration source is diffused the device is called an absorber. Passive devices are tuned to a particular flight condition. In general, they incur a large weight penalty. About 70% reduction of vibration is possible with a passive device at the tuned frequency.

In active control devices the vibration source is suppressed. Compared to passive devices, active devices can be tuned in flight, and can easily target multiple frequencies. The weight penalty is less than passive devices. More than 90% reduction in vibration is possible with a passive device.

10.6 Passive Vibration Control

10.6.1 Vibration Isolators

Vibration isolators are often used to reduce helicopter vibration. Isolating materials are pads of rubber, cork or felt, or metalli springs. These are placed between the vibrating system and its supporting structure. All of these materials possess damping as well as elastic properties and can be effective in reducing the maximum transmitted force from the vibrating system to the support. It is not uncommon to use a soft mounting of the rotor and transmission to the airframe. However one has to be careful with the soft mounting, in particular with articulated rotors, in order not to seriously impair the ground resonance instability.

10.6.2 Vibration Absorbers

Dynamic absorbers are used to reduce vibration in helicopters. In its simplest form, a dynamic absorber is a single-degree-of-freedom spring-mass system that is added to a structure whose vibration needs to be reduced. For example, consider a mass M attached to a foundation by a spring k vibrating in response to a force $F \sin \omega t$ applied on the mass. See Fig. 10.2. By itself, the support reaction at the foundation would be $R = F \sin \omega t$.

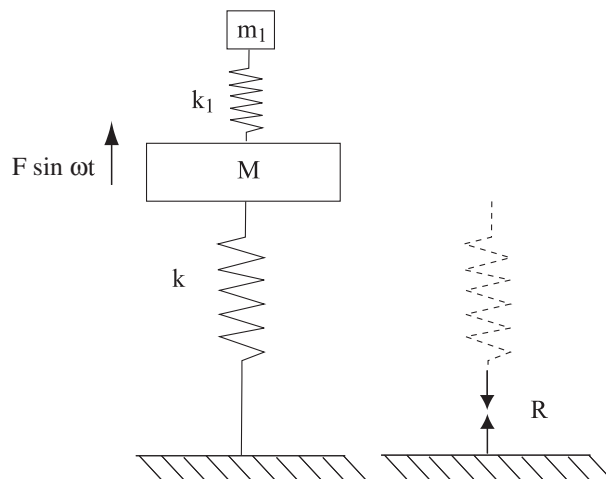


Figure 10.2: A simple two degree of freedom spring-mass vibration absorber

The support reaction can be reduced to zero, $R = 0$, by the following method. Attach an auxiliary single-degree-of-freedom spring-mass system of mass m_1 and stiffness k_1 to the existing structure such that

$$\sqrt{\frac{k_1}{m_1}} = \omega$$

The amplitude of vibration of M now becomes zero. The absorber is effective when the excitation frequency is fixed. Sometimes a damper is introduced. This is called the damped dynamic absorber. In the case of a helicopter, a dynamic absorber can be installed on the body tuned to the troublesome frequency, say N/rev . If the design is perfect and the frequency is fixed, the auxiliary mass vibrates to add to the support structure an oscillating force that is equal and opposite to the force that is causing the vibration.

The best design is not to use any extra weight for vibration absorbers. Sikorsky has used batteries and Bell has developed the Node-Matic system that uses transmissions as the moving weight.

10.6.3 Bifilar Pendulum absorber

An example of the dynamic absorber is a simple or bifilar pendulum mounted on each rotor blade near the hub. Typically it is a spherical ball of small mass compared to the blade mass and is mounted on a cantilevered beam. It is tuned to a particular frequency and acts as a dynamic absorber.

Sikorsky has successfully applied a bifilar pendulum to its 4-bladed helicopters (S-76, S-92, UH-60 series), tuned to two frequencies, $3/\text{rev}$ and $5/\text{rev}$ in the inplane direction. See Fig. 10.3. The S-92 has four heavy pendulum masses that oscillate at small amplitudes. F is the force produced by opposing bifilar masses at one instant in time. This force rotates in the direction of rotor rotation at $N - 1/\text{rev}$.

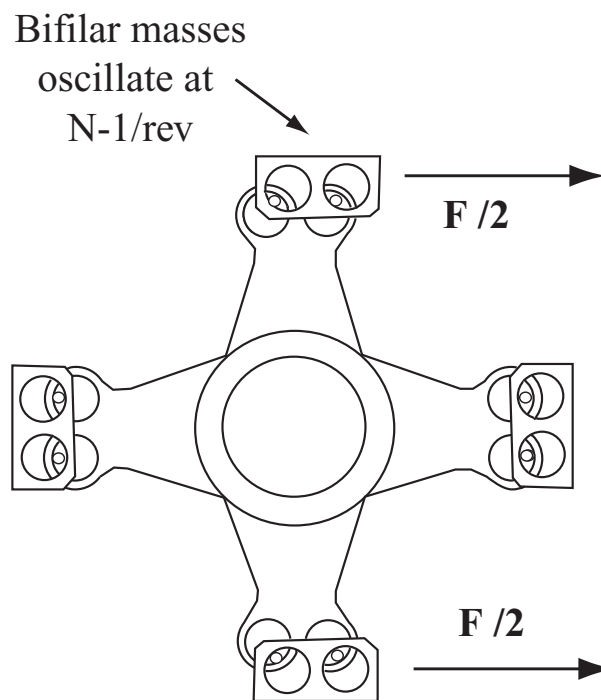


Figure 10.3: Bifilar pendulum of the S-92 helicopter

10.7 Active Vibration Control

In active vibration control the vibration is suppressed by eliminating the prime source of excitation – the unsteady aerodynamic forces on the blades. The primary components of an active vibration suppression system are:

1. Acceleration transducers that sense the vibratory response of the fuselage.
2. A actuator system to implement the control algorithm.
3. A flightworthy micro-computer, which incorporates the algorithm for suppressing vibration.
4. A signal conditioning system, i.e. an electronic control unit, which interfaces between the sensors, the computer, and the actuators.

10.7.1 Multicyclic Vibration Control or Higher Harmonic Control (HHC)

In Higher Harmonic Control (HHC) the entire blade is excited at higher harmonics of rotational speed ($2/\text{rev}$ and higher) in addition to the $1/\text{rev}$ control inputs. The unsteady airloads are changed to cancel the existing troublesome harmonics. The net effect is that the existing airloads at higher frequencies are reduced with little effect on the basic rotor performance.

Many options of implementation of higher harmonic control of different types of rotors have been considered. The most common one is full blade feathering at the root. In addition to vibration reduction, the application of HHC can be used for blade stress reduction, for improved performance by delaying the onset of retreating blade stall, and for gust load alleviation.

Both, small scale and full scale models have been tested in the wind tunnel for HHC of vibration. McDonnell Douglas Helicopters (formerly Hughes, now Boeing, Mesa) has successfully applied HHC on the OH-6 helicopter and demonstrated the concept through flight testing of the aircraft. For the modified OH-6A, higher harmonic blade pitch control was achieved by superimposing $4/\text{rev}$

swashplate motion on top of the basic collective and cyclic control inputs. Consider a swashplate lateral tilt of ϕ_X . The pitch link is attached to the swashplate at a radial distance of r_p . It is ahead of the blade azimuth by an angle α_p . If the blade is at an azimuth ψ the vertical displacement of the pitch link is

$$d = \phi_X r_p \sin(\psi + \alpha_p)$$

If the pitch horn length is a_p , then assuming a straight pitch link, the blade root angle is given by

$$\sin \theta = \left(\frac{\phi_X r_p}{a_p} \right) \sin(\psi + \alpha_p)$$

Similarly for a swashplate longitudinal tilt of ϕ_Y , the blade root angle is given by

$$\sin \theta = - \left(\frac{\phi_Y r_p}{a_p} \right) \cos(\psi + \alpha_p)$$

When both ϕ_X and ϕ_Y are prescribed, we have assuming a small θ ,

$$\theta(\psi) = \left(\frac{\phi_X r_p}{a_p} \right) \sin(\psi + \alpha_p) - \left(\frac{\phi_Y r_p}{a_p} \right) \cos(\psi + \alpha_p)$$

In addition to longitudinal and lateral tilts, a vertical displacement Z can be prescribed. Thus in general the swashplate displacement and tilts are related to the blade root pitch angle by

$$\theta(\psi) = Z + \left(\frac{\phi_X r_p}{a_p} \right) \sin(\psi + \alpha_p) - \left(\frac{\phi_Y r_p}{a_p} \right) \cos(\psi + \alpha_p)$$

A special case is when the pitch link is attached 90° ahead of the blade, i.e. $\alpha_p = \pi/2$. Then

$$\theta(\psi) = Z + \left(\frac{\phi_X r_p}{a_p} \right) \cos \psi + \left(\frac{\phi_Y r_p}{a_p} \right) \sin \psi$$

First, constant values of swashplate tilt introduces 1/rev cyclic inputs at the blade root. Second, N /rev harmonics of swashplate tilt introduces $N \pm 1$ /rev harmonics of cyclic inputs. Third, a vertical displacement get transferred to the blades directly as a collective input. Thus, perturbing the swashplate at 4/rev both collectively (in Z) and in pitch (ϕ_Y) and roll (ϕ_X) results in 3, 4, and 5/rev blade feathering in the rotating system. The main rotor rotational speed for the OH-6A is 8 Hz. Thus a 4/rev input is 32 Hz. The pitch, roll, and collective motion of the stationary swashplate at this frequency was provided by three electro-hydraulic high frequency servo-actuators. The three actuators were installed in the stationary system where they replaced the conventional rod-end links between the control mixer and the stationary swashplate.

Generally, the helicopter model is expressed in the frequency domain through a transfer function relating the input harmonics to the output response harmonics. Different control concepts have been tried to implement the higher harmonic controls. A complete discussion on these controllers can be found in Chopra and McCloud [13].

HHC model testing in wind tunnel have been performed by McCloud (71,78), Sissingh (75), Shaw (75,80,85), Hammond (78), Lehmann (85). HHC flight testing have been reported in Bell (62), U.S.Army-McDonnell Douglas (82), Sikorsky (86), Aerospatiale (86). Numerical simulations mostly have been limited to unstalled conditions.

10.7.2 Control Algorithms

Different control algorithms have been implemented for HHC of helicopter vibration. In order to implement the algorithms a helicopter model is required. The model relates the HHC inputs to the vibration. One simple linear quasi-static frequency-domain representation of the helicopter is given below. Here, Z is the response vector, Θ is the multi-cyclic input vector, T is the transfer function which relate the two, and Z_0 is the uncontrolled response vector. Also added is the measurement noise v which is random in nature.

$$Z = Z_0 + T\Theta + v \tag{10.17}$$

A pictorial representation is given in Fig. 10.4. The vibrations Z , Z_0 and the control inputs Θ can be in the rotating or fixed frame. T and Z_0 depend on flight conditions. For example, Z can be a vector of 12 components (dimension 12×1) consisting of the sine and cosine harmonics of the six 4/rev vibratory hub loads in the fixed frame. The input vector Θ can be a vector of 6 components (dimension 6×1) consisting of the sine and cosine components of the 3, 4, and 5/rev multi-cyclic root pitch inputs in the rotating frame. The transfer matrix T then has a dimension of (12×6) . The measurement noise v is assumed to be Gaussian white noise with zero mean that has a variance or noise level defined by

$$E(v_n v_i) = r_n \delta_{ni}$$

The r_n represents measurement noise and is based on sensor accuracy. A meaningful value can be assigned to r_n . The above representation of the helicopter can be cast into two types of models: (i)

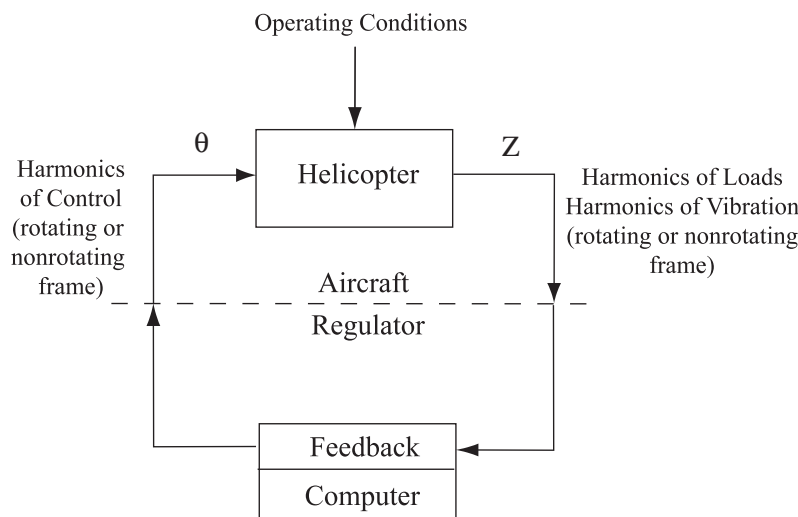


Figure 10.4: Multicyclic Control of Helicopter Vibration

a global model and (ii) a local model. The global model is linear over the entire range or duration of control. At any time step n we have

$$Z_n = Z_0 + T\Theta_n + v \tag{10.18}$$

The local model is linear only about a current control value

$$Z_n = Z_{n-1} + T_{n-1} (\Theta_n - \Theta_{n-1}) + v \tag{10.19}$$

Thus the local model is applicable even for nonlinear conditions. The T -matrix is linearized about the current control value and the range of $\Delta\Theta_n = \Theta_n - \Theta_{n-1}$ is assumed small. The current time t_n is given by

$$t_n = n\Delta t$$

where Δt is assumed to be long enough so that the transients have died down. This is typically about one or two rotor revolutions. Before the HHC control algorithms can be implemented, the model characteristics, Z_0 and T must be estimated. This estimation can be performed using flight test data, wind tunnel data, or from a mathematical model e.g. a comprehensive analysis. The procedure is called model identification.

The different control algorithms implemented for HHC were classified by Johnson [14]. From the simplest to the most refined they are as follows.

1. **Open-loop, off-line:** Model behavior (i.e., Z_0 and T) is identified off-line. The inputs (i.e., Θ) are based on uncontrolled vibration (i.e., Z_0).
2. **Closed-loop, off-line:** Model behavior is identified off-line. The inputs are based on measured vibration.
3. **Open-loop, adaptive:** Model behavior is identified on-line. There are two categories: (i) only the uncontrolled vibration Z_0 is identified on-line, and (ii) both Z_0 and the transfer matrix T is identified on-line. Both the categories involve feedback loops. The inputs are however still based on the identified uncontrolled vibration. Hence this is still termed open-loop.
4. **Closed-loop, adaptive:** Model behavior is identified online. The inputs are based on measured vibration.

For the off-line identification algorithms (the first two items given above) the characteristics of the multicyclic control system, Z_0 and T are assumed invariant with time. They are identified at the start and the control gains are fixed. Thus, this identification is applicable only to a global model. For the on-line identification algorithms, the characteristics of the control system are continuously updated with time; the control gains also vary with time. Thus this identification is applicable to both global and local models. In case of the local model, the T -matrix need to be identified for each and every time cycle. The meaning of open-loop control is that the inputs Θ_n depend only on the uncontrolled vibration level, Z_0 . For closed-loop control Θ_n depend on the measured vibration level of the previous time cycle, Z_{n-1} .

In this section, we assume a deterministic controller i.e., the properties of the model are known. In this case, for optimal control, the dependance, which relates the control inputs to the vibration levels, is based on the minimization of a performance function.

$$J = Z_n^T W_Z Z_n + \Theta_n^T W_\Theta \Theta_n + \Delta \Theta_n^T W_{\Delta\Theta} \Delta \Theta_n \quad (10.20)$$

where W_Z , W_Θ , and $W_{\Delta\Theta}$ are the weighting matrices for response, pitch controls, and the pitch control rates. Typically, these are diagonal matrices. The first term controls the vibration. Setting any of the diagonal entrees to zero unconstrains that component of vibration. The diagonal entrees can be selected differently to introduce different weights to different components of vibration depending on their severity. The second term controls the inputs, e.g. constrains the actuator displacement. The third term controls the control rate and reduces large transients. For optimal control inputs the performance function J is minimized, which means

$$\frac{\partial J}{\partial \Theta_n} = 0 \quad \text{for each component of } \Theta_n$$

Assume that equal weight is given to all loads, i.e. $W_Z = I$, and the control inputs are unconstrained, i.e. $W_\Theta = 0$. The optimization result can be put in one of the following two forms

$$\begin{aligned} \Theta_n &= \Theta_{n-1} + CZ_{n-1} \quad \text{used in closed loop control} \\ \Theta_n &= CZ_0 + C_{\Delta\Theta} \Theta_{n-1} \quad \text{used in open loop control} \end{aligned} \quad (10.21)$$

where

$$C = -DT^T W_Z \quad (10.22)$$

$$C_{\Delta\Theta} = DW_{\Delta\Theta} \quad (10.23)$$

$$D = (T^T W_Z T + W_{\Delta\Theta})^{-1} \quad (10.24)$$

$W_{\Delta\Theta}$ does not affect the steady-state solution but affects the convergence time due to control sluggishness. The gain matrix C depends on the transfer matrix T . For on-line identification, T is updated continuously and hence C is updated continuously. In open-loop control Θ_n depends on Z_0 and T (via C), not Z_{n-1} , hence the name open-loop. But Z_0 and T can be identified at time n using Z_{n-1} . Then the system is called open-loop adaptive system. Note that it is a feedback system but as the inputs do not depend directly on Z_{n-1} it is classified as open loop.

In the next sections methods by which the control parameters of the system can be identified are described. The following symbols will be used.

T, Z_0 : Actual helicopter characteristics

\hat{T}, \hat{Z}_0 : Estimated or identified helicopter characteristics

10.7.3 Off-line Identification

For off-line identification, a set of input-output measurements are used with a least-squared-error method. The off-line identification is useful not only for control algorithms which use this method, but also for control algorithms which use on-line identification. In the latter case, a good off-line estimate of initial rotor characteristics are important for stabilizing the system, reduce transients, and faster convergence. Consider the following dimensions

$Z : j \times 1$ for example $j = 12$

$Z_0 : j \times 1$ same dimension as Z

$\Theta : m \times 1$ for example $m = 6$

$T : j \times m$ for example 12×6

The measurement noise v introduced in the output harmonics (eqn. 10.17) is assumed to be random with a Gaussian distribution. They are identified by their mean and standard deviation. Θ is assumed to contain no noise. For off-line identification, both T and Z_0 can be estimated simultaneously. Alternatively, Z_0 can be obtained directly by setting $\Theta = 0$. Then identify only the T matrix. For a set of N control inputs, independent of each other, the T matrix is identified by the least-squared-error method as

$$T = Z\Theta^T (\Theta\Theta^T)^{-1} \quad (10.25)$$

Θ here consists of N columns of independent control inputs. Z consists of N columns of output vibration. Thus

$Z : j \times N$ for example $12 \times N$

$\Theta : m \times N$ for example $6 \times N$

The minimum number of measurements N necessary is same as the dimension of input harmonics, m . For a good estimate typically N is two or three times this value.

10.7.4 On-line Identification

For on-line identification, the model characteristics are continuously updated with time, using a Kalman filter estimation [17]. The reason for using a Kalman-filter is as follows. Let us say there are 6 control inputs, i.e. $m = 6$, and 12 vibration measurements, i.e. $j = 12$. Then the T matrix has $j \times m = 12 \times 6$ entries. At a given time n we have only 12 measurements. Thus the number of unknowns is greater than equations. Through the Kalman filter, the T matrix is divided into 12 states (instead of 12×6 entries); a prior estimation of the state is made at the time of measurement and then the estimation of the state is updated using the current measurement. This is the basic idea of a Kalman filter, the combining of the previous estimate with the current measurement based on the relative accuracy of the two quantities, to refine the estimate of unknowns which are greater in number than the number of equations.

For purposes of notation let each row of T be organized into a column vector denoted by t_j . A typical form of the j -th measurement Z_j is then

$$Z_j = \Theta^T t_j + v_j$$

$$Z_j : 1 \times 1$$

$$\Theta_T : 1 \times m$$

$$t_j : m \times 1$$

To denote that the j -th measurement is taken at time n the above can be re-written as

$$Z_{jn} = \Theta^T t_{jn} + v_{jn}$$

The actual form depends on whether Z_0 is being identified and whether the global or local model is being used. For convenience, drop j , and write the j -th measurement of Z at time n as

$$Z_n = \Theta^T t_n + v_n \quad j\text{-th measurement of } Z$$

The variation of t is assumed to follow

$$t_{n+1} = t_n + u_n$$

where u is the process noise. The process noise u is assumed to be Gaussian white noise with zero mean that has a variance or noise level defined by

$$E(u_n u_i) = Q_n \delta_{ni}$$

The elements of Q represent the variation of the actual t from the estimated one. For changing flight conditions, Q can be large. A large value of Q can cause convergence problems. Thus, while the measurement noise level r is relatively easy to assign, Q is difficult to assign. An acceptable value can be found using trial and error based on the quality of estimation that results. Assume that we have an estimate of t (i.e. t_j , the j -th row of the transfer matrix T) at the $(n-1)$ -th cycle. Now want a new estimate of t based on the current measurements made in the n -th cycle. The Kalman filter gives a minimum-error variance solution

$$\hat{t}_n = \hat{t}_{n-1} + K_n (Z_n - \Theta_n^T \hat{t}_{n-1}) \tag{10.26}$$

$$\hat{t}_n, \hat{t}_{n-1} : m \times 1$$

$$K_n : m \times 1$$

$$Z_n - \Theta_n^T \hat{t}_{n-1} : 1 \times 1$$

where

$$\begin{aligned} K_n &= \frac{P_n \Theta_n}{r_n} \\ P_n &= M_n - \frac{M_n \Theta_n \Theta_n^T M_n}{r_n + \Theta_n^T M_n \Theta_n} \\ M_n &= P_{n-1} + Q_{n-1} \end{aligned} \quad (10.27)$$

M_n is the covariance of error in the estimate of t_n before measurement. P_n is the covariance of error in the estimate of t_n after measurement. To simplify calculations, it is possible to assume Q and r do not vary with time. Also, Q , r and P_0 can be assumed to be proportional to the same function f_j , where j represents the measurement. This results in

$$P_{jn} = f_j P_n \quad \text{and} \quad M_{jn} = f_j M_n$$

where P_n is a function of time and f_j is a function of measurement. The Kalman gain matrix is same for all measurements. Assume that the ratio Q_{jn}/r_{jn} is the same for every measurement. Then the Kalman state equations put together gives

$$\hat{T}_n = \hat{T}_{n-1} + \left(Z_n - \hat{T}_{n-1} \Theta_n \right) K_n^T \quad (10.28)$$

Note that P_n and K_n are calculated only once during each time cycle. The entire matrix T_n is then identified in a single step, a big reduction in computation time.

10.7.5 Open-Loop Off-Line Control

T and Z_0 are identified off-line. The weighting function for input rates $W_{\Delta\Theta}$ must be zero. The optimal control solution is

$$\Theta = C \hat{Z}_0 \quad (10.29)$$

When implemented gradually in n cycles, $n = 1, 2, \dots, N$, it becomes

$$\Theta_n = \frac{n}{N} C \hat{Z}_0 \quad (10.30)$$

10.7.6 Closed-Loop Off-Line Control

The model characteristics are identified initially and assumed invariant. This controller is applicable only to a global model. The optimal control solution is

$$\Theta_n = \Theta_{n-1} + C Z_{n-1} \quad (10.31)$$

Substitute

$$Z_{n-1} = Z_0 + T \Theta_{n-1} + v_{n-1}$$

to obtain

$$\Theta_n = D \left[\hat{T}^T \left(\hat{T} - T \right) + W_{\Delta\Theta} \right] \Theta_{n-1} - D \hat{T}^T \left(Z_0 + v_{n-1} \right) \quad (10.32)$$

where

$$D = \left(\hat{T}^T W_Z \hat{T} + W_{\Delta\Theta} \right)^{-1} \quad (10.33)$$

The stability of the closed system is determined by the eigenvalues of

$$D \left[\hat{T}^T \left(\hat{T} - T \right) + W_{\Delta\Theta} \right]$$

10.7.7 Open-Loop On-Line Control

The model characteristics are continuously updated with time. The open-loop on-line (i.e., adaptive) controllers are classified according to the parameter being identified. There are two types: (i) Z_0 is identified on-line; T is identified off-line initially and assumed invariant, and (ii) both Z_0 and T are identified on-line. Both require an initial transfer function T .

On-Line Identification of Z_0 only

The Kalman estimate of Z_0 is

$$\hat{Z}_{0n} = \hat{Z}_{0n-1} + \left(Z_n - \hat{T}\Theta_n - \hat{Z}_{0n-1} \right) K_n \quad (10.34)$$

where K_n is determined as follows

$$M_n = P_{n-1} + Q \quad (10.35)$$

$$P_n = rM_n / (r + M_n) \quad (10.36)$$

$$K_n = M_n / (r + M_n) \quad (10.37)$$

Note that P_n and M_n are simply scalars in this case. The optimal controls are

$$\Theta_n = C\hat{Z}_{0n-1} + C_{\Delta\Theta}\Theta_{n-1} \quad (10.38)$$

where C and $C_{\Delta\Theta}$ are feedback gains fixed with time. The vibration response is

$$Z_n = Z_0 + T\Theta_n + v_n$$

where T and Z_0 are the true model characteristics. The estimation and control equations can be combined to obtain

$$\begin{bmatrix} I & 0 \\ (\hat{T} - T)K_n & I \end{bmatrix} \begin{Bmatrix} \Theta_n \\ Z_{0n} \end{Bmatrix} = \begin{bmatrix} C_{\Delta\Theta} & C \\ 0 & (I - K_n)I \end{bmatrix} \begin{Bmatrix} \Theta_{n-1} \\ Z_{0n-1} \end{Bmatrix} + \begin{Bmatrix} 0 \\ (Z_0 + v_n)K_n \end{Bmatrix} \quad (10.39)$$

The stability of the system is determined by the eigenvalues of

$$\begin{bmatrix} I & 0 \\ (\hat{T} - T)K_n & I \end{bmatrix}^{-1} \begin{bmatrix} C_{\Delta\Theta} & C \\ 0 & (I - K_n)I \end{bmatrix}$$

On-Line Identification of T and Z_0

Here both T and Z_0 are identified continuously with time-cycles using a Kalman-filer estimation. This is therefore more suitable for varying flight conditions than the first case where only Z_0 is identified. The Kalman estimation is

$$\begin{bmatrix} \hat{T}_n \\ \hat{Z}_{0n} \end{bmatrix} = \begin{bmatrix} \hat{T}_{n-1} \\ \hat{Z}_{0n-1} \end{bmatrix} + \begin{bmatrix} K_n \\ Kz_n \end{bmatrix} \left(Z_n - \hat{Z}_{0n-1} - \hat{T}_{n-1}\Theta_n \right) \quad (10.40)$$

where K_n is determined as follows

$$M_n = P_{n-1} + Q_{n-1} \quad (10.41)$$

$$P_n = M_n - \frac{M_n \begin{bmatrix} \Theta_n \\ 1 \end{bmatrix} (\Theta_n^T I) M_n}{[r_n + (\Theta_n^T I) M_n] \begin{bmatrix} \Theta_n \\ 1 \end{bmatrix}} \quad (10.42)$$

$$K_n = \frac{P_n \begin{bmatrix} \Theta_n \\ 1 \end{bmatrix}}{r_n} \quad (10.43)$$

The optimal controls are same as before

$$\Theta_n = C\hat{Z}_{0n-1} + C_{\Delta\Theta}\Theta_{n-1} \quad (10.44)$$

except that the feedback gains, C and $C_{\Delta\Theta}$, are now continuously updated with time.

10.7.8 Closed-Loop On-Line Control

The model characteristics are updated continuously with time. The controller may use both global and local models.

Global Model

The controller here is similar to the open-loop adaptive case with on-line identification of both T and Z_0 , except that here the control inputs are based on the measured response, not the estimated uncontrolled response.

$$\Theta_n = \Theta_{n-1} + CZ_{n-1} \quad (10.45)$$

Local Model

This controller is applicable even to a nonlinear model. The transfer function T is assumed linear about the current control inputs. The control inputs are based on the measured response.

$$\Delta\Theta_n = CZ_{n-1} \quad (10.46)$$

where $\Delta\Theta_n = \Theta_n - \Theta_{n-1}$. The feedback gain C gets updated with time via T . The Kalman estimation of T is given by

$$\hat{T}_n = \hat{T}_{n-1} + \left(\Delta Z_n - \hat{T}_{n-1} \Delta\Theta_n \right) K_n^T \quad (10.47)$$

where we have

$$\Delta Z_n = Z_n - Z_{n-1} \quad (10.48)$$

$$M_n = P_{n-1} + Q_{n-1} \quad (10.49)$$

$$P_n = M_n - \frac{M_n \Delta\Theta_n \Delta\Theta_n^T M_n}{r_n + \Delta\Theta_n^T M_n \Delta\Theta_n} \quad (10.50)$$

$$K_n = \frac{P_n \Delta\Theta_n}{r_n} \quad (10.51)$$

Table 10.2: Longitudinal Hub Load H Transmitted by Blades to Hub

Drag Shear at Blade Root Harmonics s_x	Radial Shear at Blade Root Harmonics s_r	Hub Load H in Fixed Frame		
		2-Bladed Rotor	3-Bladed Rotor	4-Bladed Rotor
s_{x_0}	s_{r_0}	0	0	0
$s_{x_{1c}} \cos \psi_m$	$s_{r_{1c}} \cos \psi_m$	$s_{r_{1c}} + s_{x_{1c}} \sin 2\psi + s_{r_{1c}} \cos 2\psi$	$(3/2)s_{r_{1c}}$	$2s_{r_{1c}}$
$s_{x_{1s}} \sin \psi_m$	$s_{r_{1s}} \sin \psi_m$	$s_{x_{1c}} - s_{x_{1s}} \cos 2\psi + s_{r_{1s}} \sin 2\psi$	$(3/2)s_{x_{1c}}$	$2s_{x_{1c}}$
$s_{x_{2c}} \cos 2\psi_m$	$s_{r_{2c}} \cos 2\psi_m$	0	$(3/2)s_{x_{2c}} \sin 3\psi + (3/2)s_{r_{2c}} \cos 3\psi$	0
$s_{x_{2s}} \sin 2\psi_m$	$s_{r_{2s}} \sin 2\psi_m$	0	$-(3/2)s_{x_{2s}} \cos 3\psi + (3/2)s_{r_{2s}} \sin 3\psi$	0
$s_{x_{3c}} \cos 3\psi_m$	$s_{r_{3c}} \cos 3\psi_m$	$-s_{x_{3c}} \sin 2\psi + s_{r_{3c}} \cos 2\psi + s_{x_{3c}} \sin 4\psi + s_{r_{3c}} \cos 4\psi$	0	$2s_{x_{3c}} \sin 4\psi + 2s_{r_{3c}} \cos 4\psi$
$s_{x_{3s}} \sin 3\psi_m$	$s_{r_{3s}} \sin 3\psi_m$	$s_{x_{3s}} \sin 2\psi + s_{r_{3s}} \cos 2\psi + s_{x_{3s}} \sin 4\psi + s_{r_{3s}} \cos 4\psi$	0	$-2s_{x_{3s}} \sin 4\psi + 2s_{r_{3s}} \sin 4\psi$
$s_{x_{4c}} \cos 4\psi_m$	$s_{r_{4c}} \cos 4\psi_m$	0	$-(3/2)s_{x_{4c}} \sin 3\psi + (3/2)s_{r_{4c}} \cos 3\psi$	0
$s_{x_{4s}} \sin 4\psi_m$	$s_{r_{4s}} \sin 4\psi_m$	0	$(3/2)s_{x_{4s}} \cos 3\psi + (3/2)s_{r_{4s}} \sin 3\psi$	0
$s_{x_{5c}} \cos 5\psi_m$	$s_{r_{5c}} \cos 5\psi_m$	$-s_{x_{5c}} \sin 4\psi + s_{r_{5c}} \cos 4\psi + s_{x_{5c}} \sin 6\psi + s_{r_{5c}} \cos 6\psi$	$(3/2)s_{x_{5c}} \sin 6\psi + (3/2)s_{r_{5c}} \cos 6\psi$	$-2s_{x_{5c}} \sin 4\psi + 2s_{r_{5c}} \cos 4\psi$
$s_{x_{5s}} \sin 5\psi_m$	$s_{r_{5s}} \sin 5\psi_m$	$s_{x_{5s}} \sin 4\psi + s_{r_{5s}} \cos 4\psi + s_{x_{5s}} \sin 6\psi + s_{r_{5s}} \cos 6\psi$	$-(3/2)s_{x_{5s}} \cos 6\psi + (3/2)s_{r_{5s}} \sin 6\psi$	$2s_{x_{5s}} \cos 4\psi + 2s_{r_{5s}} \sin 4\psi$
$s_{x_{6c}} \cos 6\psi_m$	$s_{r_{6c}} \cos 6\psi_m$	0	0	0
$s_{x_{6s}} \sin 6\psi_m$	$s_{r_{6s}} \sin 6\psi_m$	0	0	0

Table 10.3: Lateral Hub Load Y Transmitted by Blades to Hub

Drag Shear at Blade Root s_x Harmonics	Radial Shear at Blade Root s_r Harmonics	Hub Load Y in Fixed Frame		
		2-Bladed Rotor	3-Bladed Rotor	4-Bladed Rotor
s_{x_0}	s_{r_0}	0	0	0
$s_{x_{1c}} \cos \psi_m$	$s_{r_{1c}} \cos \psi_m$	$-s_{r_{1c}}$	$-(3/2)s_{x_{1c}}$	$-2s_{x_{1c}}$
		$s_{x_{1c}} \cos 2\psi$		
		$s_{r_{1c}} \sin 2\psi$		
$s_{x_{1s}} \sin \psi_m$	$s_{r_{1s}} \sin \psi_m$	$s_{r_{1c}} - s_{x_{1s}} \sin 2\psi$	$(3/2)s_{r_{1s}}$	$2s_{r_{1s}}$
		$s_{r_{1s}} \cos 2\psi$		
$s_{x_{2c}} \cos 2\psi_m$	$s_{r_{2c}} \cos 2\psi_m$	0	$-(3/2)s_{x_{2c}} \cos 3\psi +$	0
			$(3/2)s_{r_{2c}} \sin 3\psi$	
$s_{x_{2s}} \sin 2\psi_m$	$s_{r_{2s}} \sin 2\psi_m$	0	$-(3/2)s_{x_{2s}} \sin 3\psi -$	0
			$(3/2)s_{r_{2s}} \cos 3\psi$	
$s_{x_{3c}} \cos 3\psi_m$	$s_{r_{3c}} \cos 3\psi_m$	$-s_{x_{3c}} \cos 2\psi$	0	$-2s_{x_{3c}} \cos 4\psi$
		$s_{r_{3c}} \sin 2\psi$		$2s_{r_{3c}} \sin 4\psi$
		$s_{x_{3c}} \cos 4\psi$		
		$s_{r_{3c}} \sin 4\psi$		
$s_{x_{3s}} \sin 3\psi_m$	$s_{r_{3s}} \sin 3\psi_m$	$-s_{x_{3s}} \sin 2\psi$	0	$-2s_{x_{3s}} \sin 4\psi$
		$s_{r_{3s}} \cos 2\psi$		$2s_{r_{3s}} \cos 4\psi$
		$s_{x_{3s}} \sin 4\psi$		
		$s_{r_{3s}} \cos 4\psi$		
$s_{x_{4c}} \cos 4\psi_m$	$s_{r_{4c}} \cos 4\psi_m$	0	$-(3/2)s_{x_{4c}} \cos 3\psi -$	0
			$(3/2)s_{r_{4c}} \sin 3\psi$	
$s_{x_{4s}} \sin 4\psi_m$	$s_{r_{4s}} \sin 4\psi_m$	0	$-(3/2)s_{x_{4s}} \sin 3\psi +$	0
			$(3/2)s_{r_{4s}} \cos 3\psi$	
$s_{x_{5c}} \cos 5\psi_m$	$s_{r_{5c}} \cos 5\psi_m$	$-s_{x_{5c}} \cos 4\psi$	$-(3/2)s_{x_{5c}} \cos 6\psi +$	$-2s_{x_{5c}} \cos 4\psi$
		$s_{r_{5c}} \sin 4\psi$	$(3/2)s_{r_{5c}} \sin 6\psi$	$2s_{r_{5c}} \sin 4\psi$
		$s_{x_{5c}} \cos 6\psi$		
		$s_{r_{5c}} \sin 6\psi$		
$s_{x_{5s}} \sin 5\psi_m$	$s_{r_{5s}} \sin 5\psi_m$	$-s_{x_{5s}} \cos 4\psi$	$-(3/2)s_{x_{5s}} \sin 6\psi -$	$-2s_{x_{5s}} \sin 4\psi$
		$s_{r_{5s}} \sin 4\psi$	$(3/2)s_{r_{5s}} \cos 6\psi$	$2s_{r_{5s}} \cos 4\psi$
		$s_{x_{5s}} \cos 6\psi$		
		$s_{r_{5s}} \sin 6\psi$		
$s_{x_{6c}} \cos 6\psi_m$	$s_{r_{6c}} \cos 6\psi_m$	0	0	0
$s_{x_{6s}} \sin 6\psi_m$	$s_{r_{6s}} \sin 6\psi_m$	0	0	0

Table 10.4: Hub Roll Moment M_X

Flap Moment at Blade Root n_f Harmonics	Hub Roll Moment M_X in Fixed Frame		
	2-Bladed Rotor	3-Bladed Rotor	4-Bladed Rotor
n_{f_0}	0	0	0
$n_{f_{1c}} \cos \psi_m$	$n_{f_{1c}} \sin 2\psi$	0	0
$n_{f_{1s}} \sin \psi_m$	$n_{f_{1s}} (1 - \cos 2\psi)$	$(3/2)n_{f_{1s}}$	$2n_{f_{1s}}$
$n_{f_{2c}} \cos 2\psi_m$	0	$(3/2)n_{f_{2c}} \sin 3\psi$	0
$n_{f_{2s}} \sin 2\psi_m$	0	$-(3/2)n_{f_{2s}} \cos 3\psi$	0
$n_{f_{3c}} \cos 3\psi_m$	$-n_{f_{3c}} \sin 2\psi$ +	0	$2n_{f_{3c}} \sin 4\psi$
	$n_{f_{3c}} \sin 4\psi$		
$n_{f_{3s}} \sin 3\psi_m$	$n_{f_{3s}} \cos 2\psi$ -	0	$-2n_{f_{3s}} \cos 4\psi$
	$n_{f_{3s}} \cos 4\psi$		
$n_{f_{4c}} \cos 4\psi_m$	0	$-(3/2)n_{f_{4c}} \sin 3\psi$	0
$n_{f_{4s}} \sin 4\psi_m$	0	$(3/2)n_{f_{4s}} \cos 3\psi$	0
$n_{f_{5c}} \cos 5\psi_m$	$-n_{f_{5c}} \cos 4\psi$ +	$(3/2)n_{f_{5c}} \sin 6\psi$	$-2n_{f_{5c}} \sin 4\psi$
	$n_{f_{5c}} \cos 6\psi$		
$n_{f_{5s}} \sin 5\psi_m$	$n_{f_{5s}} \sin 4\psi - n_{f_{5s}} \sin 6\psi$	$-(3/2)n_{f_{5s}} \cos 6\psi$	$2n_{f_{5s}} \cos 4\psi$
$n_{f_{6c}} \cos 6\psi_m$	0	0	0
$n_{f_{6s}} \sin 6\psi_m$	0	0	0

Table 10.5: Hub Pitch Moment M_Y

Flap Moment at Blade Root n_f Harmonics	Hub Pitch Moment M_Y in Fixed Frame		
	2-Bladed Rotor	3-Bladed Rotor	4-Bladed Rotor
n_{f_0}	0	0	0
$n_{f_{1c}} \cos \psi_m$	$-n_{f_{1c}} (1 + \cos 2\psi)$	$-(3/2)n_{f_{1c}}$	$-2n_{f_{1c}}$
$n_{f_{1s}} \sin \psi_m$	$-n_{f_{1s}} \sin 2\psi$	0	0
$n_{f_{2c}} \cos 2\psi_m$	0	$-(3/2)n_{f_{2c}} \cos 3\psi$	0
$n_{f_{2s}} \sin 2\psi_m$	0	$-(3/2)n_{f_{2s}} \sin 3\psi$	0
$n_{f_{3c}} \cos 3\psi_m$	$-n_{f_{3c}} \cos 2\psi$ +	0	$-2n_{f_{3c}} \cos 4\psi$
	$n_{f_{3c}} \cos 4\psi$		
$n_{f_{3s}} \sin 3\psi_m$	$-n_{f_{3s}} \sin 2\psi$ -	0	$-2n_{f_{3s}} \sin 4\psi$
	$n_{f_{3s}} \sin 4\psi$		
$n_{f_{4c}} \cos 4\psi_m$	0	$-(3/2)n_{f_{4c}} \cos 3\psi$	0
$n_{f_{4s}} \sin 4\psi_m$	0	$-(3/2)n_{f_{4s}} \sin 3\psi$	0
$n_{f_{5c}} \cos 5\psi_m$	$-n_{f_{5c}} \cos 4\psi$ -	$-(3/2)n_{f_{5c}} \cos 6\psi$	$-2n_{f_{5c}} \cos 4\psi$
	$n_{f_{5c}} \cos 6\psi$		
$n_{f_{5s}} \sin 5\psi_m$	$-n_{f_{5s}} \sin 4\psi$ -	$-(3/2)n_{f_{5s}} \sin 6\psi$	$-2n_{f_{5s}} \sin 4\psi$
	$n_{f_{5s}} \sin 6\psi$		
$n_{f_{6c}} \cos 6\psi_m$	0	0	0
$n_{f_{6s}} \sin 6\psi_m$	0	0	0

Bibliography

- [1] Crews, S. T., "Rotorcraft Vibration Criteria, A New Perspective," In *Proceedings of the 43rd Annual Forum of the American Helicopter Society*, St. Louis, MO, May 1987.
- [2] Schrage, D. P., Peskar, R. E., "Helicopter Vibration Requirements," *Proceedings of the 33rd Annual Forum of the American Helicopter Society*, May 1977.
- [3] William G. Bousman, "Putting the Aero Back Into Aeroelasticity," 8th Annual ARO Workshop on Aeroelasticity of Rotorcraft Systems, University Park, PA, October, 1999.
- [4] Bousman, W. G. and Maier, T. "An Investigation of Helicopter Rotor Blade Flap Vibratory Loads," *American Helicopter Society 48th Annual Forum Proceedings*, Washington D.C., June 3–5, 1992.
- [5] Datta, A., and Chopra, I., "Validation of Structural and Aerodynamic Modeling using UH-60A Airloads Program Data," *Journal of the American Helicopter Society*, Vol. 51, (1), January 2006, pp. 43–58.
- [6] Datta, A., Sitaraman, J., Chopra., I, and Baeder, J., "CFD/CSD Prediction of Rotor Vibratory Loads in High Speed Flight," *Journal of Aircraft*, Vol. 43, (6), November–December 2006, pp. 1698–1709.
- [7] Roget, B., Chopra, I., "Individual Blade Control Methodology for a Rotor with Dissimilar Blades," *Journal of the American Helicopter Society*, July 2003.
- [8] Roget, B., Chopra, I., "Wind Tunnel Testing of an Individual Blade Controller for a Dissimilar Rotor," Presented at the American Helicopter Society 60th Annual Forum, Baltimore, MD, June 7-10, 2004.
- [9] Chopra, I., "Status of Application of Smart Structures Technology to Rotorcraft Systems," *Journal of the American Helicopter Society*, Vol. 45, No. 4, October 2000, pp 228-252.
- [10] Straub, F. K., "A Feasibility Study of Using Smart Materials for Rotor Control," *Smart Materials and Structures*, Vol. 5, (1), February 1996, pp. 1-10.
- [11] Bao, J., Nagaraj, V. T., Chopra, I., Bernhard, A. P. F., "Wind Tunnel Testing of Low Vibration Mach Scale Rotor with Composite Tailored Blades," Presented at the American Helicopter Society 58th Annual Forum, Baltimore, MD, June 7-10, 2004.
- [12] Chopra, I., "Review of State of Art of Smart Structures And Integrated Systems," *AIAA Journal*, Vol. 40, No. 11, November 2002.
- [13] Chopra, I. and McCloud, J. L., "A Numerical Simulation Study of Open-Loop, Closed-Loop and Adaptive Multicyclic Control Systems," *Journal of the American Helicopter Society*, Vol. 28, (1), January, 1983, pp. 529–541.

- [14] Johnson, W., "Self-Tuning Regulators for Multicyclic Control of Helicopter Vibration," NASA TP 1996, March 1982.
- [15] McCloud, J. L., III, "The Promise of Multicyclic Control," *Vertica*, Vol. 4, (1), 1980.
- [16] Shaw, J. and Albion, N., "Active Control of the Helicopter Rotor for Vibration Reduction," *Journal of the American Helicopter Society*, Vol. 26, (3), 1981.
- [17] Bryson, A. E., Jr. and Ho, Y. C., *Applied Optimal Control*, Blaisdell Publishing Company, Waltham, Mass., 1969.

Chapter 11

Rotor Tests in Wind Tunnel and in Flight

11.1 Wind Tunnel Models

Scaled models are built and tested in the wind tunnel to study aeromechanical stability, vibratory blade response and loads, performance and concept feasibility. The models simulate the essential characteristics of the full-scale system, depending on the phenomenon under investigation. The models generally fall under the following three categories:

1. Rigid models
2. Froude-scaled models
3. Mach-scaled models

Rigid models simulate only aerodynamic profile and are used to study the basic aerodynamic characteristics under ideal conditions. Such models are useful to validate computational fluid dynamic and other aerodynamic analyses as well as to generate basic data base. These models incorporate geometric details but are often less expensive to build than Froude and Mach scaled models. For example, catilevered blade models (nonrotating) are used to determine airfoil characteristics as well as three-dimensional characteristics at the tip. Rigid blades with offset hinges (rotating) are frequently used to study the basic performance. Simple rotor and body are used to determine rotor-body interactional aerodynamics

Froude-scaled models are used to study aeromechanical stability of rotors. These models are less complex and less expensive to build than Mach scale models. Froude-scaled models essentially simulate steady elastic deflections. Scaled structural, inertial and aerodynamic characteristics are simulated in these models. Compressibility effects are not simulated.

Mach-scaled models are used to study basic performance and vibratory loads characteristics. These models simulate compressibility effects, i.e. the same tip Mach number. If compressibility effects are important for aeromechanical stability, then it is necessary to build Mach scaled models. These models are complex and expensive to build. In practice, Froude number and Mach number of full-scale cannot be simulated at the same time unless the test media is changed (from air to freon), that too for a selected few flight conditions. Also, it is not possible to represent the Reynolds number in the scaled rotor model. It is important however, to keep the Reynolds number high enough to ensure the proper viscous flow on the model. Aeroelastic rotor models are normally tested in large size low speed wind tunnels because of testing cost, safety, simulation of more details and less tunnel interference.

11.1.1 Froude-Scaled Models

In Froude-scaled models, the blade deflection under its own weight is scaled in the same manner as the model dimensions. If the model is s -times smaller than full scale then the deflections will also be s -times smaller. Because aeromechanical stability is a nonlinear phenomena it is important to simulate its static deflections. Therefore, Froude-scaled models are used to determine aeroelastic behavior of rotor systems. The aeroelastic stability equations are governed by the following non-dimensional parameters:

1. Locke number $\gamma = \frac{\rho ac R^4}{I_b}$
2. Nondimensional mass distribution $\bar{m} = \frac{m}{m_0}$
3. Froude number $\frac{m_0 g R^3}{EI}$
4. Nondimensional stiffness $\frac{EI}{m_0 \Omega^2 R^4}$ or $\frac{GJ}{m_0 \Omega^2 R^4}$
5. Advance ratio $\mu = \frac{V \cos \alpha}{\Omega R}$
6. Structural damping ξ
7. Airfoil profile

The maximum dimension of the model is determined by the size of the wind tunnel test section. Let the model properties be denoted by the subscript m , and the full scale properties by f . If the model is s times smaller than full scale, where s is the scaling parameter, then the ratio of the model radius to the full scale radius is given by

$$\frac{R_m}{R_f} = s \quad (11.1)$$

Similarly the chord ratio is also

$$\frac{c_m}{c_f} = s \quad (11.2)$$

The ratio of air density is fixed. Assume both are at sea level. The acceleration due to gravity is same.

$$\begin{aligned} \frac{\rho_m}{\rho_f} &= 1 \\ \frac{g_m}{g_f} &= 1 \end{aligned} \quad (11.3)$$

From the equality of Lock number we have

$$\frac{m_{0m}}{R_m^2} = \frac{m_{0f}}{R_f^2}$$

Thus the equivalent mass per unit length is scaled by

$$\frac{m_{0m}}{m_{0f}} = s^2 \quad (11.4)$$

The mass distribution has to be the same

$$\frac{m_m}{m_{0m}} = \frac{m_f}{m_{0f}}$$

Hence the mass per unit length is also scaled by

$$\frac{m_m}{m_f} = s^2 \quad (11.5)$$

From the equality of Froude number we have

$$\frac{EI_m}{EI_f} = \frac{GJ_m}{GJ_f} = \frac{m_{0m}}{m_{0f}} \left(\frac{R_m}{R_f} \right)^3 = s^5 \quad (11.6)$$

Because the nondimensional stiffness must remain the same, the rotor rpm ratio can be determined

$$\frac{\Omega_m}{\Omega_f} = \frac{m_{0m}}{m_{0f}} \left(\frac{R_m}{R_f} \right)^4 \frac{EI_m}{EI_f} = s^{-\frac{1}{2}} \quad (11.7)$$

The nondimensional frequencies of the system must be kept same as the full scale (e.g. $\nu_\beta=1.04/\text{rev}$, $\nu_\zeta = 0.3/\text{rev}$, $\nu_\theta = 4.5/\text{rev}$, say, for both the model and full scale rotors), thus the dimensional frequencies also scale in the above manner

$$\frac{\omega_m}{\omega_f} = s^{-\frac{1}{2}} \quad (11.8)$$

Also note that, because the blade azimuth is given by $\psi = \Omega t$, for a given time t , the azimuthal angle traversed by the model blade is related to the angle traversed by the full scale blade by the same ratio

$$\frac{\psi_m}{\psi_f} = s^{-\frac{1}{2}} \quad \text{at same time } t \quad (11.9)$$

From the equality of advance ratio we have the required tunnel speed as a ratio of flight speed. The shaft tilt is same for both.

$$\frac{V_m}{V_f} = \frac{\omega_m R_m}{\omega_f R_f} = s^{\frac{1}{2}} \quad (11.10)$$

It is not possible to scale structural damping, but attempt is made to keep it as low as possible. The equality of nondimensional mass and stiffnesses, the scaling of rotor radius, and the equality of the Froude number, produces blade deformations that are scaled in the same manner as the dimensions

$$\frac{w_m}{w_f} = s \quad (11.11)$$

Using the azimuthal scaling, the nondimensional velocity and acceleration are scaled as

$$\begin{aligned} \frac{w_m^*}{w_f^*} &= s^{\frac{1}{2}} \\ \frac{w_m^{**}}{w_f^{**}} &= 1 \end{aligned} \quad (11.12)$$

The other structural properties are scaled as follows. The flap moment of inertia ($\text{kg}\cdot\text{m}^2$) is scaled by

$$\frac{I_{bm}}{I_{bf}} = \frac{m_m}{m_f} \left(\frac{R_m}{R_f} \right)^3 = s^5 \quad (11.13)$$

The pitch link stiffness (N/m) is scaled by

$$\frac{k_m}{k_f} = \frac{m_{0m}}{m_{0f}} \frac{\Omega_m^2 R_m}{\Omega_f^2 R_f} = s^2 \quad (11.14)$$

A torsional spring (N-m/rad) is scaled by

$$\frac{k_{\theta m}}{k_{\theta f}} = \frac{m_{0m} \Omega_m^2 R_m^4}{m_{0f} \Omega_f^2 R_f^4} = s^4 \quad (11.15)$$

An example of a Froude-scaled model is the Boeing four-bladed bearingless ITR (Integrated Technology Rotor) model tested in December 1984, by Boeing Vertol (now Boeing Helicopters) at the University of Maryland's Glenn L. Martin Wind Tunnel. The model diameter was 6 ft, and it was a 1/8-th Froude-scaled dynamic model of the full-scale rotor.

11.1.2 Mach-Scaled Models

A Mach-scaled model reproduces the exact Mach number at the blade tip. For performance and dynamic loads studies, compressibility effects are important and therefore Mach-scaled models are used. For standard wind tunnels, Froude and Mach numbers cannot be satisfied simultaneously.

The important nondimensional parameters in this case are as follows. These parameters must be same between the model and full scale rotors.

1. Locke number $\gamma = \frac{\rho a c R^4}{I_b}$
2. Tip Mach number $M = \frac{\Omega R}{a}$
3. Advance ratio $\mu = \frac{V \cos \alpha}{\Omega R}$
4. Nondimensional mass distribution $\bar{m} = \frac{m}{m_0}$
5. Nondimensional stiffness $\frac{EI}{m_0 \Omega^2 R^4}$ or $\frac{GJ}{m_0 \Omega^2 R^4}$
6. Structural damping ξ
7. Airfoil profile

The model size is determined by the wind tunnel test section. Let the model dimensions be s -times the full scale dimensions. Then the ratio of the model radius to the full scale radius is given by

$$\frac{R_m}{R_f} = s \quad (11.16)$$

Similarly the chord ratio is also

$$\frac{c_m}{c_f} = s \quad (11.17)$$

The ratio of air density is fixed. Assume both are at sea level. Assume that the speed of sound is same in the wind tunnel as in flight.

$$\begin{aligned} \frac{\rho_m}{\rho_f} &= 1 \\ \frac{a_m}{a_f} &= 1 \end{aligned} \quad (11.18)$$

From the equality of Mach number we have

$$\frac{\Omega_m}{\Omega_f} = \frac{R_m}{R_f} \frac{a_m}{a_f} = s^{-1} \quad (11.19)$$

To simulate the sectional Mach numbers in forward flight, the advance ratio must be the same between the model and the full scale rotor. From the equality of advance ratio we have

$$\frac{V_m}{V_f} = 1 \quad (11.20)$$

Thus the wind speed in the test section is the same as flight speed. From the equality of Lock numbers we have the ratio of equivalent mass per unit length

$$\frac{m_{0m}}{m_{0f}} = \left(\frac{R_m}{R_f}\right)^2 = s^2 \quad (11.21)$$

The nondimensional mass distributions must be the same. Thus the mass per unit length also scales by the same ratio

$$\frac{m_m}{m_f} = s^2 \quad (11.22)$$

From the equality of nondimensional stiffness we have

$$\frac{EI_m}{EI_f} = \frac{GJ_m}{GJ_f} = \frac{m_{0m}}{m_{0f}} \left(\frac{\Omega_m}{\Omega_f}\right)^2 \left(\frac{R_m}{R_f}\right)^4 = s^4 \quad (11.23)$$

The airfoil profile is very important and must be simulated precisely. The structural damping is impossible to scale and is kept as small as possible. From the above scaling, the static deflection of the model with respect to the full scale rotor under its own weight is given by

$$\left(\frac{w}{R}\right)_m / \left(\frac{w}{R}\right)_f = \left(\frac{m_0 g R^3}{EI}\right)_m / \left(\frac{m_0 g R^3}{EI}\right)_f = \frac{m_{0m}}{m_{0f}} \left(\frac{R_m}{R_f}\right)^3 \frac{EI_m}{EI_f} = s \quad (11.24)$$

or

$$\frac{w_m}{w_f} = s^2 \quad (11.25)$$

If the model is 1/8-th scale, then elastic deflection will be 1/64-th scale. Mach-scaled models are much more stiff than Froude-scaled models. The velocity and accelerations are scaled as

$$\begin{aligned} \frac{w_m^*}{w_f^*} &= s \\ \frac{w_m^{**}}{w_f^{**}} &= 1 \end{aligned} \quad (11.26)$$

The static strains in these models are much smaller than the full scale values.

11.1.3 Model Fabrication

Ideally, one must build a replica construction which scales all the details. In practice it is not feasible. Therefore models are built to simulate the essential characteristics approximately. Fabrication of models is an art, and success comes with practice and experience. There is no hard and defined rule in the selection of materials, type of construction and fabrication process. Simple design and adequate details are enough. The blades are typically built using a single spar made of Aluminum, Magnesium, Kevlar, or glass, ribs made of balsa, and skin made of fabric or glass sheet. A typical construction is shown in Fig. 11.1

11.1.4 Model Instrumentation

The models are instrumented with several pickups. Typically strain gages are mounted near the blade root. These gages are installed in a conventional bridge arrangement to measure blade flapping, lead-lag and torsional moments. Static and unsteady pressure pickups are used to determine pressures at different stations. Accelerometers are typically placed near the blade tip and in the

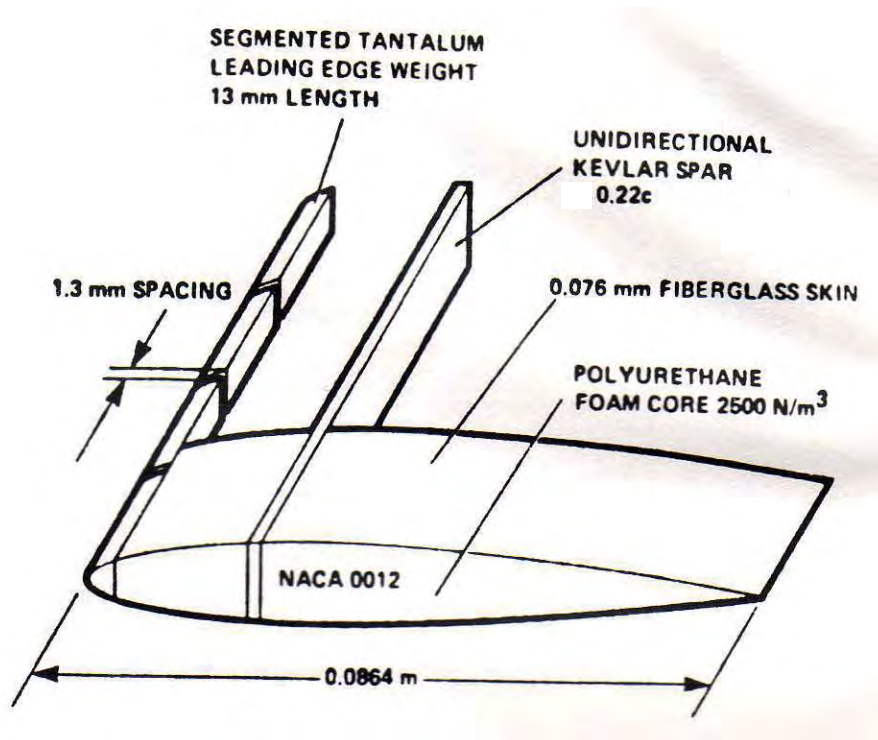


Figure 11.1: A typical experimental model blade design

airframe to obtain vibration levels (in terms of accelerations). Potentiometers and Hall-effect sensors are used at the hinges and pitch bearing to measure angular displacements. The swashplate position and hence the blade pitch input are determined by linear potentiometers mounted at each actuator. A gear tooth and photocell arrangement is used to provide 1/rev pulse. Data signals from various pickups on blades are transferred through a multi-channel slip-ring assembly to the fixed frame. Rotor loads are measured with a six component strain-gauge balance. The rotor balance is isolated from the transmission by means of a flexible diaphragm coupling. All signals are conditioned and amplified by bridge amplifiers with anti-aliasing filter, digitized using Analog to Digital (A/D) converters before being analyzed by the computer.

11.2 Model Testing

Five types of model tests are performed. They are

1. Static tests
2. Vacuum chamber tests
3. Hover tests
4. Vibration tests, and shake tests of the wind tunnel mounts
5. Wind tunnel tests

The static tests are performed on the model and the individual components of the model to check the simulation of structural stiffness and inertial characteristics. The vacuum chamber tests are performed to check the integrity of the structure to centrifugal loads. The hover tests are performed to check the integrity of the structure to both centrifugal and steady aerodynamic loads. The blade

to blade dissimilarities lead to imbalance in the rotor system. This imbalance is rectified. Usually the hover test stands are very stiff. Before, the model is tested in the wind tunnel, extensive vibration tests are performed after set up on the non-rotating model to obtain the natural frequencies and damping characteristics of all modes. Shake tests are performed on the rotating model to determine the natural frequencies and structural damping of the support structure and the rotor. These frequencies are used to check the possibility of ground resonance instability at the operating rotational speed. The rotor is then tracked in hover conditions using a strobe light at increasing speeds up to the nominal operating speed. Tracking is accomplished iteratively by making minor adjustments to the length of each pitch link. The rotor is also checked for tracking at higher collective pitch angles. With the rotor tracked correctly, it is then carefully balanced by adding small weights and short lengths of adhesive backed aluminum tape at the blade pitch housing.

In forward flight, the rotor is first brought to the operating rpm at a small collective pitch, and then the wind is turned off. The wind speed is slowly increased in a step wise manner, while adjusting the cyclic pitch inputs at each step to minimize first harmonic flapping, and thus the oscillatory bending loads at the root. This is the trim procedure. Once the desired forward speed is obtained, the collective pitch is raised to the desired level. For each test point, the rotor is re-trimmed for the particular combination of shaft angle and collective pitch setting by adjusting the longitudinal and lateral cyclic to minimize the blade cyclic flapping. This ensures that the tip path plane is perpendicular to the rotor shaft axis.

11.2.1 Testing for Isolated Rotor Stability

For blade stability measurement, the swashplate is cyclically oscillated at the regressing lag mode frequency to excite the rotor. After the rotor reaches a new steady state, the excitation is cut off and the transient response is recorded. Then, typically the Moving-Block technique is used to estimate the damping and frequency from transient signals. The testing for isolated rotor stability depends on the number of blades.

1. *One blade*: Single lead-lag and flap modes. The lead-lag mode couples with the drive system, but the drive system must have infinite impedance to represent isolated rotor. The flap mode couples with the stand.
2. *Two blades*: Two lead-lag and two flap modes. The collective lead-lag mode couples with the drive system. The differential lead-lag mode is a good approximation of isolated rotor but couples with the stand. The collective flap mode is uncoupled. The differential flap mode couples with the stand. Blade matching is not critical.
3. *Three blades*: Three lead-lag and three flap modes. Collective lead-lag mode couples with the drive system. Cyclic lead-lag modes are a good approximation of the isolated rotor but couple with stand and wake. The collective flap mode is uncoupled. The cyclic flap modes couple with stand. Blade matching is critical.

11.2.2 Spectra for Various Inputs

11.3 Major Model and Full Scale Rotor Tests

Accurate prediction of helicopter vibration and rotor vibratory loads is a complex, multi-disciplinary and difficult problem. Development of a reliable prediction capability requires careful comparison of theory and experiment. Over the last fifty years, major wind tunnel and flight tests have been conducted where detailed blade airloads and structural loads were measured. An enormous volume of data is available from the NACA/Langley 2 bladed, 15 ft dia. teetering model tested by Rabbott

and Churchill in the 1950s to the most recent U.S.Army/NASA Ames 4 bladed, 52 ft dia. articulated Black Hawk flight tests in the 1990s.

Test data, model scale and full scale, for various types of rotor systems and blade numbers are necessary for the development and validation of theoretical analysis. A theoretical analyses is successfully validated when - (i) it captures the fundamental loading patterns common to all rotor systems and (ii) captures the differences observed among different rotor configurations.

An survey of all major rotor tests, wind tunnel and full-scale, from the 1950s to the first half of the 1980s can be found in Hooper [1]. It focussed on measured airloads and identified consistent patterns that are common to all rotor systems - regardless of blade number, size and trim conditions. The work showed that the vibratory airloads are remarkably consistent in the transition regime. At high speed, they were similar but in general more variable.

Bousman [2] made a comprehensive survey of full scale rotor tests focusing on the vibratory structural response. Like in the case of vibratory airloads, consistent patterns were identified in vibratory structural response behavior, largely independent of rotor configuration. For example, the dominant vibratory flap response always occurs at 3/rev, the root chord bending moment shows a negative to positive loading at the start of the third quadrant and the pitch-link loads for articulated rotors showed large positive-negative oscillations between the first and second quadrants. On the other hand the vibratory chord bending moments differed significantly between rotor to rotor. The pitch-link load of teetering rotors like the AH-1G differed significantly from that of articulated rotors like the UH-60A.

A summary of the major rotor tests, which focussed on airloads and blade loads of main rotor systems are given in table 11.1. Tiltrotor tests have been left out of this summary. Acoustic tests have also been left out, except, the HART and ONERA tests, from which airloads measurements are often used for validation purposes.

Other rotor test programs for loads measurements are those of Lynx fitted with BERP blades [19], NASA model hover test [20], DNW tests of the Boeing 360 rotor [21] and McDonnell Douglas HARP rotor [22]. The BERP data were helpful in identifying regions of blade stall and the NASA model rotor was used to study blade-vortex interactions. UTRC and Sikorsky, under sponcership of U.S.Army (USAAATD) have carried out extensive wind-tunnel testing (at Duits Nederlands Windtunnel, DNW, in Holland) of a 4 bladed 9.4 ft dia scale (1:5.73) model of the UH-60A Black-Hawk articulated rotor system [23]. The hover test program included blade pressures, surface flow, performance, wake geometry and flow field velocities (using a laser velocimeter). The tests were extended to forward flight in 1989 and included acoustic, dynamic, performance and airloads measurements of baseline pressure-instrumented rotors and non-instrumented rotors with modified tip geometries. An detailed discussion of the measured airloads can be found in Lorber [24].

In addition, two recent acoustic tests provide reliable airloads data. They are the HART/HART II [26] and HELISHAPE [25]. The HART test was conducted on 40% geometrically and aeroelastically scaled model of a hingeless BO-105 rotor in the DNW tunnel, in 1994. The HART II test was conducted in 2001. The HART II tests were carried out to emphasize on wake measurements. Both were collaborations between German DLR, French ONERA, NASA Langley and U.S.Army. The HELISHAPE program was an initiative between all 3 European manufacturers, Eurocopter, Augusta and Westland, and 13 other Research Institutes and Universities. Airloads measurements are available for the ONERA-Eurocopter swept-back parabolic/anhedral tip 7AD1 blade and rectangular tip 7A blades [25].

Although all the above tests were used to validate numerical models, in general, each test focussed on a specific set of phenomenon. None of them were fully comprehensive, covering steady and maneuvering flight, high thrust dynamic stall conditions, pressure data, strain gauge data, pitch link loads and fuselage vibration measurements. Wind tunnel models, even when full scale, do not include full helicopter components. For example, the model UH-60A rotor did not have a non-linear lag damper or bifilar pendulums at the hub. On the one hand, wind tunnel tests are

Table 11.1: Major Rotor Tests

Rotor Test	Configuration	Reference
NASA Langley model rotor	2 bladed teetering rotor 15 ft dia	1956 [3]
Bell UH-1 flight tests	2 bladed teetering rotor	1961 [4]
Sikorsky H-34 (CH-34) flight test, NASA Langley	4 bladed articulated	1964 [5]
H-34 (CH-34) full scale wind tunnel test, NASA Ames	4 bladed articulated	1966 [6]
Vertol CH-47A flight tests, USAAVLABS	3 bladed tandem rotor	1968 [7]
Lockheed XH-51A flight tests	4 bladed compound helicopter	1968 [8]
Sikorsky NH-3A flight tests	5 bladed, compound version of the S-61	1970 [9]
Sikorsky CH-53A flight tests, U.S.Navy	6 bladed articulated	1970 [10]
Bell AH-1G flight tests, U.S.Army	2 bladed teetering. Test conducted for aero and structural loads	1976 [11]
Bell AH-1G flight tests, NASA	2 bladed teetering. Test conducted for aero-acoustic measurements	1983 [12]
Sikorsky S-76 full scale wind tunnel tests	4 bladed articulated	1980 [13]
Bell AH-1G flight tests	2 bladed teetering	1988 [14]
Aerospatial SA-330 Research Puma flight tests	4 bladed articulated	1983, 1986.[15]
Aerospatial SA 349/2 Gazelle flight tests	3 bladed articulated	1986 [16]
Westland Lynx flight tests	4 bladed hingeless	1993 [17]
McDonnell Douglas MDART full scale wind tunnel tests	4 bladed advanced bearingless rotor, pre-production version of MD900 rotor	1993 [18]

more controlled thereby limiting uncertainties in atmospheric conditions, variations in speed due to gusts and sideslip angles, pilot error etc. On the other hand, the real objective of measuring fuselage vibration cannot be accomplished by wind tunnel models. Only a full-scale flight test program can provide fuselage vibration data, with associated rotor airloads, blade loads, control loads, performance data and vehicle trim data, which can then be used to validate all aspects of a comprehensive analysis consistently. A truly extensive flight test program would cover steady level flight, steady and unsteady maneuvers, low speed and high speed flight, low thrust and high thrust flight, each conducted multiple times to ensure repeatability and accuracy of the data. The test conditions and the blade and helicopter properties (fuselage properties, e.g. location, fuel content, armament weight and placement etc) must be accurately and carefully documented before and after each flight, minimizing uncertainties as much as possible. The U.S.Army/NASA-Ames UH-60A Black Hawk Airloads Program [27] is such a detailed flight test program. The comprehensive set of repeatable test data from the UH-60A Airloads Program have established benchmarks to validate various aspects of a comprehensive rotor analyses.

The UH-60A flight test program conducted 31 flights. They covered Steady flight (7 flights), Maneuver flight (3), Ground Acoustic Measurements (9), In-flight Acoustic Measurements (6) and

Flight dynamics (6). Pressure gauge measurements (airloads obtained by integrating) were taken at 9 stations, flap bending gauges at 9 stations, chord bending gauges at 8 stations and torsion bending gauges at 4 stations. All four pitch links were instrumented to measure control loads. This is perhaps the most extensive instrumentation suites used in a flight test, providing reliable and repeatable test data. The present work uses the UH-60A flight test data. Details of the structural, aerodynamic and trim data sets are discussed in the appropriate chapters.

Bibliography

- [1] W.E.Hooper, "The Vibratory Airloading of Helicopter Rotors," Paper No.46, 9th European Rotorcraft Forum, Stresa, Italy, September, 1983.
- [2] W.G.Bousman, "Response of Helicopter Rotors to Vibratory Airloads," *Journal of the American Helicopter Society*, Vol. 35, No. 4, Oct, 1990, pp. 53-62.
- [3] Rabbot, J. P., Churchill, G. B., "Experimental Investigation of the Aerodynamic Loading on a Helicopter Rotor Blade in Forward Flight," NACA RM L56107, Oct. 1956.
- [4] Bell Helicopter, "Measurement of Dynamic Air Loads on a Full-Scale Semi-Rigid Rotor," TCREC TR 62-42. Dec. 1962.
- [5] Scheiman, J., "A Tabulation of Helicopter Rotor-Blade Differential Pressures, Stresses, and Motions as Measured in Flight," NASA TM X-952, March 1964.
- [6] Rabbott, J. P., Lizak, A. A., Paglino, V. M., "A Presentation of Measured and Calculated Full-Scale Rotor Blade Aerodynamic and Structural Loads", USAAVLABS TR66-31, July 1966.
- [7] Pruyne, R. R., "In-Flight Measurement of Rotor Blade Airloads, Bending Moments, and Motions, Together with Rotor Shaft Loads and Fuselage Vibration, on a Tandem Rotor Helicopter," USAAVLABS TR 67-9A,B,C and D, Nov. 1967.
- [8] Bartsch, E. A., "In-Flight Measurement and Correlation with Theory of Blade Airloads and Resources in the XH-51A Compound Helicopter Rotor," USAAVLABS TR 68-22A, May 1968.
- [9] Fenaughty, R., Beno, E., "NH-3A Vibratory Airloads and Vibratory Rotor Loads," Department of the Navy SER 611493, Jan. 1970.
- [10] Beno, E., "CH-53A Main Rotor and Stabilizer Vibratory Airloads and Forces," Department of the Navy SER 65593. June 1970.
- [11] Shockey, G. A., Cox, C. Z., Williams, J. W., "AH-1G Helicopter Aerodynamic and Structural Load Survey," USAAMRDL TR-76-39.
- [12] Shockey, G. A., et al, "AH-1G Tip Aero-Acoustic Test," NASA.
- [13] Johnson, W., "Performance and Loads Data on a Full-Scale Rotor with Four Tip Planforms," NASA TM 81229, 1980.
- [14] Cross, J. L., Watts, M. E., "Tip Aerodynamics and Acoustics Test," NASA RP 1179, Dec. 1988.

- [15] Bousman, Young, C., Toulmay, F., Gilbert, N. E., Strawn, R. C., Miller, J. V., Maier, T. H., Costes, M. and Beaumier P., "A Comparison of Lifting-Line and CFD Methods with Flight Test Data from a Research Puma Helicopter," NASA TM 110421, October 1996.
- [16] Heffernan, R., Gaubert, M., "Structural and Aerodynamic Loads and Performance Measurements of an SA 349/2 Helicopter with an Advanced Geometry Rotor," NASA TM 88370, Nov. 1986.
- [17] Lau, B. H., Louie, A. W., Sotiriou, C. P., Griffiths, N., "Correlation of the Lynx-XZ170 Flight-Test Results Up To and Beyond the Stall Boundary," American Helicopter Society Forum. May 1993.
- [18] Nguyen, K., Lauzon, D., Anand V., "Computation of Loads on the McDonnell Douglas Advanced Bearingless Rotor," American Helicopter Society Forum, May 1994.
- [19] Isaacs, N. C. G., Harrison R. J., "Identification of Retreating Blade Stall Mechanisms Using Flight Test Pressure Measurements," American Helicopter Society 45th Annual Forum, Boston, MA, May 1989.
- [20] Caradonna, F. X., Tung, G., "Experimental and Analytical Studies of a Model Helicopter Rotor in Hover," NASA TM 81232, USAAVRADCOTR-81-A-23, 1980.
- [21] Dadone, L., Dawson, S., Boxwell, D., Ekquist, D., "Model 360 Rotor Test at DNW - Review of Performance and Blade Airload Data," American Helicopter Society 43rd Annual Forum, St. Louis, MO, May 1987.
- [22] Dawson, S., Jordan, D., Smith, S., Ekins, J., Silverton, L., Tuttle, B., "HARP Model Rotor Test at the DNW," American Helicopter Society 45th Annual Forum, Boston, MA, May 1989.
- [23] Yu, Y. H., Liu, S. R., Landgrebe, A. J., Lorber, P. F., Pollack, M. J., Martin, R. M., Jordan, D., "Aerodynamic and Acoustic Test of a United Technologies Model Scale Rotor at DNW," American Helicopter Society 46th Annual Forum, Washington D.C., May 1990.
- [24] Peter F. Lorber, "Aerodynamic Results of a Pressure-Instrumented Model Rotor Test at the DNW," *Journal of the American Helicopter Society*, Vol. 38, No. 3, July 1993, pp. 26-34.
- [25] Philippe, J. J., "Survey on ONERA Code Developments and Validation Studies for Multi-disciplinary Research on Rotor Aeromechanics," American Helicopter Society Aeromechanics Specialists' Conference, San Francisco, CA, January 19-21, 1994.
- [26] Yung, H. Y., et al, "The HART-II Test : Rotor Wakes and Aeroacoustics with Higher-Harmonic Pitch Control (HHC) Inputs - The Joint German/French/Dutch/US Project," American Helicopter Society 58th Annual Forum, Montreal, Canada, June 11-13, 2002.
- [27] Kufeld, R. M., Balough, D., Cross, J. L., Studebaker, K. F., Jennison, C. D., Bousman, W. G., "Flight Testing the UH-60A Airloads Aircraft," American Helicopter Society 50th Annual Forum Proceedings, Washington, D.C., May, 1994.

**Alfred Gessow Rotorcraft Center
University of Maryland**

Dynamic Aspects in Design of a Bearingless Rotor



Inderjit Chopra
Director Alfred Gessow Rotorcraft Center &
Alfred Gessow Professor of Aerospace Engineering
Presentation At: Korea Aerospace Research Institute (KARI), Daejeon
June 27-30, 2011

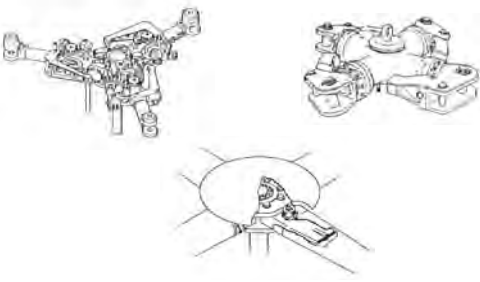
Bearingless Rotor

Bearingless Main Rotor (BMR)

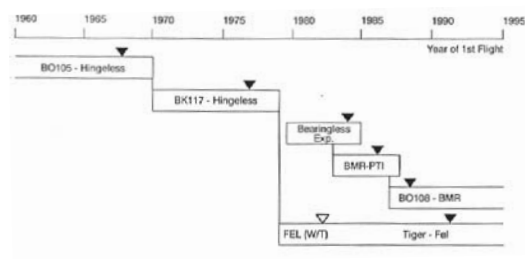
Flap and lag hinges as well as pitch bearing are eliminated:

- Reduction in parts count and maintenance cost
- Reduction in drag and weight
- **Redundancy in load paths at root**
- **Large elastic deformations**
- **Became possible because of composite materials and elastomeric dampers**

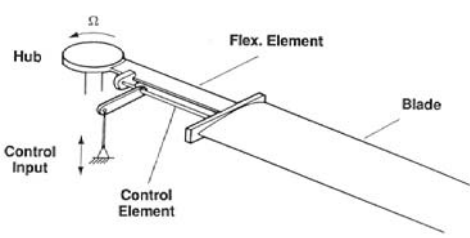
Rotor Systems Development



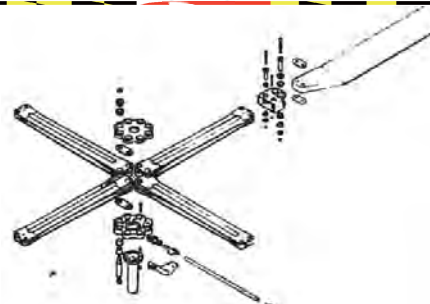
MBB's Main Rotor Technology Development



Principal Build-up of a Bearingless Rotor System



Boeing Vertol Bearingless Rotor (1978)



Matched BO 105 (hingeless) rotor characteristics (flap freq. 1.12/rev, e/R=14%, lag freq. .68/rev)
Flexbeam: Twin C-channel cross-section; Torque Rod: mid-section; Prepitch 12.5 deg

Aerospatiale/Eurocopter France: Triflex (1972)

Matched SA 341 Gazelle characteristics; flap freq. 1.06/rev, lag freq. 0.72/rev
 Flexbeam: fiberglass-epoxy yarns embedded in elastomeric matrix, Low damping

Highes/MDHC/Boeing: HARP (1982)

4-Bladed flap hinge 8%, elastomeric damper
 Flexbeam: Single Kevlar/Graphite beam with cruciform section
 Transitioned into MD-900 Explorer 5-bladed rotor

Westland/AW

Matched Lynx rotor; 4-Bladed

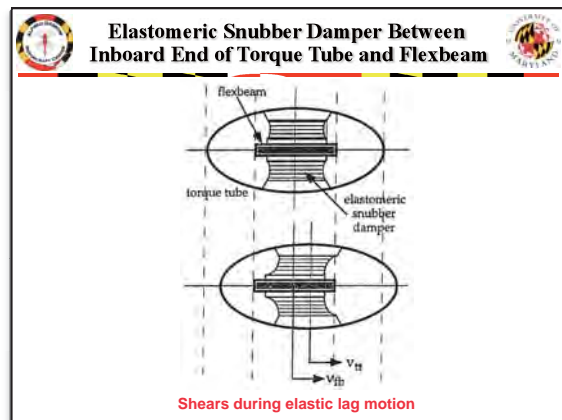
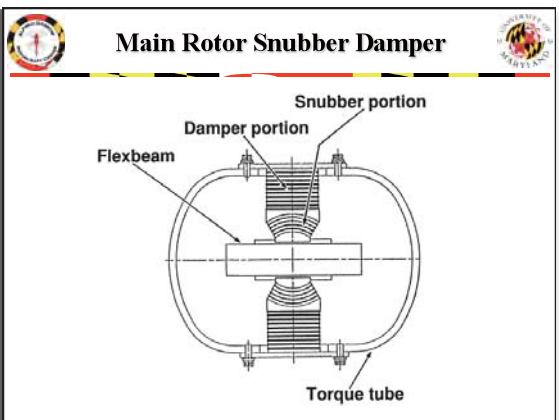
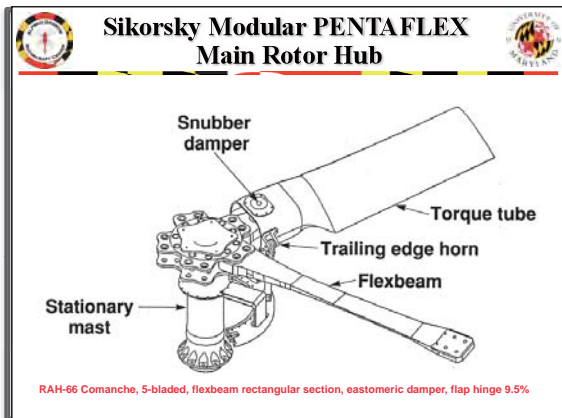
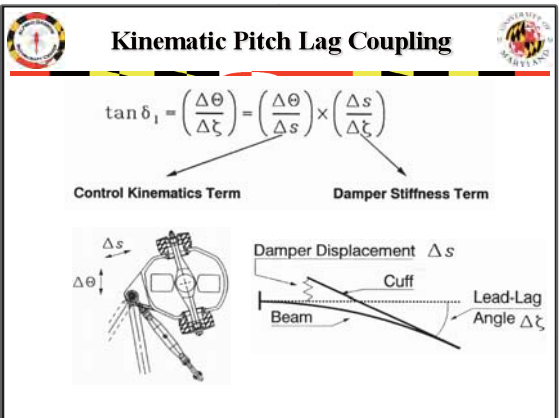
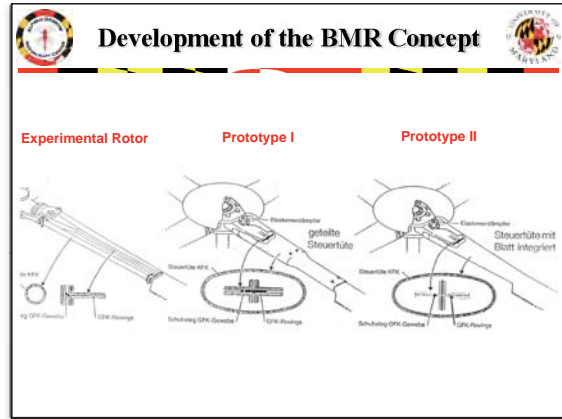
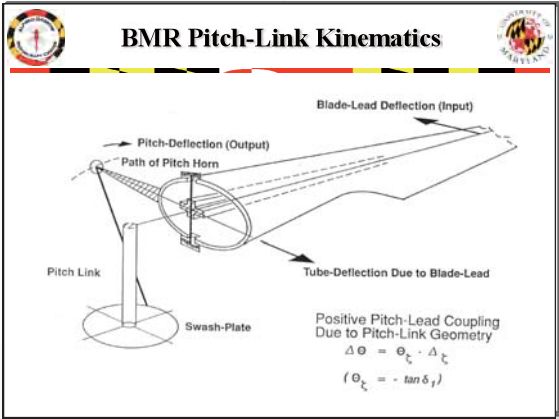
Bell Model 680 Rotor System (1982)

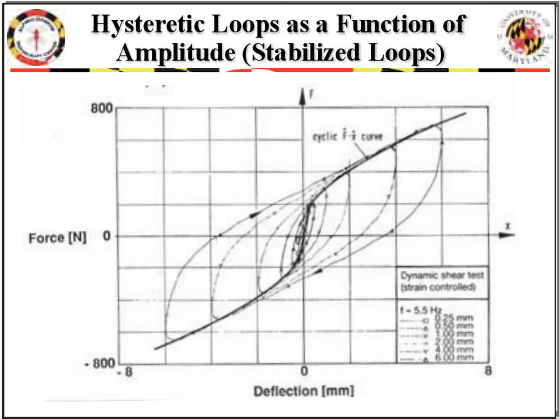
Flexbeam: One piece fiberglass, flap flexure inboard and torsionally flexible outboard; Torque Tube: torsionally stiff cuff wrapped around flexbeam; Flap hinge 2-3%

Basic Design Parameters

- Fundamental blade flap frequency or "hinge"-offset
- Fundamental blade lead-lag frequency
- Pitch-lag coupling
- Inplane damping

Evolution of Flexbeam Cross Sections





Modeling of Elastomeric Dampers and Effects on Aeromechanical Stability

- Dampers are nonlinear; Behavior dependent on the amplitude, frequency of motion, temperature, prestress
- Early efforts in elastomeric modeling were inadequate
 - Hausmann: modeled in *frequency domain*, need nonlinear hysteresis cycles, iterative solution process
 - Felker: G' , G'' independently obtained, lacks generality
- Goal is to seek a *consistent* Damper Model represented in the *time-domain* by a nonlinear differential equation
 - Predict behavior under multi-frequency/large amplitude excitations, include effects of equilibrium deformations
 - Easily integrated into a comprehensive rotor analysis

Spring-Dashpot Model

NONLINEAR

LINEAR

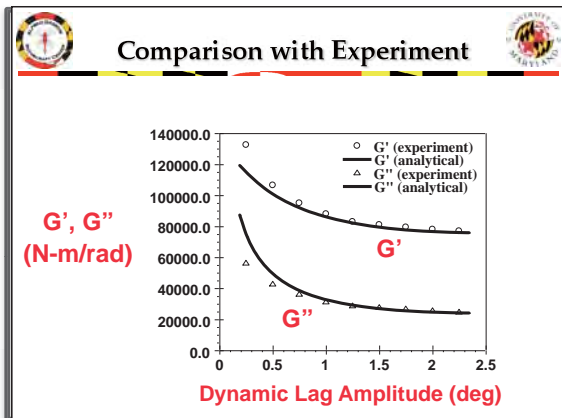
Elastomeric modeled by combination of linear and nonlinear springs and dashpots

- Derive constitutive differential equation (symbolically) For nonlinear spring + single Kelvin Chain

$$K_2 \zeta + C_2 \dot{\zeta} = K_2 f(D) + C_2 \frac{df(D)}{dD} \dot{D} + D$$

K_2, C_2 : Spring/Dashpot parameters in Kelvin chain
 $\zeta = f(D)$: nonlinear force/displacement relation of lead spring
 D : Total damper force

- Parameters determined through System Identification



Augmented Elastomeric Damper Model

OLD MODEL

$\zeta_{S1} = f(D)$

AUGMENTED MODEL

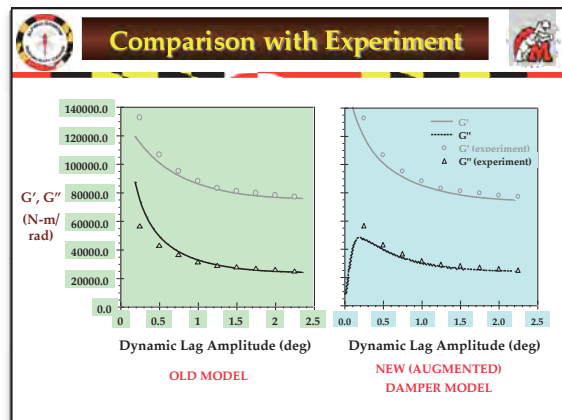
$$f(D) = (\text{sign } D) \left(c_1 |D| + c_2 |D|^2 + c_3 |D|^3 + c_4 |D|^4 \right) + (\text{sign } D) \frac{1}{c_6} \ln \left(\frac{|D|}{c_5} + 1 \right)$$

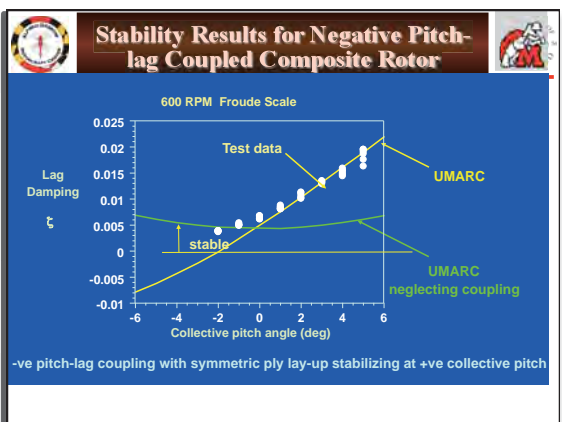
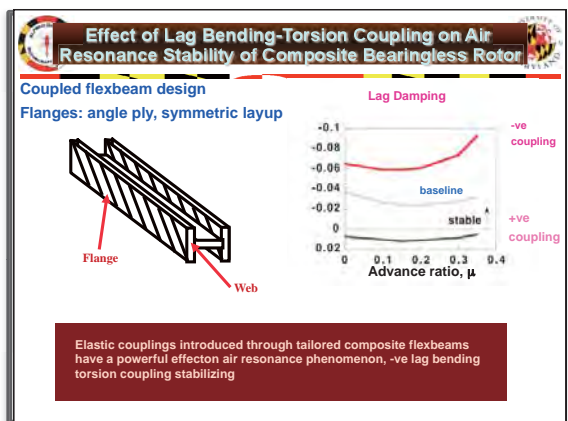
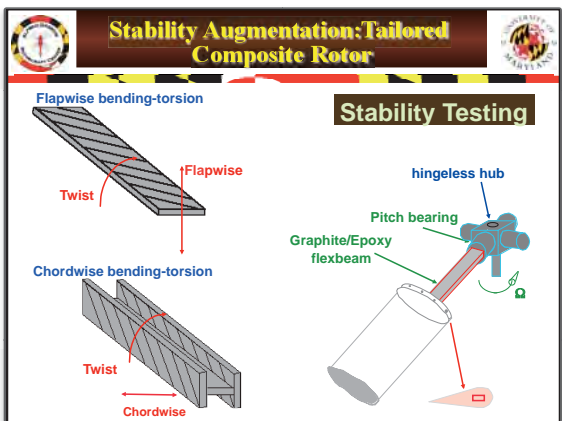
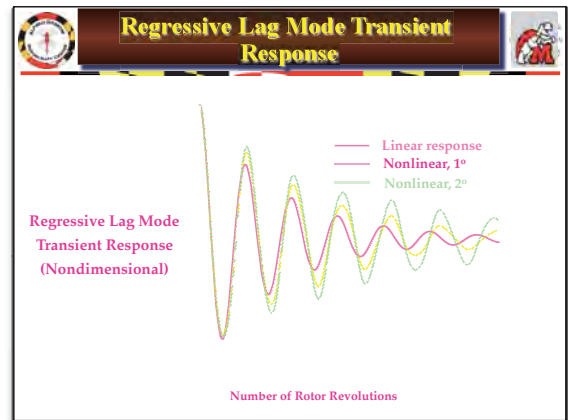
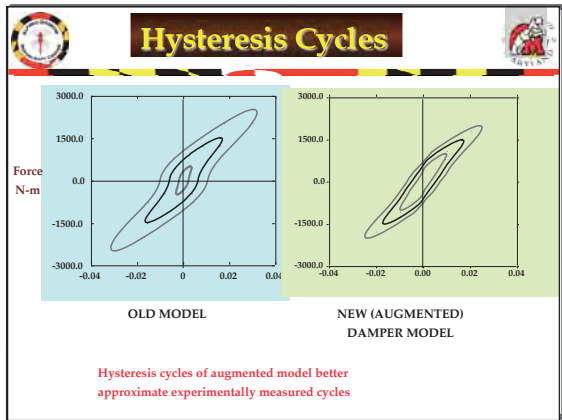
$$K_2 \zeta + C_2 \dot{\zeta} = K_2 f(D) + C_2 \frac{df}{dD} \dot{D} + D$$

$$D_{S4} = g(\zeta) = (\text{sign } \zeta) c_7 (1 - e^{-c_8 |\zeta|})$$

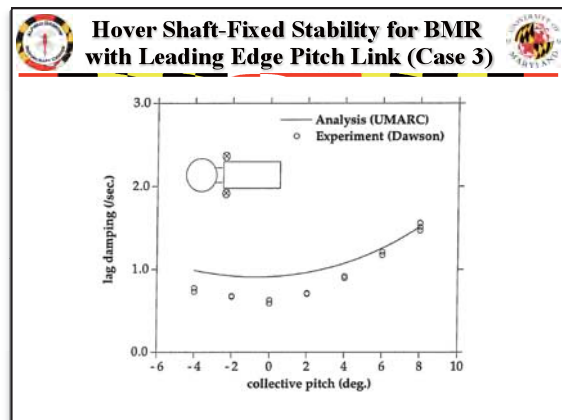
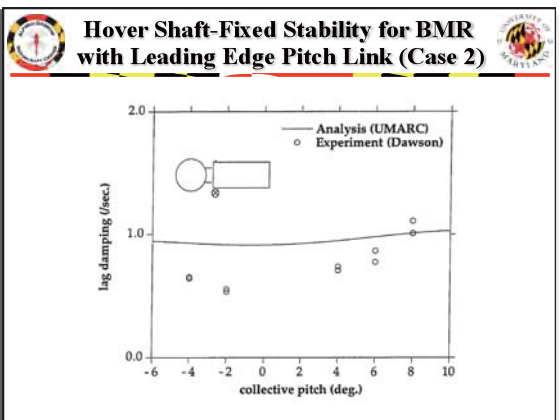
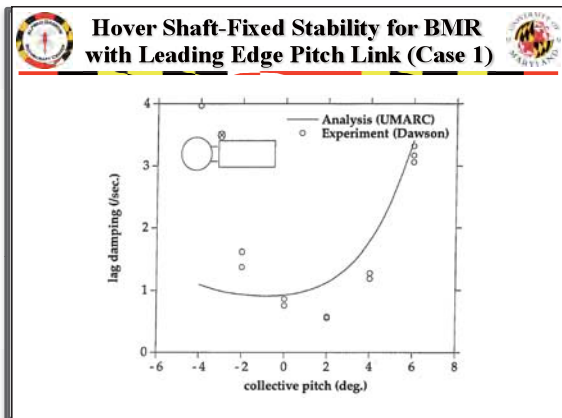
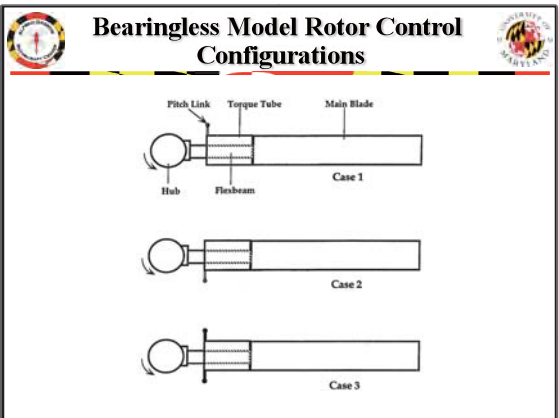
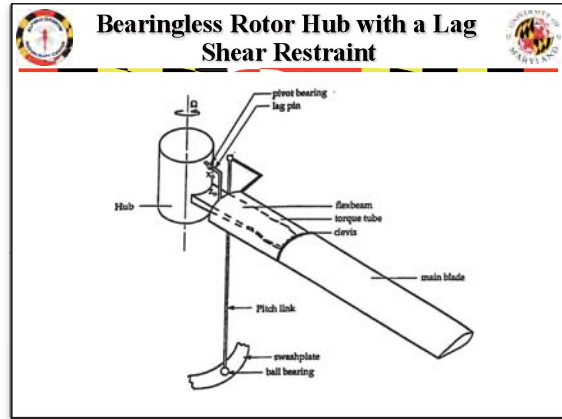
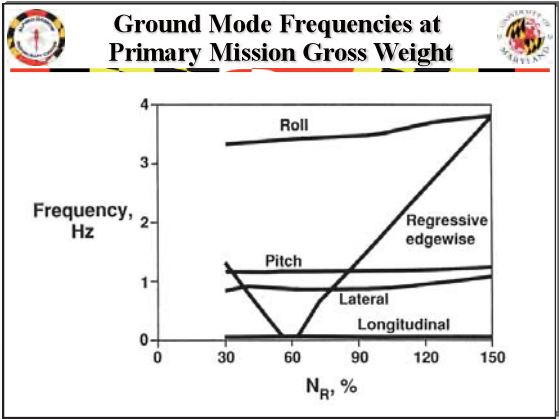
Total Damper Force = D

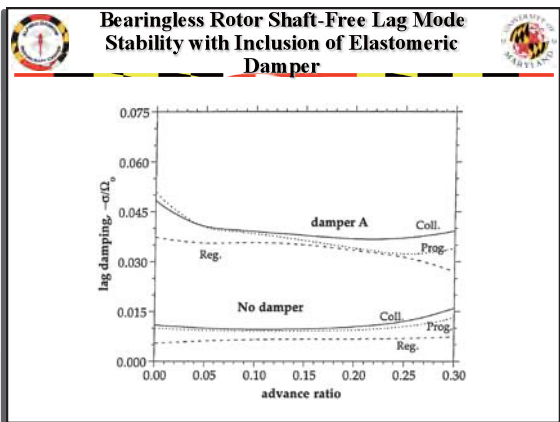
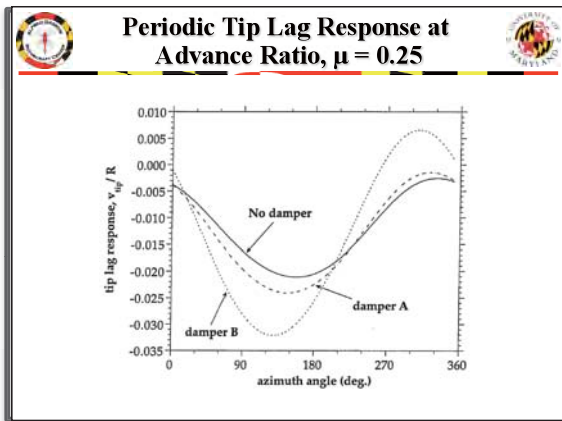
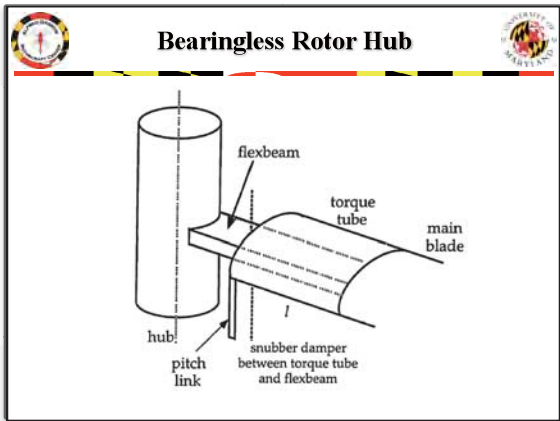
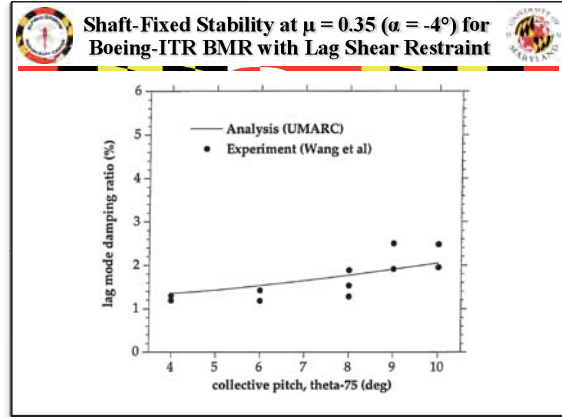
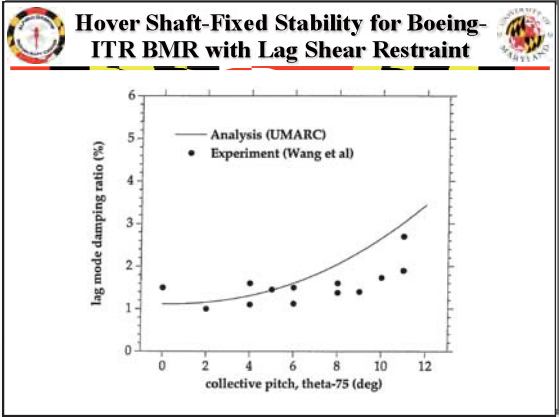
Total Damper Force = $D + D_{S4}$





- ### Snubber Design Issues
- Trade off between high loss factor and snubber life
 - Design for 1P motions superimposed on subharmonic motions
 - Stiffness and damping characteristics non-linear with amplitude
 - High stiffness at cold temperatures
 - Snubber stiffness variability affects 1P vibration
 - Stiffness variability may affect frequencies of modes contributing to 5P vibration





Analysis of Bearingless Main Rotor Aeroelasticity Using an Improved Time Domain Nonlinear Elastomeric Damper Model



Farhan Gandhi*
Rotorcraft Fellow



Inderjit Chopra
Professor and Director

Center for Rotorcraft Education and Research
Department of Aerospace Engineering
University of Maryland at College Park

An elastomeric damper model comprising a nonlinear spring and a Kelvin chain is augmented to represent experimentally observed degradation in G'' (damping) at very low dynamic amplitudes, and occurrence of limit cycle oscillations (jitter) due to applied perturbations. The damper model is described in the time domain by a nonlinear differential equation. Integration into a bearingless rotor comprehensive analysis results in the addition of damper states to the rotor/fuselage state vector, and augmentation of the baseline modal mass, damping and stiffness matrices, and load vector. The influence of the damper is examined on bearingless rotor aeroelastic behavior, including aeromechanical stability in forward flight. Damper stiffness results in a significant variation of second lag frequency with advance ratio. The nonlinear characterization of the damper results in greater stability augmentation of the lag mode at low advance ratios than at higher advance ratios.

Introduction

The main rotor is a key component on the helicopter, providing thrust, propulsive force, and most vehicle controls. It has traditionally involved complexity of hinges, bearings and dampers. Over the last two decades, strong emphasis on design simplicity has culminated in the development of the bearingless main rotor (Ref. 1). In this type of rotor, the flap and lag hinges, as well as the pitch bearing, are eliminated resulting in a substantial reduction in parts count, weight, drag, and maintenance cost, along with increased control power. The main blade of the bearingless rotor is attached to the hub by means of a torsionally soft flexure that allows most of the flap and lag bending, as well as elastic twist. Pitch control of the main blade is achieved by rotating a torsionally rigid torque tube, surrounding the flexbeam, with the pitch link. This in turn rotates the main blade, and twists the flexbeam in the process.

Since the bearingless main rotor is usually designed as a soft-inplane rotor, it is susceptible to aeromechanical instabilities (Ref. 2). To alleviate these instabilities, most bearingless rotors need to be equipped with lag dampers. In contrast to the conventional hydraulic lag dampers seen on articulated rotors, elastomeric material based lag dampers have been popular for bearingless rotors, as they provide simplicity and a reduction in moving parts, ease in maintenance, and ease in installation. Rapid advances in material science, leading to the development of specialized high loss-factor elastomers (Refs. 3, 4) has greatly contributed to the increasing popularity of elastomeric material based dampers. However, analytical modeling of the complex, nonlinear behavior of elastomeric dampers has been a challenge. This paper formulates

and implements an improved elastomeric damper model in a bearingless rotor comprehensive analysis, and examines its effects on the aeroelastic behavior of the bearingless rotor.

The aeroelastic analysis of bearingless rotors is more challenging than hingeless or articulated rotors due to the presence of redundant load paths, complex hub kinematics, and large elastic twisting of the flexbeam during the application of pitch control. The earlier analytical models for bearingless main rotors, such as FLAIR (Refs. 5, 6) and GRASP (Ref. 7), were developed for hover condition only. Sivaneri and Chopra (Ref. 8) were the first to apply the finite element method to the analysis of bearingless main rotors. Researchers at the University of Maryland (Refs. 9-13) used the finite element formulation developed in Ref. 8 to examine the aeroelastic and aeromechanical stability of several bearingless rotor configurations in hover and forward flight conditions. In the above analyses, the blade periodic response in forward flight was calculated using a temporal finite element formulation, after transforming the spatially discretized blade equations to a few normal mode equations, to reduce computation time.

Recognizing that the direct use of normal modes is fraught with difficulty on account of the large elastic deformations due to the application of pitch control (particularly the large twist in the flexbeam), the authors (Ref. 14) recently developed a refined aeroelastic analysis for bearingless rotor helicopters in forward flight. In this analysis, large elastic deformations due to pitch control application are purged from the total deformations and calculated independently, in vacuo. Since the elastic deformations due to aerodynamic and inertial loads have been separated from the large elastic deformations due to pitch control, normal mode methods can now be used for the aeroelastic analysis.

Since elastomeric dampers strongly influence the dynamic and aeroelastic characteristics of the bearingless main rotor (Ref. 1), a reliable analytical damper model that can be conveniently integrated into bearingless rotor comprehensive analyses is required. Development of such a model, that can characterize the behavior over the complete

Presented at the AHS 51st Annual Forum, Fort Worth, Texas, May 9-11, 1995. Manuscript submitted April 1995; accepted April 1996.

*Currently Assistant Professor of Aerospace Engineering, The Pennsylvania State University

range of operating conditions, has been a challenge, as the behavior of elastomeric dampers is extremely complex and nonlinearly dependent on several factors such as the amplitude and frequency of motion, the equilibrium condition, damper configuration and temperature. Current bearingless rotor analyses use very simple elastomeric damper models, or table look-up methods (Ref. 15).

Previous efforts toward the analytical modeling of these dampers by Hausmann (Refs. 16, 17), and Felker *et al* (Ref. 18), had certain limitations. For example, in the Felker time-domain model there is no provision for derivatives of damper force and displacement, and the model does not account for dependence of damper behavior on *equilibrium condition*. The Hausmann model addresses these issues, but is a frequency domain approach based on complex modulus. Such an approach is less attractive for nonlinear viscoelastic materials because of the variation of the complex moduli, G' and G'' , with *dynamic amplitude*, and the inability to use superposition for multifrequency excitations. A more detailed discussion on these models is available in (Ref. 19).

Gandhi *et al* (Ref. 20) recently developed a nonlinear elastomeric damper model that overcomes many of the limitations of the previous models. The elastomeric damper is represented by a combination of linear and nonlinear springs and dashpots, and its behavior is described in the *time-domain* by a nonlinear differential equation. The constitutive equation characterizes the nonlinear behavior of the elastomeric damper, for large amplitude vibrations, at different equilibrium conditions and under multi-frequency excitations. The authors examined the influence of this elastomeric damper model on hover aeromechanical stability (Ref. 21) and forward flight flap-lag stability (Ref. 22) of articulated and hingeless rotor helicopters represented by simple *rigid blade* approximations. It was concluded that the rotor lag mode stability characteristics are influenced by the steady lag displacement in hover, and the periodic lag response in forward flight.

More recently, additional behavioral characteristics of elastomeric dampers have been observed, such as the degradation of complex modulus component G'' at very small dynamic amplitudes (Refs. 17, 23), and the existence of limit cycle oscillations of rotor blades with these nonlinear elastomeric dampers. The analytical model developed in Ref. 20 does not account for these characteristics. Thus, the objectives of the present paper are three-fold: (i) Augment the damper model in Ref. 20 to represent the additional behavioral characteristics — reduction in G'' (damping) at very low dynamic amplitudes, and limit cycle oscillations, (ii) Systematically integrate the damper model into the bearingless rotor comprehensive analysis developed in Ref. 14, and (iii) Examine the effects of the nonlinear damper on bearingless rotor aeroelastic behavior, including aeromechanical stability, in different operating conditions.

Augmented Spring-Dashpot Model for Nonlinear Elastomeric Damper

The elastomeric damper model developed in Ref. 20 consisted of a nonlinear spring, S1, in series with a linear Kelvin chain (denoted as *original model* in Fig. 1). The spring S1 was softening in nature to represent the instantaneous force/displacement behavior of an elastomer, and was described by

$$\zeta_{S1} = f(D) = \text{sign}(D) \left(c_1|D| + c_2|D|^2 + c_3|D|^3 + c_4|D|^4 \right) \quad (1)$$

where D is the force and ζ_{S1} is the displacement in S1. The original model was able to represent the experimentally measured variation of complex moduli (G' and G'') with dynamic amplitude, as shown in Fig. 2. Recent investigations, however, have revealed that the imaginary part, G'' , of the complex modulus can be considerably degraded at very low dynamic amplitudes (Refs. 17, 23). This behavior has not

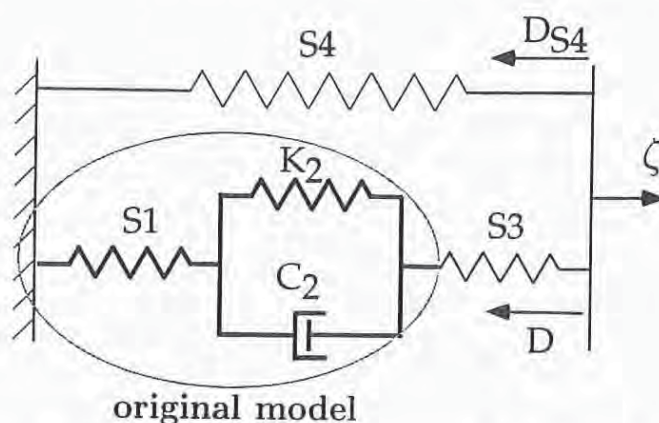


Fig. 1. Schematic spring-dashpot representation of elastomeric damper.

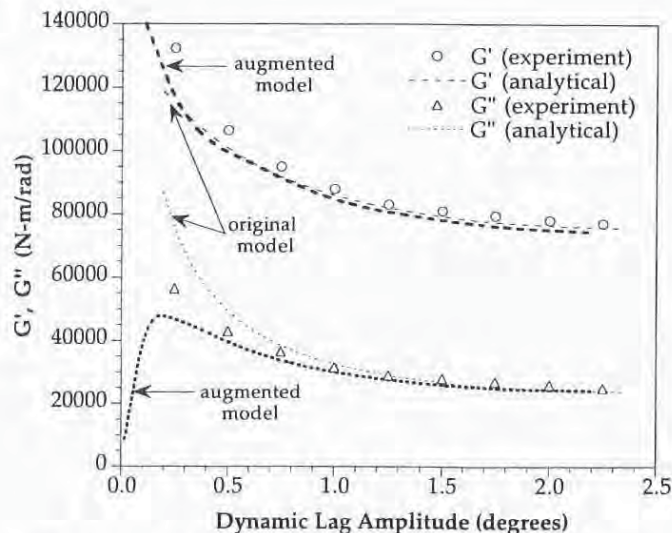


Fig. 2. Variation of complex modulus components, G' (stiffness) and G'' (damping), with dynamic amplitude.

been represented in the original model presented in Ref. 20. It has also been observed that perturbation of rotor blades with elastomeric dampers can result in a transient that settles to constant amplitude stable limit cycle oscillations (jitter phenomenon). The original elastomeric damper model is augmented with additional nonlinear springs S3 and S4 (Fig. 1) to model these behavioral characteristics.

An understanding of the nonlinear damping mechanism in the original model is a useful guide in determining the behavior of the augmenting springs S3 and S4. The high stiffness of S1 at low displacement amplitude results in considerable damping (high G'') as the majority of the damper motion occurs in the Kelvin chain (comprising of linear spring K_2 and dashpot C_2). As displacement amplitude increases, significant motion is obtained in the spring S1 due to its softening behavior, causing a decrease in G'' (damping) associated with the reduced motion in the Kelvin chain.

It is hypothesized that a reduction in G'' at small displacement amplitudes could be obtained by introducing a series spring, S3, that is very soft in the small displacement regime (so that the majority of the damper motion occurs in *this spring* rather than the dashpot in the Kelvin chain) and *rapidly hardens* thereafter, rendering it ineffective in the large displacement regime. The force/displacement behavior of

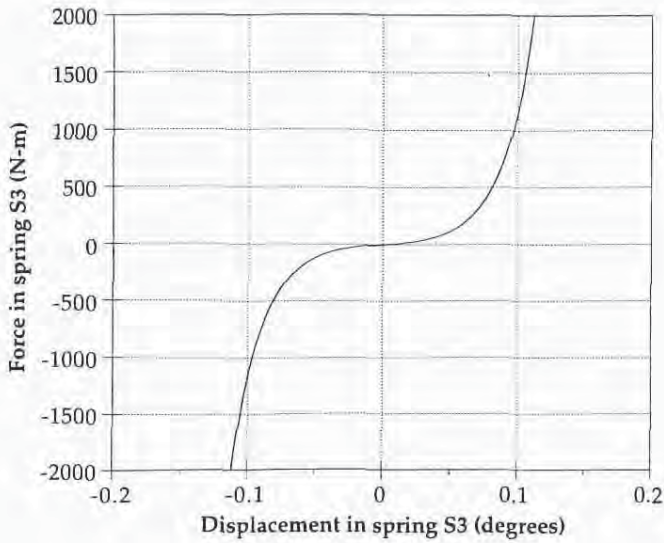


Fig. 3. Force versus displacement behavior of nonlinear spring S3 of the augmented model.

spring S3 is shown in Fig. 3 and described by

$$D = \text{sign}(\zeta_{S3}) \left[c_5(e^{c_6|\zeta_{S3}|} - 1) \right] \quad (2)$$

$$\text{or } \zeta_{S3} = \text{sign}(D) \left[\frac{1}{c_6} \ln \left(\frac{|D|}{c_5} + 1 \right) \right] \quad (3)$$

where D is the force and ζ_{S3} is the displacement in S3. While augmenting the model with such a spring alone expectedly reduces G'' at low amplitudes of excitation, it results in a decrease in G' , as well. To alleviate the reduction in G' at small amplitudes, spring S4 is introduced in parallel with the series configuration consisting of the Kelvin chain and springs S1 and S3, as shown in Fig. 1. The nonlinear behavior of spring S4 is expressed as

$$D_{S4} = g(\zeta) = \text{sign}(\zeta) \left[c_7(1 - e^{-c_8|\zeta|}) \right] \quad (4)$$

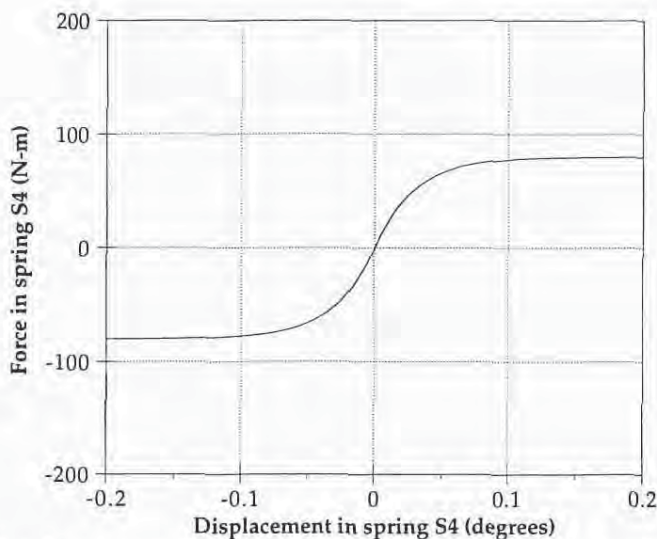


Fig. 4. Force versus displacement behavior of nonlinear spring S4 of the augmented model.

and is shown in Fig. 4. In the above equation, D_{S4} is the force in the spring S4, and ζ is the total damper displacement. The high stiffness at small displacement amplitudes prevents the decrease of G' , whereas the very low stiffness at higher amplitudes renders the branch virtually ineffective in the large displacement regime.

In Ref. 20, a rigorous mathematical procedure was presented for the evaluation of the parameters (c_1, c_2, c_3, c_4) of the nonlinear spring S1, and the linear elements (K_2, C_2) in the Kelvin chain. These parameters were determined by employing a least square fit to experimental complex modulus data, at various amplitudes of excitation. Fig. 2 shows the variation of G' and G'' with dynamic amplitude, obtained using the augmented model (with a judicious selection of parameters c_5, c_6 , and c_7, c_8 , of springs S3 and S4 respectively). From the figure it can be seen that the additional springs in the augmented model effectively decrease G'' at small amplitudes, while having no additional detrimental effect on the variation of G' or G'' with increasing dynamic amplitude.

For analysis purposes, the two nonlinear springs S1 and S3 can be treated as a single nonlinear spring. If $\zeta_{non} = \zeta_{S1} + \zeta_{S3}$ is the total displacement in the two nonlinear springs S1 and S3, and D is the force, from Eqs. (1) and (3)

$$\begin{aligned} \zeta_{non} &= \bar{f}(D) \\ &= \text{sign}(D) \left[c_1|D| + c_2|D|^2 + c_3|D|^3 \right. \\ &\quad \left. + c_4|D|^4 + \frac{1}{c_6} \ln \left(\frac{|D|}{c_5} + 1 \right) \right] \end{aligned} \quad (5)$$

The relation between D and the total damper displacement ζ can then be written as

$$K_2\zeta + C_2 \dot{\zeta} = K_2 \bar{f}(D) + C_2 \frac{d\bar{f}(D)}{dD} \dot{D} + D \quad (6)$$

Note that the total elastomeric damper force is the sum of the forces D (in the branch containing the Kelvin chain), and D_{S4} (in the parallel spring S4), as shown in Fig. 1.

Hysteresis Cycles

The force/displacement hysteresis cycles of the augmented elastomeric damper model can be calculated by the application of a single frequency sinusoidal excitation $\zeta = \zeta_0 e^{i\Omega t}$ to Eqs. (4) and (6). For a linear viscoelastic material, the hysteresis cycles are ellipses, and can be described mathematically by standard equations. However, for the nonlinear elastomeric damper, the nature of the hysteresis cycles changes with both dynamic amplitude and static preload. Fig. 5 shows hysteresis cycles of different amplitudes at zero static preload for the augmented damper model developed in the previous section. These hysteresis cycles better represent the nature of experimentally measured cycles (Refs. 16, 17) than do cycles based on the original damper model in Ref. 20. Fig. 5 also shows the static force/displacement behavior of the augmented elastomeric damper model. It can be seen that the model represents the softening behavior of elastomeric materials under static loads.

Limit Cycle Oscillations

To examine whether the augmented elastomeric damper model can predict limit cycle oscillations, the damper nonlinear differential equation is solved simultaneously with the isolated blade lag equation in the rotating frame. The blade lag equation can be written as

$$\zeta^{**} + \nu \zeta^2 + \bar{D} = M \zeta \quad (7)$$

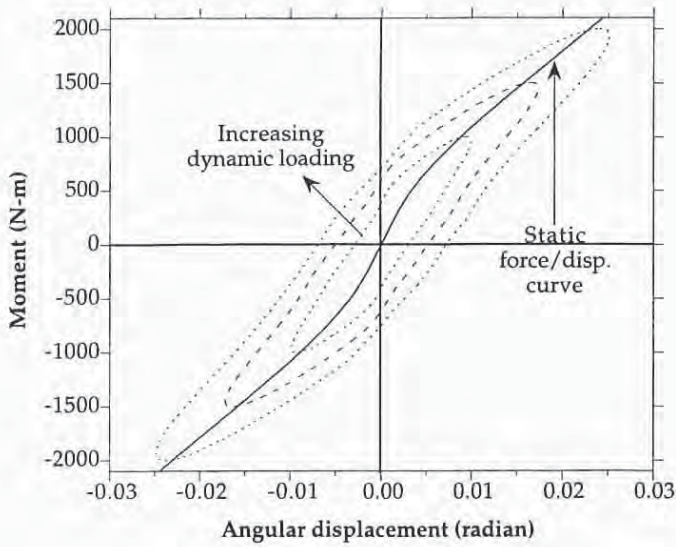


Fig. 5. Nonlinear hysteresis cycles for augmented damper model, about zero equilibrium position, and at different dynamic loads.

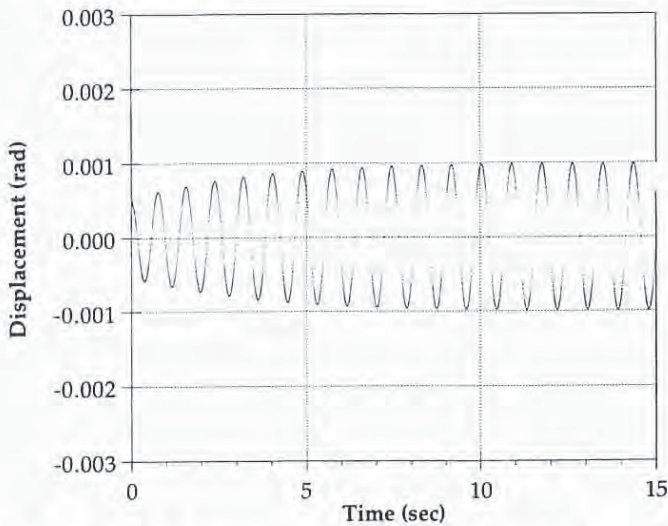


Fig. 6a. Transient lag response for a perturbation $\xi_o=0.0005$ radian.

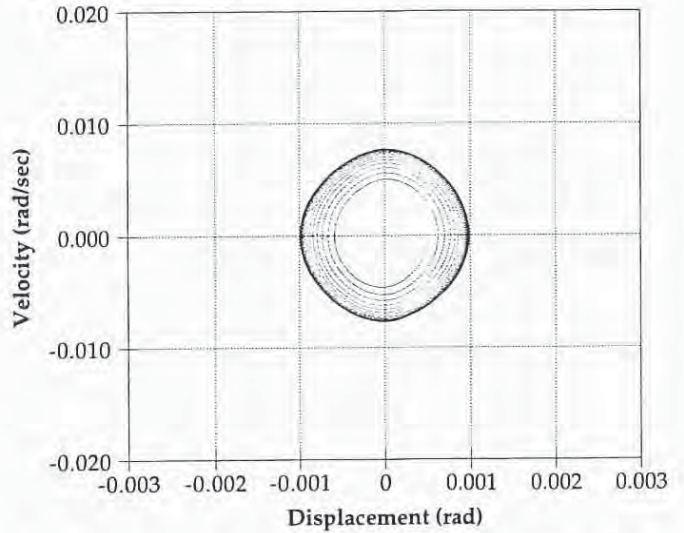


Fig. 6b. Transient lag response for a perturbation $\xi_o=0.0005$ radian.

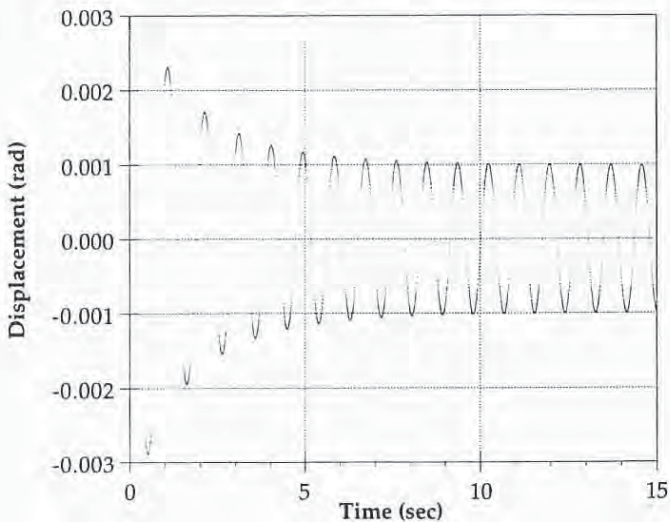


Fig. 7a. Transient lag response for a perturbation $\xi_o=0.0030$ radian.

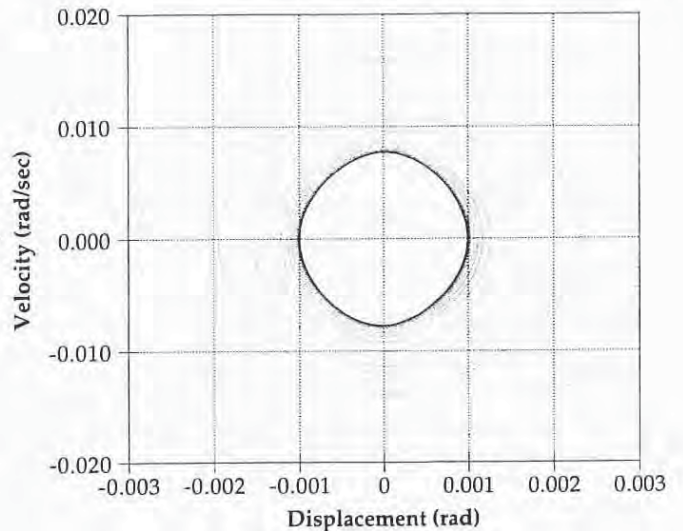


Fig. 7b. Transient lag response for a perturbation $\xi_o=0.0030$ radian.

where \bar{D} is the nondimensional elastomeric damper force, ζ is the lag displacement, ν_ζ is the rotating lag frequency, and M_ζ is the aerodynamic lag moment. Expressing the total damper force \bar{D} as the sum of D and D_{s4} , and using Eq. (4) for D_{s4} , the lag equation can be written as

$$\zeta^{**} + \nu_\zeta^2 \zeta + D + g(\zeta) = M_\zeta \quad (8)$$

Eq. (8) is solved simultaneously with the nonlinear differential equation, (6), for the force, D , in the Kelvin chain branch of the damper.

To evaluate the transient response of the system, the aerodynamic lag moment, M_ζ , is set to zero, and the system is successively given initial perturbations of $\xi_o = 0.0005$ radian and 0.003 radian. In both cases, within a short time the transient settles to stable self-sustained limit cycle oscillations, as shown in Figs. 6a and 7a. Figs. 6b and 7b show the transient responses represented in the phase-plane (velocity/displacement plane). Limit cycles are known to be characterized by *orbits* in the phase plane, implying a periodic motion. In Figs. 6 and 7, the different initial perturbations, expectedly, yield stable limit cycle oscillations of the same amplitude, as it is known that the amplitude is dependent only on the characteristics of the nonlinear system and is independent of the initial perturbation size.

Integration of Damper Into Bearingless Rotor Analysis

To study the effects of the elastomeric lag damper on the aeroelastic behavior of a bearingless main rotor helicopter, the damper model is integrated into a bearingless rotor comprehensive analysis developed by the authors in Ref. 14. The rotor blades are modeled as elastic beams undergoing coupled flap bending, lag bending, elastic torsion, and axial deformations. The finite element method is used in the structural modeling of the rotor blades as it is extremely convenient for bearingless rotors with redundant load paths and complex hub kinematics. The refined aeroelastic analysis is carried out in two steps: (i) Calculation of elastic deformations (particularly the large flexbeam twist) experienced by the bearingless blades as a result of a prescribed washplate motion, in the absence of aerodynamic forces, and (ii) Use of *modified nonlinear equations*, obtained by the systematic inclusion of the effect of control deformations on the strain energy, to determine the behavior of the bearingless rotor under aerodynamic forces. Thus, by purging the large elastic control deformations from the total blade deformations, this approach has the advantage of permitting the use of normal modes for low computational cost, while including the *effect of the control deformations* on the nonlinear blade response under aerodynamic loads. The analysis is robust, showing good convergence behavior in the evaluation of blade periodic response even at high advance ratios.

Lag damping in the bearingless rotor is generally introduced by means of an elastomeric snubber damper, attached between the inboard end of the torque tube and the flexbeam (Figs. 8 and 9). The snubber damper, in addition to augmenting the stability of the lowly damped lag mode, alleviates pitch-flap coupling and keeps the flexbeam centered with respect to the torque tube.

Since the lag damper behavior is governed by a nonlinear *differential equation*, an expression for damping force in terms of lag displacement and velocity is not available for direct substitution into the blade lag equation. Thus, the damper differential equation is solved simultaneously with the blade and fuselage equations, with damper force or an internal damper displacement appearing as an independent state.

The coupled bending-torsion-axial equations of motion of the bearingless rotor blade are obtained by introducing expressions for the variations in strain energy, δU , kinetic energy, δT , and the virtual work δW due to external aerodynamic loads, in Hamilton's Principle:

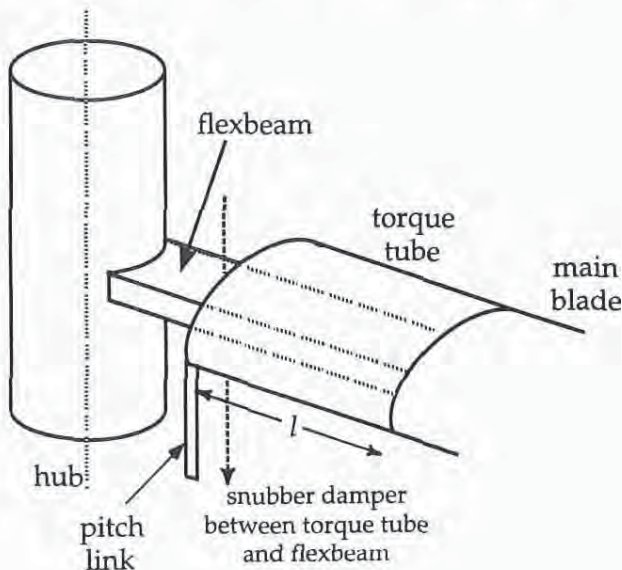


Fig. 8. Bearingless rotor hub.

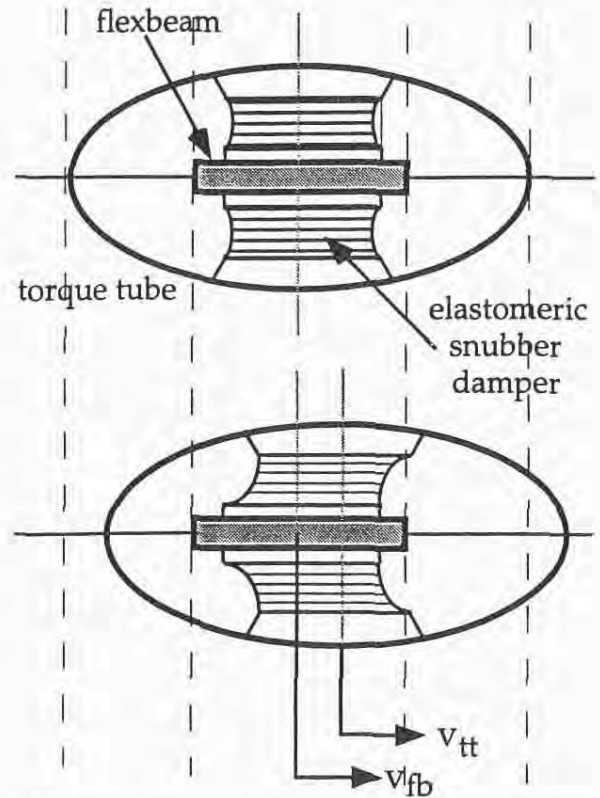


Fig. 9. Elastomeric snubber damper attached between inboard end of torque tube and flexbeam shears during relative lag motion.

$$\delta\pi = \int_{\psi_1}^{\psi_2} (\delta U - \delta T - \delta W) d\psi = 0 \tag{9}$$

Spatial discretization of Hamilton's Principle results in a set of finite element equations

$$\delta\pi = \int_{\psi_1}^{\psi_2} \delta\mathbf{q}^T \left[\mathbf{M}(\psi) \ddot{\mathbf{q}} + \mathbf{C}(\psi) \dot{\mathbf{q}} + \mathbf{K}(\psi)\mathbf{q} - \mathbf{F}(\psi, \mathbf{q}) \right] d\psi = 0 \tag{10}$$

where \mathbf{M} , \mathbf{C} , and \mathbf{K} are the assembled global mass, damping, and stiffness matrices, respectively, \mathbf{F} is the global load vector, and \mathbf{q} is the blade nodal displacement vector. The blade aerodynamic loads are obtained using quasi-steady strip theory and linear inflow assumption. The solution of Eq. (10) yields the rotor blade periodic response.

Rotor Periodic Response and Vehicle Trim

Since Eq. (10) represents a system of *nonlinear* differential equations with *periodic coefficients*, its solution is obtained iteratively, using a temporal finite element method. To reduce the computational time, Eq. (10) is first transformed into a system of normal mode equations, expressed as

$$\delta\pi = \int_0^{2\pi} \left(\delta\mathbf{p}^T \delta \dot{\mathbf{p}}^* \right) \left\{ \begin{matrix} \bar{\mathbf{F}} - \bar{\mathbf{C}} \dot{\mathbf{p}}^* - \bar{\mathbf{K}}\mathbf{p} \\ \bar{\mathbf{M}} \dot{\mathbf{p}}^* \end{matrix} \right\} d\psi = 0 \tag{11}$$

where $\bar{\mathbf{M}}$, $\bar{\mathbf{C}}$, and $\bar{\mathbf{K}}$ are the modal mass, damping, and stiffness matrices, respectively, $\bar{\mathbf{F}}$ is the modal load vector, and \mathbf{p} and $\dot{\mathbf{p}}$ are the modal displacement and velocity vectors. Typically 6 to 8 coupled rotating

modes are used to evaluate the rotor response.

Introducing the elastomeric damper nonlinear differential equation yields

$$\int_0^{2\pi} \left(\delta \mathbf{p}_a^T \delta \dot{\mathbf{p}}_a^* \right) \left\{ \begin{matrix} \bar{\mathbf{F}}_a - \bar{\mathbf{C}}_a \dot{\mathbf{p}}_a^* - \bar{\mathbf{K}}_a \mathbf{p}_a \\ \bar{\mathbf{M}}_a \dot{\mathbf{p}}_a^* \end{matrix} \right\} d\psi = 0 \quad (12)$$

where the subscript *a* denotes augmented matrices and vectors due to the additional damper state. In Eq. (12),

$$\bar{\mathbf{K}}_a = \begin{bmatrix} \bar{\mathbf{K}} & \bar{\mathbf{K}}_{bd} \\ \bar{\mathbf{K}}_{db} & \bar{\mathbf{K}}_{dd} \end{bmatrix} \quad (13)$$

$$\bar{\mathbf{C}}_a = \begin{bmatrix} \bar{\mathbf{C}} & \mathbf{0} \\ \bar{\mathbf{C}}_{db} & \mathbf{0} \end{bmatrix} \quad (14)$$

$$\bar{\mathbf{M}}_a = \begin{bmatrix} \bar{\mathbf{M}} & \mathbf{0} \\ \mathbf{0} & \mathbf{0} \end{bmatrix} \quad (15)$$

$$\bar{\mathbf{F}}_a = \begin{bmatrix} \bar{\mathbf{F}} \\ \bar{F}_d \end{bmatrix} \quad (16)$$

$$\mathbf{p}_a = \begin{bmatrix} \mathbf{p} \\ D \end{bmatrix} \quad (17)$$

where $\bar{\mathbf{K}}_{bd}$ is the blade-damper coupling vector, $\bar{\mathbf{K}}_{db}$ and $\bar{\mathbf{C}}_{db}$ are the damper-blade coupling vectors, $\bar{\mathbf{K}}_{dd}$ is the damper stiffness, $\bar{\mathbf{F}}_a$ contains the damper nonlinear terms, and *D* is the damper force. Since inclusion of the damper requires only the augmentation of the original rotor matrices and vectors, it is extremely convenient and simple to implement.

To obtain expressions for $\bar{\mathbf{K}}_{bd}$, $\bar{\mathbf{K}}_{db}$ and $\bar{\mathbf{C}}_{db}$, the lag displacement ξ in the damper equation, (6), is related to the torque tube and flexbeam nodal lag displacements (v_u and v_{fb}) at the damper attachment points, (Fig. 9), and expressed in terms of modal coordinates. Eq. (6) is then written as

$$\begin{aligned} & K_2 f(D) + C_2 \frac{df}{dD} \dot{D} + D \\ & - K_2 \sum \frac{\phi_{fb}^{(j)} - \phi_{tt}^{(j)}}{l} p^{(j)} \\ & - C_2 \sum \frac{\phi_{fb}^{(j)} - \phi_{tt}^{(j)}}{l} \dot{p}^{(j)} = 0 \end{aligned} \quad (18)$$

In Eq. (18) the torque tube radial length *l* is used to convert the relative translational lag displacement at the damper attachment points, $v_u - v_{fb}$ (expressed as a summation of modal contributions), into an angular lag displacement, required in the damper equation, (6). $\phi^{(j)}$ denotes the *j*th normal mode vector, and the subscripts *tt* and *fb* denote the elements of that vector corresponding to lag motion at the points of damper attachment to the torque tube and the flexbeam, respectively. The summation is over the number of modes used to estimate the response.

Using Eq. (18), the *j*th element of the damper-blade coupling vectors can be obtained as

$$\bar{\mathbf{K}}_{db}^{(j)} = \frac{K_2}{l} (\phi_{fb}^{(j)} - \phi_{tt}^{(j)}) \quad (19)$$

$$\bar{\mathbf{C}}_{db}^{(j)} = \frac{C_2}{l} (\phi_{fb}^{(j)} - \phi_{tt}^{(j)}) \quad (20)$$

Similarly, the *j*th blade-damper coupling element can be expressed as

$$\bar{\mathbf{K}}_{bd}^{(j)} = \frac{1}{l} (\phi_{fb}^{(j)} - \phi_{tt}^{(j)}) \quad (21)$$

Remaining damper related terms in Eqs. (13) and (16) are

$$\bar{\mathbf{K}}_{dd} = -1 \quad (22)$$

$$\bar{F}_d = K_2 f(D) + C_2 \frac{df}{dD} \dot{D} \quad (23)$$

Eq. (12) can be symbolically expressed as

$$\int_0^{2\pi} \delta \mathbf{y}^T \mathbf{Q} d\psi = 0 \quad (24)$$

where

$$\mathbf{y} = \begin{bmatrix} \mathbf{p}_a \\ \dot{\mathbf{p}}_a^* \end{bmatrix}$$

and

$$\mathbf{Q} = \begin{bmatrix} \bar{\mathbf{F}}_a - \bar{\mathbf{C}}_a \dot{\mathbf{p}}_a^* - \bar{\mathbf{K}}_a \mathbf{p}_a \\ \bar{\mathbf{M}}_a \dot{\mathbf{p}}_a^* \end{bmatrix} \quad (25)$$

The matrices $\bar{\mathbf{K}}_a$ and $\bar{\mathbf{C}}_a$ contain periodic terms while $\bar{\mathbf{F}}_a$ is both nonlinear and periodic. To solve the nonlinear periodic system, (24), the time interval for one rotor revolution of 2π is divided into a number of temporal elements. The blade governing equations can then be expressed as the sum of the elemental equations. Further, Eq. (24) is expanded as a first order Taylor series about a steady value \mathbf{y}_o , to yield

$$\sum_{i=1}^{N_t} \int_{\psi_i}^{\psi_{i+1}} \delta \mathbf{y}_i^T [\mathbf{Q}_i(\mathbf{y}_o) + \mathbf{K}_{ti}(\mathbf{y}_o) \Delta \mathbf{y}_i] d\psi = 0 \quad (26)$$

where $\psi_1 = 0$, $\psi_{N_t+1} = 2\pi$, N_t is the number of time elements used and \mathbf{K}_{ti} is the tangential stiffness matrix of the *i*th temporal element, given by

$$\mathbf{K}_{ti} = \begin{bmatrix} \frac{\partial \bar{\mathbf{F}}_a}{\partial \mathbf{p}_a} - \bar{\mathbf{K}}_a & \frac{\partial \bar{\mathbf{F}}_a}{\partial \dot{\mathbf{p}}_a^*} - \bar{\mathbf{C}}_a \\ \mathbf{0} & \bar{\mathbf{M}}_a \end{bmatrix}_i \quad (27)$$

The blade response \mathbf{p}_a is expressed within each time element in terms of temporal shape functions, and nodal values, ξ_i . Introducing such an expression into Eq. (26) yields a system of nonlinear algebraic equations

$$\sum_{i=1}^{N_t} \int_{\psi_i}^{\psi_{i+1}} \delta \xi_i^T \mathbf{N}^T [\mathbf{Q}_i + \mathbf{K}_{ti} \mathbf{N} \Delta \xi_i] d\psi = 0 \quad (28)$$

where \mathbf{N} is the matrix of temporal shape functions and derivatives. During assembly of the global temporal finite element equations, periodicity is imposed by connecting the first and last azimuthal elements. The solution of Eq. (28) for the global response ξ is obtained using an iterative procedure based on the Newton-Raphson method.

A coupled trim procedure is adopted, whereby, convergence of the blade periodic response and vehicle equilibrium, are simultaneously accomplished. The updated blade response obtained after successive Newton-Raphson iterations is used in the calculation of the hub loads, which influence vehicle orientation and control settings. These new controls, in turn, are used in the subsequent blade response iteration. This procedure accurately determines the vehicle trim, blade periodic response and periodic damper force, which are known to have a significant influence on the stability characteristics of the system (Refs. 21, 22).

Stability of Perturbation Equations

To evaluate the stability of the rotor-fuselage-damper system, the state variables are subject to small perturbations about the trim condition. Hamilton's Principle, Eq. (9), can then be written as

$$\delta\pi = \delta\pi_o + \delta\Delta\pi = 0 \tag{29}$$

where $\delta\pi_o$ is due to the trim condition, and $\delta\Delta\pi$ is due to the perturbation motion about the trim condition. Since the trim condition is evaluated as the solution to $\delta\pi = 0$, from Eq. (29),

$$\delta\Delta\pi = \delta\Delta\pi_F + \delta\Delta\pi_R = \delta\Delta\pi_F + \sum_{i=1}^{N_b} \delta\Delta\pi_i = 0 \tag{30}$$

In Eq. (30), the subscripts *F* and *R* refer to fuselage and rotor, respectively. Further, the rotor contribution, $\delta\Delta\pi_R$ is due to the sum of the contributions of N_b individual blades. After spatial finite element discretization, and transformation to normal mode coordinates, Eq. (30) can be expressed as,

$$\begin{bmatrix} \mathbf{K}_1 & \dots & 0 & \mathbf{K}_{1F} & \mathbf{K}_{bd}^{(1)} & \dots & 0 \\ \dots & \dots & \dots & \dots & \dots & \dots & \dots \\ 0 & \dots & \mathbf{K}_{N_b} & \mathbf{K}_{N_bF} & 0 & \dots & \mathbf{K}_{bd}^{(N_b)} \\ \mathbf{K}_{F1} & \dots & \mathbf{K}_{FN_b} & \mathbf{K}_{FF} & 0 & \dots & 0 \\ \mathbf{K}_{db}^{(1)} & \dots & 0 & 0 & \mathbf{K}_{dd}^{(1)} & \dots & 0 \\ \dots & \dots & \dots & \dots & \dots & \dots & \dots \\ 0 & \dots & \mathbf{K}_{db}^{(N_b)} & 0 & \dots & \dots & \mathbf{K}_{dd}^{(N_b)} \end{bmatrix} \begin{Bmatrix} \Delta p_1 \\ \dots \\ \Delta p_{N_b} \\ \Delta x_F \\ \Delta D_1 \\ \dots \\ \Delta D_{N_b} \end{Bmatrix} + \begin{bmatrix} \mathbf{C}_1 & \dots & 0 & \mathbf{C}_{1F} & 0 & \dots & 0 \\ \dots & \dots & \dots & \dots & \dots & \dots & \dots \\ 0 & \dots & \mathbf{C}_{N_b} & \mathbf{C}_{N_bF} & 0 & \dots & 0 \\ \mathbf{C}_{F1} & \dots & \mathbf{C}_{FN_b} & \mathbf{C}_{FF} & 0 & \dots & 0 \\ \mathbf{C}_{db}^{(1)} & \dots & 0 & 0 & \mathbf{C}_{dd}^{(1)} & \dots & 0 \\ \dots & \dots & \dots & \dots & \dots & \dots & \dots \\ 0 & \dots & \mathbf{C}_{db}^{(N_b)} & 0 & \dots & \dots & \mathbf{C}_{dd}^{(N_b)} \end{bmatrix} \begin{Bmatrix} \Delta \dot{p}_1 \\ \dots \\ \Delta \dot{p}_{N_b} \\ \Delta \dot{x}_F \\ \Delta \dot{D}_1 \\ \dots \\ \Delta \dot{D}_{N_b} \end{Bmatrix} + \begin{bmatrix} \mathbf{M}_1 & \dots & 0 & \mathbf{M}_{1F} & 0 & \dots & 0 \\ \dots & \dots & \dots & \dots & \dots & \dots & \dots \\ 0 & \dots & \mathbf{M}_{N_b} & \mathbf{M}_{N_bF} & 0 & \dots & 0 \\ \mathbf{M}_{F1} & \dots & \mathbf{M}_{FN_b} & \mathbf{M}_{FF} & 0 & \dots & 0 \\ 0 & \dots & 0 & 0 & 0 & \dots & 0 \\ \dots & \dots & \dots & \dots & \dots & \dots & \dots \\ 0 & \dots & 0 & 0 & \dots & \dots & 0 \end{bmatrix} \begin{Bmatrix} \Delta \ddot{p}_1 \\ \dots \\ \Delta \ddot{p}_{N_b} \\ \Delta \ddot{x}_F \\ \Delta \ddot{D}_1 \\ \dots \\ \Delta \ddot{D}_{N_b} \end{Bmatrix} = 0 \tag{31}$$

where \mathbf{K}_i , \mathbf{C}_i , and \mathbf{M}_i are the linearized modal stiffness, damping and mass matrices of the i^{th} blade; \mathbf{K}_{iF} , \mathbf{C}_{iF} , and \mathbf{M}_{iF} are blade-fuselage coupling matrices; \mathbf{K}_{Fi} , \mathbf{C}_{Fi} , and \mathbf{M}_{Fi} are fuselage-blade coupling matrices; and x_i is the fuselage motion vector. A detailed description of these is available in Ref. 24. The damper related terms are described below.

The j^{th} element of the blade-damper coupling vector, $\mathbf{K}_{bd}^{(i)}$, in Eq. (31) is given by

$$\mathbf{K}_{bd}^{(i)} \Big|_j = \frac{1}{l} (\phi_{fb}^{(j)} - \phi_{tt}^{(j)}) \tag{32}$$

The j^{th} elements of the damper-blade coupling vectors, $\mathbf{K}_{db}^{(i)}$, and $\mathbf{C}_{db}^{(i)}$, in Eq. (31) are

$$\mathbf{K}_{db}^{(i)} \Big|_j = -\frac{K_2}{l} (\phi_{fb}^{(j)} - \phi_{tt}^{(j)}) \tag{33}$$

$$\mathbf{C}_{db}^{(i)} \Big|_j = -\frac{C_2}{l} (\phi_{fb}^{(j)} - \phi_{tt}^{(j)}) \tag{34}$$

In Eqs. (32)-(34), the superscript *i* refers to vectors pertaining to the i^{th} blade and damper. The stiffness and damping of the i^{th} damper are respectively expressed as

$$K_{dd}^{(i)} = 1 + K_2 \frac{df}{dD} \Big|_{D_T^{(i)}} + C_2 \frac{d^2f}{dD^2} \Big|_{D_T^{(i)}} \dot{D}_T^{(i)} \tag{35}$$

$$C_{dd}^{(i)} = C_2 \frac{df}{dD} \Big|_{D_T^{(i)}} \tag{36}$$

where $D_T^{(i)}$ and $\dot{D}_T^{(i)}$ denote the trim or equilibrium i^{th} damper force and its derivative. After transforming the blade-damper-fuselage equations, (31), to nonrotating coordinates using multiblade coordinate transforms, stability of the linearized periodic system can be evaluated using Floquet transition matrix theory, as described in Ref. 24.

Results and Discussion

A numerical study of elastomeric damper effects on the lag mode stability of a 3-bladed model bearingless rotor is presented in this section. The baseline rotor (without damper) was tested in hover at the Ames Research Center by the US Army Aeroflightdynamics Directorate as part of the Integrated Technology Rotor (ITR) program (Ref. 25). Recently, validation of the experimental results in Ref. 25, and a comprehensive analytical investigation of the shaft-fixed and shaft-free lag mode stability of the baseline rotor in forward flight has been carried out in Ref. 14. For the dynamic and aeroelastic analysis in the present paper, the bearingless rotor blade is discretized into eight spatial elements, three each for the main blade and the flexbeam, and two elements for the torque tube. The nondimensional stiffness and inertial properties, and geometry, for the different elements are available in Table 1. The nondimensional fundamental lag frequency for the baseline rotor is $\nu_\xi = 0.75/rev$. Blade aerodynamic loads in the evaluation of both periodic response and perturbation stability are obtained using quasi-steady strip theory and linear inflow assumption.

The elastomeric damper is attached between the inboard end of the torque tube, and the flexbeam, as indicated in Figs. 8 and 9. Since the damper analytical model was developed based on full scale damper experimental data, it is scaled down appropriately for integration into the model rotor. Two different damper sizes are considered. Damper A increases the fundamental lag frequency, ν_ξ , to 0.785/rev, while Damper B is stiffer and increases ν_ξ to 0.88/rev. Although the stiffness of the two dampers is different, both have the same nonlinear behavioral characteristics as the full scale damper. It should be pointed out that the result-

Table 1: Bearingless Rotor Blade Properties.

Element	$\frac{l_i}{R}$	$\frac{m_i}{m_o}$	$\frac{EI_y}{m_o \Omega^2 R^4}$	$\frac{EI_z}{m_o \Omega^2 R^4}$	$\frac{GJ}{m_o \Omega^2 R^4}$	$\frac{EA}{m_o \Omega^2 R^2}$	
1	0.5	0.702	0.0055	0.1488	0.0029	113.5	main blade
2	0.234	0.702	0.0055	0.1488	0.0029	113.5	main blade
3	0.0684	26.29	0.2621	0.4321	0.2904	184.5	main blade
4	0.1018	0.979	0.00157	0.00616	0.000205	365.3	flexbeam
5	0.1018	0.979	0.00157	0.00616	0.000205	365.3	flexbeam
6	0.0454	75.42	8.064	4.910	16.61	275.1	flexbeam
7	0.0509	11.25	4.473	4.495	1.664	304.7	torque tube
8	0.0509	11.25	4.473	4.495	1.664	350.0	torque tube

radius, $R=3'$, $m_o=3.0745 \times 10^{-3}$ slug/ft, $\Omega = 1100$ rpm

ing high lag frequencies would be unusual on an actual rotor due to the larger dynamic stresses they would produce. In a typical rotor design, the stiffness of the baseline rotor (without damper) would be lower (say ν_ζ of about 0.5 to 0.6/rev), with the addition of the elastomeric damper increasing the lag frequency, ν_ζ , in the range of 0.6 to 0.7/rev.

In the evaluation of the blade periodic response in forward flight, the blade modal matrices and vectors were first calculated *without considering the damper*. Inclusion of the damper nonlinear differential equation then resulted in the augmentation of the system with damper states. However, the above method can require more iterations for the convergence of the blade response, even in hover. This is because the lag modes used are not accurately representative of the physical deformations. The damper imposes a restraint resulting in modes with reduced or constrained motion between the flexbeam and torque tube. Fig. 10 shows the first lag mode deformations in the hub region with and without inclusion of the damper. Fig. 11 shows the second lag mode for the two cases. In Figs. 10 and 11, O and P' denote the radial points of attachment of the damper to the flexbeam and torque tube, respectively. Neglecting damper influence yields a mode, in which the inboard end of the torque tube, P, is less restrained, relative to the flexbeam. This effect is more pronounced for the second lag mode than the first lag mode. In order to improve blade response convergence, damper stiffness may be considered between the torque tube and the flexbeam in the *evaluation of the modes*. These modes are used in the calculation of the *baseline* bearingless rotor modal matrices, which are subsequently

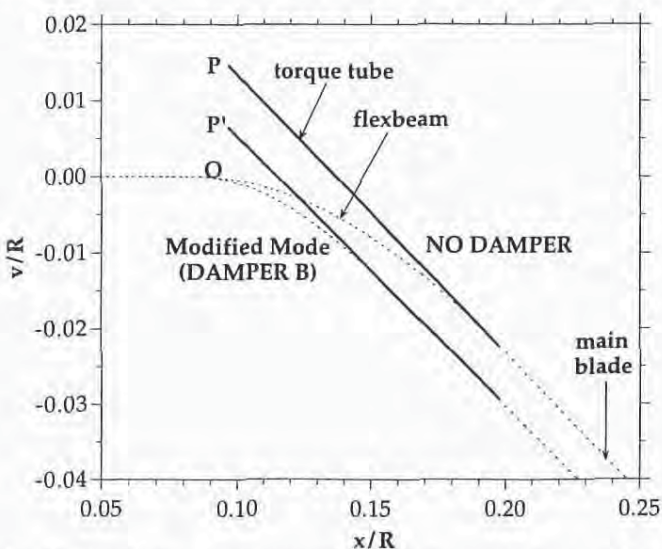


Fig. 10. Bearingless main rotor blade first lag mode shape, with and without inclusion of damper stiffness.

augmented due to the inclusion of the damper nonlinear differential equation. Thus, the stiffer damper, B, which increases ν_ζ to 0.88/rev, results in a larger lag response than damper A, which increases ν_ζ to 0.785/rev. The phase shift (damping effect) for damper B is also seen to be greater.

Figs. 13 and 14, respectively, show the variation of shaft-fixed and

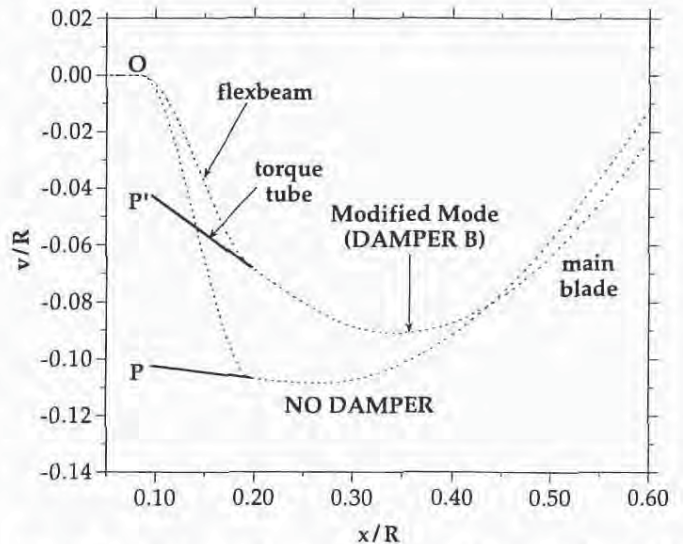


Fig. 11. Bearingless main rotor blade second lag mode shape, with and without inclusion of damper stiffness.

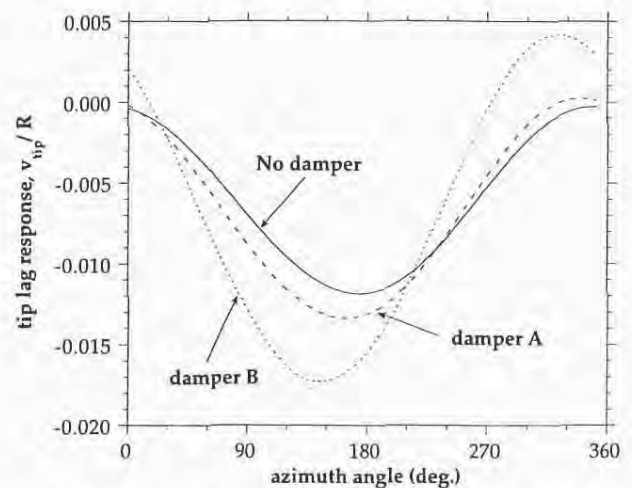


Fig. 12. Periodic tip lag response at advance ratio $\mu=0.15$.

shaft-free lag mode damping with advance ratio, for the baseline rotor (no elastomeric damper) at $C_r/\sigma = 0.07$. For the isolated rotor (Fig. 13), as expected, the damping in the collective, progressive and regressive modes is practically the same. Structural damping in the lag mode was assumed to be 1%. The increased damping at higher advance ratios is due to aerodynamic effects. When fuselage motion is included, the damping in the regressive lag mode decreases due to its interaction with body pitch/roll motion (Fig. 14).

Fig. 15 shows the shaft-fixed isolated rotor lag mode stability with the inclusion of the elastomeric damper. The stiffer damper B results in greater stability of the lag mode, over the entire range of advance ratios. The inclusion of the elastomeric damper is seen to bring about a qualitative change in the nature of lag damping variation with advance ratio. Unlike the baseline rotor, the lag damping shows a general decrease with increasing advance ratio. This can be attributed to the nonlinear behavior of the damper, specifically, the decrease in G'' (damping) at higher amplitudes of periodic lag motion (Fig. 2). Since the amplitude of the periodic lag response increases with advance ratio, it results in a

decrease in damping capabilities of the nonlinear elastomeric damper. Thus, there are two factors contributing to the lag mode damping: (i) aerodynamic effects, which result in an increase in lag damping at higher advance ratios, and (ii) nonlinear damper behavior which results in the decrease in lag damping at higher advance ratios. For the stiffer damper B, the damper nonlinear behavior predominates, and lag damping is seen to decrease with advance ratio. For the less stiff damper A, its nonlinear behavior is dominant at low advance ratios, but the increasing aerodynamic damping at high advance ratios causes a slight increase in the lag mode damping. The above hypothesis is verified by examining the lag damping calculated using a *linear* elastomeric damper. Fig. 16 shows that if a *linear* elastomeric damper is assumed, the overall lag mode stability is greater than that of the damperless rotor, but the *variation with advance ratio* is almost identical to the case of the damperless rotor. Thus it is clear that the nonlinear characterization of the damper results in the reduced lag mode stability at higher advance ratios.

Figs. 17 and 18 show the shaft-free aeromechanical stability of the bearingless rotor with the inclusion of dampers A and B, respectively.

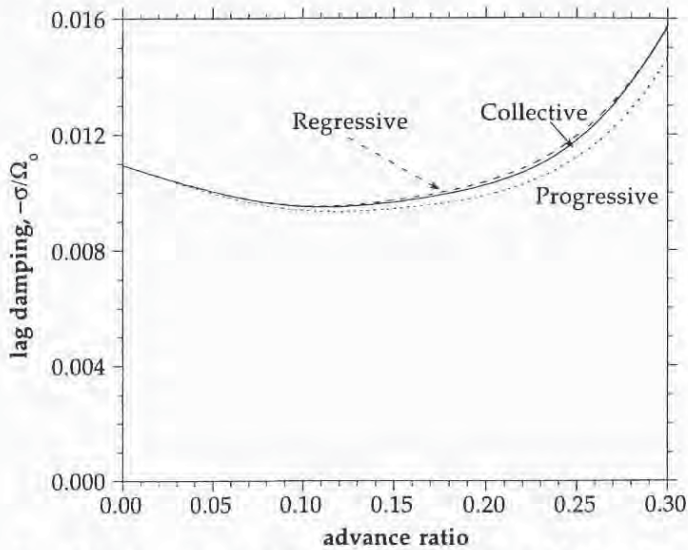


Fig. 13. Variation of shaft-fixed lag mode stability of the baseline (damperless) rotor with advance ratio.

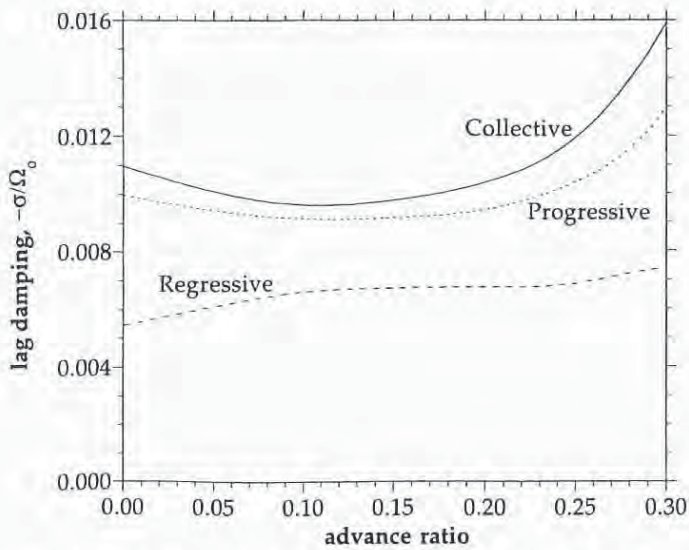


Fig. 14. Variation of shaft-free lag mode stability of the baseline (damperless) rotor with advance ratio.

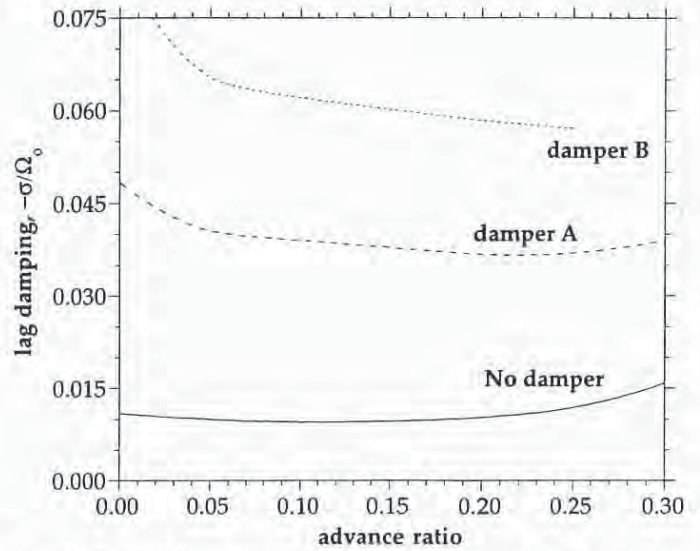


Fig. 15. Bearingless rotor shaft-fixed lag mode stability with inclusion of nonlinear elastomeric damper.

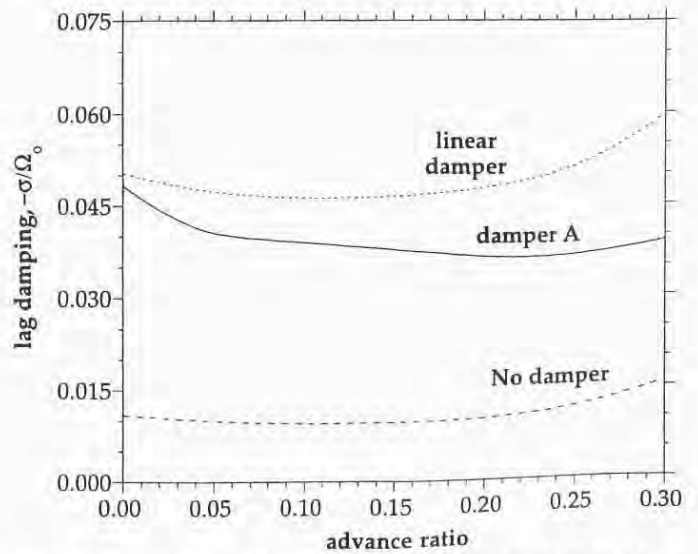


Fig. 16. Comparison of bearingless rotor shaft-fixed lag mode stability using linear and nonlinear damper.

While the elastomeric damper has a stabilizing influence on the collective, progressive as well as regressive lag modes, the damping of the regressive lag mode is considerably lower than that of the progressive and collective modes, with damper B (Fig. 18). Since this phenomenon is not observed for the shaft-fixed case, nor with the use of the weaker damper A (for both shaft-fixed and shaft-free conditions), it may be concluded that the lower regressive mode damping must be due to the influence of damper B dynamics on the coupled regressive lag/fuselage mode.

Another interesting observation is the effect of the elastomeric damper on the second lag mode frequency. Fig. 19 shows the variation of the second lag mode frequency with advance ratio, due to the nonlinear characterization of the damper. While the elastomeric damper also increases the first lag mode frequency, such a variation with advance ratio is not observed. To understand this phenomenon, it is useful to consider the damper equilibrium deformations as a sum of modal contributions. From Eq. (18), the damper deformation can be expressed

in modal coordinates as $\sum \frac{\phi_{fb}^{(j)} - \phi_{te}^{(j)}}{l} p_j$. Although the first lag

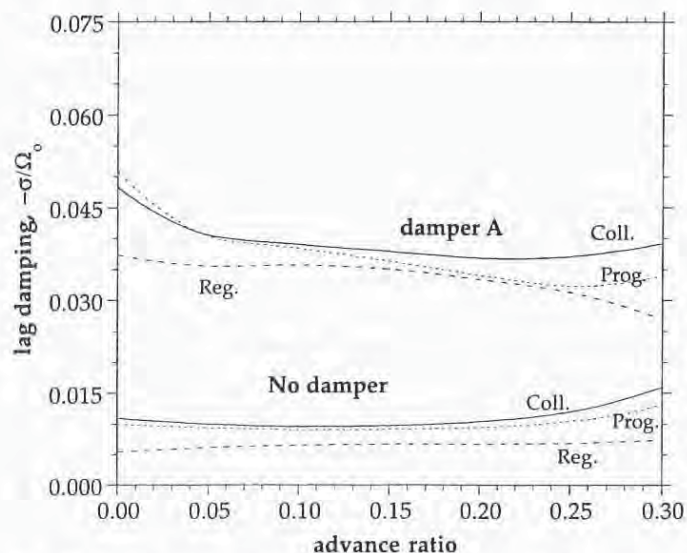


Fig. 17. Bearingless rotor shaft-free lag mode stability with inclusion of damper A.

mode coordinate, p_1 , could be larger than the second lag mode coordinate, p_2 , a comparison of Figs. 10 and 11 clearly shows that $(\phi_{fb}^{(j)} - \phi_{te}^{(j)})$ (distance from O to P or P') for the second lag mode is substantially larger (7-8 times) than the first lag mode. Thus, if the damper periodic motion is predominantly second mode, it stands to reason that decrease in damper stiffness with increasing periodic motion (Fig. 2) obtained at higher advance ratios, will also manifest itself in the second mode. Fig. 20 shows the second lag mode frequency versus advance ratio for a linear damper. Expectedly, since the nonlinear characterization is not considered, a constant increase in frequency is obtained, and no variation in frequency is observed with advance ratio.

Summary and Concluding Remarks

An elastomeric damper model comprising of a nonlinear spring and a Kelvin chain is augmented with additional nonlinear springs to represent experimentally observed degradation in G'' (damping) at very low dynamic amplitudes, and occurrence of limit cycle oscillations (jitter)

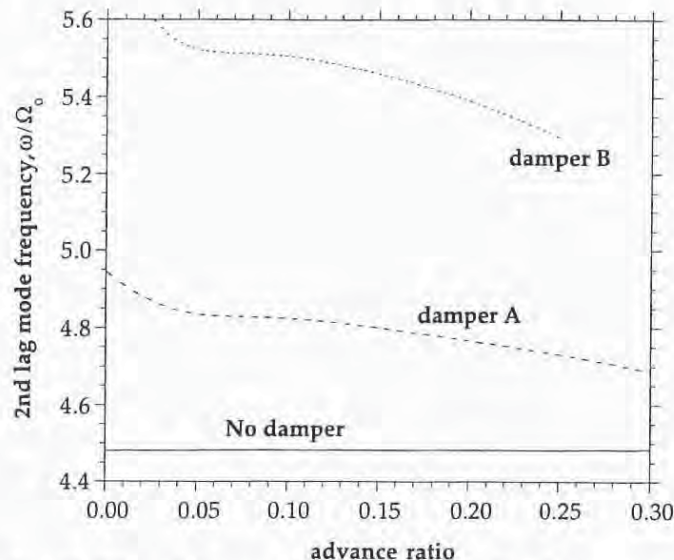


Fig. 19. Effect of elastomeric damper on second lag frequency.

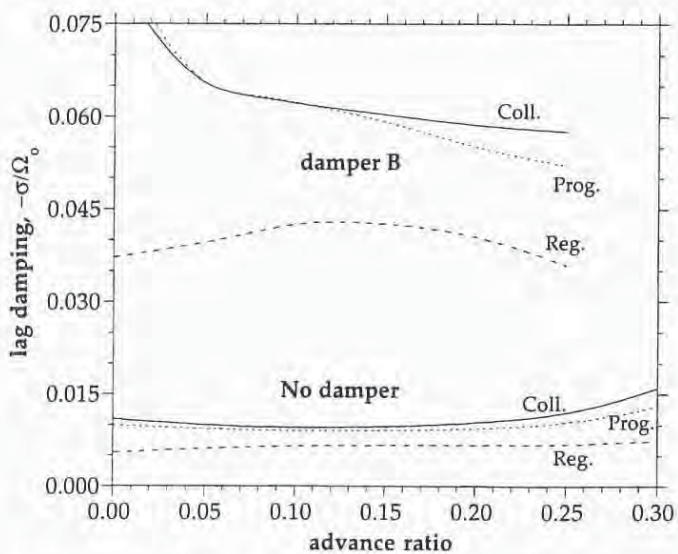


Fig. 18. Bearingless rotor shaft-free lag mode stability with inclusion of damper B.

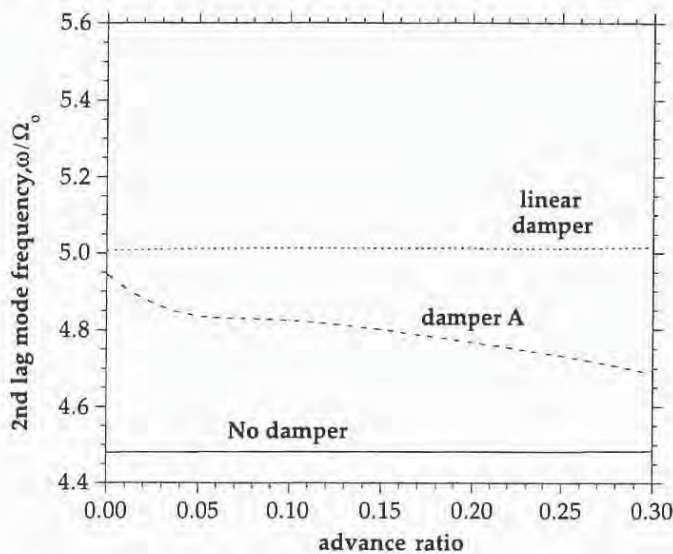


Fig. 20. Comparison of linear and nonlinear damper effects on second lag frequency.

due to applied perturbations. The hysteresis cycles calculated with the augmented model better represent the experimentally measured force/displacement behavior under cyclic loading. The damper model is described in the time domain by a nonlinear differential equation.

Integration of the damper into a bearingless rotor comprehensive analysis results in the augmentation of the rotor/fuselage state vector with additional damper states. The rotor/fuselage mass, damping and stiffness matrices, and load vector, are first evaluated without considering the damper. The damper differential equation is then introduced, resulting in augmented system matrices and vectors. This approach is easy to implement since it requires very few changes in an existing bearingless rotor comprehensive analysis.

The influence of the damper on bearingless rotor aeroelastic and aeromechanical behavior in forward flight is examined. The following observations were made:

(i) Consideration of damper stiffness between the torque tube and flexbeam in the *evaluation of modes* improves blade response convergence significantly. These modes can be used in calculation of baseline blade modal matrices and load vector, which are subsequently augmented due to inclusion of the damper nonlinear differential equation.

(ii) Since an elastomeric damper increases the fundamental lag frequency closer to the first rotor harmonic ($1/rev$), it results in an increase in amplitude of periodic lag response.

(iii) Since damper stiffness and damping capabilities are directly dependent on its periodic motion (both decreasing at higher amplitudes), its behavior varies, accordingly, with advance ratio. The lag mode damping trends with advance ratio depend on the relative contributions of the nonlinear elastomeric damper and aerodynamic effects. Additionally, influence of damper dynamics on coupled regressive lag/fuselage motion could result in a diminished damping effect, for some cases.

(iv) An estimate of modal contributions of damper motion shows that second lag mode is much more predominant than the first lag mode. Thus, the nonlinear characterization of the damper results in a variation of second lag mode frequency with increasing advance ratio (increasing periodic motion), not observed for the first lag mode frequency.

Acknowledgments

This research work is supported by the Army Research Office under the Center for Rotorcraft Education and Research, Grant No. DAAH04-93-G-0001; Technical Monitors Dr. Tom Doligalski and Dr. Robert Singleton.

References

- ¹Huber, H., "Will Rotor Hubs Lose Their Bearings? A Survey of Bearingless Main Rotor Development," Proceedings of the 18th European Rotorcraft Forum, Avignon, France, Sept 1992.
- ²Chopra, I., "Perspectives in Aeromechanical Stability of Helicopters," *Vertica*, Vol. 14, No.4, 1990, pp. 457-508.
- ³Potter, J.L., "Improving Reliability and Eliminating Maintenance with Elastomeric Dampers for Rotor Systems," Lord Library No. LL2120, 1976.
- ⁴McGuire, D.P., "The Application of Elastomeric Lead-Lag Dampers to Helicopter Rotors," Lord Library No. LL2133, 1976.
- ⁵Hodges, D.H., "A Theoretical Technique for Analyzing Aeroelastic Stability of Bearingless Rotors," *AIAA Journal*, Vol. 17, No. 4, Oct 1978, pp. 400-407.
- ⁶Hodges, D.H., "An Aeromechanical Stability Analysis for Bearingless Rotor Helicopters," *Journal of the American Helicopter Society*, Vol. 24, No. 1, Jan 1979, pp. 2-9.
- ⁷Hodges, D.H., Hopkins, A.S., Kunz, D.L., and Hinnant, H.E., "Introduction to GRASP - General Rotorcraft Aeromechanical Stability Program - A Modern Approach to Rotorcraft Modeling," Proceedings of the 42nd Annual Forum of the American Helicopter Society, Washington DC, June 1986.

⁸Sivaneri, N.T., and Chopra, I., "Finite Element Analysis for Bearingless Rotor Blade Aeroelasticity," *Journal of the American Helicopter Society*, Vol. 29, No. 2, Apr 1984, pp. 42-51.

⁹Dull, A.L., and Chopra, I., "Aeroelastic Stability of Bearingless Rotors in Forward Flight," *Journal of the American Helicopter Society*, Vol. 33, No. 4, Oct 1988, pp. 38-46.

¹⁰Jang, J., and Chopra, I., "Ground and Air Resonance of an Advanced Bearingless Rotor in Hover," *Journal of the American Helicopter Society*, Vol. 33, No. 3, July 1988, pp. 20-29.

¹¹Jang, J., and Chopra, I., "Air Resonance of an Advanced Bearingless Rotor in Forward Flight," Proceedings of the 2nd International Conference on Rotorcraft Basic Research, College Park, Maryland, Feb 1988.

¹²Hong, C.H., and Chopra, I., "Aeroelastic Stability Analysis of a Composite Bearingless Rotor Blade," *Journal of the American Helicopter Society*, Vol. 31, No. 4, Oct 1986, pp. 29-35.

¹³Tracy, A.L., and Chopra, I., "Aeroelastic Analysis of a Composite Bearingless Rotor in Forward Flight with Improved Warping Modeling," Proceedings of the American Helicopter Society Aeromechanics Specialists' Conference, San Francisco, California, Jan 1994.

¹⁴Gandhi, F., and Chopra, I., "A Refined Analysis Methodology for Bearingless main Rotor Helicopters in Forward Flight," Presented at the ASME Winter Annual Meeting (Special Symposium on Aeroelasticity and Fluid Structure Interaction), Chicago, Illinois, Nov 1994.

¹⁵Wang, J.M., Duh, J., and Fuh, J-S., "Stability of the S-76 Bearingless Main Rotor," Proceedings of the 49th Annual Forum of the American Helicopter Society, St. Louis, Missouri, May 1993.

¹⁶Hausmann, G., "Structural Analysis and Design Considerations of Elastomeric Dampers with Viscoelastic Material Behavior," Proceedings of the 12th European Rotorcraft Forum, Garmisch-Partenkirchen, Federal Republic of Germany, Sept 1986.

¹⁷Hausmann, G., and Gergley, P., "Approximate Methods for Thermoviscoelastic Characterization and Analysis of Elastomeric Lead-Lag Dampers," Proceedings of the 18th European Rotorcraft Forum, Avignon, France, Sept 1992.

¹⁸Felker, F., Lau, B., McLaughlin, S., and Johnson, W., "Nonlinear Behavior of an Elastomeric Lag Damper Undergoing Dual Frequency Motion and its Effect on Rotor Dynamics," *Journal of the American Helicopter Society*, Vol. 32, No. 4, Oct 1987, pp. 45-53.

¹⁹Gandhi, F., and Chopra, I., "Analysis of Bearingless Main Rotor Dynamics with the Inclusion of an Improved Time Domain Nonlinear Elastomeric Damper Model," Proceedings of the AHS 51st Annual Forum, Fort Worth, Texas, May 1995.

²⁰Gandhi, F., Chopra, I., and Lee, S.W., "A Nonlinear Viscoelastic Damper Model: Constitutive Equation and Solution Scheme," Proceedings of the 1994 (SPIE) North American Conference on Smart Structures and Materials, Orlando, Florida, Feb 1994.

²¹Gandhi, F., and Chopra, I., "An Analytical Model for a Nonlinear Elastomeric Lag Damper and its Effect on Aeromechanical Stability in Hover," *Journal of the American Helicopter Society*, Vol. 39, No. 4, Oct 1994, pp. 59-69.

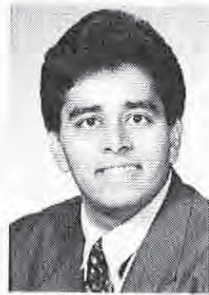
²²Gandhi, F., and Chopra, I., "Elastomeric Lag Damper Effects on Flap-Lag Stability in Forward Flight," Proceedings of the AIAA/ASME/ASCE/AHS/ACS 35th Structures, Structural Dynamics and Materials Conference, Hilton Head, South Carolina, Apr 1994.

²³Ingle, S.J., Weber, T.L., and Miller, D.G., "Concurrent Handling Qualities and Aeroservoelastic Specification Compliance for the RAH-66 Comanche," Proceedings of the American Helicopter Society Aeromechanics Specialists' Conference, San Francisco, California, Jan 1994.

²⁴Bir, G., Chopra, I., *et al*, "University of Maryland Advanced Rotor Code (UMARC) Theory Manual," UM-AERO Report 92-02, Aug 1992.

²⁵Dawson, S., "An Experimental Investigation of a Bearingless Model Rotor in Hover," *Journal of the American Helicopter Society*, Vol. 28, No. 4, Oct 1983, pp. 29-34.

An Aeroelastic Analysis Methodology for Bearingless Main Rotor Helicopters



Farhan Gandhi
Assistant Professor
Rotorcraft Center of Excellence
Department of Aerospace Engineering
The Pennsylvania State University
University Park, PA 16802



Inderjit Chopra
Minta Martin Professor and Director
Alfred Gessow Rotorcraft Center
Department of Aerospace Engineering
University of Maryland
College Park, MD 20742

A methodology for the aeroelastic analysis of bearingless main rotor helicopters in forward flight is presented. The large elastic twist experienced by the flexbeam during pitch control application can influence the nonlinear aeroelastic behavior. Including its effects by eliminating the rigid pitch control rotation, θ , and using an angle, $\hat{\phi}$, to represent the spanwise distribution of cross-sectional torsional orientation would preclude the use of normal mode equations in the evaluation of blade periodic response in forward flight. In the present analysis, the elastic deformations due to pitch control are independently evaluated as the in vacuo structural response to a prescribed swashplate motion. Modified nonlinear equations of motion that include the effect of flexbeam elastic deformations due to pitch control, are used in the aeroelastic analysis. The present analysis is robust and has good convergence behavior in the evaluation of blade periodic response. Good correlation with experimental lag damping data is obtained for two different bearingless rotor configurations. Different types of pitch-flap coupling due to leading edge or trailing edge pitch links in a snubberless configuration are seen to have a strong effect on torsional response. The forward flight shaft-fixed and shaft-free stability characteristics are examined for the two pitch link configurations.

Notation

a	Bearingless rotor pitch horn chordwise offset	w_{pl}	Pitch link elastic deformation
C_T	Rotor thrust coefficient	w_{sp}	Pitch link vertical motion due to swashplate control
e_A	Chordwise offset of tensile axis ahead of elastic axis	W	Work done
EA	Axial stiffness	x, y, z	Undeformed blade coordinate system
EB_1, EB_2	Section stiffness constants	x_o	Lag pin radial offset
EC_1	Warping rigidity	z_o	Lag pin vertical offset
EC_2	Section warping constant	δT	Variation in kinetic energy
EL_y, EL_z	Flap bending stiffness, lag bending stiffness	δU	Variation in strain energy
F^{NL}	Load vector due to structural nonlinearities	δU_b	Strain energy variation for blade
GJ	Torsional stiffness	δU_{pl}	Strain energy variation for pitch link
k_A	Radius of gyration of blade cross-section	δW	Virtual work
K^G	Global structural stiffness matrix	ϵ_{xx}	Axial strain
K_{pl}	Pitch link axial stiffness	$\epsilon_{xy}, \epsilon_{xz}$	Engineering shear strain
p	Bearingless rotor pitch horn radial offset	θ_o	Rigid pitch angle due to control
q_b	Global nodal displacement vector	λ_T	Warping function
u	Blade displacement in x direction	ξ, η, ζ	Rotating deformed blade coordinate system
u_e	Displacement in x direction due to elastic stretching (Note, $u'_e = u' + \frac{v'^2}{2} + \frac{w'^2}{2}$)	σ	Rotor solidity ratio
U	Strain Energy	σ_{xx}	Axial stress
v	Blade displacement in y direction	σ_{xy}, σ_{xz}	Shear stresses
w	Blade displacement in z direction	$\hat{\phi}$	Elastic cross-sectional torsional orientation (Note, $\phi = \hat{\phi} + \int_0^x w' v''$)
		()'	$\partial(\)/\partial x$
		()''	$\partial^2(\)/\partial x^2$
		$\delta(\)$	Variation in ()
		() _c or () _F	due to control application via swashplate
		() _{tt}	denotes inboard end of the torque tube
		() _{total}	due to control application as well as aeroelastic loads

Introduction

Over the last three decades, strong emphasis on rotor design simplicity has culminated in the development of the bearingless main rotor. In this type of rotor, the flap and lag hinges, as well as the pitch bearing, are eliminated, resulting in a substantial reduction in parts count, weight, drag, and maintenance costs. The main blade of the bearingless rotor is attached to the hub by means of a torsionally soft flexure that allows flap and lag bending as well as elastic twist. The flexbeam is generally surrounded by a torsionally stiff torque tube, which is attached to the main blade/flexbeam at the outboard end, and to a pitch link at the inboard end. Pitch control of the main blade is achieved by rotating the torque tube with the pitch link. This in turn rotates the main blade, elastically twisting the flexbeam in the process. It is this pitch control mechanism that primarily distinguishes a bearingless rotor from a hingeless rotor.

Since production bearingless rotors are designed as soft-inplane rotors, their susceptibility to aeromechanical instability is a major concern. Consequently, a large number of model as well as full scale configurations have been tested by both the major helicopter manufacturers as well as NASA/Army Labs, to examine their aeroelastic and aeromechanical stability characteristics. A very detailed and comprehensive description of the various experimental as well as design and developmental efforts is available in a recent review by Huber (Ref. 1).

Simultaneously, considerable efforts have also been directed towards the analytical modeling of bearingless main rotors. This is much more involved than the analysis of hingeless or articulated rotors due to presence of multiple load paths, complex hub kinematics, and large elastic deformations in the flexbeam during pitch control application. The major rotorcraft manufacturers have individually developed and refined their own in-house methodologies and computational codes for the prediction of bearingless rotor aeroelastic behavior. These are based on a variety of methods such as the Mykelstead method, modal method, etc. However, no detailed documentation of these analyses is available in the literature. One of the earliest analytical models for bearingless main rotors reported in the literature was the FLAIR program, developed at the Army Aeroflight-dynamics Directorate (Refs. 2,3). In this analysis, the flexbeam was modeled as a Bernoulli-Euler beam undergoing elastic bending, torsion and axial deformation, while the main blade was assumed to be rigid. While this formulation was useful in calculating the aeromechanical stability characteristics of a few bearingless rotor configurations, it could not be used for evaluating blade dynamic stresses, rotor vibratory hub loads, or even flutter type instabilities involving higher modes. Soon after, the Aeroflight-dynamics Directorate developed GRASP (Ref. 4) which considered the elastic deformations in the main blade, as well. However, both the analyses were developed only for a hover condition.

The first report in the literature on the application of the finite element method to bearingless rotor analysis was by Sivaneri and Chopra (Ref. 5). This is a very suitable approach for bearingless rotor analysis as it can accurately model the complex hub kinematics and the redundant load paths of such a rotor. Using this finite element model as the basis, researchers at the University of Maryland (Refs. 6-10) conducted analytical investigations on the aeroelastic and aeromechanical stability characteristics of various bearingless rotor configurations in hover and forward flight conditions. Dull and Chopra (Ref. 6) examined the shaft-fixed aeroelastic stability of bearingless rotors with and without torque-tube shear restraints. This was followed by a study of the shaft-free aeromechanical stability characteristics of the Boeing-ITR model bearingless rotor (with torque tube shear restraint), in hover (Ref. 7) and forward flight conditions (Ref. 8), by Jang and Chopra. The dynamics of bearingless main rotors with tailored composite flexbeams was examined by Hong and Chopra (Ref. 9), in a hover condition. Tracy and Chopra (Ref. 10) used an improved structural model, including transverse shear effects and refined

cross-section warping for composite flexbeams, and examined the aeroelastic stability in forward flight. In the above analyses, the blade periodic response in forward flight was first calculated using a temporal finite element method, after transforming the spatially discretized elastic blade equations to a few normal mode equations, to reduce computation time. Stability of the perturbation equations was then calculated using Floquet theory.

Since bearingless rotor flexbeams experience large elastic twisting during pitch control application, the use of normal modes in the evaluation of blade periodic response is fraught with difficulty. In References (Refs. 6-10), the effects of the flexbeam elastic twist due to pitch control were only approximately included in the bearingless rotor analysis. However, in order to successfully design optimized or tailored flexbeams for improved stability and performance, and reduced hub loads, it is necessary to more carefully include the flexbeam deformations due to pitch control application in the analysis, as the aeroelastic behavior could depend significantly on the initially deformed configuration. In the present paper, an aeroelastic analysis for bearingless main rotors in forward flight is developed. The analysis is carried out in two steps: (i) calculation of the elastic deformations experienced by the bearingless blade as a result of pitch control application *in the absence of aerodynamics*, and (ii) use of a *modified set of equations*, which includes the influence of the previously calculated elastic deformations due to pitch control, to evaluate the aeroelastic characteristics of the bearingless rotor. Validation of the present analysis with experimental lag damping data is presented, and a systematic study of the aeroelastic and aeromechanical stability in forward flight is undertaken for bearingless rotors with leading edge and trailing edge pitch link configurations.

Analysis

Strain Energy Associated with Elastic Deformations due to Blade Pitch Control

The rotor blades are modeled as elastic beams undergoing coupled flap bending, lag bending, elastic torsion, and axial displacements. The nonlinear equations of motion, adapted from the work of Hodges and Dowell (Ref. 11), are derived using Hamilton's principle:

$$\int_{t_1}^{t_2} (\delta U - \delta T - \delta W) dt = 0 \quad (1)$$

where δU and δT are the variations in strain energy and kinetic energy, respectively, and δW is the virtual work done by external (aerodynamic) forces. In Ref. 11, δU was formulated for bending, stretching, and elastic twisting deformations about a pitch setting, θ_0 . Since θ_0 represented a rigid rotation and not an elastic deformation, it did not directly contribute to the strain energy variation, δU . While this is an appropriate modeling assumption for articulated and hingeless rotors, it is not entirely valid for bearingless rotors. This is because in the pitch control of a bearingless rotor a rigid rotation, θ_0 , of the main blade (and torque tube) is accompanied by a corresponding elastic twisting of the flexbeam. The elastic twisting can be of significant magnitude and its spanwise distribution for a nonuniform flexbeam can be quite complex. For the analysis of bearingless main rotors, it is necessary to take into consideration the elastic twist deformations in the flexbeam due to pitch control, as the aeroelastic behavior of the rotor can be affected by its initially deformed configuration.

Before elaborating on methods for including the effects of the elastic twisting of the bearingless rotor flexbeam during pitch control application, it is useful to briefly discuss the kinematics of deformation of the elastic rotor blade. The rotor blade is assumed to undergo elastic bending deformations, w and v , elastic stretching, u_c , and twisting. When moderate deflections are assumed, the final orientation angle of any cross-section is de-

noted as $\hat{\phi}$ (with respect to a pitch setting). The elastic twist rate required in the computations of the strain energy can then be expressed as

$$\phi' = \hat{\phi}' + w'v'' \quad (2)$$

In the present analysis $\hat{\phi}$ is used as the fundamental torsional variable due to convenience in calculation of aerodynamic loads.

To include the effect of flexbeam elastic twist due to pitch control, one possible method would be through the elimination of the rigid pitch rotation, θ_0 , and the use of a distributed cross-sectional orientation angle, $\hat{\phi}_{\text{total}}$, to include both pitch control effects as well as the subsequent aeroelastic deformations. Pitch control application would, of course, result in a zero twist rate over the blade and torque tube, so that the only contributions to the strain energy would come from the flexbeam. In this case, the strain-displacement relations are, in general,

$$\epsilon_{xx} = u'_e - \lambda_T \phi''_{\text{total}} + (\eta^2 + \zeta^2) \left\{ \frac{\phi'^2_{\text{total}}}{2} \right\} - v'' \{ \eta \cos(\hat{\phi}_{\text{total}}) - \zeta \sin(\hat{\phi}_{\text{total}}) \} - w'' \{ \eta \sin(\hat{\phi}_{\text{total}}) + \zeta \cos(\hat{\phi}_{\text{total}}) \} \quad (3a)$$

$$\epsilon_{x\eta} = -\zeta \phi'_{\text{total}} = -\zeta (\hat{\phi}'_{\text{total}} + w'v'') \quad (3b)$$

$$\epsilon_{x\zeta} = \eta \phi'_{\text{total}} = \eta (\hat{\phi}'_{\text{total}} + w'v'') \quad (3c)$$

The main drawback of such an approach is that the small angle assumption cannot be made on $\hat{\phi}_{\text{total}}$ since it inherently contains the pitch control angle which can assume values in excess of 20° in high speed forward flight or maneuvering flight. This would preclude the use of normal mode approximations of the blade equations of motion. The inability to transform spatially discretized blade finite element equations to a few normal mode equations would result in a significant increase in computation time for the evaluation of the blade periodic response in forward flight.

The approach taken in the present paper is to consider $\hat{\phi}_{\text{total}}$ (or ϕ_{total}) to be composed of two distinct components

$$\phi_{\text{total}} = \phi_c + \phi \quad (4)$$

(i) ϕ_c — the elastic deformations of the bearingless blade due to the application of pitch control, calculated in the rotating condition. Unlike the rigid pitch rotation, θ_0 , in Ref. 11, ϕ_c directly contributes to the elastic strain energy of the bearingless rotor flexbeam. The term ϕ_c , evaluated as the deformation field to a given swashplate displacement, would take on a constant value over the main blade and torque tube ($\phi'_c = 0$, implying that they undergo rigid rotations), while varying over the flexbeam length ($\phi'_c \neq 0$, implying that elastic twisting occurs).

(ii) ϕ — due to aeroelastic loads (as in Ref. 11) superposed over the known twist distribution, $\hat{\phi}_c$. Since large control rotations due to swashplate input are not present in ϕ , small angle approximations are made, and trigonometric expansions $\sin(\hat{\phi}_{\text{total}}) = \sin \hat{\phi}_c + \hat{\phi} \cos \hat{\phi}_c$ and $\cos(\hat{\phi}_{\text{total}}) = \cos \hat{\phi}_c - \hat{\phi} \sin \hat{\phi}_c$ are carried out (in Eq. 3a) to obtain algebraic expressions for $\hat{\phi}$. The spatially discretized blade equations of motion are transformed to the normal mode domain for the evaluation of periodic response in forward flight. The normal modes used for this purpose are the structural normal modes calculated in the rotating condition in the absence of aerodynamic loads, i.e., about the undeformed configuration.

Some bearingless configurations, such as a snubberless single pitch link configuration, or a configuration with a torque-tube shear restraint, result in kinematic pitch-flap or pitch-lag couplings. For such configurations, a swashplate control motion can produce flapwise or lagwise bending in addition to the elastic twisting of the flexbeam. Thus, it is assumed in general that the swashplate control motion results in an elastic twist as well as elastic flap bending, w_c , lag bending, v_c , and axial deformation,

u_{e_c} , all calculated in the rotating condition. The total deformation field is represented by Eq. 4 and

$$\begin{aligned} w_{\text{total}} &= w_c + w \\ v_{\text{total}} &= v_c + v \\ u_{e_{\text{total}}} &= u_{e_c} + u_e \end{aligned} \quad (5)$$

Figure 1 shows the undeformed cross-section, as well as the configuration achieved after undergoing the total deformation due to swashplate control [ϕ_c , w_c , v_c , u_{e_c}] and aeroelastic influences [ϕ , w , v , u_e]. Strain-displacement relations based on the total deformation field [ϕ_{total} , w_{total} , v_{total} , $u_{e_{\text{total}}}$], are used to obtain the strain energy variation δU , which is introduced into Hamilton's principle (Eq. 1). The strain-displacement relations are written as

$$\begin{aligned} \epsilon_{xx} &= u'_e + u'_{e_c} - \lambda_T (\phi'_c + \phi'') + (\eta^2 + \zeta^2) \frac{(\phi'_c + \phi')^2}{2} \\ &\quad - (v'' + v''_c) \{ \eta \cos(\phi_c + \hat{\phi}) - \zeta \sin(\phi_c + \hat{\phi}) \} \\ &\quad - (w'' + w''_c) \{ \eta \sin(\phi_c + \hat{\phi}) + \zeta \cos(\phi_c + \hat{\phi}) \} \end{aligned} \quad (6a)$$

$$\epsilon_{x\eta} = -\zeta (\phi'_c + \phi') = -\zeta \{ \hat{\phi}'_c + \hat{\phi}' + (w' + w'_c)(v'' + v''_c) \} \quad (6b)$$

$$\epsilon_{x\zeta} = \eta (\phi'_c + \phi') = \eta \{ \hat{\phi}'_c + \hat{\phi}' + (w' + w'_c)(v'' + v''_c) \} \quad (6c)$$

The strain energy variation is

$$\delta U = \int_0^R \int_A (E \epsilon_{xx} \delta \epsilon_{xx} + G \epsilon_{x\eta} \delta \epsilon_{x\eta} + G \epsilon_{x\zeta} \delta \epsilon_{x\zeta}) d\eta d\zeta dx \quad (7)$$

On evaluating the integrals over the cross section, δU can be written in the following form

$$\begin{aligned} \delta U &= \int_0^R (U_{u_e} \delta u'_e + U_{v_c} \delta v'' + U_w \delta w' + U_w \delta w'' \\ &\quad + U_{\hat{\phi}} \delta \hat{\phi} + U_{\hat{\phi}} \delta \hat{\phi}' + U_{\hat{\phi}} \delta \hat{\phi}'') dx \end{aligned} \quad (8)$$

Baseline expressions $U_{u_e}^0$, $U_{v_c}^0$, U_w^0 , U_w^0 , $U_{\hat{\phi}}^0$, $U_{\hat{\phi}}^0$, and $U_{\hat{\phi}}^0$ (based on strain-displacement relations in Ref. 11) are available in Ref. 12. The augmented expressions due to the use of strain-displacement relations (Eqs. 6) are given below:

$$\begin{aligned} U_{u_e} &= U_{u_e}^0 + E A k_A^2 \frac{\phi_c'^2}{2} + E A k_A^2 \phi_c' w_c' v'' + E A k_A^2 \phi_c' w' v'' \\ &\quad + E A k_A^2 \phi_c' w_c' v_c'' - E A e_A w_c'' \sin \phi_c - E A e_A w_c'' \hat{\phi} \cos \phi_c \\ &\quad - E A e_A v_c'' \cos \phi_c + E A e_A v_c'' \hat{\phi} \sin \phi_c + E A u_{e_c} \\ U_{v_c} &= U_{v_c}^0 - E C_2 \phi_c'' \sin \phi_c - E C_2 \phi_c'' \hat{\phi} \cos \phi_c - E B_2 \frac{\phi_c'^2}{2} \cos \phi_c + E B_2 \frac{\phi_c'^2}{2} \hat{\phi} \sin \phi_c \\ &\quad + E B_1 w_c' \frac{\phi_c'^3}{2} + E B_1 w_c' \frac{\phi_c'^2}{2} \hat{\phi}' + w_c'' (E I_z - E I_y) \cos \phi_c \sin \phi_c \\ &\quad + w_c'' (E I_z - E I_y) \hat{\phi} \cos 2\phi_c + E A k_A^2 \phi_c' u_e' w_c' + E B_1 \phi_c'^2 w_c' \hat{\phi}' \\ &\quad + E B_1 w_c' \frac{\phi_c'^3}{2} + E B_1 w_c' \frac{\phi_c'^2}{2} \hat{\phi}' + v_c'' (E I_z \cos 2\phi_c + E I_y \sin^2 \phi_c) \\ &\quad - \hat{\phi} v_c'' (E I_z - E I_y) \sin 2\phi_c - E A e_A u_{e_c}'' \cos \phi_c + E A e_A u_{e_c}'' \hat{\phi} \sin \phi_c \\ &\quad + E A k_A^2 \phi_c' u_{e_c}' w_c' + E A k_A^2 \phi_c' u_{e_c}' w' + G J w_c' \phi_c' + G J w' \phi_c' + G J w_c' \hat{\phi}' \\ U_w &= U_w^0 + E B_1 v'' \frac{\phi_c'^3}{2} + E B_1 v'' \frac{\phi_c'^2}{2} \hat{\phi}' + E B_1 v_c'' \frac{\phi_c'^3}{2} + E B_1 v_c'' \frac{\phi_c'^2}{2} \hat{\phi}' \\ &\quad + E B_1 v_c'' \phi_c'^2 \hat{\phi}' + E A k_A^2 \phi_c' v_c' u_{e_c}' + E A k_A^2 \phi_c' v_c' u_e' + E A k_A^2 \phi_c' v'' u_{e_c}' \\ &\quad + G J v_c'' \phi_c' + G J v'' \phi_c' + G J v_c'' \hat{\phi}' \end{aligned}$$

$$\begin{aligned}
 U_w'' &= U_w^0'' + \underline{EC_2\phi_c''\cos\phi_c} - \underline{EC_2\phi_c''\hat{\phi}\sin\phi_c} - \underline{EB_2\frac{\phi_c'^2}{2}\sin\phi_c} \\
 &\quad - \underline{EB_2\frac{\phi_c'^2}{2}\hat{\phi}\cos\phi_c} + \underline{w_c''EI_z\sin^2\phi_c} + \underline{w_c''EI_y\cos^2\phi_c} \\
 &\quad + \underline{w_c''(EI_z - EI_y)\hat{\phi}\sin 2\phi_c} + \underline{v_c''(EI_z - EI_y)\cos\phi_c\sin\phi_c} \\
 &\quad + \underline{v_c''(EI_z - EI_y)\hat{\phi}\cos 2\phi_c} - \underline{EAe_Au_{ec}'\sin\phi_c} - \underline{EAe_Au_{ec}'\hat{\phi}\cos\phi_c} \\
 U_{\hat{\phi}} &= U_{\hat{\phi}}^0 - \underline{EC_2w''\phi_c''\sin\phi_c} - \underline{EC_2v''\phi_c''\cos\phi_c} - \underline{EB_2w''\frac{\phi_c'^2}{2}\cos\phi_c} \\
 &\quad + \underline{EB_2v''\frac{\phi_c'^2}{2}\sin\phi_c} + \underline{w_c''^2(EI_z - EI_y)\cos\phi_c\sin\phi_c} - \underline{EC_2w_c''\phi_c'^2\sin\phi_c} \\
 &\quad - \underline{EB_2v_c''\phi_c'^2\cos\phi_c} + \underline{2w_c''w''(EI_z - EI_y)\cos\phi_c\sin\phi_c} \\
 &\quad + \underline{v_c''w_c''(EI_z - EI_y)\cos 2\phi_c} - \underline{v_c''^2(EI_z - EI_y)\cos\phi_c\sin\phi_c} \\
 &\quad + \underline{v_c''w_c''(EI_z - EI_y)\cos 2\phi_c} - \underline{EC_2v_c''\phi_c''\cos\phi_c} + \underline{EB_2v_c''\frac{\phi_c'^2}{2}\sin\phi_c} \\
 &\quad - \underline{2v_c''v''(EI_z - EI_y)\cos\phi_c\sin\phi_c} + \underline{v_c''w''(EI_z - EI_y)\cos 2\phi_c} \\
 U_{\phi_c'} &= U_{\phi_c'}^0 + \underline{EB_1\frac{\phi_c'^3}{2}} + \underline{EB_1\frac{\phi_c'^2}{2}\hat{\phi}'} - \underline{EB_2\phi_c'\phi_c''\sin\phi_c} - \underline{EB_2\phi_c'\phi_c''\cos\phi_c} \\
 &\quad + \underline{EAk_A^2\phi_c'u_{ec}'} + \underline{EAk_A^2\hat{\phi}'u_{ec}'} + \underline{GJ\phi_c'} + \underline{GJw_c'v_c''} + \underline{GJw_c'v_c''} + \underline{GJw_c'v_c''} \\
 U_{\hat{\phi}''} &= U_{\hat{\phi}''}^0 + \underline{EC_1\phi_c''} + \underline{EC_2w_c''\cos\phi_c} - \underline{EC_2v_c''\cos\phi_c} \tag{9}
 \end{aligned}$$

In Eqs. 9, two distinct types of terms are present:

- (i) Underlined terms: These depend only on the elastic deformation field as a result of pitch control application (ϕ_c , w_c , v_c and u_{ec}). They represent the strain energy stored in the system (primarily in the flexbeam) due to the work done in pitching the blade.
- (ii) Non-underlined terms: These depend on both the known elastic deformation field due to pitch control application, and the elastic deformations (ϕ , w , v , and u_e) due to aeroelastic forces. These terms represent the change in aeroelastic behavior of the blade due to its initial elastic deformation during pitch control application.

It should be noted that inclusion of the work done during pitch control application in δW would result in the cancellation of the underlined terms. Thus, the underlined terms, as well as the work done in pitching the blade, can both be dispensed with in the analysis. The non-underlined terms, however, need to be retained.

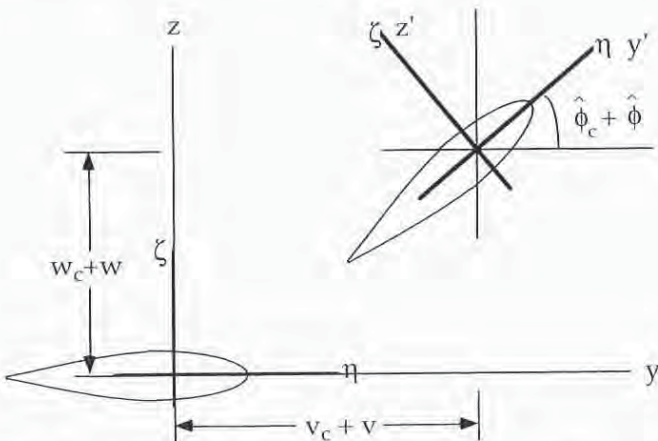


Fig. 1. Deformed configuration due to swashplate control and aerodynamic forces.

Finite Element Discretization of the Bearingless Blade

Expressions for the strain energy variation, δU , with the inclusion of elastic deformations effects due to pitch control, are used in Hamilton's principle, Eq. 1, to obtain a modified set of nonlinear equations for the bearingless rotor blade. The finite element method used to spatially discretize these equations, is well suited for application to bearingless rotor blades as it enables the accurate modeling of the redundant load paths and complex hub kinematics. The main blade, torque tube, and flexbeam are each discretized into a number of elements, with each element having two end nodes, three internal nodes, and a total of fifteen degrees of freedom (Ref. 5). Individual elements are assembled to enforce continuity of flap and lag bending displacements and slopes (w , v , w' , v'), axial displacement (u_e), and torsional orientation angle ($\hat{\phi}$), between elements. Special attention is required to enforce (i) kinematic constraints at the inboard end of the torque tube, and (ii) compatibility between the main blade inboard element and torque tube and flexbeam outboard elements, at their interface.

Kinematics at the Inboard End of the Torque Tube, and Evaluation of Deformations due to Pitch Control Application

Elastic Pitch Link

Figure 2 shows the kinematics of deformation at the inboard end of the torque tube of a bearingless blade with a vertical elastic pitch link. When the swashplate is moved, the pitch link is assumed to move vertically. In practice it may deviate slightly from the vertical position but this inclination is not included in the analysis. From the figure it can then be seen that

$$w_{sp} + w_{pl} - w_{tt} = a \sin\theta_{tt} \tag{10}$$

where w_{sp} is the applied swashplate displacement, w_{pl} is the elastic deformation in the pitch link, w_{tt} and θ_{tt} denote torque tube flapwise displacement and pitch, respectively, and a is the pitch horn chordwise offset. The torque tube and pitch link deformations include contributions due to both swashplate motion and aerodynamic loads. Thus Eq. 10 can be written as

$$w_{sp} + (w_{pl}^c + w_{pl}^{aero}) - w_{tt}^c - w_{tt}^{aero} = a \sin\phi_{tt}^c + a \cos\phi_{tt}^c \phi_{tt}^{aero} \tag{11}$$

The quantities with the superscript 'c' are the contributions due to swashplate control motion, and the quantities with the superscript 'aero' are due to aeroelastic loads. For swashplate control motion, alone,

$$w_{pl}^c = w_{tt}^c + a \sin\phi_{tt}^c - w_{sp} \tag{12}$$

If the pitch link stiffness is k_{pl} , its elastic strain energy due to swashplate motion is

$$U_{pl} = \frac{1}{2} K_{pl} w_{pl}^c{}^2 \tag{13}$$

From Eqs. (12) and (13) we can obtain

$$\delta U_{pl} = (\delta w_{tt} \delta\phi_{tt}) \left(K_{pl} \left\{ w_{tt} + a \sin\phi_{tt} \right\} - K_{pl} w_{sp} \left\{ a \cos\phi_{tt} \right\} \right) \tag{14}$$

δU_{pl} adds to the strain energy variation, δU_b , of the blade, so that the total strain energy variation of the bearingless blade is

$$\delta U_{total} = \delta U_b + \delta U_{pl} \tag{15}$$

δU_b can be expressed as

$$\delta U_b = \delta q_b^T K_b^G + \delta q_b^T F^{NL} \quad (16)$$

where K_b^G is the global structural stiffness matrix of the bearingless blade, q_b is the global nodal displacement vector, and the vector, F^{NL} , contains the nonlinear structural terms. After introducing Eqs. (14) and (16) into (15), a solution for the deformation field, q_b , of the bearingless blade can be obtained for a given swashplate control displacement, w_{sp} , in the absence of aerodynamic forces. In forward flight, w_{sp} varies along the azimuth, and q_b would have to be evaluated at several different azimuthal locations, ψ , as solutions to the input $w_{sp}(\psi)$.

However, if F^{NL} is neglected in the expression for δU_b (Eq. 16), and a small angle assumption is made on ϕ_{tt}^c in the expression for δU_{pl} so that Eq. 14 reduces to

$$\delta U_{pl} = (\delta w_{tt}^c \quad \delta \phi_{tt}^c) \left(K_{pt} \begin{bmatrix} 1 & a \\ a & a^2 \end{bmatrix} \begin{Bmatrix} w_{tt}^c \\ \phi_{tt}^c \end{Bmatrix} - K_{pl} w_{sp} \begin{Bmatrix} 1 \\ a \end{Bmatrix} \right) \quad (17)$$

only a single evaluation of the deformation field (\bar{q}_b) is required, for a unit displacement, $\bar{w}_{sp} = 1$. The deformation field at any azimuthal location could then be obtained as

$$q_b(\psi) = \bar{q}_b w_{sp}(\psi) \quad (18a)$$

or

$$q_b(\psi) = \bar{q}_b \frac{(\theta_o + \theta_{1c} \cos \psi + \theta_{1s} \sin \psi)}{\phi_{tt}^c} \quad (18b)$$

where θ_o is the collective pitch, θ_{1c} and θ_{1s} are cyclic pitch control components, and $\bar{\phi}_{tt}^c$ is the torque tube pitch due to $\bar{w}_{sp} = 1$. Although such an approach gives only an approximate elastic deformation field due to pitch control application, it results in considerable simplification of the solution process. The control deformations, q_b (consisting of ϕ_c , w_c , v_c , and u_c), thus obtained, are used in the modification of the bearingless blade strain energy expressions (non-underlined terms in Eq. 9).

For the evaluation of the blade steady response under aeroelastic force, Eq. 11 gives

$$w_{pl}^{aero} = w_{tt}^{aero} + a \cos \phi_{tt}^c \phi_{tt}^{aero} \quad (19)$$

Eq. 19 can be used to obtain

$$\delta U_{pl} = (\delta w_{tt} \quad \delta \phi_{tt}) K_{pt} \begin{bmatrix} 1 & a \cos \phi_{tt}^c \\ a \cos \phi_{tt}^c & a^2 \cos^2 \phi_{tt}^c \end{bmatrix} \begin{Bmatrix} w_{tt} \\ \phi_{tt} \end{Bmatrix} \quad (20)$$

Introducing Eq. 20 into Eq. 15 results in the augmentation of the bearingless blade global stiffness matrix due to the effects of pitch link stiffness.

If the pitch horn has a non-zero radial offset, p , Eq. 10 becomes

$$w_{sp} + w_{pl} - w_{tt} + p w'_{tt} = a \sin \theta_{tt} \quad (21)$$

where w'_{tt} is the flap bending slope at the inboard end of the torque tube. Again, augmentation of the bearingless blade global stiffness, and the evaluation of the deformation field due to w_{sp} , is carried out by adding the pitch link strain energy variation to δU_b .

Rigid Pitch Link

If the axial stiffness of the pitch link is very high, as is very often the case, the analyst may choose to model the pitch link as a 'rigid' member, in which case w_{pl} in Eqs. 10 and 21 is zero, yielding the kinematic constraint

$$\phi_{tt} = -\frac{1}{a} w_{tt} + \frac{p}{a} w'_{tt} + \frac{1}{a} w_{sp} \quad (22)$$

Introducing this constraint into Hamilton's principle (Eq. 1) results in the reduction in size of the inboard torque tube element matrices and vectors from 15 to 14, due to the elimination of the torsional degree of freedom.

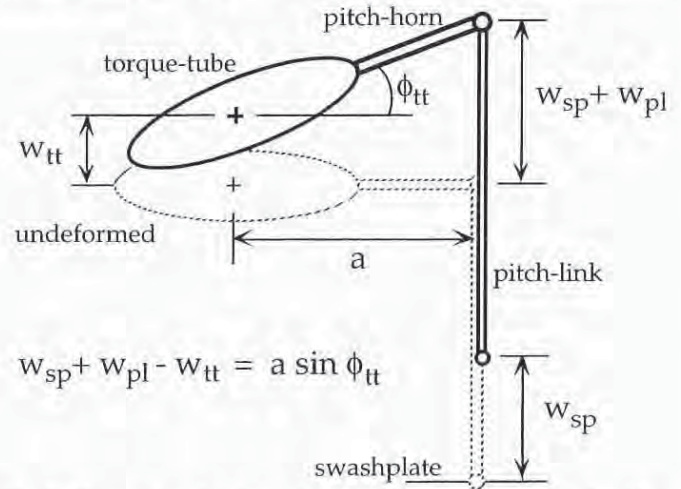


Fig. 2. Kinematics of deformation of a bearingless rotor blade with single vertical pitch link at the leading edge.

Torque tube or Lag shear restraint

Figure 3 shows a bearingless rotor blade with torque tube or lag shear restraint. The presence of a lag shear restraint imposes additional constraints at the inboard end of the torque tube. In addition to the pitch link kinematics, its presence imposes the following kinematic constraint relations.

$$-z_o \phi_{tt} + v_{tt} = v'_{tt} x_o \quad (23a)$$

$$w_{tt} = w'_{tt} x_o \quad (23b)$$

In Eqs. 23, z_o and x_o are the vertical and radial offsets of the lag pin, and v_{tt} and v'_{tt} are the torque tube lagwise bending displacement and slope. If the pitch link is rigid, the three kinematic constraints are used to eliminate three degrees of freedom, ϕ_{tt} , w_{tt} and v_{tt} , resulting in a reduction in size of the inboard torque tube element matrices and vectors from 15 to 12. Once again, the deformation field due to swashplate control motion, w_{sp} , is used to modify the blade strain energy expressions (Eq. 9).

Although the lag shear restraint concept described above was studied and tested during the bearingless rotor development phases, an elastomeric snubber is most commonly used in modern bearingless rotors to keep the flexbeam centered with respect to the torque tube. The snubber additionally provides lead-lag damping to alleviate aeromechanical instabilities. For a configuration with an elastomeric snubber damper, none of the degrees of freedom at the inboard end of the torque tube are eliminated, but the relative motions between the torque tube and the flexbeam are constrained due to the presence of the snubber.

Compatibility Conditions at the Clevis

The main blade inboard end and the flexbeam and torque tube outboard ends connect at the clevis, as shown in Fig. 3. The axial displacement, u_c , flap-bending displacement, w , and slope, w' , lag-bending displacement, v , and slope, v' , of the main blade, flexbeam and torque tube are identical at the clevis. The elastic twist at the clevis end of the flexbeam is equal to the main blade and torque tube elastic twist at the clevis ($\hat{\phi}$, due to aeroelastic loads) plus the elastic twist due to pitch control. However, by having sep-

arately accounted for the effects of elastic twist due to pitch control, only the elastic twist in the flexbeam due to aerodynamic loads ($\hat{\phi}$) needs to be considered. $\hat{\phi}$ for the flexbeam, torque tube and main blade are identical at the clevis, enabling assembly of the spatial finite elements.

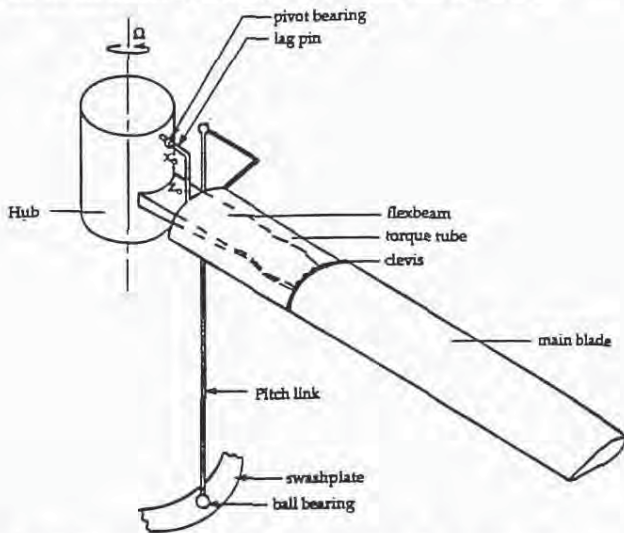


Fig. 3. Bearingless rotor hub with torque shear restraint.

Aeroelastic Analysis

The aeroelastic analysis involves the calculation of the vehicle trim, steady blade response and stability of the rotor-body perturbation motion. The steady periodic blade response is calculated using a temporal finite element method after the nonlinear equations in space are transformed into normal mode equations. In the temporal finite element method, the azimuth is discretized into a number of time elements, with a polynomial distribution for response being assumed within each element. Periodicity of response is imposed by connecting the first and last elements in one rotor revolution, during assembly of time element matrices. The nonlinear vehicle trim and blade response equations are solved iteratively as a coupled solution. The blade response in each iteration is used to calculate the hub loads, which influence the vehicle orientation and control settings. The new pitch control settings are used to calculate the blade response in the following iteration, and the procedure continues until specified convergence criteria are met. It should be noted that at this stage only the deformations due to aeroelastic forces ($\hat{\phi}$, w , v , u_c) are being evaluated. Since the largest part of the deformations, due to pitch control application, had already been evaluated and removed from the total deformations, the normal mode method could be applied, resulting in a substantial decrease in problem size. The influence of the deformations due to pitch control are accounted for in Eq. 9. For the stability analysis, the linearized normal mode perturbation equations are obtained about the steady state condition. Here, the structural normal modes used are obtained about the deformed condition, resulting from collective pitch only. The equations have periodic coefficients in forward flight and are solved using Floquet transition matrix theory. Additional details on the aeroelastic analysis procedure are available in Ref. 12.

Results and Discussion

Validation with Experiment

Two different test cases for which experimental data were available, were analyzed to validate the aeroelastic stability results pre-

dicted by the present bearingless rotor analysis. The 3-bladed model bearingless rotor consisted of a flexbeam with wrap-around torque tube, attached rigidly to the main blade at the clevis. The inboard end of the torque tube was connected to a pitch link but did not have any connection to the flexbeam whatsoever (floating cuff). This rotor was tested in hover and results of this test are available in Ref. 13. The rotor structural properties for the two cases were identical, with the only difference being the pitch link location. The pitch link was attached to the leading edge for case 1 and to the trailing edge for case 2. Case 1 was tested at 1100 RPM, while case 2 was tested at 900 RPM as it experienced flutter instability at 1100 RPM. The bearingless blade was modeled with eight elements, three elements each for the main blade and the flexbeam, and two elements for the torque tube. The nondimensionalized stiffness and inertial properties and geometric dimensions for the different elements are presented in Table 1. Note that the value of rotational speed used in nondimensionalizing the stiffness and inertial properties is $\Omega = 1100$ RPM.

Figures 4a and 4b show the variation of lag damping with collective pitch in hover, for the two cases. For the leading edge pitch link (case 1) Fig. 4a shows good correlation with experiment and generally predicts the trend with collective pitch. For the trailing edge pitch link (case 2) Fig. 4b shows even better correlation over the range of collective pitch, with the analysis accurately capturing the much gentler variation of lag damping with collective pitch.

The difference in lag damping at higher collectives between the two cases can be related to the kinematic pitch-flap couplings, which result in substantially different thrust conditions for the same collective pitch setting. For a leading edge pitch link configuration (Fig. 5a) the lift generated on the main blade due to a given collective pitch setting (position A), results in the main blade coning upward and the torque tube inboard end moving downward (to position B). Since this results in an increase in the effective blade pitch the thrust level and aerodynamic damping, increase as well. For the trailing edge pitch link configuration (Fig. 5b), the downward motion of the torque tube inboard end due to lift on the main blade results in a nose down rotation that decreases the effective angle of attack of the blade. The thrust of the blade and the aerodynamic damping, decrease accordingly. For both pitch-link configurations, the solution for the pitch orientation angles, $\hat{\phi}$, contain moderate kinematic rotations, in addition to elastic twisting. It should be noted that a bearingless rotor configuration with a shear restraint would significantly limit the kinematic pitch-flap couplings.

Blade Response, Aeroelastic and Aeromechanical Stability, in Forward Flight

The shaft-fixed aeroelastic stability characteristics and the shaft-free aeromechanical stability characteristics for the leading edge and trailing edge pitch link configurations (cases 1 and 2, respectively) are examined in forward flight. Perturbation stability was evaluated about a propulsive trim condition in cruise, at a thrust coefficient $C_T/\sigma = 0.07$.

Table 1. Bearingless rotor blade properties

Element	$\frac{l_i}{R}$	$\frac{m_i}{m_o}$	$\frac{EI_y}{m_o \Omega^2 R^4}$	$\frac{EI_x}{m_o \Omega^2 R^4}$	$\frac{GJ}{m_o \Omega^2 R^4}$	$\frac{EA}{m_o \Omega^2 R^4}$	
1	0.5	0.702	0.0055	0.1488	0.0029	113.5	main blade
2	0.234	0.702	0.0055	0.1488	0.0029	113.5	main blade
3	0.0684	26.29	0.2621	0.4321	0.2904	184.5	main blade
4	0.1018	0.979	0.00157	0.00616	0.000205	365.3	flexbeam
5	0.1018	0.979	0.00157	0.00616	0.000205	365.3	flexbeam
6	0.0454	75.42	8.064	4.910	16.61	275.1	flexbeam
7	0.0509	11.25	4.473	4.495	1.664	304.7	torque tube
8	0.0509	11.25	4.473	4.495	1.664	350.0	torque tube

radius, $R = 3'$, $m_o = 3.074 \times 10^{-3}$ slug/ft, $\Omega = 1100$ rpm

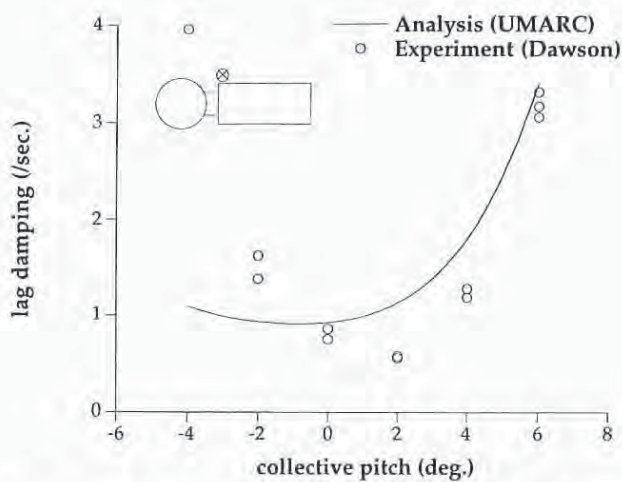


Fig. 4a. Hover shaft-fixed stability for BMR with leading edge pitch link (Case 1).

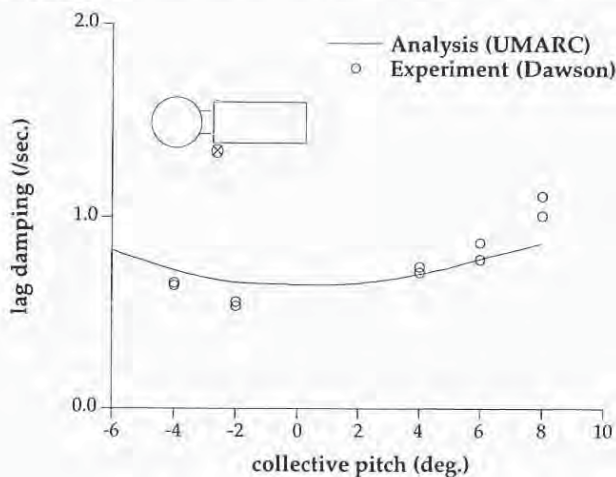


Fig. 4b. Hover shaft-fixed stability for BMR with trailing edge pitch link (Case 2).

Shaft-fixed aeroelastic stability

Figures 6a and 6b show the variation of the regressing lag mode damping with advance ratio for cases 1 and 2, respectively. Note that the stability results for both cases are calculated at 1100 RPM. For both cases, it can be seen that the lag damping increases at high advance ratios. It is assumed that this increase is associated with the higher aerodynamic damping due to large cyclic flap. Results obtained using both 'flexible' and 'rigid' pitch link analyses revealed that a 'flexible' pitch link with a nondimensional stiffness $K_{pl}/m_o\Omega^2R = 291$, behaves much like a rigid pitch link. Reduction in pitch link stiffness was generally found to have a small effect on the lag damping. This differs from the case of a bearingless rotor with torque tube shear restraint, (Ref. 6), where the influence of pitch link stiffness on lag damping was much more significant. Softening the pitch link had virtually no influence on the aeroelastic stability of the trailing edge pitch link configuration (Fig. 6b) while the leading edge configuration (Fig. 6a) showed a slight decrease in stability. A pitch mode flutter instability was observed for the trailing edge pitch link configuration (Fig. 7). From the figure the flutter instability is seen to grow weaker with increasing advance ratio, and finally the pitch mode becomes stable at advance ratios greater than $\mu = 0.3$. It should be noted that a flutter instability for this configuration was also observed experimentally by Dawson (Ref. 13) in hover condition.

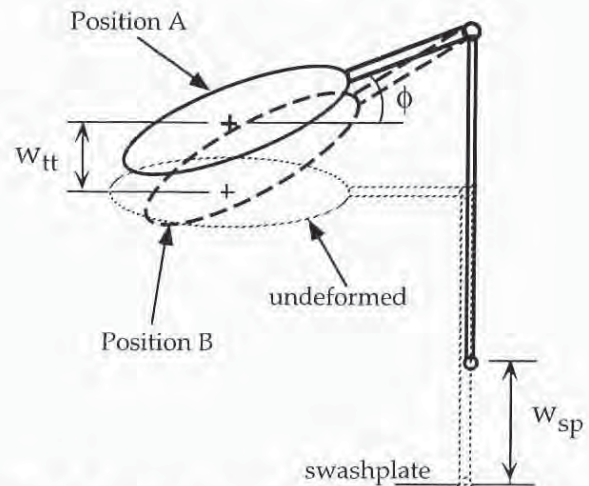


Fig. 5a. Flap up-pitch up kinematic coupling of the leading edge pitch link configuration.

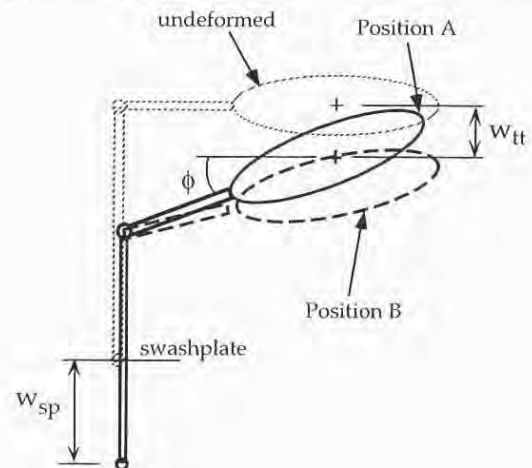


Fig. 5b. Flap up-pitch down kinematic coupling of the trailing edge pitch link configuration.

It is interesting to note that the pitch control settings required to trim the two configurations to the same thrust condition, vary significantly. For example, in hover, the pitch control angle, θ , required to trim to a thrust coefficient $C_T/\sigma = 0.07$, is 3.146° for case 1, and 8.986° for case 2. The corresponding tip torsional orientations, $\hat{\phi}$, are 2.302° and -3.583° , respectively. It can be easily seen that the effective aerodynamic angle of attack, $\theta + \hat{\phi}$, is virtually the same for the both cases (about 5.4°). Consequently, the blade tip flap displacement values were also identical ($w_{tip}/R = 0.0641$, for both cases). In Ref. 13, a third configuration with dual pitch links (at both the leading as well as trailing edge) was also examined. For this configuration, when the leading edge pitch link was moved upward, the trailing edge pitch link was moved downward by the same amount, so that the torque tube did not experience any vertical motion during pitch control application. This eliminated the pitch flap coupling. For such a configuration, it is found that a collective pitch setting of 5.748° was required to trim to a C_T/σ of 0.07, and the tip torsional deflection, $\hat{\phi}$, took on a much smaller value, -0.283° . The effective angle of attack, $\theta + \hat{\phi}$, was once again very nearly equal to 5.4° , and w_{tip}/R took a value of 0.0621. The wide variation in cross-sectional orientations, $\hat{\phi}$, between the configurations can be attributed to a nose-up rigid rotation component in case 1, a nose-down rigid rotation component in case 2, and virtually no kinematic rotations in the case of the dual pitch link configuration.

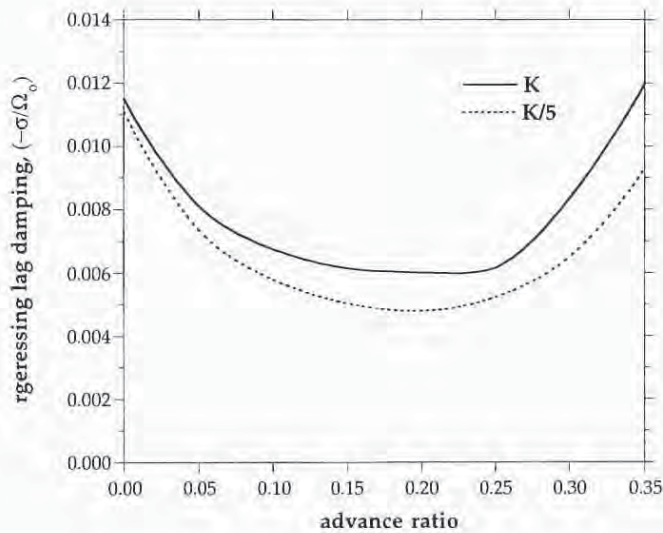


Fig. 6a. Shaft-fixed stability in forward flight (Case 1 — leading edge pitch link).

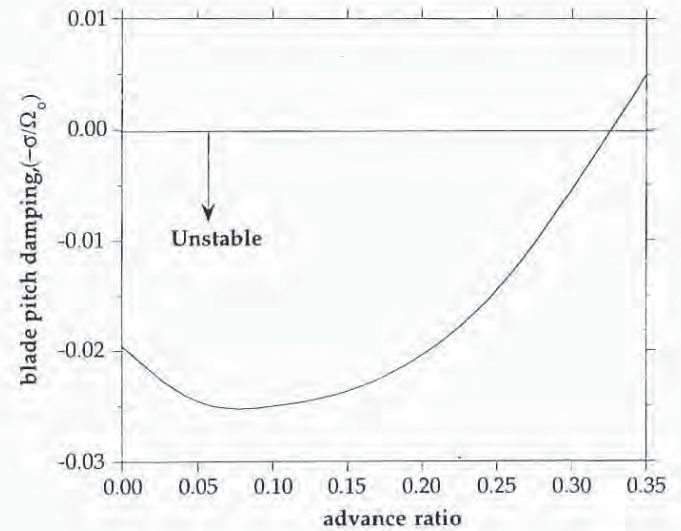


Fig. 7. Pitch-flap flutter for trailing edge pitch-link configuration at 1100 RPM.

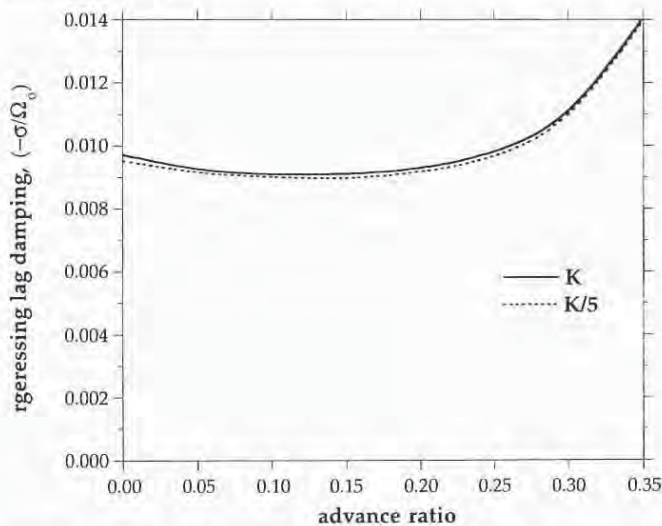


Fig. 6b. Shaft-fixed stability in forward flight (Case 2 — trailing edge pitch link).

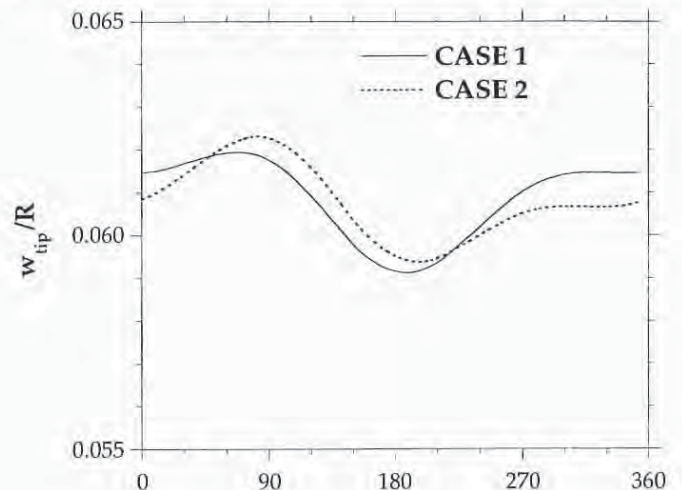


Fig. 8. Flap response at blade tip at advance ratio, $\mu = 0.1$.

This trend of virtually identical flap displacements and widely differing cross-sectional orientations between the different pitch link configurations persists in forward flight as well. From Fig. 8 it can be seen that at an advance ratio, $\mu = 0.1$, both the leading as well as trailing edge pitch link configurations have a very similar tip flap response versus azimuth. Tip cross-sectional orientation angle, ϕ , at various advance ratios is presented in Figs. 9a and 9b, for cases 1 and 2, respectively. The large cross-sectional orientations, ϕ , for cases 1 and 2 are of opposite sign and contain substantial rotations of the blade due to kinematic pitch-flap coupling, in addition to elastic twist.

From Figs. 6a and 6b it can also be observed that the leading edge pitch link configuration (case 1) shows a considerable decrease in lag damping at low to moderate advance ratios, as compared to case 2. A possible explanation to this could be due to the interaction with the flap modes. The first flap frequency for the leading edge pitch link configuration (with a flap-up, pitch-up kinematic coupling), is significantly reduced to approximately 0.36/rev as compared to a frequency of 1.05/rev for the case with almost zero pitch-flap coupling. The corresponding frequencies for the re-

gressing and progressing flap modes are 0.64/rev and 1.36/rev. As the advance ratio increases, the two low frequency flap modes are seen to converge toward and interact with each other (Fig. 10a) resulting in a pair of modes that cannot be clearly classified as 'collective' and 'regressing.' These low frequency modes have substantially different aerodynamic damping, one high and the other very low (Fig. 10b). The low damping in one flap mode may possibly be influencing the reduced lag damping observed in Fig. 6a. In contrast, for the trailing edge pitch link configuration, the first flap frequency is increased to approximately 1.44/rev. The corresponding progressing and regressing flap frequencies are 2.44/rev and 0.44/rev, and no coalescence occurs between these well separated modes as the advance ratio increases. The first lag frequency for the both configurations is approximately 0.757/rev.

Shaft-free aeromechanical stability

Figures 11a and 11b show the variation of shaft-free lag damping with advance ratio, for the leading and trailing edge pitch link configurations,

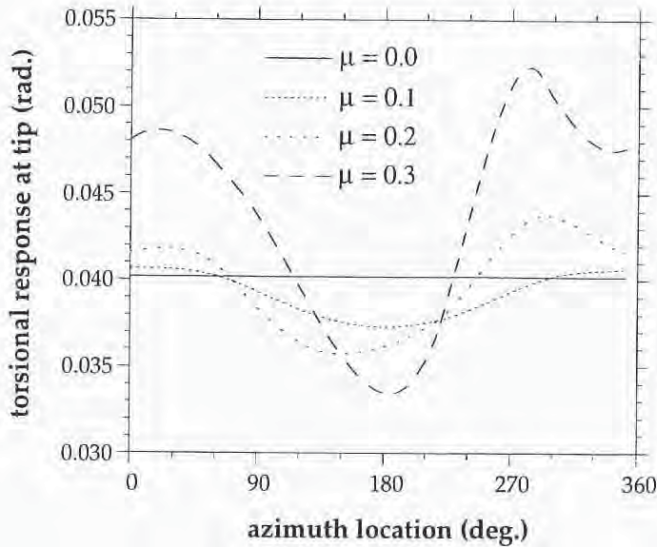


Fig. 9a. Blade tip torsional response (Case 1 — leading edge pitch link).

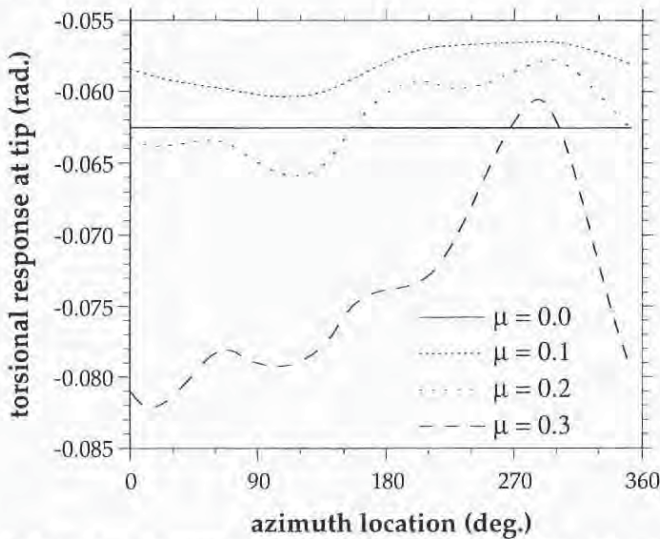


Fig. 9b. Blade tip torsional response (Case 2 — trailing edge pitch link).

respectively. Comparing these figures with the corresponding shaft-fixed lag damping variations (Figs. 6a and 6b) reveals that hub motion has a small effect on the collective and progressing lag modes, but a significant influence on the damping of the regressing lag mode. In hover, the regressing lag damping is considerably reduced for both pitch link configurations. For the leading edge pitch link configuration, the regressing lag damping rapidly increases with advance ratios (Fig. 11a). For the trailing edge pitch link configuration, a much smaller variation in regressing lag damping with advance ratio is observed (Fig. 11b).

Other than the damping in the regressing mode, inclusion of hub motion barely affected the dynamic and aeroelastic characteristics of either configuration. For the trailing edge pitch link configuration, pitch-flap flutter was again seen much as it was in the absence of hub motion.

Summary and Concluding Remarks

An aeroelastic analysis methodology for bearingless main rotor helicopters in forward flight is developed. The significant elastic twist experi-

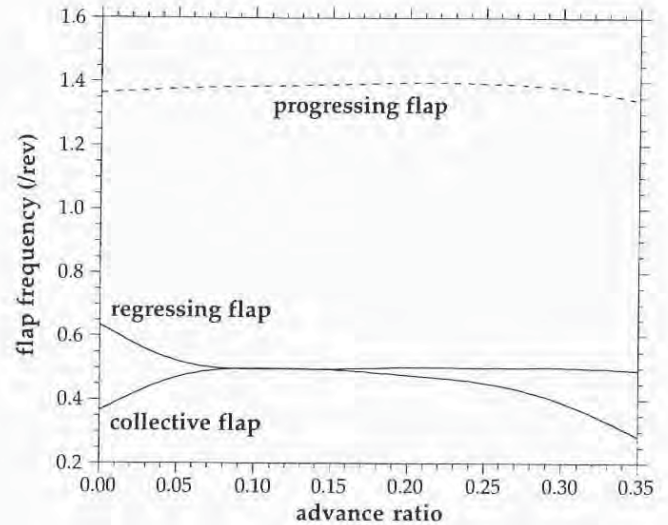


Fig. 10a. First flap modal frequencies (Case 1 — leading edge pitch link).

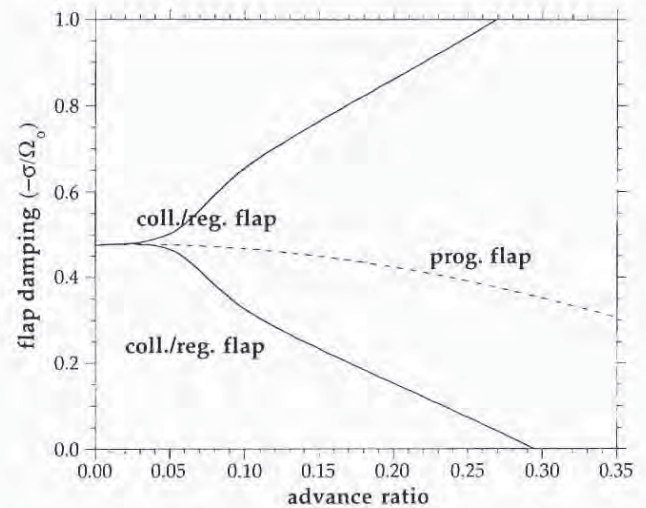


Fig. 10b. First flap modal damping (Case 1 — leading edge pitch link).

enced by the flexbeam during pitch control application can influence the nonlinear behavior of the blade under aeroelastic forces. In the present analysis, the elastic deformations due to pitch control are independently evaluated as the invacuo structural response to a prescribed swashplate motion. The aeroelastic response is obtained by the use of modified nonlinear equations of motion which account for the influence of the elastic deformations due to pitch control. The present analysis is robust and has good convergence behavior in evaluation of blade periodic response.

Good correlation with experimental lag damping data is obtained for a model bearingless rotor without shear restraint, and with pitch links located at the leading or trailing edge. Pitch link location at the leading or trailing edge (which induces different types of pitch-flap coupling) is seen to have a strong effect on torsional response and thrust of the rotor. For a given blade pitch setting, flap up-pitch up kinematic coupling of a leading edge pitch link configuration results in large positive torsional response, which increases the thrust. The flap up-pitch down kinematic coupling of a trailing edge pitch link configuration has the opposite effect. The large negative torsional response in this case, decreases the thrust. The blade tor-

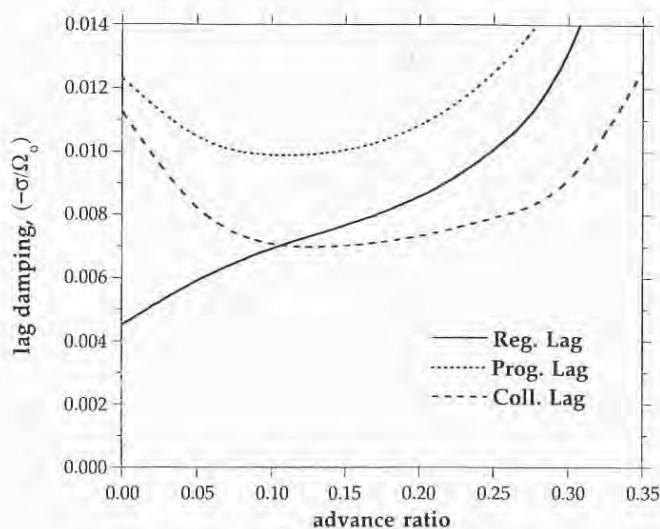


Fig. 11a. Shaft-free stability in forward flight (Case 1 — leading edge pitch link).

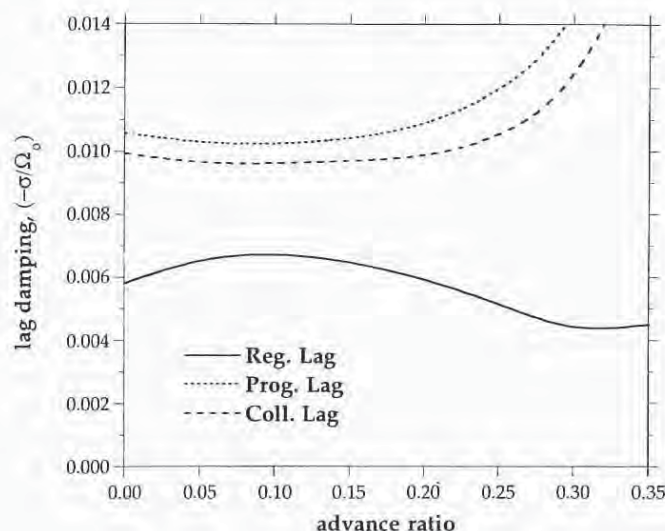


Fig. 11b. Shaft-free stability in forward flight (Case 2 — trailing edge pitch link).

sional responses for both configurations contain moderate kinematic rotations, in addition to elastic twist. Consequently, lower pitch settings would be required for the leading edge pitch link configuration to achieve the same thrust.

Shaft-fixed stability of both pitch link configurations improves at high advance ratios. It is assumed that this increase is associated with the higher aerodynamic damping due to large cyclic flap. Pitch link flexibility is seen to have a minimal influence on the shaft-fixed forward flight lag mode stability characteristics of the trailing edge configuration, and the influence is only slightly greater for a leading edge pitch link configuration. For the leading edge pitch link configuration, coalescence of the collective and regressing flap modes is seen at moderate advance ratios.

The inclusion of hub motion results in a reduction of regressing lag damping for the trailing edge pitch link configuration over the range of advance ratios. For the leading edge pitch link configuration, regressing lag damping is reduced at hover, but increases with advance ratio.

For the trailing edge pitch link configuration, occurrence of pitch-flap flutter is predicted by the analysis. The instability grows weaker with increasing advance ratio. The inclusion of hub motion does not influence the flutter instability.

Acknowledgements

This research work is supported by the Army Research Office under the University of Maryland Center for Rotorcraft Education and Research, Grant No. DAAH04-93-G-0001; Technical Monitor Dr. Tom Doligalski.

References

¹Huber, H., "Will Rotor Hubs Lose Their Bearings? A Survey of Bearingless Main Rotor Development," Presented at the Eighteenth European Rotorcraft Forum, Avignon, France, Sep 15-18, 1992.
²Hodges, D. H., "A Theoretical Technique for Analyzing Aeroelastic Stability of Bearingless Rotors," *AIAA Journal*, Vol. 17, No. 4, 1978.
³Hodges, D. H., "An Aeromechanical Stability Analysis for Bearingless Rotor Helicopters," *Journal of the American Helicopter Society*, Vol. 24, No. 1, Jan 1979, pp. 2-9.
⁴Hodges, D. H., Hopkins, A. S., Kunz, D. L., and Hinnant, H. E., "Introduction to GRASP — General Rotorcraft Aeromechanical Stability

Program — A Modern Approach to Rotorcraft Modeling," *Journal of the American Helicopter Society*, Vol. 32, No. 2, 1987, pp. 78-90.

⁵Sivaneri, N. T., and Chopra, I., "Finite Element Analysis for Bearingless Rotor Blade Aeroelasticity," *Journal of the American Helicopter Society*, Vol. 29, No. 2, Apr 1984, pp. 42-51.

⁶Dull, A. L., and Chopra, I., "Aeroelastic Stability of Bearingless Rotors in Forward Flight," *Journal of the American Helicopter Society*, Vol. 33, No. 4, Oct 1988, pp. 38-46.

⁷Jang, J., and Chopra, I., "Ground and Air Resonance of an Advanced Bearingless Rotor in Hover," *Journal of the American Helicopter Society*, Vol. 33, No. 3, Jul 1988, pp. 20-29.

⁸Jang, J., and Chopra, I., "Air Resonance of an Advanced Bearingless Rotor in Forward Flight," Proceedings of the 2nd International Conference on Rotorcraft Basic Research, College Park, MD, Feb 1988.

⁹Hong, C. H., and Chopra, I., "Aeroelastic Stability Analysis of a Composite Bearingless Rotor Blade," *Journal of the American Helicopter Society*, Vol. 31, No. 4, Oct 1986, pp. 29-35.

¹⁰Tracy, A. L., and Chopra, I., "Aeroelastic Analysis of a Composite Bearingless Rotor in Forward Flight with Improved Warping Modeling," Presented at the American Helicopter Society Aeromechanics Specialists' Conference, San Francisco, California, Jan 19-21, 1994.

¹¹Hodges, D. H., and Dowell, E. M., "Nonlinear Equations for the Elastic Bending and Torsion of Twisted Nonuniform Rotor Blades," NASA-TND-7818, Dec 1974.

¹²Bir, G., Chopra, I., et al, "University of Maryland Advanced Rotorcraft Code (UMARC) Theory Manual," UM-AERO Report 92-02, Aug 1992.

¹³Dawson, S., "An Experimental Investigation of a Bearingless Model Rotor in Hover," *Journal of the American Helicopter Society*, Vol. 28, No. 4, Oct 1983, pp. 29-34.

"WILL ROTOR HUBS LOSE THEIR BEARINGS?" A SURVEY OF BEARINGLESS MAIN ROTOR DEVELOPEMENT

Helmut Huber
Eurocopter Deutschland GmbH
Munich, Germany

Abstract

Main rotor systems have since long been the subject of intensive research and development work in the helicopter industry. This is due to the fact that, historically, rotor heads have always been the most complex helicopter components, difficult to maintain and costly to operate. Advances in composite materials have made it feasible to develop new rotor concepts during the past 25 years, which totally eliminate the system of hinges and bearings - the bearingless-rotor design.

A review of the developments in BMR-technology is presented. The paper includes a history of the BMR concepts that have been developed and flown by the different manufacturers over the past 20 years. The critical aspects of bearingless-hub design are summarized; they include the design of the flexbeam and pitch-control structure, the possibilities of providing inplane-damping through various couplings and emphasizes design aspects of elastomeric materials damping devices. Representative results of recent designs are presented to illuminate the achievements made. Finally, an outlook into possible future trends in BMR-technology is given.

Introduction

Helicopter main rotors are commonly recognised as the more complex components which make up for the general complexity of this type of air vehicle. Indeed, the design of a main rotor is not a simple task and conceals a number of difficult problems to guarantee proper functioning.

Having that in mind, since the birth of the helicopter, the classical constructors have always been active in looking for novel ideas - both in terms of novel concepts and for detail improvement. New designs for rotor heads have been proposed fairly regularly. In the quest for design simplicity, there were mainly two developments that practically provided the necessary conditions for the design of new rotor heads in the past 20 years. These are: (1) The development of composite materials, which, besides its light weight, have "fail-safe" features inherent to their fibrous nature, and (2) the development of viscoelastic (elastomeric) materials which can be efficiently used for the design of laminated

bearings or for high hysteresis type of elastomeric elements, which provide high levels of damping.

These technological developments have made it feasible to design and develop new rotor concepts, eliminating partly or totally the system of hinges and bearings, the Bearingless Main Rotors (BMR). These rotors aim for a complete deletion of all three hinges of a conventional rotor. Figure 1 shows a schematic of a bearingless rotor build-up. Blade motions in the flapwise and chordwise directions are accomplished through elastic bending, and blade pitch-control is achieved by elastically twisting the inboard (flexbeam) portion of the spar. The moment applied to the blade from the pushrod is transmitted through a pitch-control element, which has to be rather rigid in torsion. The main goal in such design is simplicity, because of the favourable implications for rotor system weight, cost, reliability and maintainability.

The purpose of the present paper is to provide a review of the BMR-systems designed and tested, to discuss the main aspects in the design, and the achievements made so far. Finally, some prospects for future developments in BMR technology are presented.

Bearingless Main Rotor Developments

At one time or another, most of the companies of the helicopter industry have worked towards the development of bearingless rotors and have investigated in eliminating the blade retention/pitch change bearings from their main rotor systems.

Interestingly, the first successful efforts to apply bearingless rotor technology were made on tail rotors, during the design competition for the UTTAS-Helicopter in the early 1970's, in which both competitors used stiff-inplane bearingless designs for the tail rotors (References 1 and 2). These efforts have continued at Hughes with the AH-64A composite Flexbeam Tail Rotor (Reference 3), and with prototype tail rotors development at Aerospa-tiale (Reference 4), and MBB (Reference 5).

The design of a bearingless main rotor, quite obviously, remained a more difficult problem. When examining the variety of BMR baseline concepts, the manufacturers went different ways in their design approaches. The following is a brief history of the BMR concepts that have been developed and tested.

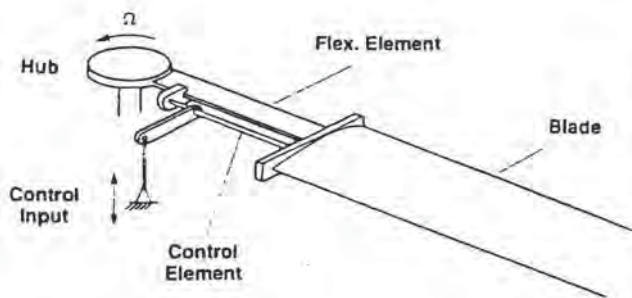


Fig. 1 Schematic of a bearingless rotor built-up

Lockheed

The first major effort to develop a bearingless main rotor was conducted by Lockheed, California, who developed a matched-stiffness rotor installed on the XH-51A helicopter in 1966. The rotor was four-bladed and used steel flexures at the root with polar symmetry for a matched stiffness configuration. Pitch control was by means of a steel torque rod forward of the flexbeam. The low inplane stiffness was mainly necessary to achieve the desired torsional flexibility. The rotor had negative pitch/flap and pitch/lag coupling, which was destabilizing.

The rotor underwent flight testing on a XH-51A helicopter (Figure 2). The testing was only partially successful, the aircraft showed marginal air resonance stability, and ground resonance stability was acceptable only on a smooth prepared surface. From the today's point of view, this development, was somewhat premature, due to the limited knowledge of aeromechanical stability and of the use of conventional materials at that date. Reference 6 described the development of the Lockheed BMR system.



Fig. 2 Matched-stiffness rotor test aircraft XH-51A

Boeing Vertol

Boeing Vertol, Philadelphia, USA began the development of a Bearingless Rotor in 1978 under a US-Army Government contract. For flying qualities, the design goal was set to depart as little as possible from the characteristics of the BO 105 Hinge-

less Rotor, i.e. to match both the basic first flap frequency dynamics (1.12/rev), corresponding to an equivalent hinge-offset around 14 percent, and the first chord frequency of 0.68/rev (soft inplane design). References 7 and 8 described the development of the BMR design.

The rotor (Figure 3) consisted of two parallel fiberglass flexures with a C-channel cross section that were rigidly attached to a rotor shaft fitting. A torque rod was placed between the two C-beams, at the center of twist. The flexbeam used 12.5 degrees prepitch to introduce structural flap/lag coupling, and 2.5 degrees negative droop to improve stability. At the outboard end of the beam, the blades were attached to individual blade-to-beam joints. The rotor had no sort of elastomeric or other type of damping device.

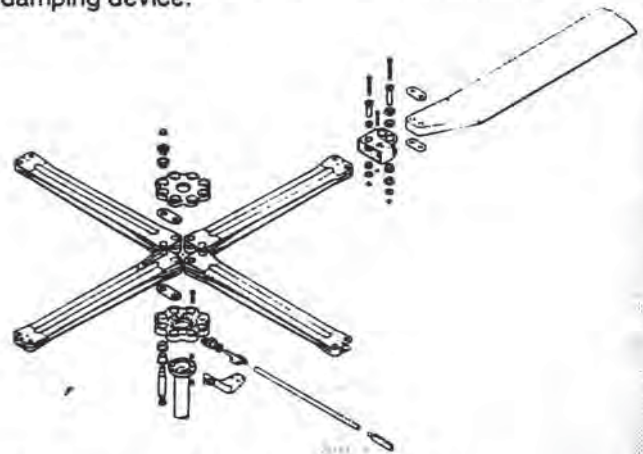


Fig. 3 Boeing Vertol bearingless rotor

The Boeing BMR first flew in 1978 on a BO 105 test vehicle (Figure 4). Initial flight tests indicated that ground resonance damping was inadequate, which was cured by stiffening the landing gear. It had similar air resonance characteristics to the Baseline BO 105 rotor, except at lower collective pitch settings. The original Boeing BMR was subsequently tested in the NASA Ames Wind tunnel, where some elastomeric damping material was bonded to the beams. The rotor was finally destroyed in the tunnel in 1982 due to an operator's error.



Fig. 4 BO105 with BMR in flight

Boeing Vertol continued its BMR efforts under the US-Army's Integrated Technology Rotor (ITR) Programme. This activity was cancelled when Boeing teamed with Sikorsky for the LHX program.

Aerospatiale/ECF

Aerospatiale, France, was always investing a large part of its research and design work to finding new solutions for simplifying the basic functions of rotorheads, as summarized in Reference 9. Among the various types of heads experimented on a SA 341 "Gazelle" helicopter was also a bearingless rotor head, called Triflex. Its development began in 1972. The three-bladed, soft-inplane rotor (Figure 5) was an attempt to eliminate not only the blade retention/pitch change bearings, but also the control rod reaction bearing as well. The rotor head consisted primarily of a set of fiberglass-epoxy yarns that were imbedded in an elastomeric matrix to form a flexible arm. The elastomeric matrix served also a second role, i.e. to introduce some structural damping for the lead-lag motion. The ends of the flexible arms were rigid fiberglass attachment blocks that connected the arms to the rotorshaft and blades. These arms had torsional flexibility, while the flapping and inplane stiffness was relatively high. The rotor had a flap frequency of 1.06/rev, a lag frequency of 0.72/rev and 2.5 degrees precone.

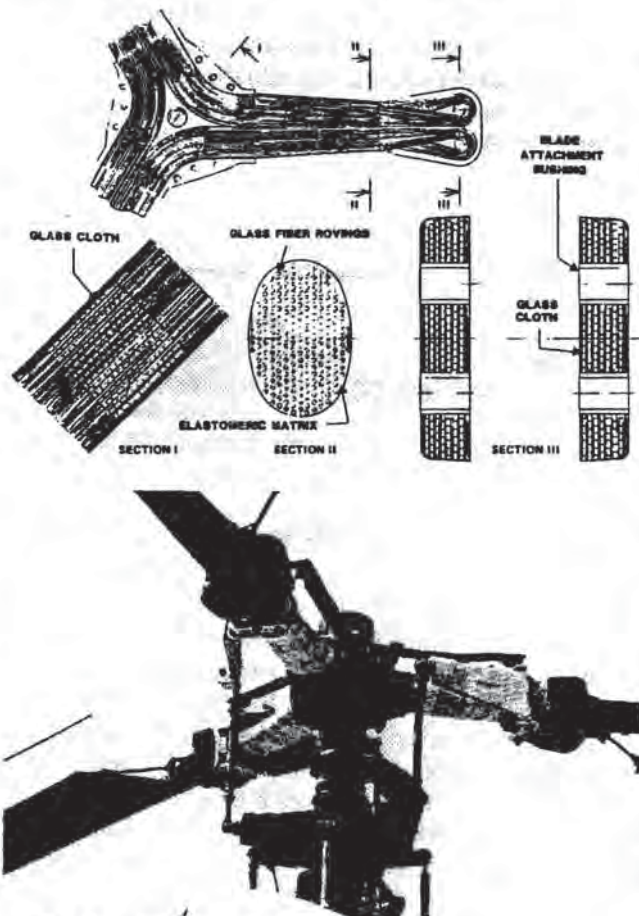


Fig. 5 Triflex hub construction



Fig. 6 SA 341 Gazelle helicopter

The flight tests of the 3-bladed Triflex rotor head were performed on a "Gazelle" (Figure 6). Apparently, most of the results were rather successful, however, the lead-lag damping was very low, resulting in a weak tendency for ground resonance instability, which was cured by installation of a hydraulic damper on the landing gear. Due to some coupling problems, also the lead-lag stresses and vibration levels were very high in certain flight conditions. The knowledge of the effect of several head and blade parameters was not yet developed at that time, and practical solutions to these problems were not found. Reference 10 reviews this development.

In further development of the Triflex rotor, Aerospatiale increased the number of blades to four, to reduce vibrations, and installed a lag damper to ensure ground resonance stability. A limited flight test was conducted. Primary development of the Triflex rotor hub configuration was completed and the conclusion was made that solutions of the various problems noted would be possible. In the following phase, Aerospatiale has shelved development of its Triflex BMR in favour of its Spheriflex elastomeric rotor (Reference 9).

Bell

Bell Helicopter Company, Texas, throughout the 1970's and 1980's has been experimenting on composite hubs (References 13). The four-bladed BMR, the Model 680 rotor (Figure 7), consists of a one-piece fiberglass structure that forms the flexbeams for all four blades. Each arm has a torsionally flexible feathering element outboard and a flapping flexure inboard. Pitch change is transmitted from the pitch links to the blade by torsionally stiff cuff assemblies that surround the arms of the flexbeams. The inboard portion of the cuffs are connected to elastomeric shear restraints and elastomeric lead-lag dampers. The flexbeams extend to 22 percent of rotor radius, where the beam, blade and cuff are bolted together. This rotor systems incorporates the Bell design philosophy of low flapping hinge offset (2-3 percent), including flexible mast and transmission suspension for some

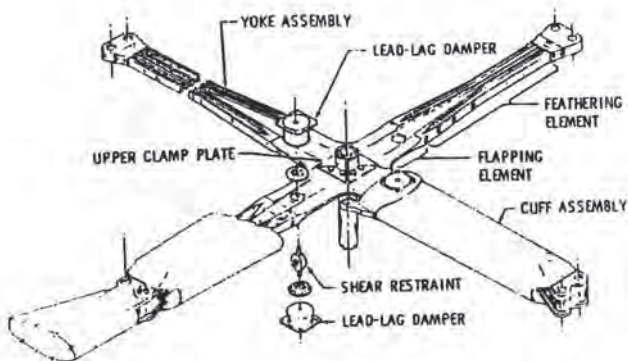


Fig. 7 Bell Model 680 rotor system

rotor flapping relief. Further design criteria were high structural lead-lag damping and uncoupled flapping, lead-lag, and pitch-change motions. Also, the flex-beam shows a highly tailored geometry for optimum stiffness and stress distributions.

The Model 680 BMR first flew in 1982 on a Model 222 helicopter (Figure 8). There were basically two problems with the Model 680 rotor: (1) The hub drag associated with the blade/cuff/flexbeam attachment was worse than expected, however, this problem could be significantly improved on the next Bell design. (2) The flapping ability of the low hinge offset flexbeam: A flapping failure mode from inter-laminar shear stresses was limiting the design to only 3 degrees flapping although the design was made for 5 degrees. With 3.5 percent rotor damping available from the lag dampers alone, ground and air resonance was no problem. The biggest advantage of the rotor was the excellent vibration level, well below 0.1 g for all flight conditions, which was achieved through a linked-focused pylon and the LIVE-isolation in the vertical axis. References 11 and 12 described the Model 680 development.



Fig. 8 Model 222 with 680-BMR

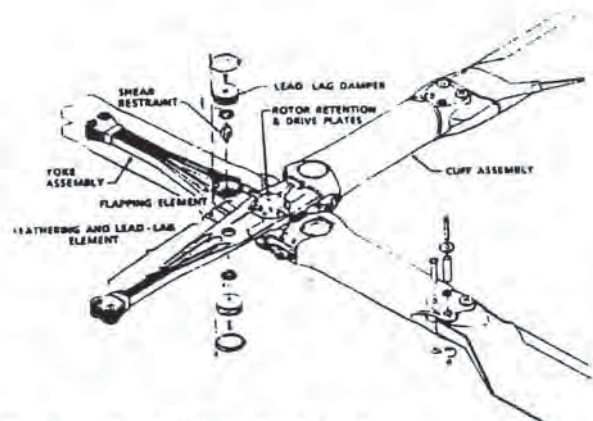


Fig. 9 4BW bearingless rotor

Having the basis of previous IR&D developments, the logical step was to apply the 680 BMR system technology to other helicopters products. Such new design is the 4-bladed Main Rotor System for the AH-1W-helicopter. The 4 BW main rotor hub (Figure 9) has now two single piece structural members, called yokes, that are bolted together at the top of the mast. Relative to the Model 680 rotor, the rotor hub drag was reduced by a cuff with elliptical cross section and fairings in the hub to blade attachment area.

Flight tests on a modified AH-1W-helicopter (Figure 10) showed very encouraging results, indicating excellent agility, low vibrations and good handling qualities. A description of the development work on this rotor system is given in Reference 14.



Fig. 10 4BW on a modified AH-1W helicopter

Hughes/MDHC

Hughes, Tempe/Arizona, began its bearingless main rotor development late 1982, within its HARP-Program. The 4-bladed HARP-Rotor is designed as a single flexbeam type, the beam made out of Kevlar and Graphite (Figure 11). The longest portion of the flexbeam has a cruciform cross section, inboard the cruciform transmissions into two flat legs, which allow for flap motion. The flapping hinge offset is approximately 8 percent and the flex-beam extends to 23 percent rotor radius. The HARP

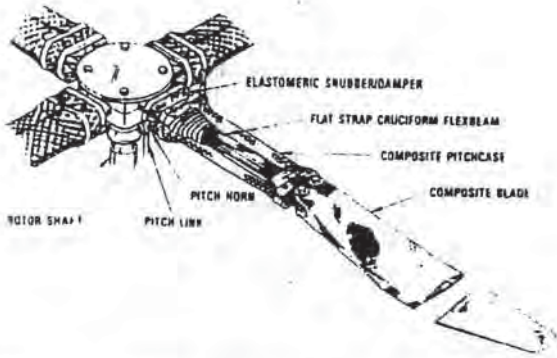


Fig. 11 HARP rotor configuration



Fig. 12 HARP rotor on MDHC Model 500E

also has pitch change cuffs, consisting of a hollow graphite box, and supported in its inboard end through an elastomeric snubber/damper unit. The manual folding arrangement has two attachment joints on each arm, which adds complexity and weight.

A comprehensive flight test program was conducted in 1985, using a 500 E helicopter (Figure 12). The flight test revealed the expected results regarding rotor stability, loads, performance and vibration characteristics. A summary of the development work and the results achieved is given in References 15 and 16.

With this basis, MDHC continued with the application of the BMR technology to its new project, the MD-900 Explorer light twin commercial helicopter. The rotor basically follows the basis worked out during the HARP-Program, but is the first five-bladed BMR ever built (Figure 13). The 33.8 ft diameter rotor has a slightly lower hinge offset and a rectangular flexbeam cross section. Five blades were chosen for the rotor to minimize noise and vibration. The characteristics of the rotor were successfully demonstrated on the whirl stand and in the 40x80 tunnel at NASA Ames up to wind speeds of 200 kts. The rotor is due to fly on the MD-900 first prototype aircraft in summer 1992.

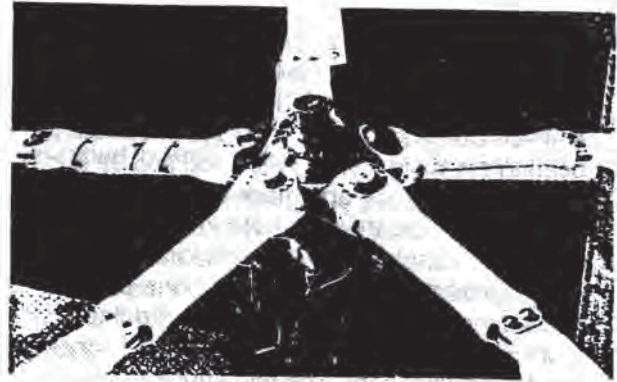


Fig. 13 MDHC five-bladed BMR for the Explorer

Sikorsky

Sikorsky Aircraft in Stratford, Connecticut, began the research and development of bearingless concepts on bearingless tail rotors, which are in production today on the Black Hawk and S-76.

The search for a low-offset main rotor bearingless concept have first lead to a unique stiff-inplane design, the Dynaflex (Figure 14). The Dynaflex rotor is a so-called "Gimballed" rotor system in which a stiff hub is attached to the driveshaft via an elastomeric constant-velocity joint to allow the hub to tilt and relieve the lead-lag stresses. The drive torque and flapping restraint are provided by a composite diaphragm, which transmits the torque from the shaft to the rotor, while at the same time retaining it by means of the carbon-fibre spring. Thus, the rotor provides an equivalent 5 percent hinge-offset, which is similar to articulated rotors. The gimbal concept allows to gain a substantially higher rotor tip path plane tilt over a conventional rotor (Reference 17).

The Dynaflex rotor, obviously, has the best drag of the BMR designs, but at the same time shows also a higher complexity. Sikorsky was performing many model tests with this hub concept, and completed a design of a full-scale rotor suitable for a high-speed Black-Hawk type helicopter, but never went into hardware.

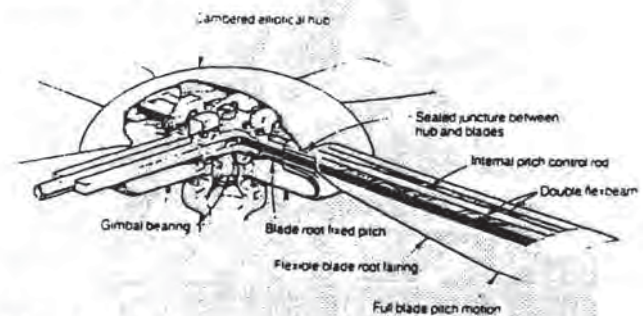


Fig. 14 Dynaflex Gimballing bearingless rotor configuration

During the LHX-Proposal phase to the US-Army, Sikorsky became responsible for the main rotor design, but did not follow the Dynaflex concept. The RAH-66 Comanche main rotor system employs a bearingless main rotor, five-bladed and 39 ft in diameter (Figure 15). Parts made using composite materials include the blade, torque tube, flexbeam, rotating swashplate, rotating scissors and quill shaft. The original design consisted of a one-piece fiberglass structure that formed the inboard flap flexures of all 5 blades and extended out to the connection bolt for the flexbeam. The hub structure was slightly changed, the PENTAFLEX rotor head being replaced by inboard blade attachments with modular fittings, that allow individual blade removal from the hub assembly for airtransportability and in case of damage. The flexbeam has rectangular cross section and inboard elastomeric damping/shear restraint elements. The equivalent flapping hinge offset lies around 9.5 percent of radius (Reference 18).

In 1991, a S-76 BMR test article, representative of the RAH-66 design concept was tested on the whirl stand (Figure 16). It is also scheduled to be tested at the NASA Ames wind tunnel facility.

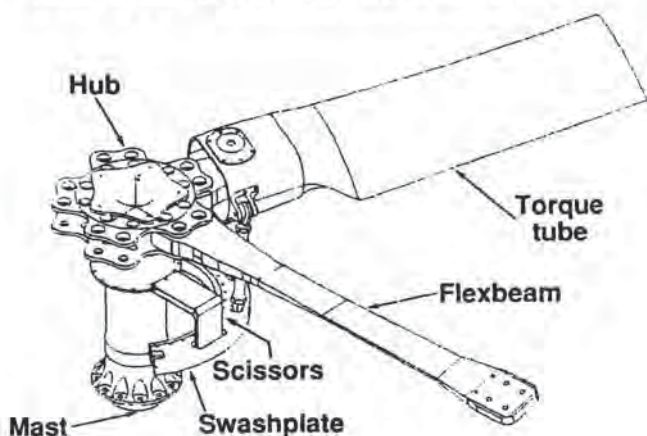


Fig. 15 RAH-66 Comanche rotor system

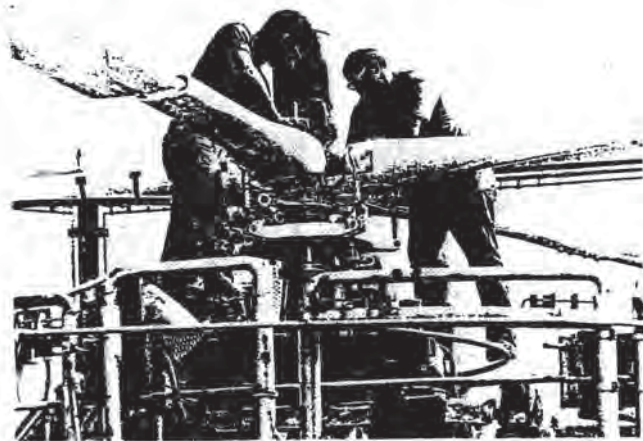


Fig. 16 S-76 BMR demonstrator on whirl tower

MBB/ECD

MBB (now Eurocopter Deutschland), Ottobrunn, Germany, began its fiberglass technology development in 1961, which resulted in the successful Hingeless Rotor System. Based on this tradition, MBB began experimenting with bearingless rotors in 1981. The development was conducted in three steps: In the first concept, which was a pure research configuration, a BO 105 hingeless hub was modified to carry experimental flexbeam blades, with the original pitch change bearings fixed at a 10 degrees prepitch angle (Figure 17). Similar to the Boeing approach, the design goal was to match the BO 105 rotor system dynamics as far as possible and, hence, the flapping hinge offset was outboard at 14 percent radius. The first chord frequency was at 0.69/rev. The flexbeam had a T-shaped cross-section, and a pitch control tube was placed behind it, mounted with flexible couplings to the hub and blades. In order to provide acceptable stability, elastomeric damping strips were bonded to the flexbeam, and constrained by an outer layer of graphite epoxy laminate.

The rotor was flown on a BO 105 test helicopter in 1984 (Figure 17). Although compromised, the experimental rotor yielded basically promising flight test results; however, the rotor stability was low and the hub drag was high. The development is summarized in Reference 19.



Fig. 17 MBB's FVW-Rotor experimental configuration

MBB was then developing a second prototype rotor in a more advanced design, where the stability and drag issues were particularly addressed (Figure 18). It uses a cruciform cross section flexible beam, and around this is an elliptical carbonfibre control cuff. It is made in two pieces which could be telescoped for flexbeam inspection. In this design the flapping hinge offset was reduced to about 9 percent, to provide the best compromise between agility, vibration/loads and structural integrity. The flexbeam could be shortened down by 25 percent. The rotor was tested on the whirlstand with several modifications on the hardware, to optimize the cuff

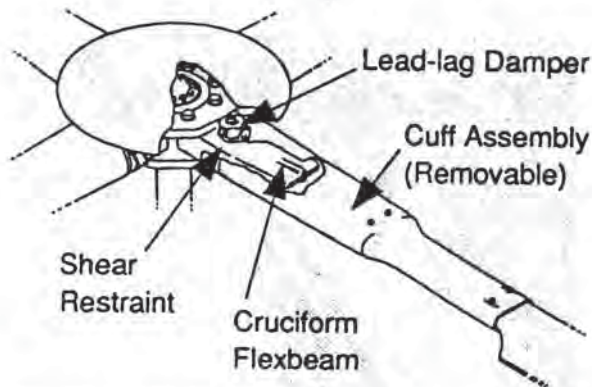


Fig. 18 BMR-P1 bearingless rotor concept



Fig. 19 Rotor installed on the BO105

design and elastomeric damper effectiveness. In 1986, the rotor was flight tested on a BO 105 with good results (Figure 19). Publications on the development of these MBB Bearingless Rotors are listed as References 20 to 22.

The results achieved during these campaigns provided a good foundation for the final BMR design for the new BO 108 helicopter. The configuration in principle follows the concept tested in the phase before, but was very much refined in the details (Figure 20). The cruciform beam shows a flatplate cross section inboard, which places the flapping hinge offset at 9 percent of radius. The carbonfibre cuff is directly bonded to the inner end of the blades' airfoil section, which results in an exceptionally smooth surface from the hub out to the aerodynamic blade part. Such a design and the inboard attachment of the beam have obvious benefits in reducing the rotor hub drag.

The total development, i.e. the flexbeam and torque tube sizing and the introduction of coupling effects was an intensive, interactive approach, which finally resulted in very satisfactory damping characteristics. Through 9 percent hinge offset, the rotor shows a proper balance of inherent dynamic stability and high maneuverability, and very low

loads and vibration levels. The rotor first flew in October 1988 on the BO 108 Prototype aircraft (Figure 21), with excellent results in aeromechanical stability, handling qualities, loads and vibration, as described in Reference 23.

Besides the BMR, ECD is developing its FEL-fibre elastomeric rotor for the Franco-German PAH-2 and the Indian ALH. This rotor follows the hingeless concept and comprises a stiff composite hub and flexible blades; pitch change is achieved through elastomeric bearings.



Fig. 20 BMR refined configuration

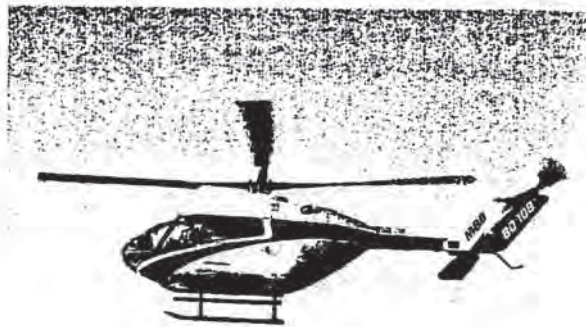


Fig. 21 BO108 with BMR during first flight

Westland Helicopters

Westland, Yeovil, England has been studying BMR's since 1980. Design feasibility studies and analytical work were performed, mainly concentrating on the assessment of ground and air resonance stability margins of such rotors in combination with existing and projected airframe configurations. To support the work, ground and air resonance tests of a four-bladed model rotor were performed. Reference 24 is a review of the analytical and experimental studies.

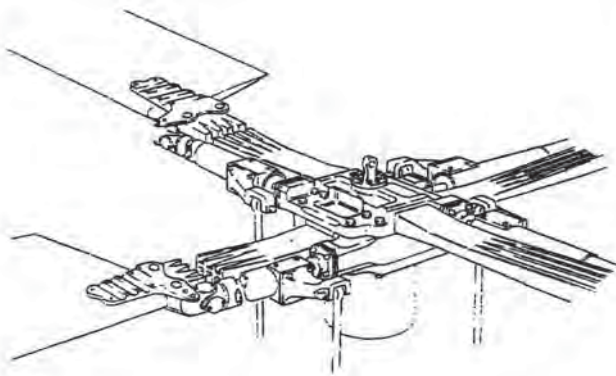


Fig. 22 Westland bearingless rotor design

In order to provide the "hard data", Westland, under a demonstrator contract of the UK-MoD, started design and manufacturing of a BMR flexure, sized for the Lynx helicopter. The rotor design, which emerged, comprised two double-ended composite glass/epoxy flexures housed in a titanium hub assembly (Figure 22). Blade pitch control is provided by a parallel torque tube, which houses an elastomeric lead-lag damper. Four full-sized flexure mouldings were produced and fatigue testing of the flexure is underway. The hardware is shown in Figure 23.

ITR/FRR - Project

In the mid-1970s, the U.S. Army Research and Technology Laboratories and NASA Ames Research Center have joined into a program to develop an Integrated Technology Rotor/Flight Research Rotor (ITR/FRR). The objective of the ITR/FRR program was to make significant advances over a broad spectrum of technologies. In the concept-definition studies a variety of hub concepts were proposed by the five US-Helicopter

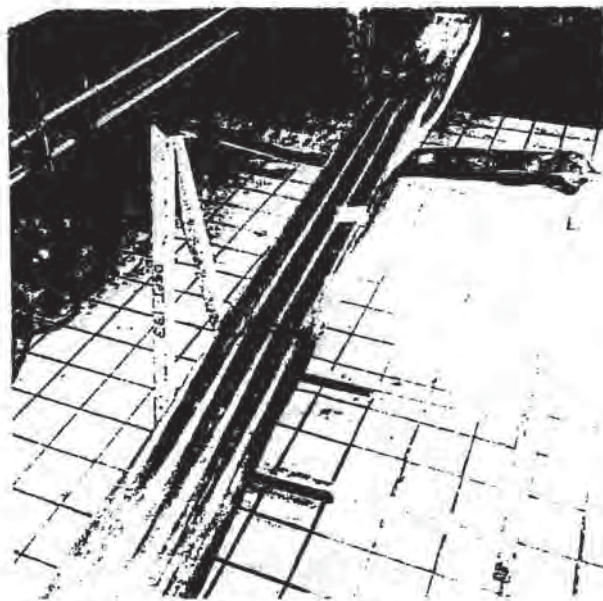


Fig. 23 Full-sized flexure hardware

manufacturers. Their description is given in References 25 to 29. Thirty-three hub-concepts were proposed, amongst them were 21 bearingless designs. Although no real design and development work was performed within this program, many of advanced design issues for new rotor hubs were examined, particularly with respect to bearingless rotor designs. The studies have also been very useful in identifying areas of weakness in the design methods. Reference 30 is a comprehensive analysis and a useful review of the concept-definition studies of the ITR/FRR-Program.

A summary and data comparison of the various bearingless hub concepts developed is given in Table 1.

Company	Type	Diameter (m)	No of Blades	Flap Hinge Offset (%)	Lag Frequency (1/rev)	Hub Precone (deg)	Control Device	Lead-Lag Damping Device	Beam Cross Section	Hub/Beam Attachment	Flown/ Tested in
Lockheed		10.70	4		0.65		Tube	No	Steel-Flex.	Bolted	1966
AS/ECF	Triflex	10.4	3	8.5	0.72	2.5	Horn	Elast/Emb	Elliptical	one Piece	1976
Bell	Model 680	12.8	4	4 (2.5)			Cuff	Elastomeric	Triple-H	one Piece	1982
	4BW	14.4	4	4 (2.5)			Cuff	Elastomeric	Triple-H	2 Pieces	1989
Boeing Vertol	BMR	9.82	4	14	0.74	0	Tube	No	Double-C	Bolted	1978
Sikorsky	Dynaflex	Model	4	5 (Gimbal)	Stiff		Tube	No	Double-C	Bolted	(Model)
	S76-Demo	13.4	5	9.5	0.7	2.5	Cuff	Elastomeric	Rectangular	Bolted	1991
MBB/ECF	FVW-Exp.	9.82	4	13.6	0.69	0	Tube	Elastomeric	T-Shape	Bolted	1984
	BMR-P1	10.0	4	9	0.75	0	Cuff	Elastomeric	Cruciform	Bolted	1986
	BMR-BO108	10.0	4	9	0.70	0	Cuff	Elastomeric	Cruciform	Bolted	1988
MDHC	HARP	8.5	4	8	0.6	2.5	Cuff	Elastomeric	Flat-X	Bolted	1985
	MD900	10.34	5				Cuff	Elastomeric	Rectangular	Bolted	1992
WHL	Exp.		4				Tube	Elastomeric	Triple-H	2 Pieces	(Model)

Table 1 Comparison of bearingless main rotor design concepts

Main Design Considerations

In order to better understand the problems related to a bearingless-hub design, it is helpful to review briefly the important design attributes and to summarize the present state of understanding.

Hub-Moment Stiffness:

A primary parameter in designing any type of rotor system is the fundamental flap stiffness, expressed also as hub-moment stiffness, or equivalent flap hinge offset. Usually, a low hub-moment stiffness is desired to improve vibratory characteristics, gust response and some aspects of flight stability. Conversely, a moderate or high hub-moment stiffness is desired to improve maneuverability, agility and fatigue life. These very basic design considerations have been addressed very systematically in the 1960's, early 1970's, when the development of the Hingeless Rotorcraft began (References 31, 32 for example). There are many literatures available; useful surveys are given in Reference 33 and 34.

When examining the variety of hub concepts and classifying them under the aspect of hub-moment stiffness (or flap hinge-offset), there were basically two categories which characterized the two ends of the full spectrum of rotor concepts, the conventional flap hinge (articulated) designs and the newer hingeless rotor designs. In terms of the flap-hinge offset, the first category, quite obviously, is limited to values below - say 5 percent. On the other side, the newer hingeless hubs show a trend towards relatively high values of flap-hinge offset, due to the fact, that the flap and lag "hinges" were no real hinges, but were realized through blade flexibilities, which lie more outboard. These concepts are characterized by flap-hinge offsets in the order of 11 to 15 percent of radius.

When looking on the current bearingless category, the design concept obviously allows for shifting the effective flap hinge more inboard, mainly due to the simple hub/flexbeam attachment, which is also desirable in order to minimize weight and hub drag. To further illustrate this trend, flap-hinge offsets are shown in Figure 24, where the values of the BMR developments during the last 15 years are plotted against a time axis (year of first flight). It does appear that there is a trend to be observed: With the exception of the pure experimental designs of BV and MBB, the more recent designs of ECD, MD and Sikorsky show hinge-offset values between 8.5 to 10 percent of radius. The Bell concepts show values in the lower range of 2.5...4 percent, which reflects its particular design philosophy of low hinge-offsets.

In-plane Stiffness:

The principal design considerations with respect to the fundamental in-plane natural frequency are very well known from many literatures (Reference

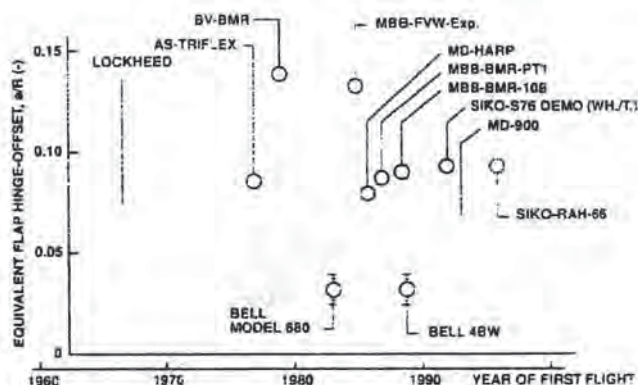


Fig. 24 Trends in BMR rotor stiffness

34). From the 10 BMR hub concepts developed and tested so far, all designs were of the soft-inplane type, with frequencies ranging from 0.6/rev to 0.75/rev (see Table 1). The soft-inplane designs give more design freedom for tailoring the flexbeam cross section, the critical chordwise loadings are low and the small dimensions of the flexbeams is a prerequisite for designing a beam with low torsional rigidity. Furthermore, the technical goals for reducing the hub weight and drag require that BMR designs be as light and compact as possible.

The critical loading conditions and the aeromechanical stability requirements for soft-inplane BMR designs were in principle known, from the substantial work that had been done on the past designs of soft-in-plane hingeless rotors (Reference 34).

Flexbeam Design

The key element of a bearingless rotor is the inboard portion of the spar, commonly called the "flexbeam". This part connects the blade to the mast and has to carry all the primary flight loads. It accommodates the elastic blade motions in flap- and chordwise directions and the elastic twist deformation for pitch control. By proper stiffness tailoring of the beam along its length, it is possible to separate the individual functions of the flexbeam. Figure 25 shows a typical flexbeam design with the different sections tailored to their specific function.

Torsional Stiffness:

The primary criterion in the flexbeam design is the torsional stiffness and strength, since the control requires to twist the beam collectively and cyclically. The shear stresses mainly depend on the achieved torsional rigidity.

In the early stages of its BMR-program, Boeing Vertol did a systematic study of several cross section shapes, like solid sections, split-tubes, I-beams and cruciforms (Reference 8). Figure 26 is a summary of the main results, and shows the tradeoff between the critical fatigue stresses under a

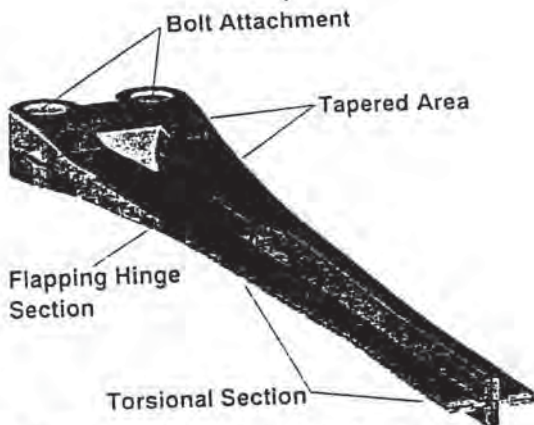


Fig. 25 Flexbeam key design areas

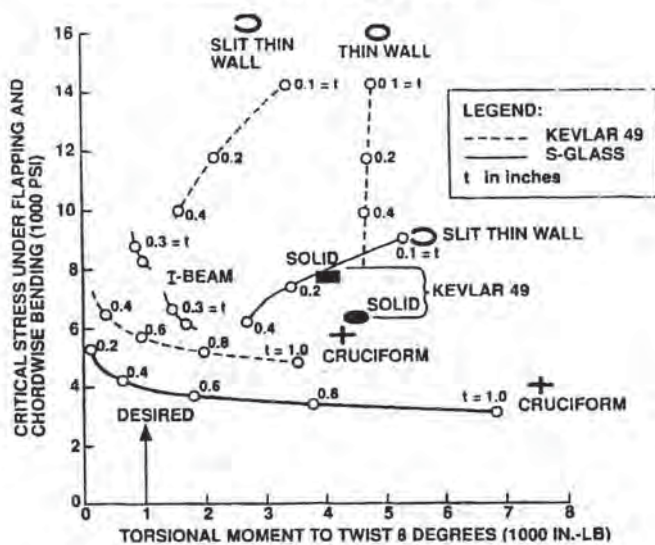


Fig. 26 Beam cross section tradeoff

given load case (alternating flap and chord moments), and the torsional moment necessary to twist the beam by a certain angle. The influence of the cross section materials is also shown.

The variety of design approaches on the present BMR designs suggests, that there is no true optimum cross section: Some of them are using highly tailored cross sections, like cruciform or Triple-H-type sections, others are using flat rectangular cross sections (Table 1). The torsional stiffness goals of all these designs can obviously be met, with careful selection of materials, tailoring of the geometry and orientation of lay-ups.

Bending Tailoring:

The need for inboard flapping flexibility leads usually to a design with a "hinge" section (Figure 25). The length of the hinge section is optimized for a minimum of mainly dynamic stresses caused by blade flapping. Current BMR designs usually apply ± 5 degrees of flapping angles without fatigue damage.

The radial variation of the cross section geometry is often highly tailored along the length of the flexbeam.

The design goal of such configurations is to achieve minimal dimensions, maximum flapping flexibility with reasonable endurance limits and low shear stresses. An example of a flexbeam with a nearly constant strain distribution can be seen in Figure 27. In the lead-lag direction, the flexbeam stiffness is governed by frequency requirements and by the need to tailor the bending mode shape in order to achieve maximum lead-lag damper efficiency.

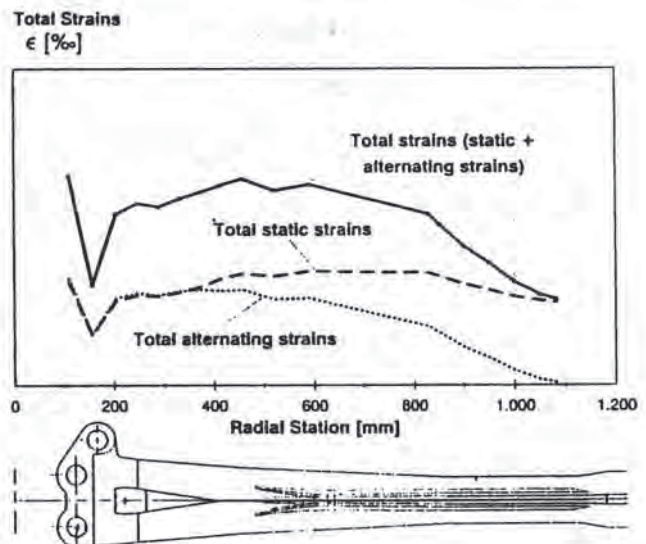


Fig. 27 Constant strain distribution

The flexbeam of the BO108 BMR uses unidirectional E-Glass/epoxy and quasi-isotropic glassfiber/epoxy fabric. Fiberglass belts are used for the attachment lugs. A flexbeam undergoing layup is shown in Figure 28.



Fig. 28 Flexbeam Manufacturing

Control cuffs or pitch cases are designed to have high torsional stiffness and high chordwise stiffness to transmit the in-plane motions to the inboard damping device. Most of the current BMR designs are using primarily graphite/epoxy material in order to achieve the stiffness goals for their cuffs. Dual torsional load transfer diminishes vulnerability and increases the damage tolerance characteristics.

Design Approaches for Damping

In general, any sort of main rotor system must be carefully designed to avoid potential aeromechanical instabilities. As is well known, for soft-in-plane rotors air and ground resonance is of primary interest. Both types of resonances are dominated by the rotor blade lead-lag motion, coupled with body motion. Whenever the regressing mode chord frequency crosses a body frequency, the potential for instability exists. To suppress these potential instabilities, some source of damping has to be introduced into the blade motions for air resonance and into the blade and/or landing gear motions for ground resonance.

The amount of mechanical damping, inherent in composite structures, typically lies in the order of 0.5 to 1 percent. Aerodynamic damping through airloads is contributing some part at 1 g thrust conditions, but has only negligible effect at zero thrust. These two sources of lead-lag damping look to be insufficient for bearingless designs. Hence, blade damping must usually be augmented by mechanical damping in the rotor system or through discrete mechanical coupling of the blade motions such that aerodynamic damping is activated.

Pitch-Lag and Flap-Lag Coupling

Pitch-lag and structural flap-lag coupling, either separately or in combination, are known to have beneficial stabilizing effects for aeromechanical stability. However, these effects are not a general rule; each particular design must be carefully analyzed and the introduction and functioning of these types of couplings must be well understood.

The phenomenon of bending-torsion coupling on helicopter rotor blades can easily be realized by considering the blade bending behaviour (Figure 29). With the total dynamic and aerodynamic forces acting the elastic blade is deflected and, in case of a hingeless rotor, bends away from the line of the feathering axis. If the blade is bent in the flapping plane, the inplane forces create a pitching moment on the arm of the flapping deflection. Likewise, when the blade is bent in the lead-lag direction, a pitching moment on the lead-lag arm is created by the lift forces. References 35 and 36 examined pitch/lag and flap/lag coupling effects on soft-in-plane rotors stability.

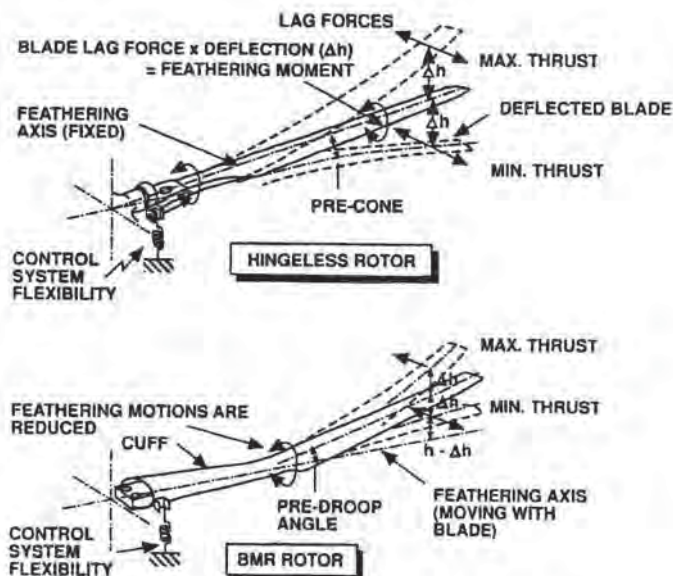


Fig. 29 Principles of lag bending-torsion coupling

When comparing a bearingless rotor with a BO 105 type hingeless concept (Figure 29) it is noticed that the inboard geometry and the sequence of the bending and feathering motions is dissimilar: The BMR does not have inboard feathering bearings and, since the effective feathering hinge for the BMR occurs outboard of the flap and lag equivalent hinges, the stabilizing coupling between the bending and feathering modes is somewhat different. Lag-torsion coupling on the BMR is reduced at low thrust due to reduction in blade-to-feathering-axis offset. Conversely, for the BO 105-rotor, minimum lag/torsion coupling occurs at around 1 g thrust collective (minimum off-axis deflection) and increases as thrust is increased or decreased.

One way of introducing beneficial pitch/lag coupling in BMR's is negative pre-droop in the portion outboard of the blade-to-beam joint. However, it must be kept in mind that blade deflections outboard of that station can partially eliminate the built-in pre-droop effect, hence, reducing the corresponding coupling. The stiffness of the control system also influences this type of mechanical coupling.

Another source of damping in bearingless rotors can be achieved through incorporation of flap-lag coupling. This coupling can principally be affected by the inclination of the principal axes of the flap and chordwise bending. This can be achieved by a pre-inclination of the flexure, as was done on the Boeing BMR. In this case, asymmetric bending of the flexure causes flap motions from chord to lag motions.

Kinematic Coupling

An additional coupling effect can result from the specific concept of the pitch-control. The most common configuration in present BMR designs involve a control cuff to twist the blade outboard of the

flexbeam. To be effective, such a cuff has to be stiff in chordwise direction and in the cuff-to-blade attachment area, such that the lag shear loads are transmitted from the blade to the shear bearing, thus activating the elastomeric damping elements. From Figure 30 it can be seen that, when the blade moves backwards, the cuff moves forward, thus deflecting the elastomeric damping elements. Depending on the geometry of the control rod, a geometric pitch-lag coupling can be introduced, which can substantially alter the damping behaviour - both positively or negatively.

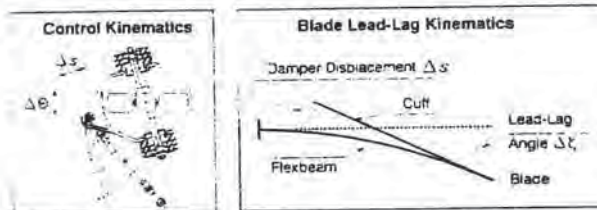
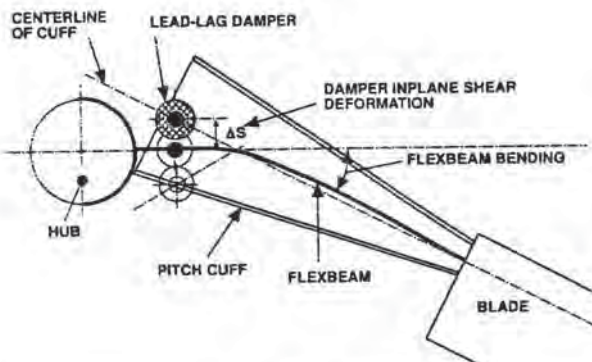


Fig. 30 Pitch/lag coupling due to blade lead-lag and control kinematics

An elementary expression of this type of pitch/lag coupling can be seen from Figure 30 (lower part), where the coupling term can be expressed by

$$\tan \delta_1 = \Delta\theta/\Delta\zeta = \Delta\theta/\Delta\delta \times \Delta\delta/\Delta\zeta$$

The first term in the equation is a control kinematics term, whereas the second one reflects the damper deflection or stiffness term.

As an example from an early MBB-concept, Figure 31 illustrates clearly, how in-plane damping could be improved by changing the damper stiffness and by introducing proper geometric pitch-lag coupling through a change in the inclination of the damper support axis. The combined effect was a doubling of damping over the whole collective pitch range. However, it should be noticed, that in case of a complete rotor-body-dynamics system like ground resonance, the influence of positive pitch-lag coupling on stability may change, and may even be negative in the resonance point. This has been demonstrated by analytical studies (Reference 37).

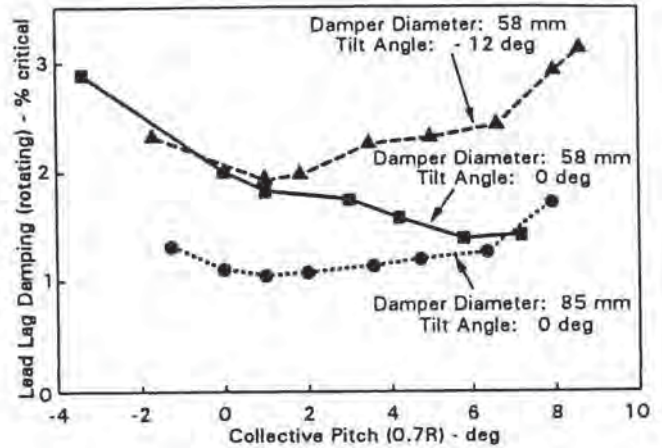


Fig. 31 Test results on coupling sensitive parameters

It is evident from these discussions, that aeroelastic coupling, on the one side, offers considerable potential for augmenting rotor damping. On the other side, stability improvements through sensitive concept parameters of this nature is a highly complex problem, which requires thorough investigation and a high level of confidence in the predictive capability of aeroelastic mathematical models.

Elastomeric Damping

The concepts described before indicate that the most common BMR configuration today involves a combined snubber/damper element at the inboard section, to control the pitch/bending coupling and to augment structural damping. A typical arrangement is shown in Figure 32. To be effective, such elements have to be strained through the inboard motion of the torque structure, thus providing an additional damping in the order of 2 to 4 percent.

The design of such elements is rather complex task. The two main characteristics which are of considerable interest are the mechanical material non-linearities and the thermoviscoelastic characteristics. Some major influences are presented below (from Reference 38).

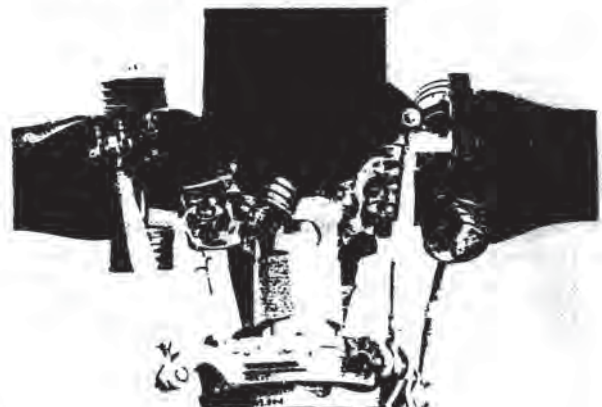


Fig. 32 Elastomeric damper elements on a BMR

Effect of Amplitude: First, the viscoelastic response of high damping elastomers shows a strong non-linear dependence on the shear loading deflections of the damping elements. Figure 33 shows the results of component tests conducted on one type of silicon damper (Reference 38). In the plotting of shear force vs. shear deflection, the strongly non-linear behaviour can clearly be seen: At small amplitudes a dynamic "hardening" of the material is observed, accompanied by a reduction in the loss factor. Conversely, with decreasing amplitudes a strain-softening is noticed.

The analysis of these results indicates that both the dynamic spring rate (curve slope) and the mechanical loss factor (hysteresis loop area) is a highly non-linear function of amplitude. A sufficiently high loss factor can only be achieved with a certain amount of damper displacement. For a concrete design it is essential to understand where this optimum working point is and how the whole system can be forced into working around this point.

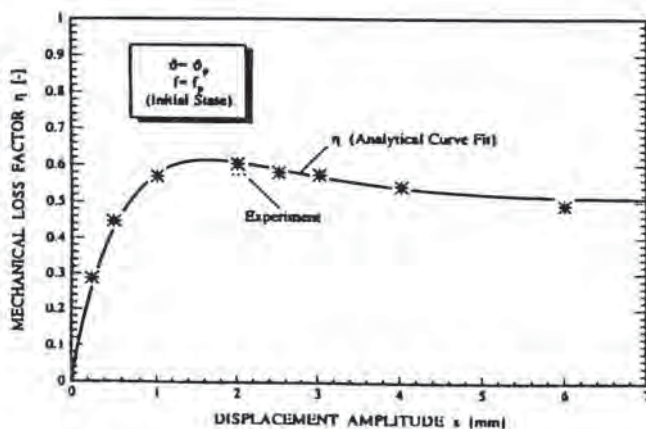
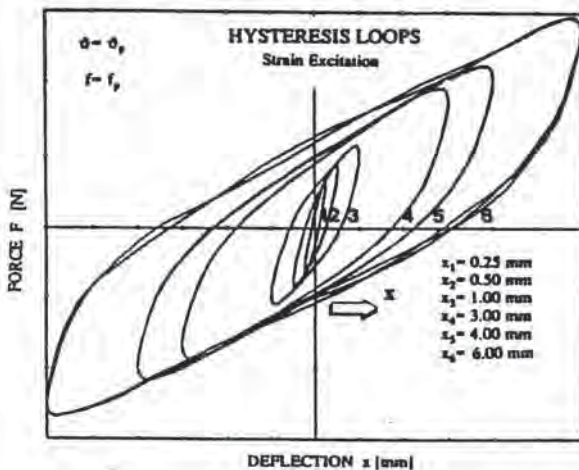


Fig. 33 Damper characteristics (complex stiffness and mechanical loss factor) as a function of displacement amplitude

Effect of Frequency: A second important effect on elastomeric damper characteristics is the influence of frequency. Component testing for a selected damper material indicate, that both the dynamic spring rate and the loss-factor (damping) increases with frequency, and it is evident again, that thorough understanding of the working conditions is required to achieve a successful design.

Effect of Temperature: Due to the particular thermomechanical behaviour of elastomeric material, the temperature is a third important parameter which has considerable influences on damper efficiency. Figure 34 shows representative effects of ambient temperature on the dynamic characteristics of a silicon type of damper. At very low temperatures a stiffening effect in the spring rate is seen, which is an important consideration in the cold start characteristics of a BMR design.

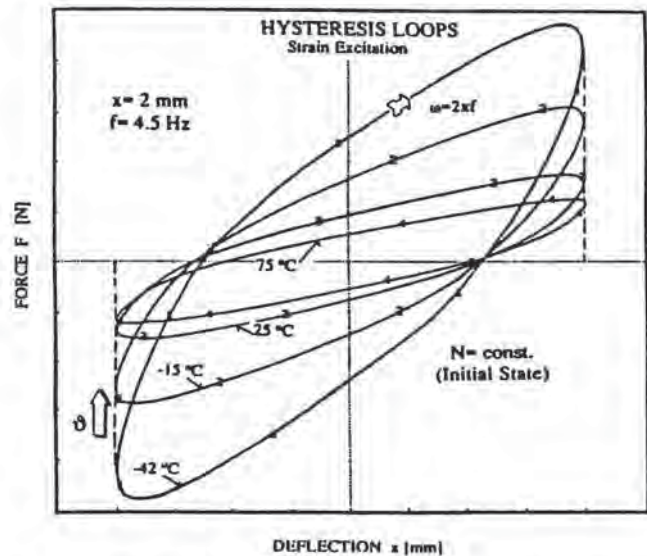


Fig. 34 Damper characteristics as a function of ambient temperature

In this context, the self-heating effect on damper characteristics during the run-up time is of importance. These effects have been thoroughly investigated through experiments during the recent years. The results show that the materials used today, even at very low temperatures show a rapid softening due to the selfheating effect, requiring only a very small number of cycles during rotor run-up.

As an example, a complete coupled thermo-viscoelastic analysis of the internal temperature field inside a damper with metal shims is presented in Figure 35. The picture shows the local temperature concentrations through internal heat buildup for a maximum amplitude case, as analyzed by FEM. The silicon rubber material can well accommodate the temperature levels shown here. The cooling effect of the two metal shims can clearly be seen. The peak temperature inside the damper would be significantly higher without the metal shims.

At 50 J16 Temperature (K)

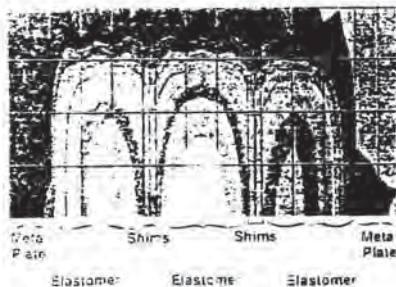


Fig. 35 Calculated temperature distribution inside an elastomeric damper (max. amplitude case)

Analytical Modelling: Due to the particular non-linear behaviour of elastomeric materials, the requirements for the analytical formulation and the procedures in the design process have changed. Pure mechanical damping can no more be treated as a simple linear term, and chordwise stiffness is no longer a constant parameter. It is important to consider that these values are depending on the operational conditions such as lead-lag amplitude, frequency and ambient temperature, for example. Hence, non-classical effects of this nature have to be incorporated into the dynamic modelling of a bearingless rotor.

Figure 36 shows a simplified steady-state model for the prediction of the modal characteristics and the aeroelastic stability behaviour, including a specific model for the elastomeric damper. The non-linear system is solved in a stepwise manner.

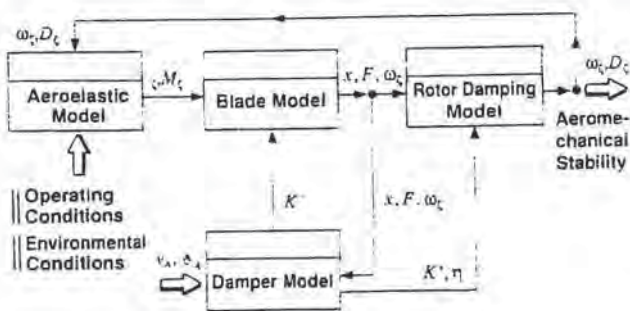


Fig. 36 Non-linear dynamics modelling

Achievements to Date and Prospects

The bearingless-rotor development efforts to date have reached a status, where a critical assessment of the achievements can be made and where future perspectives should be given.

Aeromechanical Stability Developed

Aeromechanical stability of the ground and air resonance type - a major concern in the early design - can be considered to be sufficiently developed today, as can be seen from the damping levels achieved in the various testings (References 14, 39). Inplane damping typically lies in the order of 3 to 4 percent (Figure 37). Quite obviously, the stabilizing effects of coupling parameters are understood, although other design requirements do not always allow the application of the optimum choice.

The technology of elastomeric dampers, most commonly used on the BMR-designs today, has also rapidly developed in the past decade and the understanding of the main material characteristics has strongly improved. Although, some questions have still to be finally answered to master this technology. Further work has to be done in the improvement of life-time, definition of replacement criteria, unsymmetric operations and failure analysis, for example.

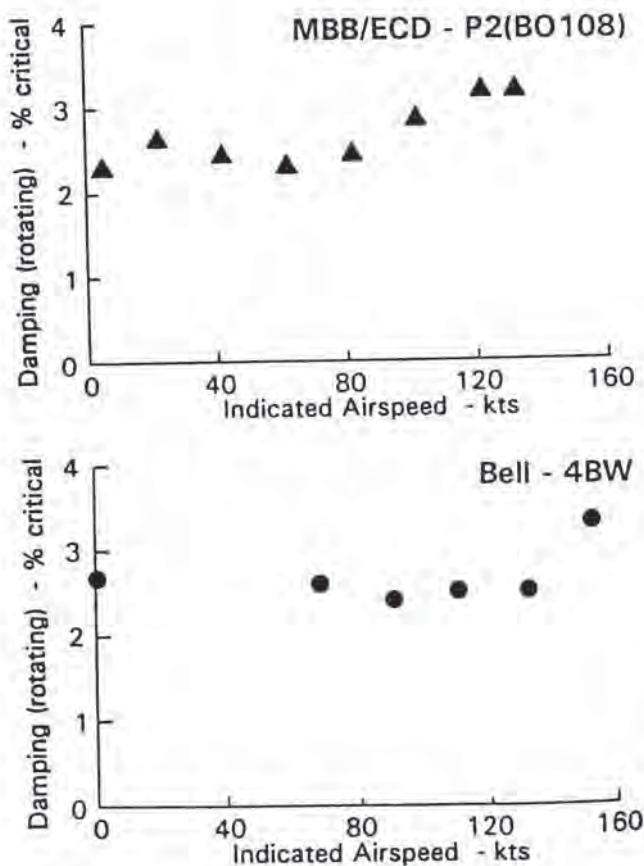


Fig. 37 Typical rotor lead-lag damping levels in flight

From the technological standpoint, the question is sometimes raised, whether such elements could even be completely dispensed in future BMR-designs. From the today's view, a complete elimination looks not likely, but any efforts should be made to minimize the damper size and the required operating amplitudes, in order to increase life-time.

Good Ride Qualities

As discussed, handling qualities and vibrations depend mainly on the hub-moment stiffness, and are not directly characteristic for the type of hub design itself. Nevertheless, the experiences gained from the handling qualities evaluations of past BMR's flight testing is in all cases very positive: The Bell 222 with a low (2.5...4 percent) hinge-offset Model 680 BMR showed significant improvements in the piloting efforts; the measured 4/rev-vibrations, particularly with the LIVE-units installed, were very low (Figure 38).

Beneficial handling qualities and vibrations were also confirmed by the BO 108 BMR prototype testing. The bearingless rotor with 9 percent hinge-offset provided the aircraft very pleasant control response, improved stability characteristics, and very good ride quality, in general. With a passive anti-resonance vibration system (ARIS) installed, the vibration levels were also highly satisfactory, with 4/rev-levels well below 0.1 g over the whole flight envelope, at all seats and in all axes (Figure 38).

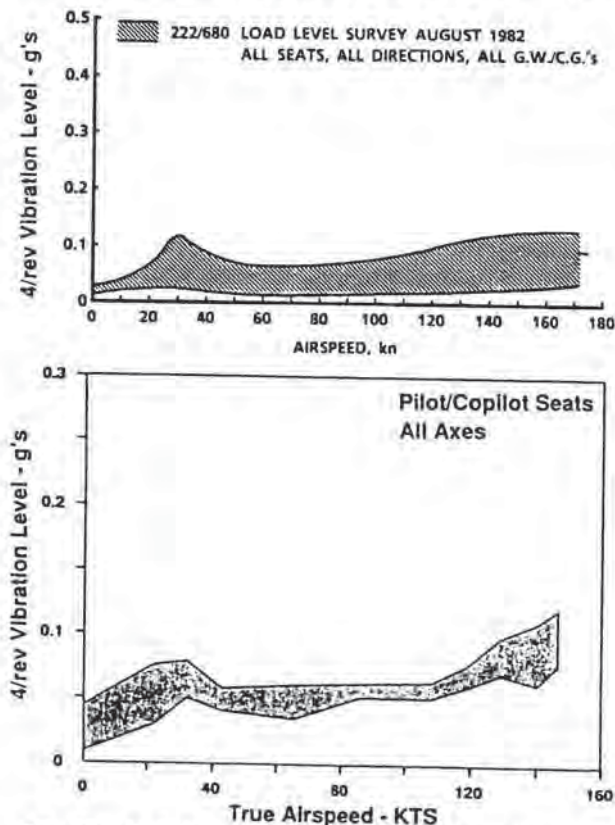


Fig. 38 Fuselage vibrations on BMR-aircraft (Top: Bell 222/680; Bottom: MBB BO108/BMR)

Low Weight

Simplicity and its favourable implications for rotor system weight is one major goal in BMR design. Although the data weight available is not enough to provide a reliable basis for such comparison, a rough assessment of the current informations should be of interest (Figure 39).

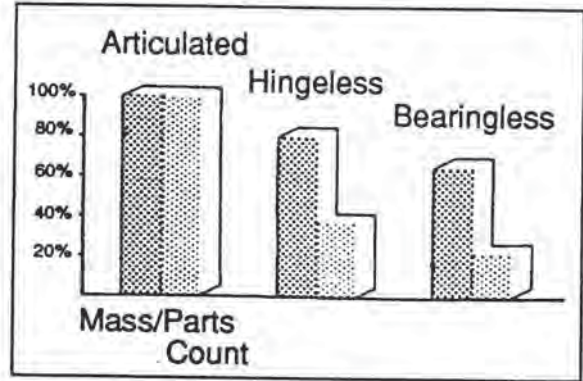


Fig. 39 Relative rotor weight and complexity

Boeing Vertol, on the basis of its experimental design, gave an early estimate for a production BMR, which would be 22 percent lighter when compared to the BO 105 hingeless rotor. Aerospatiale's Triflex hub was reported to be 48 percent lower in weight than the corresponding standard SA 341 Gazelle hub. This would compare to a weight saving of roughly 20 percent on the complete rotor. Bell, from the experience with its Model 680 rotor with 412 type of blades, shows a 9 percent lighter hub weight, which would increase to 15 to 20 percent saving with new blade designs. MBB/ECD's experience shows savings in rotor system weight of 40 kg (18 percent) on its first BMR-prototype, and of 50 kg (22 percent) in the BO-108-BMR design, when compared to the BO 105 hingeless rotor.

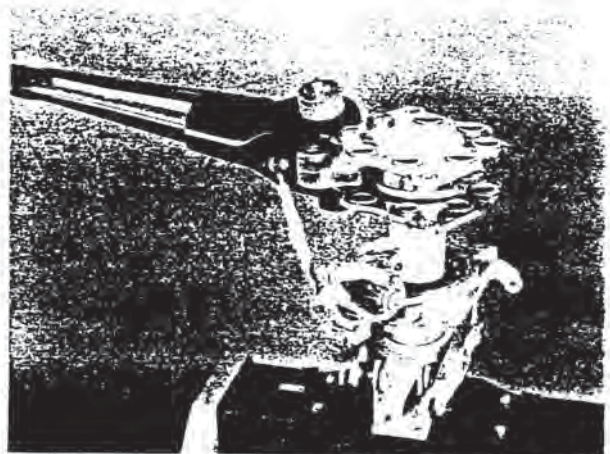


Fig. 40 Simplicity of BO108 BMR design

The reasons for the substantial weight savings are the simplification of the hub design and the intensive use of composite materials, as is evident from the BMR hardware shown in Figure 40. The composite material systems used in the design of modern bearingless rotors (hubs and blades) account for around 60 percent of the total materials used, as compared to only 12 percent for older articulated or 35 percent for hingeless rotors.

Lower Manufacturing Efforts

In examining progress in this field, parts count is a quite descriptive parameter. A high parts count is generally typical of older conventional designs, in which a system of hinges and bearings is applied on the hub. Again, based on the small data base of bearingless rotor designs, the reductions in parts count range from 50 percent (Bell) up to about 85 percent (Aerospatiale), compared to older articulated designs. In comparison to more modern designs (like hingeless rotors), the reduction is in the range of 40 percent (MBB/ECD), Figure 39.

Improved Reliability and Maintenance

The relevant drivers with respect to maintenance efforts and operating costs of conventional designs are wearing parts as bearings and joints and all life-time critical components. The progress in the new technology design stems from the fact that these parts are replaced through composites which allow for unlimited fatigue-life and show pronounced damage tolerance features inherent to their fibrous nature. Similarly, mechanical degradation in the elastomeric part shows also typical damage tolerant behaviour.

An evaluation of the fatigue characteristics indicates that, with careful design, life in excess of 10,000 hours is achievable in the composite parts. The numbers for elastomeric dampers are projected today to at least 2500 hours. These data are unquestionably a big step forward towards full on-condition replacement.

Application to New Products

It is the result of the past 10 to 15 years' research and experimental work that bearingless rotor systems are suitable for production rotors today. Recognizing the requirements for advanced components, three major new-generation civil and military projects have selected the all composite BMR system as their prime lifting device (Figure 41): The ECD BO108 (flying since 1988), the MDHC Explorer (due to fly mid 1992), and the Boeing Sikorsky Comanche (first flight scheduled for 1995). Bell did not specify to what extent its Model 680 or 4BW technology will go into production for its new products.

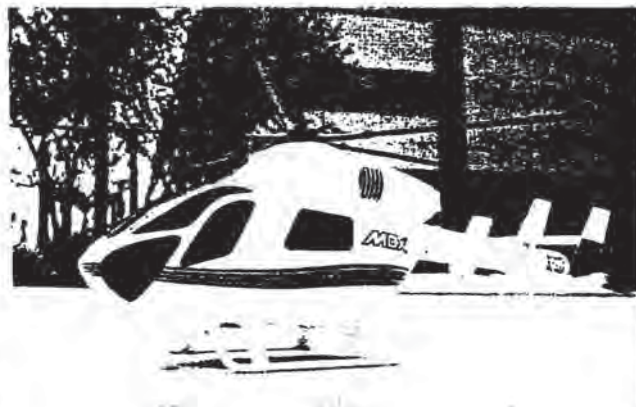


Fig. 41 ECD BO108, MDHC Explorer and Boeing Sikorsky Comanche using composite BMR systems

The expectations of the manufacturers are to take full advantage of the simplified design, the improved flight efficiency, the increased reliability and low weight, which are enabled through the introduction of the bearingless main rotor concept.

A Look to the Future

Despite all the progress made during the past decade, it can be imagined that aeromechanics and composite structural technology will not slow down in the future. Scientists and rotor design engineers will continue in thinking and creating new ideas how to make rotors better again. There are two innovative technologies coming up to date, and these are the HHC/IBC technology and, probably even more promising, the smart materials/structures technology. Currently, there are many research and experimental efforts running, to work out the fundamental technologies and to check the proof of concepts (Reference 40, 41 for example).

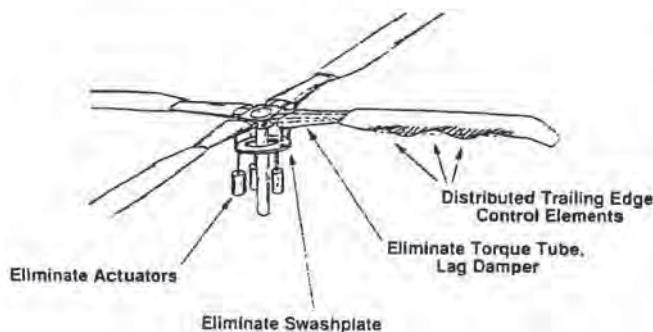


Fig. 42 "Ideal" concept possibilities

How "ideal" rotor concept possibilities could look like in the future, is shown in Figure 42, taken from Reference 42. The technology assessment indicates, that some of the required disciplines are ready today and some of them have still to be pushed forward. In this context, the aeroelastic and structural technology, worked out during the bearingless-rotor technology development, unquestionably, is an excellent basis for a full integration of smart material "actuators" within an "Intelligent Rotor".

Conclusions

There has been substantial progress in the design and development of bearingless main rotor concepts in the past decade. Nearly all of the helicopter manufacturers have worked, among other rotor systems, toward the development of bearingless-rotors, with different design approaches and with different success.

The most common bearingless-rotor configuration today involves a flexbeam with an inboard flap flexure, plus an external pitch cuff, supported by a snubber/damper at the root for the control of the pitch/bending coupling and augmentation of the structural damping. The main secrets lie in the proper design of the flexible element, and of the

damping elements. They have to accommodate the flexible blade bending and pitch-control motions, and to provide the required in-plane damping.

The successful development of such components requires an interactive approach: Material properties, load and modal analyses, kinematic/elastic coupling effects and non-linear elastomeric properties must be interactively optimized to assure proper stress distributions, adequate frequency and damping characteristics, and general structural integrity. The extensive and often non-linear finite elements analyses required within this process are available today, and most of the complex influences are understood today. Although, some questions have still to be finally answered, to fully master this technology.

A review of the recent accomplishments indicates that the aeromechanical stability of the soft-in-plane design is developed, and it is evident, that the realized concepts provide excellent flying characteristics and low vibration levels. These advantages are achieved with simplified hub designs and through a rigorous usage of composite materials, which lead to a substantial saving of weight, lower manufacturing efforts, improved reliability and reductions in maintenance.

Three new helicopter projects have selected the bearingless-rotor technology as their prime lifting device: The BO108, the Explorer and the Comanche. They are in different stages of development.

It can be imagined that aeromechanics and composite structures technology will continue to develop. New technologies are on the horizon today, which, together with the existing bearingless technology base, could lead to the "Intelligent Rotor" within the next decade.

References

1. Fenaughty, R.R., and Noehren, W.L., "Composite Bearingless Tail Rotor for UTTAS", *Journal of American Helicopter Society*, Vol. 22, No. 3, July 1977
2. Shaw, J., Jr., and Edwards, W.T., "The YUH-61A Tail Rotor: Development of a Stiff-Inplane Bearingless Flexstrap Design", *Journal of American Helicopter Society*, Vol. 23, No. 2, April 1978
3. Banerjee, D., Head, R.E., Marthe, R. and Ploudre, M., "The YAH-64A Composite Flexbeam Tail Rotor", *AHS-Specialists Meeting on Rotor Design*, Philadelphia, Oct. 1980
4. Blachere, C., and D'Ambra, F., "Tail Rotor Studies for Satisfactory Performance, Strength, and Dynamic Behaviour", *Vertica*, Vol. 6, No. 4, 1982

5. Huber, H., Klöppel, V. and Enenkl, B., "Development of Bearingless Tail Rotors", RAE's and AHS Helicopter Yaw Control Concepts Conference, London, February 1990
6. Donham, R.E., Cardinale, S.V., and Sachs, I.B., "Ground and Air Resonance Characteristics of a Soft Inplane Rigid Rotor System", Journal American Helicopter Society, Vol. 14, No. 4, Oct. 1969
7. Staley, J.A., Gabel, R., and Mac Donald, H.J., "Full Scale Ground and Air Resonance Testing of the Army-Boeing Vertol Bearingless Main Rotor", American Helicopter Society 35th Annual National Forum, Washington D.C. May 1979
8. Dixon, P.G.C. and Bishop, H.E., "The Bearingless Main Rotor", Journal American Helicopter Society, Vol. 25, No.3, 1980
9. Mouille, R., "Design Philosophy for Helicopter Rotor Heads", Second European Rotorcraft and Powered-Lift Aircraft Forum, Bückeberg, Germany, September 1976
10. Cassier, A., "Development of the Triflex Rotor Head", Fifth European Rotorcraft and Powered-Lift Aircraft Forum, Amsterdam, September 1979
11. Metzger, R., "Smooth and Simple: The Bell Model 680 Bearingless Main Rotor", Vertiflite, Vol. 29, No. 4, May-June 1983
12. Weller, W.H., "Correlation and Evaluation of Inplane Stability Characteristics for an Advanced Bearingless Main Rotor Model", NASA CR-166448, May 1983
13. Alsmiller, G., Metzger, R., and Sonneborn, W., "All-Composite Rotorcraft", American Helicopter Society, 39th Annual Forum, St. Louis, May 1983
14. Harse, J.H., "The Four-Bladed Main Rotor System for the AH-1W Helicopter", American Helicopter Society, 45th Annual National Forum, Boston, May 1989
15. Banerjee, D. and Silverthorn, L.J., "Dynamic Considerations in the Design and Flight Test of an Advanced Bearingless Rotor System", American Helicopter Society, 45th Annual National Forum, Boston, May 1989
16. Head, R.E., Alexander, J.V., and Hughes, C.W., "Design of the McDonnell Douglas Helicopter Company Advanced Composite Rotor System", American Helicopter Society, 42nd Annual National Forum, Washington D.C., 1986
17. Fradenburgh, E.A. and Dr. Carlson, R.G., "The Sikorsky Dynaflex Rotor -an Advanced Main Rotor System for the 1990's", American Helicopter Society, 40th Annual Forum, Arlington, Virginia, May 1984
18. Blackwell, R.H., "Dynamics Considerations in the Design of the Comanche Helicopter", Fourth Workshop on Dynamics and Aeroelastic Stability Modeling of Rotorcraft Systems", University of Maryland, Washington, November 1991
19. Huber, H., "Gelenk- und Lagerloser Hauptrotor in Faserverbundbauweise für dynamische Systeme zukünftiger Hubschrauber", 3. BMFT Status Seminar Luftfahrtforschung und -technologie, Hamburg, May 1983
20. Seitz, G. and Singer, G., "Structural and Dynamic Tailoring of Hingeless/Bearingless Rotors", Ninth European Rotorcraft Forum, Stresa 1983
21. Klöppel, V., Kampa, K., Isselhorst, B., "Aero-mechanical Aspects in the Design of Hingeless/Bearingless Rotor Systems", American Helicopter Society, 40th Annual National Forum, Washington 1984
22. Strehow, H., Frommlet, H., "Entwicklung Neuartiger Lagerloser Rotorsystem", 4. BMFT-Statusseminar Luftfahrtforschung und Luftfahrttechnologie, München, April 1986
23. Huber, H., "BO108 Development Status and Prospects", 16th European Rotorcraft Forum, Glasgow, September 1990
24. Juggins, P.T.W., "Substantiation of the Analytical Prediction of Ground and Air Resonance Stability of a Bearingless Rotor, Using Model Scale Tests", 12th European Rotorcraft Forum, Garmisch-Partenkirchen, Sept. 1986
25. Harse, James H., "Integrated Technology Rotor/Flight Research Rotor (ITR/FRR) Concept Definition", NASA CR 166443, 1983
26. Dixon, Peter G.C., "Integrated Technology Rotor/Flight Research Rotor Hub Concept Definition", NASA CR 166447, 1983
27. Hughes, Charles W., "Integrated Technology Rotor/Flight Research Rotor (ITR/FRR) Concept Definition Study", NASA CR 16444, 1983
28. Howes, H.E. and Tomashofski, C.A., "Integrated Technology Rotor/Flight Research Rotor (ITR/FRR) Concept Definition", NASA CR 166445, 1983
29. Carlson, Raymond G., Beno, Edward A., and Ullisnik, Harold D., "Integrated Technology Rotor/Flight Research Rotor (ITR/FRR) Concept Definition Study", NASA CR 166446, 1983

30. Bousman, W.G., Ormiston, R.A., and Mirick, P.H., "Design Considerations for Bearingless Rotor Hubs", American Helicopter Society 39th Annual National Forum, St. Louis, May 1983
31. Reichert, G. and Oelker, P., "Handling Qualities with the Bölkow Rigid Rotor System", American Helicopter Society 24th Annual National Forum, Washington D.C., May 1968
32. Huber, H., "Parametric Trends & Optimization - Preliminary Selection of Configuration - Prototype Design and Manufacture", AGARD-LS-63, 1973
33. Hohenemser, K.H., "Hingeless Rotorcraft Flight Dynamics", AGARDograph No. 197, September 1974
34. Johnson, W., "Recent Developments in the Dynamics of Advanced Rotor Systems", AGARD-LS-139, 1985
35. Ormiston, R.A. and Hodges, D.H., "Linear Flap-Lag Dynamics on Hingeless Helicopter Rotor in Hover", Journal of the American Helicopter Society, Vol. 17, No. 2, 1972
36. Huber, H.B., "Effect of Torsion-Flap-Lag Coupling on Hingeless Rotor Stability", American Helicopter Society 29th Annual National Forum, Washington, May 1973
37. Jang, J. and Chopra, I., "Ground and Air Resonance of an Advanced Bearingless Rotor in Hover", Journal of the American Helicopter Society, Vol. 33, NO. 3, July 1988
38. Hausmann, G. and Gergely, P., "Approximate Methods for Thermoviscoelastic Characterization and Analysis of Elastomeric Lead-Lag Dampers", Eighteenth European Rotorcraft Forum, Avignon, 1992
39. Schimke, D., Enenkl, B. and Allramseder E., "MBB BO108 Helicopter Ground and Flight Test Evaluation", Fifteenth European Rotorcraft Forum, Amsterdam, Sept. 1989
40. Hanagud, S., Babu, G.L.N., Won, C.C. and Obal, M.B., "Smart Structures for Helicopters", Sixteenth European Rotorcraft Forum, Glasgow, September 1990
41. Chen, P.C., Samak, D.K. and Chopra, I., "Development of an Intelligent Rotor", Fourth Workshop on Dynamics and Aeroelastic Stability Modeling of Rotorcraft Systems", University of Maryland, Washington, November 1991
42. Ormiston, R.A., "Can Smart Materials Make Helicopters Better?", Fourth Workshop on Dynamics and Aeroelastic Stability Modeling of Rotorcraft Systems", University of Maryland, Washington, November 1991




Alfred Gessow Rotorcraft Center
UNIVERSITY OF MARYLAND



**Alfred Gessow Rotorcraft Center:
Past, Present and Future**

Inderjit Chopra
*Director Alfred Gessow Rotorcraft Center &
Alfred Gessow Professor of Aerospace Engineering*

Presentation At: Korea Aerospace Research Institute (KARI), Daejeon
June 27-30, 2011




Agenda

- Monday June 27**
Introduction: Alfred Gessow Rotorcraft Center
Dynamics: Introduction to Hover & Forward Flight, Flap Dynamics
- Tuesday June 28**
Dynamics: Flap-Lag-Torsion, Unsteady Aerodynamics
MAV Challenges & Opportunities
- Wednesday June 29**
Dynamics: Aeroelastic Stability in Hover, Ground/Air Resonance
CFD Applications
- Thursday June 30**
Dynamics: Bearingless Rotor, Vibration
Review Aeromechanics
- Friday July 1: Visit to SNU & Review Cyclocopter Work**

**Department of Aerospace
Engineering**
in
A. James Clark School of Engineering
University of Maryland





Undergraduate Program

- 19 Faculty members
- 337 undergraduates
- Average SAT score 1316
- 16% female
- 92 BS degrees in 2009
- Ranked 6th by US News and World Report



Graduate Program

- Graduate students 170
- MS Students 78
- PhD Students 92
- Female Grad students 29
- Minority Grad students 13
- Non-US Citizens 54
- 69 MS awarded in 2009
- 19 PhD awarded in 2009
- Ranked 9th by US News and World Report

**Department of Aerospace Engineering
Vital Statistics 2009-10**

- 8 Major Research Program (Lead)
 - VLRCOE: Army/Navy/NASA (2011-16) Vertical Lift Research Center of Excellence
 - MURI: ONR (2006-11): Galfenol Smart Material Actuators
 - MURI: AFOSR (2008-13): Helicopter Brownout
 - CTA-MAST: ARL (2008-18): Micromechanics Center
 - NAVAIR: Rotorcraft & Propulsion + Education: (2009-14)
 - CUIP: Constellation University Institute Program; (2002-cont)
 - Space: Institute for Dexterous Space Robotics
 - Neuro-Bio Program: AFOSR (2009-14): Flying insect Performance
- Major Research Programs (Support Role)
 - MURI: AFOSR (2007-12) Flapping MAV
 - MURI: ONR (2010-15) Micro Biological Systems

• Research Grants FY09:	
Total number of grants	84
Total research expenses	\$17.3M

Alfred Gessow Rotorcraft Center

Mission of Rotorcraft Center


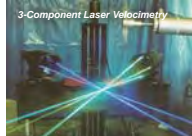
To advance rotorcraft technology through:

- Provide an exciting and effective educational environment to train the next generation rotorcraft engineers
- Carry out inter-disciplinary, multi-disciplinary basic research in rotorcraft
 - Timely solution of technical barrier problems
 - Introduce innovative and disruptive technologies
- Speedily transfer technology to industry and government laboratories



Alfred Gessow Rotorcraft Center Vital Statistics 2010

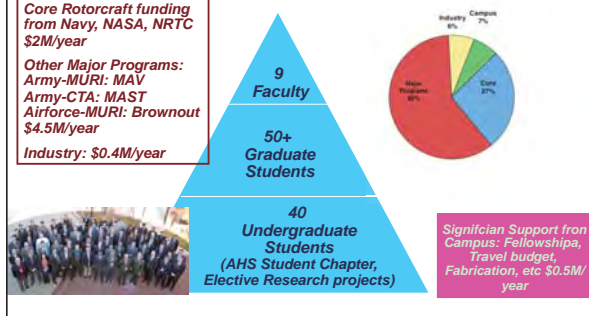
• Faculty: Rotorcraft	9
• Faculty: Non-Rotorcraft	5
• Research Scientists/ Visiting Prof.	4
• Graduate Students	50
• M.S. Degrees awarded	10
• Ph. D. Degrees awarded	5
• Presentations at Conferences AHS (28), SDM (10), SPIE(12), Other (30) 2008 AHS Forum	80 16
• Journal Publications: Published	40
• Journal Publications: Accepted	49
• 2011 Vertical Flight Scholarships	10

Rotorcraft Tech Base

Core Rotorcraft funding from Navy, NASA, NRTC \$2M/year

Other Major Programs:
 Army-MURI: MAV
 Army-CTA: MAST
 Airforce-MURI: Brownout \$4.5M/year
 Industry: \$0.4M/year

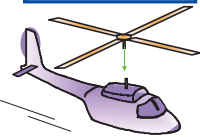


Significan Support from Campus: Fellowships, Travel budget, Fabrication, etc \$0.5M/year

Alfred Gessow Rotorcraft Center Overall Accomplishments

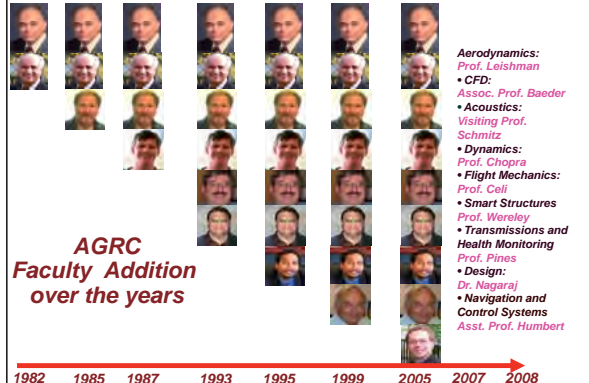
• M.S. Degrees awarded	200+
• Ph.D. Degrees awarded	100+
• Presentations at Conferences (All) AHS Forum	800+ 200+
• Journal Publications (All) AHS Journal	500+ 130
• VFF Scholarships (last 5 years)	45

Established in 1982 by Army as one of three Rotorcraft Centers of Excellence; Competitive renewal every 5 years; Program ended in June 2006



- Significant technology transfer
- Developed specialized graduate courses & unique experimental facilities
- Graduates employed by Army Labs, Industry, NASA, Navy, FAA, Academia and Army-Uniform

AGRC Faculty Addition over the years



Aerodynamics: Prof. Leishman
CFD: Assoc. Prof. Baeder
Acoustics: Visiting Prof. Schmitz
Dynamics: Prof. Chopra
Flight Mechanics: Prof. Celli
Smart Structures: Prof. Woreley
Transmissions and Health Monitoring: Prof. Pines
Design: Dr. Nagaraj
Navigation and Control Systems: Asst. Prof. Humbert

Rotorcraft Courses

Graduate:

- Rotorcraft Aerodynamics 1 & 2 (Leishman)
- Rotorcraft Dynamics (Chopra)
- Rotorcraft Stability and Control (Celi)
- Rotorcraft Design (Chopra, Nagaraj, Tishchenko)
- CFD 1 & 2 (Baeder)
- Composite Structures (Wereley)
- Engineering Optimization (Celi)
- Smart Structures (Chopra)
- Rotorcraft Aeroacoustics (Schmitz)
- Advanced Structural Dynamics (Pines, Hubbard)
- Multi-Body Dynamics (Celi)


Undergraduate:

- Rotorcraft Analysis (Baeder)






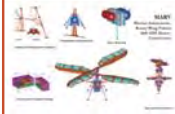
UM Winning Designs (98-02)




1998




1999



2000




2001




2002


UM Winning Designs (03-07)




2003




2004



2005




2006




2007

UM Winning Designs (08-09)



2008



2009

Rotorcraft Experimental Facilities



Rotor Rig & Glenn L. Martin Wind Tunnel



Hover Tower



Vacuum Chamber



Autoclave for Composites

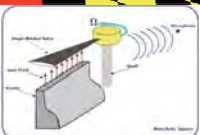


Laser Doppler Velocimetry




Bearingless Rotor Rig


Rotorcraft Experimental Facilities




Aeroacoustic Facility




6 ft Mach Scaled Rotor




Model Rotor Hub



Vacuum Hot Press




MTS Testing Machine

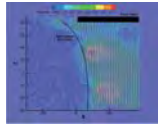


Mechanical Shock Rig


Rotorcraft Experimental Facilities




Open-Jet Wind Tunnel




PIV System for flow studies




MAV System



Autonomous Lab



Insect-Motion-Based Flapping-Wing Apparatus



MAV Hover Test Rig

Alfred Gessow Rotorcraft Center Research Programs

I. Core Aeromechanics (RCOE: 1982- 2006, VLRCOE 2011-16)

- Aerodynamics
- Dynamics
- Flight Dynamics and Control
- CFD
- Acoustics
- Transmission and Drive Trains
- Smart and Composite Structures
- Advanced Designs including Heavy Lift Rotorcraft

II. Army: MURI: Micro Hovering Air Vehicles (2004-10)

III. MAST CTA: Center for Microsystem Mechanics(2008-18)

IV. Airforce: MURI: Brownout of Rotorcraft (2008-13)

V. Smart Structures Programs (URI, 2 MURI, DARPA)

- Army: URI(92-97), MURI (96-01) Smart Structures Applications
- DARPA Galfenol Compact Actuator Development (2003-05)
- Navy-MURI on Galfenol actuators (06-11)

VI. ONR: Heavy Lift Rotorcraft Aeromechanics (2010-12)


VII. NASA: 5 NRAs (2007-11): Rotorcraft Aeromechanics

VIII. NAVAIR: (2008-13): Rotorcraft Aeromechanics

IX. Other Programs (NRTC, Sikorsky, Boeing, etc):

- Boeing: Active Rotor, Morphing Rotor
- NRTC: CFD Applications, High Performance actuators, Crashworthy seat
- Sikorsky/UTRC: Composite Rotor, Swashplateless rotor, etc.

10-Ft Diameter Vacuum Chamber




Notable Technical Capabilities

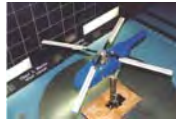
- State-of-Art Experimental facilities:**
Glenn L. Martin wind tunnel (8.5-ftx11-ft), 2 rotor rigs, 10-ft diameter vacuum chamber, hover tower, State-of-art PIV system, anechoic hover chamber, model fabrication facility, modern composite lab, extensive smart structures labs and growing MAV facilities
- Extensive set of specialized up-to-date rotorcraft courses
- Breadth and depth of core rotorcraft programs:**
Expanded activities in MAV, brownout and CFD
- Extensive micro air vehicles research program (MAST-CTA & MURI)
- Opportunity-driven faculty and team-work
- High caliber graduate students (Largest number of Vertiflite scholarships, 40% of total awards during past 10 years)
- Alfred Gessow Rotorcraft Chair & Scholarships
- Significant campus support:**
 - Extensive labs
 - Co-location of grad students

Alfred Gessow Rotorcraft Center: Major Accomplishments & Technology Transfer

- Provided trained talented graduate students to industry and government laboratories
- Provided comprehensive aeromechanics analysis and design tools to industry and laboratories
UMARC, Free-wake and unsteady models, TURNS CFD
- Provided strategic leadership in rotorcraft technologies:
 - Bearingless rotor aeromechanics
 - Composite rotor technology
 - Advanced CFD methodology
 - Smart Structures technology
 - UAV and MAV technologies
 - Rotor wakes and unsteady aerodynamics
 - Vibration prediction & active control methodologies



Smart Structures Activities at Maryland




6-ft dia Froude scale rotor model in Glenn Martin Wind tunnel: active twist with embedded piezoelectric elements



6-ft dia Mach scale rotor model in Glenn Martin Wind tunnel: trailing edge flaps actuated with multi-layered piezobimorphs




6-ft dia Mach scale rotor model on hover tower: tip actuated with embedded piezos in conjunctions with bending-torsion composite couplings



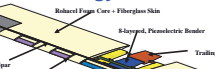
6-ft dia Mach scale rotor model on hover tower: tip actuated with embedded piezos in conjunctions with bending-torsion composite couplings

Example: Technology Transfer

Smart Structures Technology



Smart Actuator Development:
Piezostacks with L-L Amplification



Smart Rotor Development:
Mach-Scale with Piezo Actuated Flap





Diagram labels: Reinforced Edge Core + Fiberglass Skin, Kevlar[®] Piezoelectric Bender, Trailing-Edge Flap, Aluminum Root Insert, Graphite Epoxy Spar (Embed Strength > 300 lbs), Rib Cage, LE edge wings for non-hubbing

Boeing: Full-Scale Smart Rotor Development: MD-900 Rotor with Smart Flaps, Successfully tested in 40x80-ft wind tunnel in April 2008, Demonstrated 90% reduction in vibration and acoustic signatures



Smart Rotor Test in Glenn Martin Tunnel Mach-Scale with Smart Flaps

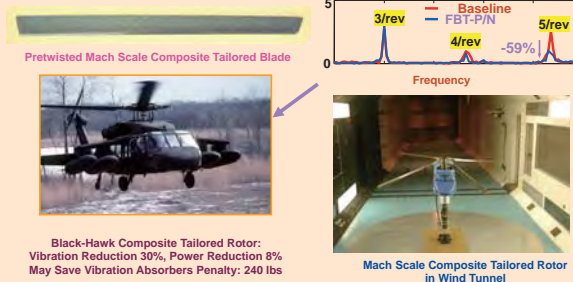
Technology Transfer

- Upgraded comprehensive rotorcraft code UMARC provided to industry, federal laboratories and academia.
- Boeing-Mesa: Helped them in their development of full-scale smart rotor system with flap actuated with piezostacks (Friedrich Straub).
- Unsteady aerodynamic analysis codes (Leishman) provided to industry and federal labs, inserted in many comprehensive codes.
- Free wake codes provided to industry, federal labs and academia, inserted in many comprehensive codes.
- Army-Ames: Assessment of active vibration control from perspective of flight mechanics (Mark Tischler)
- NREL: Helped them in identification of aerodynamic issue focused to windmills (Bir).
- Lord Corp.: Development & characterization of MR dampers (Mark Jolly).
- Sikorsky: Helped them in the assessment of composite couplings to control vibratory load and improve performance (Andy Bernhard)
- Army Science Board: Heavy Lift Cargo Rotorcraft design studies
- DARPA: Technology assessment of heavy lift systems (Don Woodbury)
- Progeny/Army: Helped them in the development of RotorChute (Murphy)

Technology Transfer

- Bell: Quadrotor performance and download studies (Bob Moulins)
- CSA: Helped them in the development of compact hybrid actuator (Eric Anderson)
- Baldwin: Helped in the design and aeromechanics issues related to mono-tiltrotor (Baldwin)
- FAA: Wire strike assessment of civil helicopters (Dy Le)
- Kaman: Helped them in the development of tab actuated flaps for primary controls (Mike Bielefeld)
- Army Picatinny Arsenal: Development of MR recoil dampers (Mike Mattice)
- Army-ARDEC: Helped them in the development of active/passive hybrid APPN smart actuator gun-fuselage vibration isolation and precision control
- Navy David Taylor Carderock: Helping them in their initiative on "Rotor Head Fault Detection" called JAHUM (David Haas).
- NASA-Ames: provided assessment for an all electric helicopter (Bill Warmbrodt)
- Army Science Board: Carried out heavy lift cargo rotorcraft design studies

Composite Rotor Technology



Pretwisted Mach Scale Composite Tailored Blade


Black-Hawk Composite Tailored Rotor:
Vibration Reduction 30%, Power Reduction 8%
May Save Vibration Absorbers Penalty: 240 lbs

Mach Scale Composite Tailored Rotor in Wind Tunnel

Graph showing Frequency vs. Amplitude. Baseline (red) and FBT-P/N (blue) are compared. A 59% reduction is noted at 4rev.

Black Hawk Loads Prediction: Technology Barrier Problem

Black Hawk Airloads at High Speed



Lift 92% R lbs/ft

25 deg Phase error

UMARC lifting-line (dashed green line) vs **UMARC/TURNS coupling** (solid red line)

Flight 8534

Vibratory Lift 92% R

Pitching Mom. 96.5% R

Comprehensive analysis + CFD

- Lift Phase error resolved
- Vibratory air loads resolved
- Transonic pitching moments captured

Unresolved Issues:

- High thrust condition (stall)
- Maneuvering flights

Accomplishments: Technology Barrier Problems (00-11)

- Rotor loads prediction: Resolving phase issue for predicted vs measured loads (Collaboration with NASA, Army & Industry)
- Composite rotor blade modeling: adequate coupled beam modeling, comprehensive aeromechanics analysis and unique vacuum chamber and wind tunnel test data
- Active vibration control (HHC & IBC) coupling with flight control stability (issue with hingeless and bearingless rotors)
- Power minimization with 2/rev active pitch input: expect nominal gain less than 5%
- Smart rotor development: smart actuator stroke limitation and innovative amplification
- Rotor wakes: resolving vortex core issue and its interaction, precise model under steady flight condition
- Rotor wakes in maneuvering flight: Time domain non-steady model and resolving off-axes response issues
- Unsteady aerodynamics of flapping rotor
- CFD couplings with comprehensive aeroelastic analyses: issue of moment coupling
- HUMS for transmissions & drive-trains: Robust ID schemes to overcome false alarms
- Comprehensive aeromechanics analyses for advanced rotor systems: bearingless (multiple load paths), tiltrotor, circulation-control, trailing-flap and smart rotor
- Flight stability and acoustics analysis in maneuvering flight

RCOE Accomplishments: Technology Barrier Problems

Damperless Rotor



Past: Hydraulic Dampers Articulated Rotors, Heavy



Present: Elastomeric Dampers Hingeless & Bearingless, Expensive



Future: ER/MR Fluid Dampers Composite Couplings and IBC Flaps active damping, Cheap and reliable

Swashplateless Rotor



Past: Swashplate with pitchlinks, Drag penalty plus maintenance cost



Present: Servo-Flap Rotor, SH-2, Mach-Scale Black-Hawk Model test in wind tunnel



Future: Smart flaps using hybrid actuators for primary controls.

Major Accomplishments over past 28 years Research

Comprehensive Analysis UMARC

Composite Rotor Analysis and Development

Smart Rotor Development

CFD/CSD Blackhawk Loads Prediction

Bearingless Rotor Analysis

Free Wake Modeling

Free Wake Models
 Bagai-Leishman (Relaxation)
 Bhagwat-Leishman (Time-marching)
 Shreyas-Leishman (Vortex filament)

Alfred Gessow Rotorcraft Center National & International Impact

- **Publications in Archival Journals and Presentation at Helicopter Conferences: Especially AHS**
- **Graduates: Extremely successful in academia, industry and federal laboratories, For example at recent American Helicopter Society Annual Forum, every fourth paper was from or had roots in Maryland.**
- **Significant technology transfer to industry and government via publications and presentations, trained graduates and comprehensive codes and cooperative arrangements.**

Major Accomplishments over past 28 years Education

Comprehensive Graduate Curriculum

Quality of graduate students

- Placement & success
- Largest number of Vertiflite Scholars
- 7 received AHS Bagnoud Awards
- 4 became Technical Fellows of AHS
- 800+ Conference papers
- 200+ AHS Forum papers
- 500+ Journal papers
- 130 AHS Journal papers
- 19 took academic appointments
- Many now in high level positions

Balanced research: between theory and experiment

AGRC: Graduates in Rotorcraft Industry

<p>Sikorsky</p> <ol style="list-style-type: none"> 1. David Matuska (MS, 83) 2. John Bate (MS 86) 3. Chris Van Buren (BS 86) 4. Mark Scott (MS 88) 5. Mike Torok (PhD 89) 6. James Wang (PhD 91) 7. Ashish Bagai (PhD 95) 8. Vinit Suharsabudhe (PhD 97) 9. Alan Coyne (MS 97) 10. Cliff Smith (PhD 99) 11. Andy Bernhard (PhD 00) 12. Dan Griffin (MS 01) 13. Mat Tarascio (MS 01) 14. Jinsong Bao (PhD 04) 15. Robin Preator (MS 04) 16. Ben Hein (MS 05) 17. Eric Parsons (MS 05) 18. Michael Brigley (MS 06) 19. Jayant Sirohi (PhD 01) 20. Lin Leo (PhD 03) 	<p>Boeing</p> <ol style="list-style-type: none"> 1. Brahamananda Panda (PhD 85) 2. Hieu Ngo (MS 87) 3. Alan Stemple (PhD 89) 4. Antonio Llanos (MS 89) 5. Dan Newman (MS 89) 6. Steven Ingle (MS 90) 7. Curtis Waiz (MS 94) 8. M. Daghir (MS 94) 9. Joseph Orso (MS 94) 10. Josh Ellison (MS 04) 11. Justin Koarns (MS 05) 12. Dan Clingman (MS 06) 13. Lynn Gravatt (MS 06) 14. Patrick Downey (PhD 08) <p>Bell</p> <ol style="list-style-type: none"> 1. Brian Schweissow (MS 85) 2. Bob idol (BS 85) 3. D. K. Samak (MS 87) 4. David Platz (MS 94) 5. Melanie Hurt (MS 96) 6. J. S. Park (MS 03) 7. Chehab Mustafa (MS 03) 8. Taech Lee (PhD 99) 9. Marc Gervais (PhD 04)
---	---

AGRC: Graduates in NASA/Army/Navy

<p>Ames: NASA/Army</p> <ol style="list-style-type: none"> 1. Bimal Aponso (MS 83) 2. Joon Lim (PhD 88) 3. Hyensoo Yeo (PhD 99) 4. Theodore Colin (PhD 00) 5. Mahindra Bhagwat (PhD 01) 6. Preston Martin (PhD 01) 7. Randy Cheng (PhD 01) 8. Anubhav Datta (PhD 04) 9. Mani Ramasami (PhD 05) 10. Carlo Malpica (PhD 08) 	<p>Navy: David Taylor/Pax River</p> <ol style="list-style-type: none"> 1. David Haas (PhD 89) 2. Neipei Bi (PhD 91) 3. Judah Milgram (Ph 97) 4. Mark Kammeyer (MS 86) 5. John Vorwald (MS 86) 6. Randy Barber (MS 86) 7. Steve Wunder (MS 88) 8. William Pogue (MS 89) 9. Chris Bruner (MS 89) 10. Joe Leifner (MS 89) 11. Darryl Lenhardt (MS 89) 12. Nancy Mueller (MS 89) 13. Steve Dirlik (MS 90) 14. Jody Smith (MS 92) 15. Andy Baker (MS 95) 16. Divyang Shukla (MS 00) 17. William Facey (MS 03) 18. Youngjoon Kim (MS 04) 19. Daniel Everson (MS 05) 20. Eric Silberg (MS 06) 21. Kristi Kleinhesselink (MS 07) 22. Sean Roark (MS 07)
---	--

Langley: Army

1. Mark Nixon (PhD 93)
2. Kevin Noonan (MS 85)
3. Jinwei Shen (PhD 03)
4. Jayana Sitaraman (PhD 03)
5. Beatrice Roget (PhD 04)
6. Ugrina Sandra (PhD 06)
7. Terry Ghee (MS 90)
8. Eric Greenwood (MS 08)
9. Rajneesh Singh (PhD 98)

UM Graduates in Academics: Faculty

1. Ed Smith (PhD 92) Professor Penn State
2. Farhan Gandhi (PhD 95) Professor, Penn State
3. Nihkil Koratkar (PhD 00) Professor, RPI
4. Chang-Ho Hong (PhD 85) Professor Choong-Nam University
5. James Milke (PhD 91) Professor, University of Maryland
6. Yong Hyup Kim (PhD 89) Professor, Seoul National University
7. Gil Crouse (PhD 92) Associate Professor, Auburn University
8. Ranjan Ganguli (PhD 94) Professor, IISc Bangalore
9. Anne Spence (PhD 94) Assistant Professor, UMBC
10. David Flemming (PhD 95) Professor, Florida Institute of Tech
11. Yang Mao (PhD 02) Associate Professor, Northwest University, China
12. Z. Xie (PhD 03) Associate Professor, Northwest University, China
13. Karthik Duraisamy (PhD 05) Lecturer, Glasgow University
14. Jayant Sirohi (PhD 01) Asst. Professor, University of Texas at Austin
15. Beatrice Roget (PhD 03) Asst. Professor, Wyoming University
16. Jaina Sitaraman (PhD 02) Asst. Professor, Wyoming University
17. Atul Atulsimha (PhD 06) Asst. Professor, Virginia Commonwealth University
18. Gang Wang (PhD, 02) Asst. Professor, University of Huntsville

Alfred Gessow Rotorcraft Center Important Honors & Awards

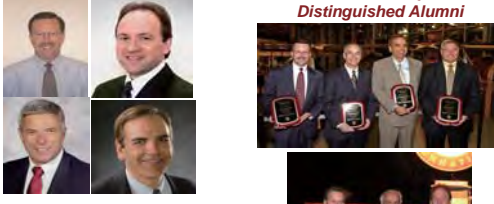
- **Chaired Professorships:** Alfred Gessow Professor (Chopra), Minta-Martin Professor (Leishman), Farvardin Professor (Pines), Techno-Sciences Professor (Wereley)
- **AHS Hon Fellow:** Gessow (81), Chopra(88); **AHS Fellows:** Schmitz(93), Chopra (96), Leishman (07)
- **AHS Alexander Nikolsky Honorary Lectureship:** Gessow (85), Schmitz (08)
- **AIAA Fellows:** Gessow (82), Chopra (91), Schmitz (04), Pines (10)
- **Royal Aero Soc Fellow:** Leishman (05); **ASME Fellow:** Chopra (03), Wereley (08), Flatau (07), Pines (09)
- **AIAA SDM Award:** Chopra(02)
- **AHS Alexander Klemm Award:** Life-time Achievement Award in rotorcraft: Gessow(96), Chopra (09)
- **ASME Adaptive Structure and Material Systems Prize:** Chopra (01)
- **SPIE Life-Time Achievement Award:** Chopra (04), Flatau (10)
- **Francois Xavier Bagnoud Vertical Flight Award:** In recognition of outstanding contributions to rotorcraft by a young engineer: Smith (94), Torok (96), Gandhi (98), Bernhard (99), Koratkar (04), Sohasrabudhe (05), Datta (06)
- **Grover E. Bell Award:** Given for outstanding research contributions to AGRC: 1992, 2002
- **ARO Young Investigator Awards** (Smith, Wereley, Koratkar)
- **NSF Young Investigator Awards** (Pines, Wereley, Etkins, Koratkar)
- **Other Important Lectureships:** Pilcher Memorial Lectureship & Medal (02), von Karman Lectureship (04), Cierva Memorial Lectureship (05), AGARD Lectureship (91), Blesplinghof-Mar-Plan (93), Paul Hamke Lectureship (04), Henry Kelley Lecture (03), Roy Aero Aus(01), AIAA SDM Lecture (03), ASME Adaptive Structures Lecture (2001)
- **Editor-in-Chief:** AHS Journal, Leishman (2004-07)
- **Editor:** Journal Intelligent Materials Systems & Structures (JIMSS): Wereley
- **Associate Editors:** JIMSS (Chopra, Pines, Flatau), Smart Mat & Struc (Chopra, Pines, Wereley), J. of Aircraft (Chopra), AHS Journal (Chopra, Vizzini, Celi, Nagaraj)
- **AHS Lichten Award:** Bernhard (96), Gervais (01)
- **AHS Student Design Competition:** Graduate Category First Place for 9 years (1999-2005, 08), 2nd Place (2006-07, 09)
- **AJ Clark School of Engineering Faculty Outstanding Research Award:** Chopra (2002)

Some RCOE Graduates in Key Positions: Industry, Government and Academia


- COL Keith Robinson, PM, Armed Scout Helicopter
- Dr. Mike Torok, Vice President & Chief Engineer CH-53K, Sikorsky
- Dr. James Wang, Vice President Research & Development, Agusta-Westland
- COL(Ret) Andy Dull, Manager Lockheed Martin
- Dr. Mark Nixon, Director U.S. Army Research Laboratory Vehicle Technology Directorate
- Dr. Ed Smith, Professor, and Director Rotorcraft Center of Excellence at Penn State
- Dr. Jeanette Epps, NASA Astronaut
- Dr. & Col (Ret) Shmuel Fedel, Senior Vice President Maintenance & Engineering, El Al Israel Airline
- Dr. Jinseok Jang, Principal Researcher & Head of Rotorcraft Program, Agency for Defense Development, Korea
- Ms Kelly McCool, Chief Engineer VH-71 (Presidential Helicopter) Program
- Col (Ret) Lazar Alon President & CEO Elbit Systems
- Mr. Chris Van Bulten, Technical Fellow & Director of Technology & Innovation, Sikorsky
- Mr. Simal Aponso, Chief NASA Aerospace Simulation Operations Branch
- Mr. Philippe Benquet, Program & Key Account Director, Thales Avionics, France
- Mr. David Matuska, Manager Engineering System Safety, Sikorsky
- Mr. Mark Scott, Chief Design Group, Sikorsky
- Dr. Andy Bernhard, Chief Engineer SAS, Sikorsky
- Ms. Megan McCluer, Program Manager Wind & Hydropower Technology, DOE
- Dr. David Haas, Head Surface Aviation Group, David Taylor, Navy
- Mr. Dan Newman, Program Manager DARPA, Formerly Head Design Office, Boeing
- Dr. Farhan Gandhi, Professor Penn State
- Dr. Bernd G. van der Wall, Head Simulation in Wind tunnel, DLR
- Mr. Carl Ockler, Head of Civil Flight Test, Eurocopter, Germany
- Mr. Mat Tarascio, Specialist Business Development/Strategic Planning, Sikorsky
- Dr. Chang-Ho Hong, Professor and Department Head Aerospace Engineering, Chooong-Nam National University
- Dr. Nishit Koratkar, Professor Aerospace Engineering, RPI
- Dr. Srinivas Turam, Manager, Elastic Mechanics, Robinson Helicopters

Notable Graduates

2007 Academy of Distinguished Alumni


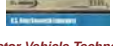









2008 AHS Hon. & Technical Fellows



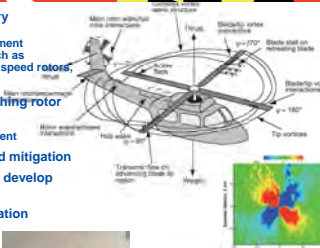



1982 1985 1987 1993 1995 1999 2005 2007

Graduate Students of Alfred Gessow Center National & International Impact

 Director of Penn State Rotorcraft Center of Excellence: Ed Smith	 Director Vehicle Technology Army/ARL Aberdeen: Mark Nixon	 Vice President Sikorsky Aircraft Co. Mike Torok
 Program Director, Thales Avionics: Philippe Benquet	 Senior VP Engineering El Al Col. Ret Fedel Shamuel	 Head of Korea Rotorcraft Program: Jinseok Jang
 Vice President S&T James Wang	 PM Armed Scout, AMCOM Col. Keith Robinson	 NASA Astronaut Jeanette Epps

Rotorcraft Aeromechanics: Future Directions

- **Expand & nurture core multidisciplinary aeromechanics programs:**
 - Maintain balance between theory & experiment
 - Tackle barrier problems systematically such as maneuvering flight aeromechanics, variable speed rotors, robust HUMS, swashplateless rotors, etc.
- **High efficiency mission-adaptive morphing rotor**
- **Expand micro air vehicle program**
 - Revolutionary concepts in gusty environment
- **Brownout/whiteout: Understanding and mitigation**
- **Exploit advanced CFD methodology to develop next-generation rotorcraft**
- **All electric/hybrid rotorcraft: green aviation**


Alfred Gessow Rotorcraft Center
University of Maryland at College Park

Emerging CFD as a Viable Tool to Predict Vibratory Loads in a Helicopter



Inderjit Chopra
Alfred Gessow Professor and Director
chopra@umd.edu

Presentation At: Korea Aerospace Research Institute (KARI), Daejeon
June 27-30, 2011

Outline

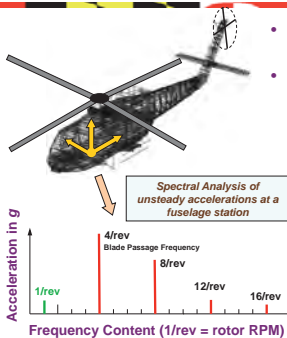
- **Introduction: Vibration**
 - Barrier Issues
- **Identification Critical Flight Conditions**
 - High speed
 - Low speed transition
 - High altitude dynamic stall
 - Severe pull-up maneuver
- **Systematic Vibration Solution using CFD**
- **Other CFD Activities and Future Work**

Swashplateless Rotor with Integrated Flaps



MR RPM : 375 rpm
Empty Weight: 1100 kg
Fuel Weight: 150 kg
Payload: 500 kg
MTOW 1750 kg

Helicopter Vibration: Definition

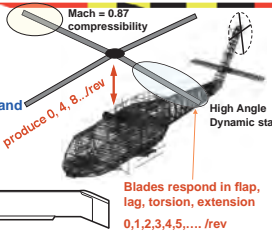


- Unsteady accelerations at a station in airframe
- Intrusion Index: weighted mean of 4 largest frequencies in vertical, lateral and longitudinal directions up to 60 Hz
- Source of vibration: Rotor Blades are excited at all harmonics, only harmonics consisting integer multiples of blade number, pN_b/rev are filtered through hub
- 1/rev due to rotor asymmetry

Rotor Dynamics in Forward Flight

Sources of Vibration

- Asymmetric flow in forward flight
- Complex wake
- Compressibility on advancing side and dynamic stall on retreating side
- Flexible rotor blades



Mach = 0.57 compressibility

produce 0, 4, 8, ... /rev

High Angle Dynamic stall

Blades respond in flap, lag, torsion, extension 0, 1, 2, 3, 4, 5, ... /rev

- Blade undergoing moderately large deformations involving coupled flap, Lag, torsion and axial motion, nonlinear inertial couplings
- Airframe 3-D structure with complex joints and cutouts, Gyroscopic nonlinear couplings in vehicle dynamics

Aerodynamics: Challenges

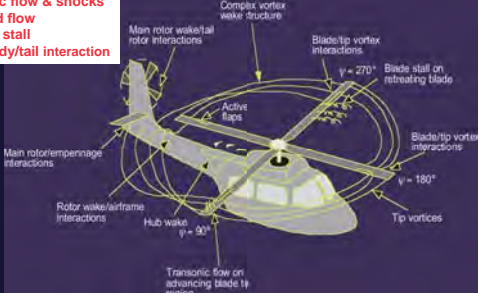
- Nonsteady and complex aerodynamics and rotor wakes

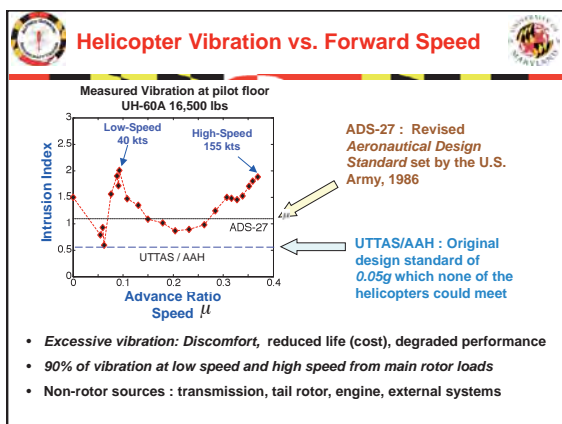
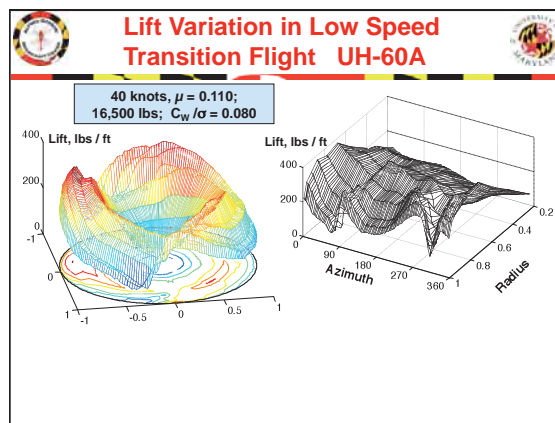
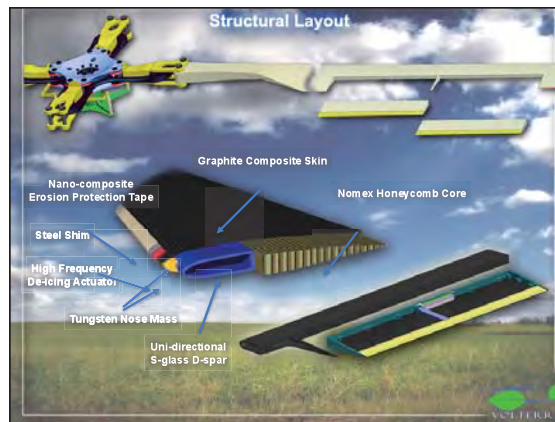
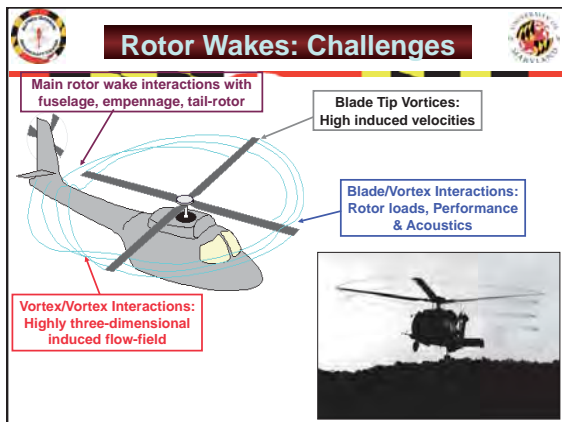
Transonic flow & shocks

Reversed flow

Dynamic stall

Rotor/body/tail interaction





Analysis Methods : Blade Structural Model

Blade Modeled as elastic 1-D beam undergoing flap bending, lag bending, elastic twist and axial deformation

Blade Model

- Linear flap-lag-torsion dynamics for small deformations (Houbolt and Brooks 1958, Ormiston 1972)
- Nonlinear equations for moderate deformations (Hodges/Dowell 1974, Hodges/Ormiston/Peters 1980, Friedmann/Rosen 1978, Johnson 1977, Kvaternik 1976)
- Anisotropic, composite rotor with cross-sectional warping and transverse shear (Hodges 1990, Smith/Chopra 1993, Bauchau 1998)
- Advanced geometry rotors with sweep and droop (Celli/Friedmann 1992, Benquet/Chopra 1989, Ganguli/Chopra, 1992)

Spatial discretization

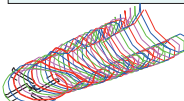
- Lumped parameter methods, transfer matrix, Myklestad (Murthy 1986, Sangha 1990)
- Finite element approach (Straub/Friedmann 1980, Chopra/Sivaneri 1982)
- Modal reduction vs. full finite element
- Topology independent multi-body formulations (Johnson 1998, Saberi 2004, Bauchau 1993, Ghiringhelli/Masarati 1999) large deformations

Analysis Methods : Unsteady Aerodynamic Modeling

- Classical inviscid, incompressible, thin airfoil theories (Theodorsen, Wagner)
- Semi-empirical indicial models
 - attached flow (Beddoes 1984, Leishman 1988)
 - separated flow (Beddoes 1983)
 - dynamic stall (Leishman/Beddoes 1989)
 - effect of sweep on dynamic stall (Leishman 1989)
 - Boeing dynamic stall model (Gormont 1970)
 - Johnson dynamic stall model (Johnson 1970)
 - ONERA EDLIN dynamic stall model (Petot 1990)
 - ONERA BH dynamic stall model (Truong 1998)
- Detailed CFD models (Euler, Full Potential, Navier-Stokes)

Analysis Methods: Wake Geometry Calculation

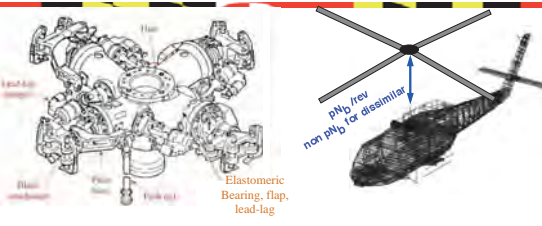
Prescribed geometry	Free Geometry	Free, time accurate
<ul style="list-style-type: none"> • Prescribed wake (Piziali/DuWaldt 1962) • Refined by experimental induced velocities (Landgrebe 1969) to improve hover performance • Kocurek/Berkovitz 1982 • Refined for forward flight, (Landgrebe/Egolf 1983, Beddoes 1985) 	<ul style="list-style-type: none"> • Relaxation model (Scully 1975) • General free wake method (Johnson 1995) • Pseudo-implicit predictor-corrector (Bagai/Leishman 1995) • Multiple trailer method (Johnson 2002) • Constant vorticity contour method (Wachspress 2003) • Multiple rotors, multiple trailers, dual peak, dissimilar blades (Bagai/Leishman 1996, Johnson 1988) 	<ul style="list-style-type: none"> • Hover (Crimi 1965, Scully 1967) instability • Clark/Leiper 1970 (enforced periodicity), forward flight (Landgrebe 1969, Sadler 1971) • Vortex lattice model (Egolf 1988), Baron/Baffadossi 1993 • Jain 1998, Chung 2000 studied hover instability • Bhagwat/Leishman 2003 for hover, steady and maneuvering flight, explained hover instabilities



Analysis Methods: Trim, Response and Loads

- Trim models
 - Free flight propulsive trim - solve for 3 rotor controls, 2 fuselage attitudes, tail rotor collective with 3 force/3 moment equations
- Rotor Response Calculation (periodic in level flight)
 - Harmonic balance (Johnson 1980) : CAMRAD, RCAS
 - Floquet theory (Dugundji/Wendell 1983)
 - Finite element in time (Panda/Chopra 1987) : UMARC
 - Numerical integration : Lockheed REXOR, Bell C81, Sikorsky DYMORE
- Blade Loads Calculation
 - Deflection or curvature or modal method
 - Force summation method superior in case of spatial discontinuity, rigid members, concentrated loads
 - Mixed formulation

Analysis Methods : Coupled Rotor-Fuselage Vibration

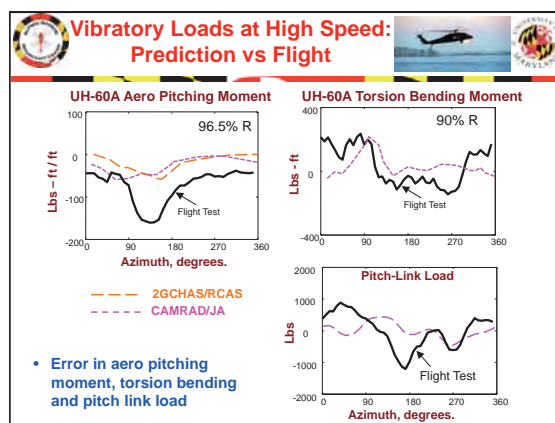
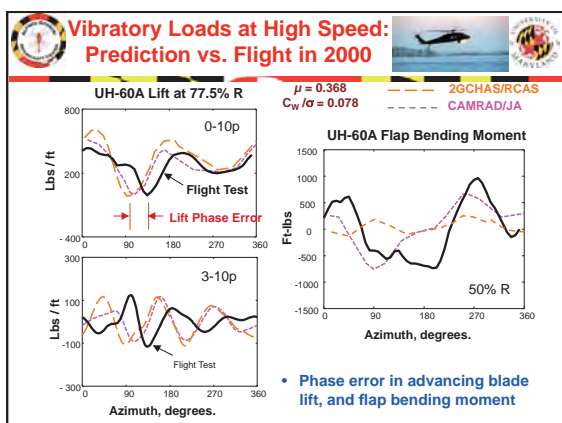
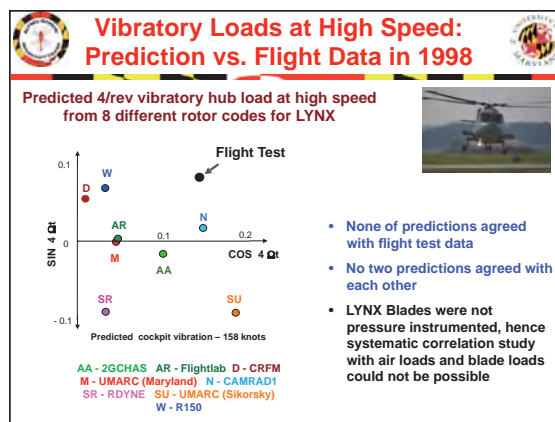
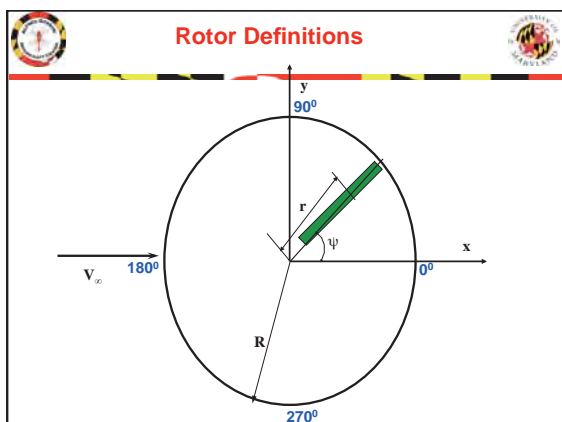


- Rotor vibratory hub harmonics (4/rev, 8/rev, etc) transmitted to elastic airframe
- Say 1P = 300 RPM or 6 Hz, 4P=24 Hz
- Airframe 20 modes less than 25 Hz, requires detailed modeling of airframe including joints, cutouts and secondary structures

Analysis Methods : Rotor Codes vs. Comprehensive Analyses

Specialized Rotor Codes	Comprehensive Codes
<ul style="list-style-type: none"> • Greater details, accuracy and scope to model some physical mechanisms while simplifying most other interactions • RotorCRAFT to CHARM – detailed free wake, rotor-fuselage aerodynamic interaction • KTRAN-RDYNE-GENHEL – structural dynamics and flight dynamics • DYMORE II – multibody rotor-fuselage dynamic model • R150 and Westland/DERA • C81 and COPTER • R85/METAR 	<ul style="list-style-type: none"> • Includes all basis components to handle multidisciplinary loads, vibration and stability, Can perform trim, transient and flutter interaction • CAMRAD family • UMARC family • 2GCHAS to RCAS • free wake model • unsteady aero, stall model • flexible blade dynamics • free flight trim • airframe dynamics • advanced geometry blades • composite, modern rotors • 3D CFD loose coupling

Vibration Prediction: Barriers



"... we have not made any significant progress in the last 30 years in the accuracy of our prediction methods."
Bousman, 8th ARO Workshop 1999

"...we do not understand the basics : is this discrepancy from the structural or aerodynamic modeling (especially wake) or both ?"
Lim, 1st UH-60A Airloads Workshop 2001

Prediction of Vibration

Vibration Validation Study

Major undertaking in 2001: Team involving industry, academia, NASA/ Army to resolve vibration barrier issues. Loads Workshop: Meet every 6 months since 2001

Vehicle: UH-60A Black Hawk, extensive flight test data with pressure instrumented blades

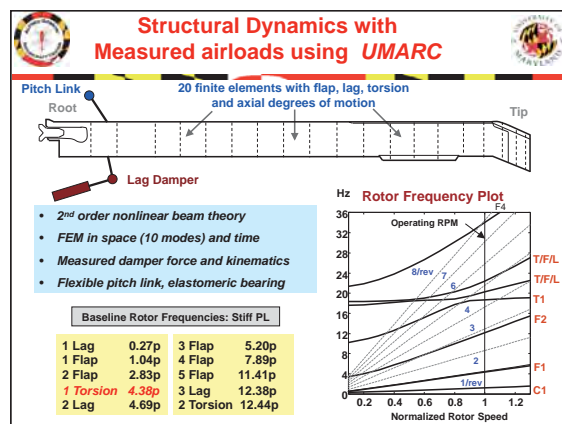
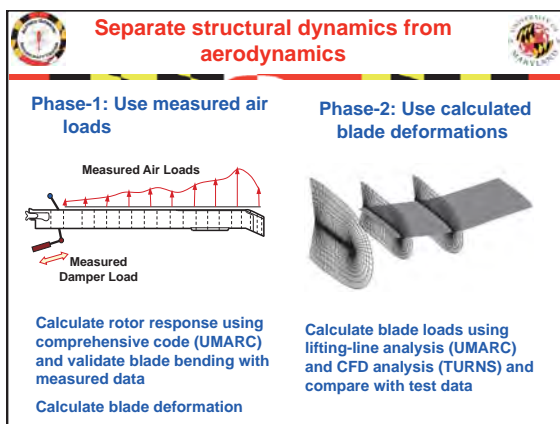
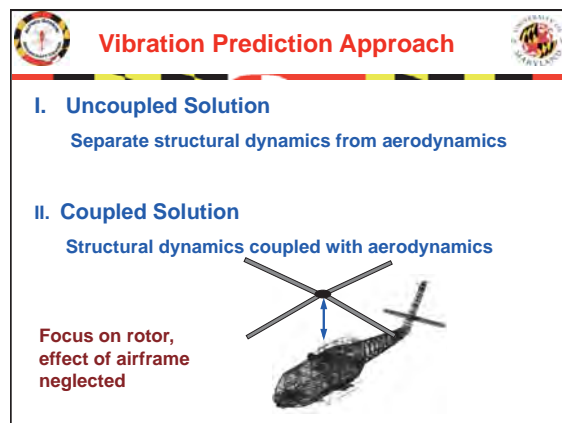
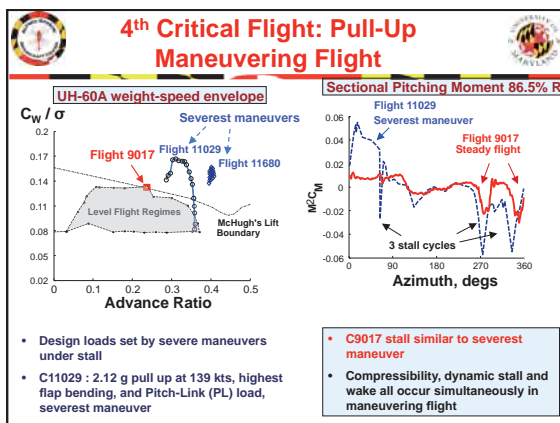
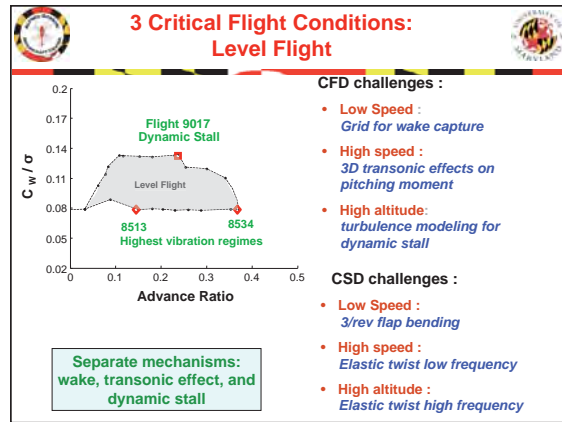
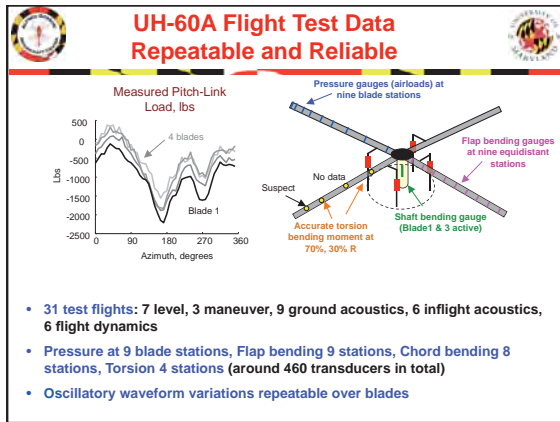
Identified 4 critical flight conditions:

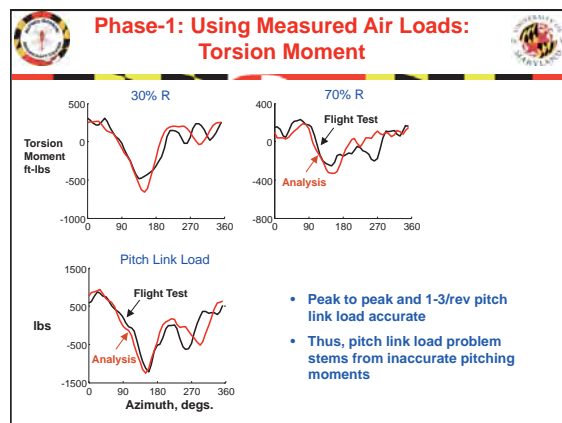
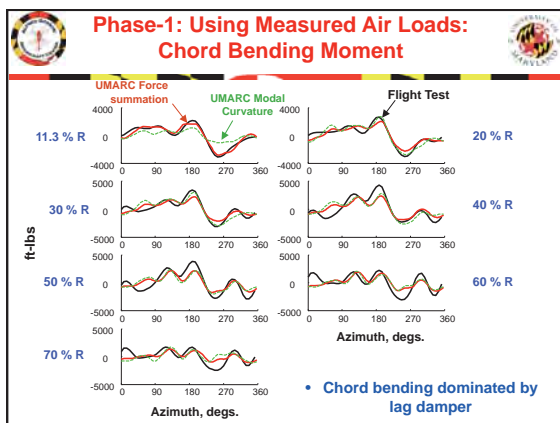
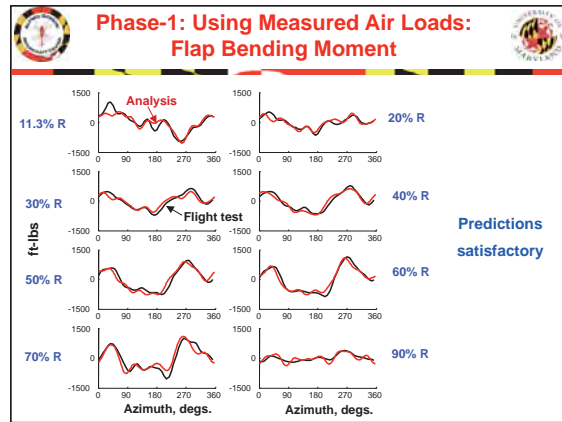
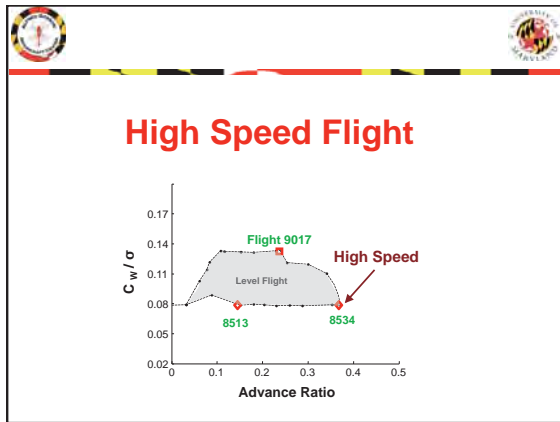
Level Flight:

- High speed $\mu = 0.37$ UH-60A flight 8534
- Low speed transition $\mu = 0.15$ UH-60A flight 8513
- High altitude dynamic stall $\mu = 0.24$ UH-60A flight 9017

Maneuver:

- Severe pull-up Maneuver $\mu = 0.341$ UH-60A flight 11029 (load factor = 2.09)





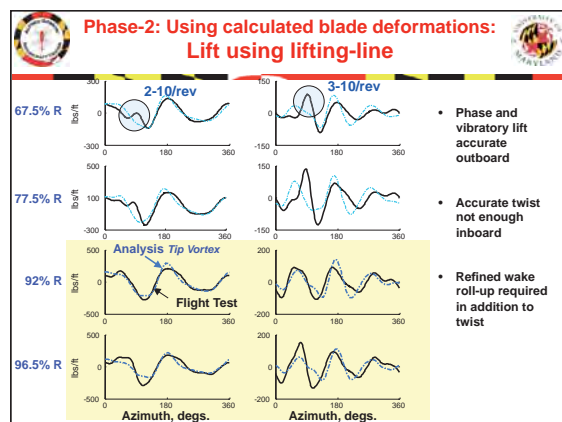
Phase-2: Using calculated deformations: Blade aero loads

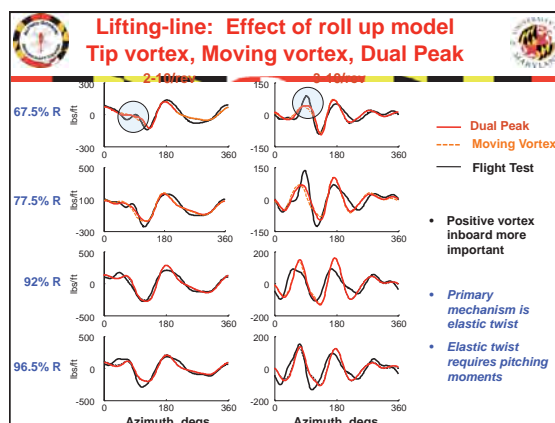
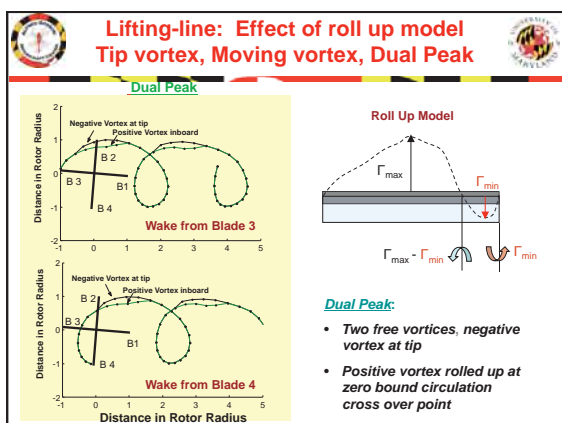
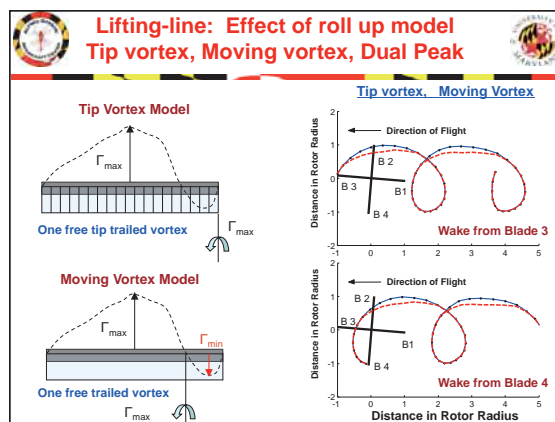
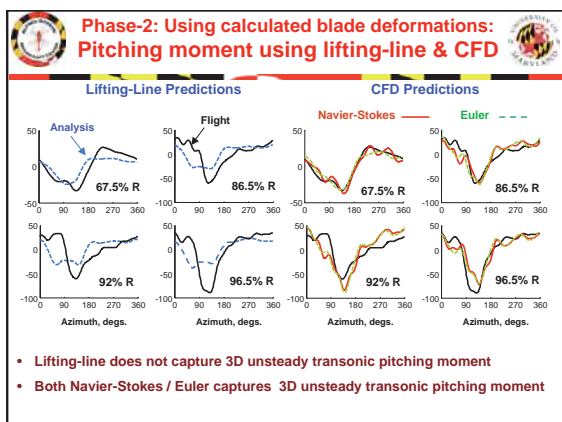
UMARC (University of Maryland Advanced Rotorcraft Code)

- Lifting line model
- Bagai-Leishman free wake fully rolled up, 5 degs., 4 turns single, moving, dual, full-span, root vortex, inboard trailers, vortex lattice
- Leishman-Beddoes unsteady model attached, separated, dynamic stall extracted for SC1095, SC1095 R8
- 2D test airfoil tables
- Weissinger-L based nonlinear near wake

Swept bound vortex line at $\frac{1}{4} c$ Increased chord for trim tab (setting unknown)

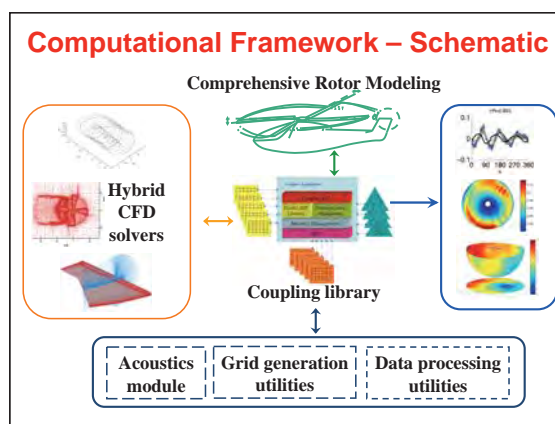
SC1095 SC1095 R8 SC1095

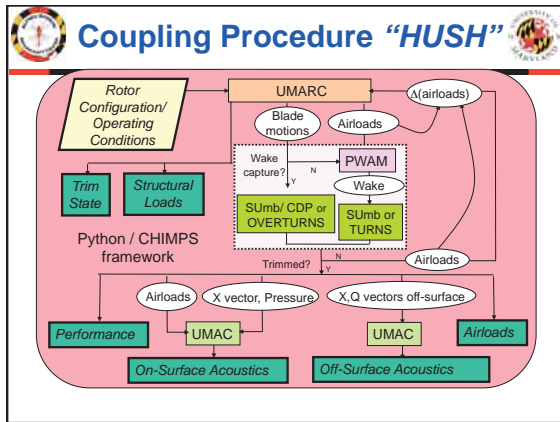




II. Coupled Solution

CFD Methodology





Wake-coupling vs. Wake-capturing

- Two strategies for predicting rotor far wake geometry and induced velocities
- Wake Coupling**
 - Stand-alone Lagrangian free-wake model (PWAM) coupled to CFD using field velocity approach
 - CFD solves only the near-body flow-field
 - Captures near wake evolution
 - Single blade sufficient for steady flight
- Wake capturing**
 - Wake calculated using CFD. Solve both near-body and off-body flow-field
 - Captures wake sheet evolution and roll-up from first principle
 - Grid resolution critical in preserving vorticity
 - Computational intensive

UMTURNS & OVERTURNS

- UMTURNS (wake coupling)**
 - Near-body solution using a C-O mesh
 - Single blade only
 - Wake effects included using field-velocity approach
 - Roe's flux differencing with MUSCL-type limiter
 - Second-order stencil for viscous terms
 - Baldwin-Lomax and Spalart-Allmaras turbulence models
- OVERTURNS (wake capture)**
 - C-O mesh used for near-body solution
 - Models all blades
 - Wake-capturing using overset meshes
 - Cylindrical background meshes
 - Essentially an overset version of UMTURN

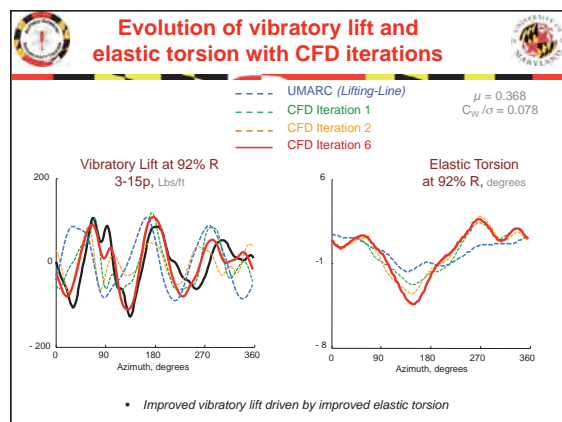
CFD-CSD Coupling

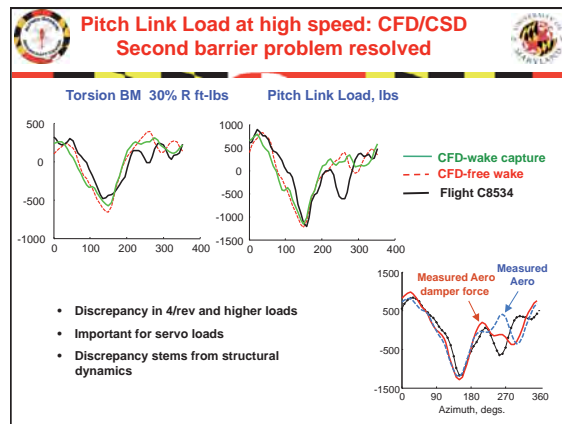
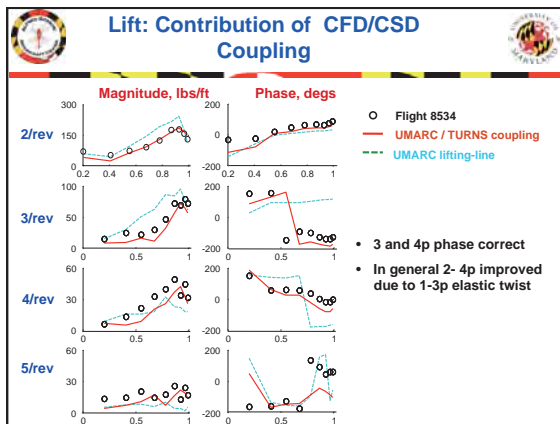
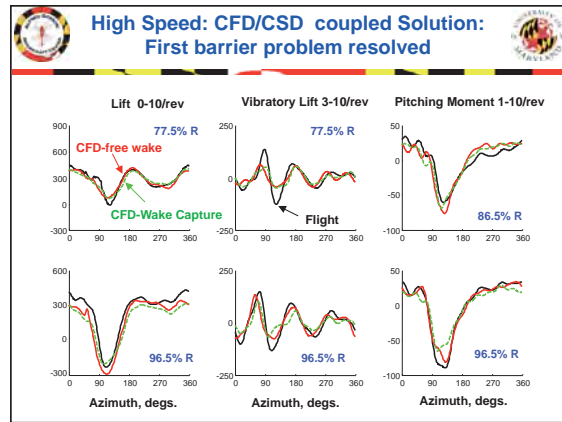
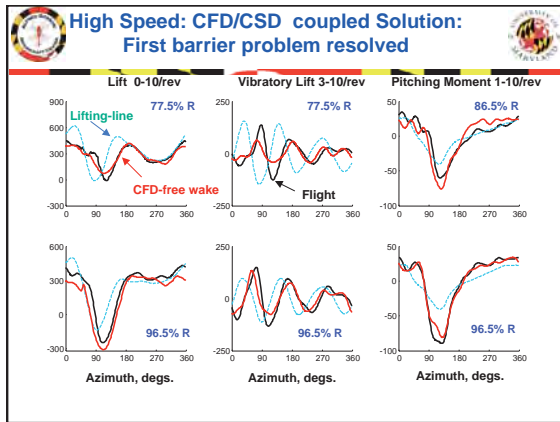
- Tight coupling**
 - Exchange data at every timestep/sub-iteration
 - Computationally intensive
- Loose coupling**
 - Exchange data every rotor revolution
 - Delta airloads methodology
 - Determine trim solution within comprehensive analysis
 - Iterate until trim convergence

Details of CFD analysis

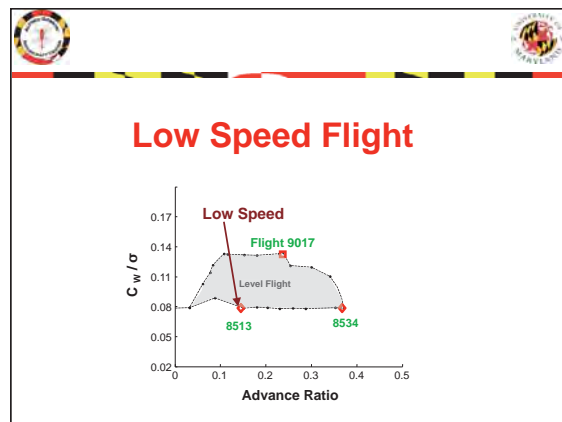
Grid spacing:

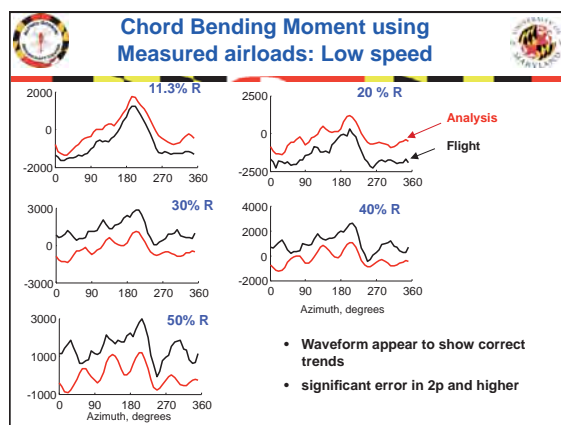
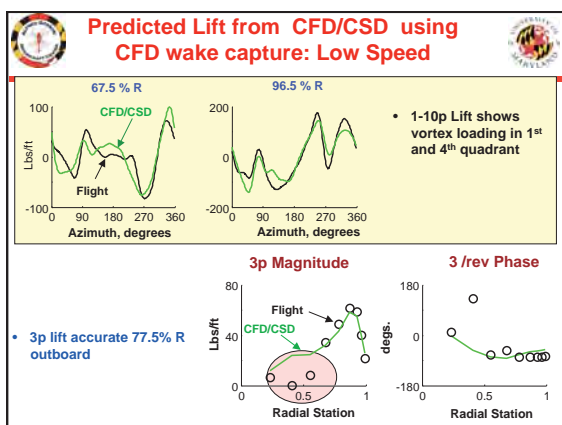
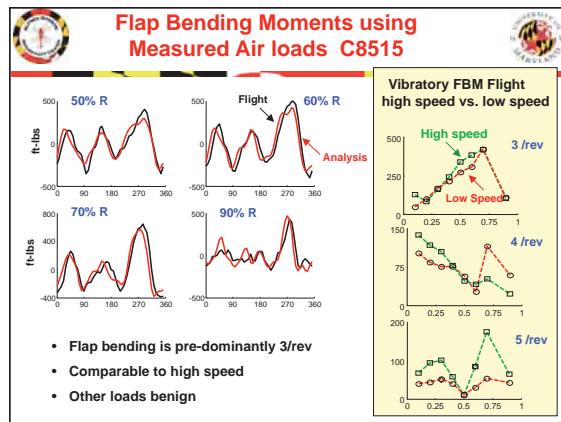
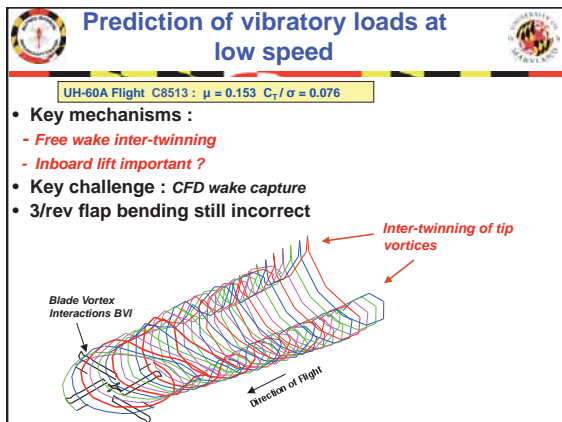
- Partial CFD: 133-43-43 (total 0.25M) coarse grid
- Full CFD: 133-125-48 (0.8 M) + background grid 2.2 M (total 3M)
- high speed airloads – grid independent
- low speed – Practically independent; refinement necessary to see grid dependency is beyond today's capability (BVI)
- Stall airloads – sensitive to grid spacing
- Power predictions – profile power (airfoil drag) sensitive to grid





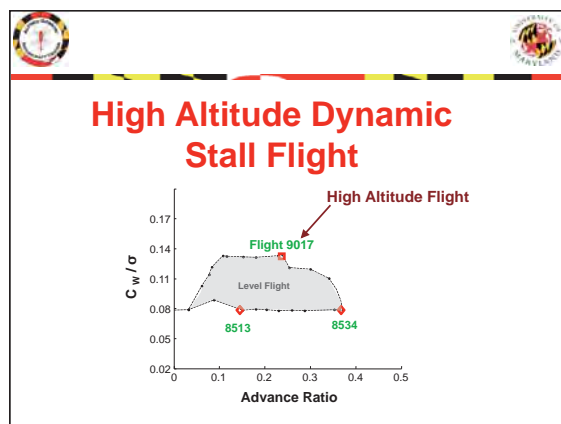
- ### Loads in High Speed Flight: Conclusions
- Key barrier problems resolved
 - Physics of vibratory lift in place: phase problem resolved
 - Peak-to-peak pitch link load captured
 - Outstanding Issues
 - 4p and higher pitch link load less satisfactory: *structure*
 - Phase error of 7-10 degree in flap bending: *aerodynamic*





Loads in Low Speed Transition : Summary

- Vibratory air-loads can be captured by CFD, but only slightly changed from lifting line results
 - 0.05c background grid adequate
 - artificial dissipation of tip vortices does not prevent capturing 3-5/rev air loads
- Key Technical Barrier :
 - 3/rev flap bending moment still wrong



Fundamental Understanding and Prediction of Dynamic Stall Loads

UH-60A Flight C9017 : $\mu = 0.237$ $C_T / \sigma = 0.129$

- **Key barriers :**
 - 2 retreating blade stall cycles
 - 3-5/rev pitch link load
- **Key mechanisms :** Trim stall and Twist stall
- **Key challenge :** CFD turbulence model

Dynamic Stall Flight 9017

- 3 - 5/rev torsion loads excite swashplate servo
- Peak flap bending and pitch link load important for design
- Trim, torsion response, and turbulence important for prediction

Flap Bending Moments: CFD/CSD vs. Measured airloads

Torsion Moments and Pitch Link Load: CFD/CSD

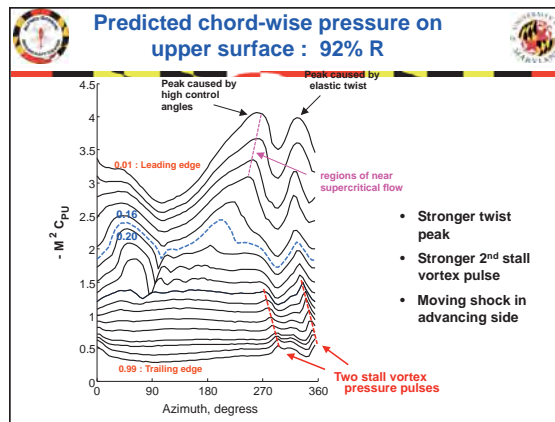
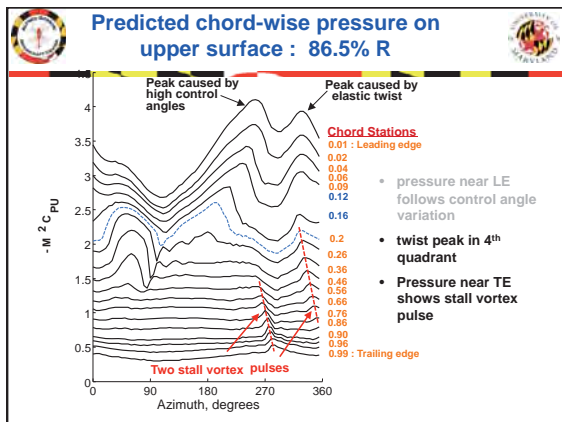
Predicted Pitching Moment and Stall Map: CFD/CSD

- 2nd stall cycle mostly 2D
- 1st cycle is 3D; stall vortex moving across span

Physical Mechanism of the two Stall Cycles: Trim and Twist

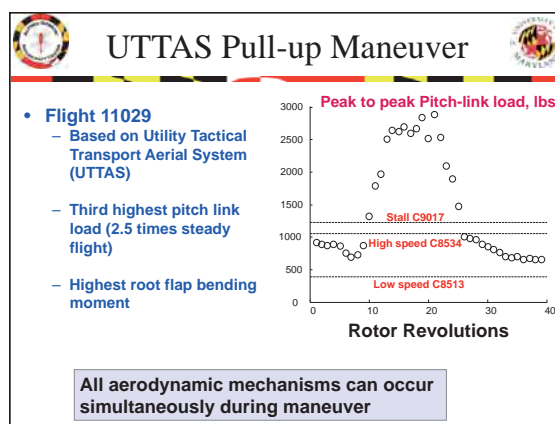
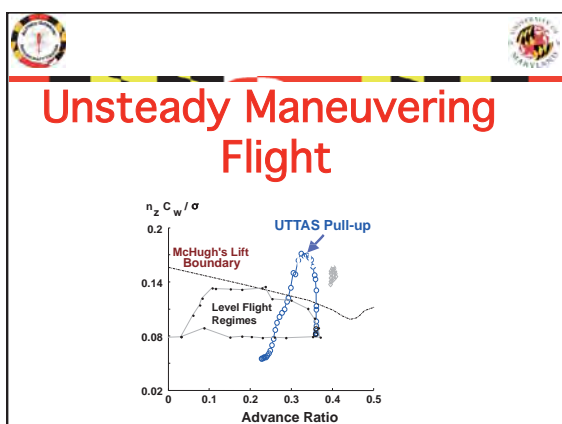
Angle of Attack study at 86.5% R

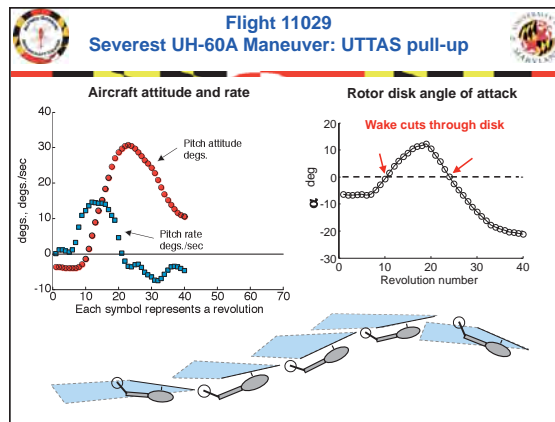
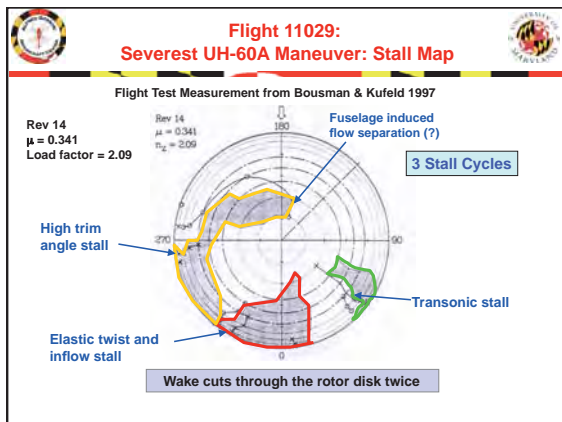
- Rise in 3rd quadrant due to high trim angles: 1st cycle is a trim stall
- 4th quadrant excitation due to 4 and 5p twist: 2nd cycle triggered by twist



- ### Loads in Dynamic Stall Flight : Summary
- Mechanism of retreating blade stall understood
 - 1st cycle due to high trim angles
 - 1st cycle excites 4 and 5p twist (torsion freq 4.38p)
 - 4 and 5p twist sets location of 2nd stall cycle
 - Inflow important
 - CFD turbulence model important
 - Stall near tip 96.5% R not captured
 - Peak to peak blade loads satisfactory
 - 4p and higher pitch link load unsatisfactory : *struct problem*
 - Important for servo loads

- ### Level Flight: Key Conclusions: CFD/CSD Coupling
- CFD provides **fundamental capability** at high speed – 3D unsteady transonic pitching moments
 - CFD provides **improved capability** at low speed and stall
 - no semi-empirical wake roll up or stall models
 - key for *calculating* loads on new rotor designs
 - Structural loads not significantly improved as air loads
 - 4p and higher torsion unsatisfactory – *struct. Problem*
 - 4p and higher chord bending unsatisfactory – *struct. Problem*





Multibody Analysis

- **Structural dynamics model**
 - Full finite element large frame (multibody) analysis capable of modeling large deformations

Pitch Link

- **Aerodynamics model: N_b bladed transient model**
 - Unsteady lifting surface including roll and pitch rates
 - Weissinger-L type lifting surface model iteratively coupled to 2D airfoil tables
 - Dynamic Stall (Leishman-Beddoes)
 - Transient Freewake (Anathan-Leishman)

Large Deformation Analysis

Large deformations can be modeled:

Approach 1: Geometrically exact beam theory

Approach 2: Second order non-linear beam theory coupled to multibody formulation

Approach 2: (Followed)

- Additional frame attached to individual elements
- Elements undergo only moderate deformation
- Rigid body motions accommodated by finite rotation of frames

Swashplate Model

Direction of flight

$\psi = 270^\circ$

$\psi = 180^\circ$

$\psi = 90^\circ$

$\psi = 0^\circ$

Aft Lateral Forward

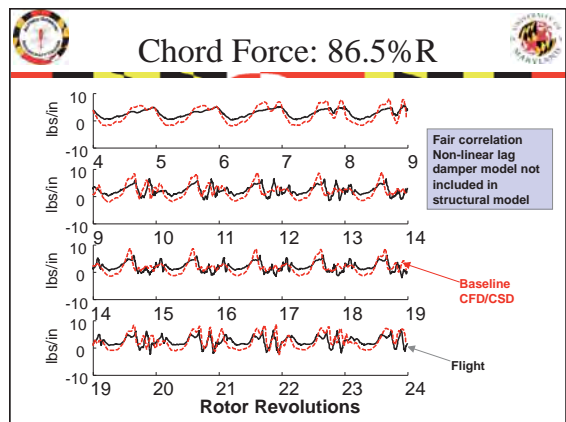
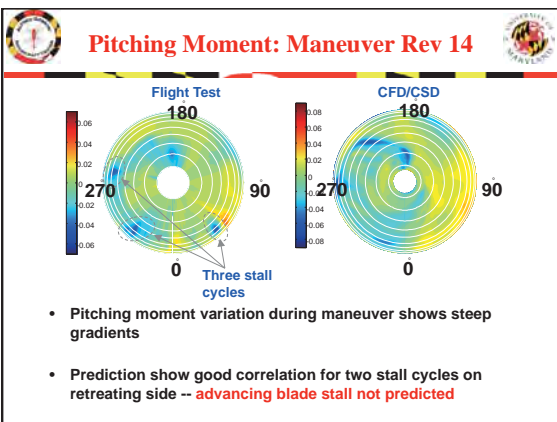
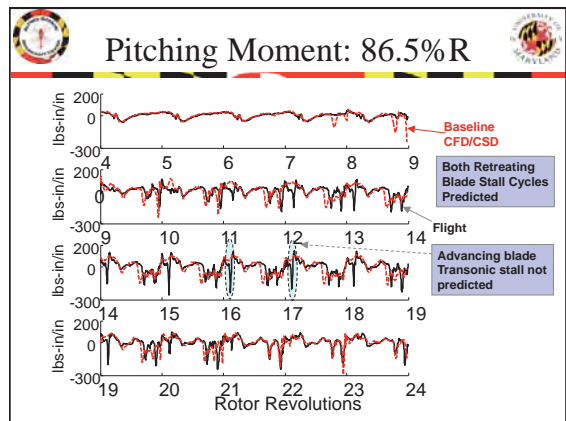
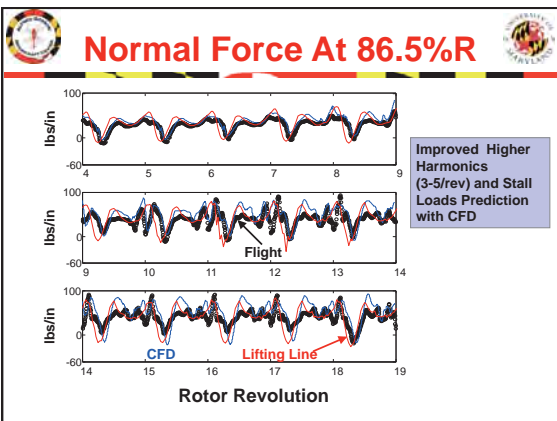
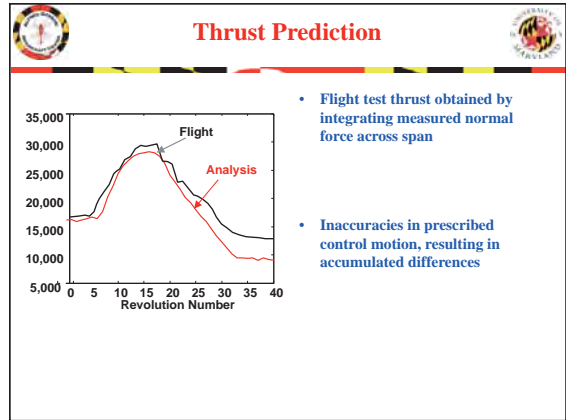
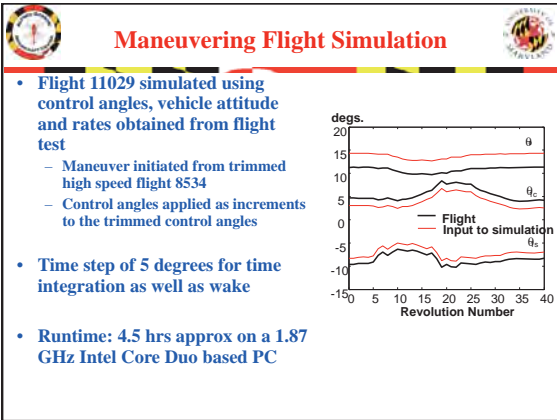
3 dof Swashplate model

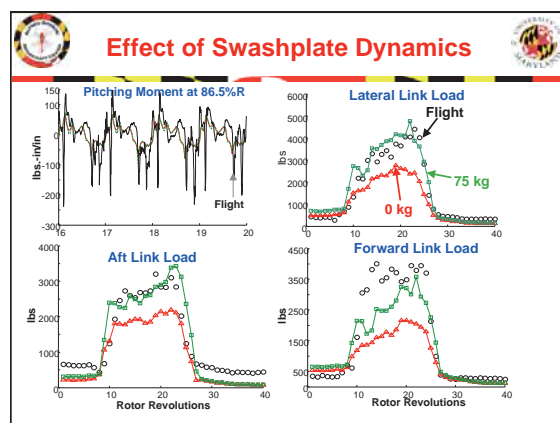
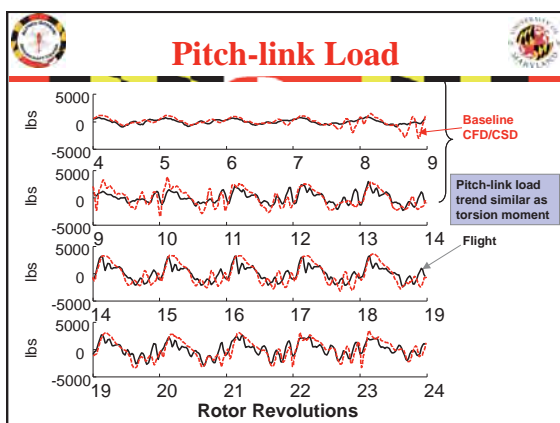
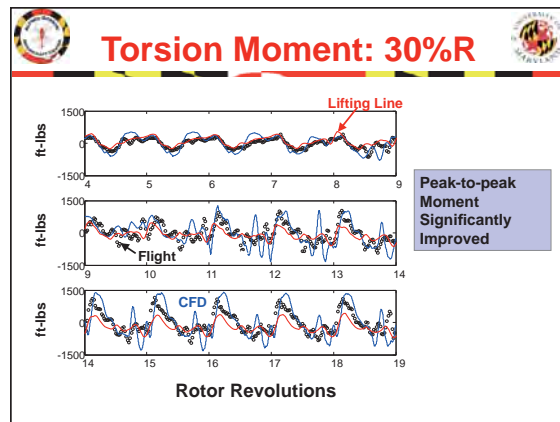
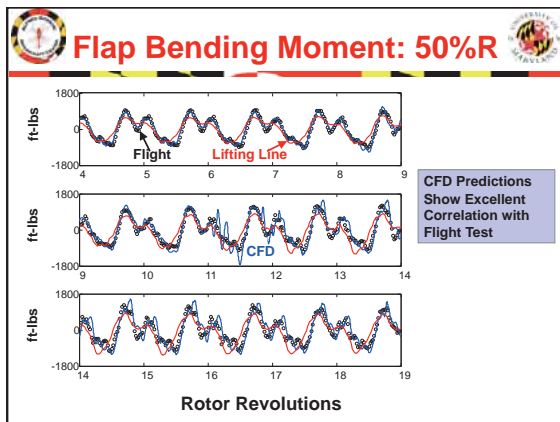
- Heave (z), pitch (α_x), and roll (α_y)
- Swashplate idealized as rigid disk
- Servos modeled as linear spring-damper system

- 4-bladed full FEM multibody model, 20 finite elements for each blade
- Pitch link stiffness (1090 ft-lbs)
- Elastomeric bearing: flap/lag damper : 100 ft-lb/rad/s

Fluid Structure Coupling


- **Inputs to aerodynamic model**
 - Blade deformations for all blades
 - Instantaneous advance ratio, shaft tilt angle, rotor pitch and roll angles, angular rates and the control angles
- **Output: instantaneous air-loads and inflow velocities**
- **Tight coupling: structure, aerodynamic, and free wake model exchange information at every time step**
 - Similar to CFD/CSD serial staggered tight coupling without sub iterations
 - Transfer of information via subroutine calls





- ### Conclusions
- Pull-up maneuver studied is a stall dominated flight.
 - Two distinct stall cycles predicted on retreating side
 - Predicted peak-to-peak torsion moment and pitch-link load show trend similar to test data.
 - Peak-to-peak magnitude under-predicted
 - Servo loads predicted satisfactorily
 - Average thrust prediction showed trend similar to test data.

- ### Other CFD Applications in Rotorcraft
- Generation of 2-D airfoil data tables (c_L , c_D , c_M) for current and future airfoils
 - Performance evaluation of new rotor configurations:
 - Coaxial rotors
 - Washplateless system with trailing-flaps
 - Stall Alleviation with leading-edge slats
 - Micro air vehicle systems (low Reynolds aerodynamics)
 - rotor based system
 - Avian-based flapping
 - Insect-based flapping
 - Mission adaptive morphing rotor
 - Parallelization of CFD methodology



Acknowledgements

PhD Students: Anubahv Datta (Ames) Jaina Sitaraman (NIA) Shreyas Ananthan (UM) Beatrice Roget (NIA) A.Abhishek (Grad) Jaye Falls (Grad) Ben Silbaug (Grad) Brandon Bush (Grad) L. Lakshminarayanan (Grad)	Faculty Colleagues Jim Baeder (Key CFD Person) Gordon Leishman
Sponsors: Army/NRTC NASA/NRA Navy/ONR Sikorsky/UTRC	Collaborators: Stanford Juan Alanso


Alfred Gessow Rotorcraft Center
 UNIVERSITY OF MARYLAND

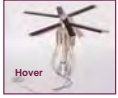


Hovering Micro Air Vehicles: Challenges & Opportunities

Inderjit Chopra
 Alfred Gessow Professor &
 Director Alfred Gessow Rotorcraft Center
 (chopra@eng.umd.edu)



Presentation At: Korea Aerospace Research Institute (KARI), Daejeon
 June 27-30, 2011

Micro Air Vehicles: Definition

- **Design Requirements**
 - No dimension exceeds 15 cm (6 inch)
 - Gross takeoff weight 100 grams
 - Loiter time of 60 minutes
 - Payload capacity of at least 20 grams
- **Additional considerations**
 - Fully autonomous (out of sight operations)
 - All weather operations
 - Low production cost
 - Rapid deployment
 - Low detection

Future Vision of Microsystems

Scenario 1: Small unit building search
 Challenges: hover and low speed, medium endurance, quiescent airflow

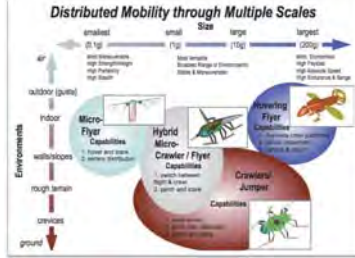
Scenario 2: Small unit cave / demolished building search
 Challenges: Hover and low speed, high endurance, mediocre gust

Scenario 3: Autonomous small unit perimeter defense
 Challenges: High speed, range and endurance, strong wind gusts

Microsystem Platforms

Range of platforms at:
 - **Macroscale (50-100 cm)**
 To verify modeling tools, performance, functionality and mobility

- Mesoscale (1-10 cm)
Final design goal
- Aerial: Rotary and flapping wings
- Hybrid: Thrust augmented entomopter, hybrid crawler/flyer



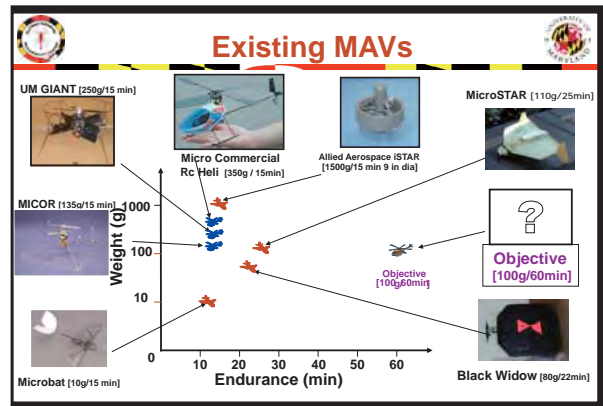
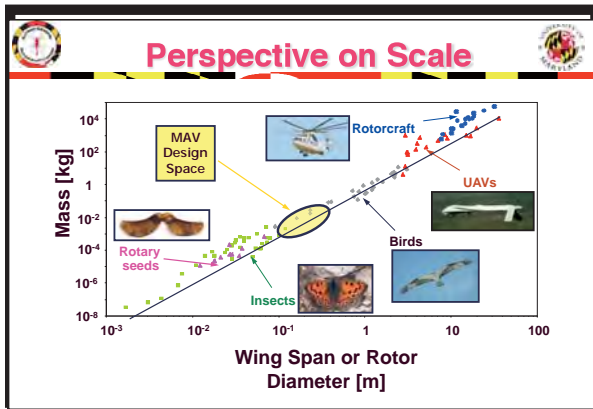
Size Scaling for MAV platforms

(Mobility)(Intelligence)(Multiplicity) = Capability

	Larger	Smaller	N*small=large
Mobility	↓	↑	↑
Gust Sensitivity	↑	↓	No change
Frequency	↓	↑	No change
CPU MIPS	↑	↓	no change
Multiplicity	↓	↑	N/A
Sensing	no change	no change*	O(N ²) ↑
Communication	↑	↓	O(N ²) ↑

Micro Air Vehicles: Key Drivers!!

- **Asymmetric warfare environment: urban warfare**
- **Micro-electronics: Miniaturized sensors availability**
- **Micro-processing: IT and transmission power growing**
- **Low cost systems: (can be organic with a soldier)**
- **Increasing focus on biologically-inspired flight systems**



- ### Micro Air Vehicles: Key Challenges!!
- Lack of knowledge how scaling affects micro-vehicle performance and limitation of existing aeromechanics tools.
 - Low efficiency of existing air vehicles
 - Extreme vulnerability to gust
 - Low mobility, maneuverability and autonomy of existing vehicles
 - Requires fundamental understanding in key areas:
 - Efficient aerodynamic performance in highly unsteady vortex dominated flows at low Reynolds number
 - Bio-inspired actuation and articulation air vehicles
 - Lightweight and adaptive structures
 - Insect-like navigation and control for autonomous operations in uncertain environment (such as gusty environment)
 - Efficient bio-inspired propulsion and efficient power distribution

- ### MICRO HOVERING AIR VEHICLES
- Non-Hovering Vehicles: Fixed-wing based
 - Hovering Vehicles: Rotor Based
 - Single main rotor (with & without tail rotor)
 - Ducted fan rotor
 - Co-axial rotor
 - Tiltrotor, tiltwing, quadrotor, hybrid systems
 - Revolutionary designs
 - Hovering Vehicles: Flapping-Wing Based
 - Bird-flight based
 - Insect-flight based (Efficiency at small scale?)
 - Hovering Vehicles: Reaction Based (power intensive)

Micro Hovering Air Vehicles: Rotor-Based

Coaxial Rotor MAV

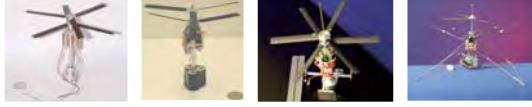
- MICOR (University of Maryland)
- 15 cm (6") dia coaxial 2-bladed rotors

Weight~100 g, Payload ~10g
8% camber circular arc airfoils
 $Re_{75R} \sim 20,000$
Endurance ~ 10 minutes
Fixed pitch, variable speed rotors (feedback on lower)

Swashplate controls only lower rotor

Coaxial Rotor MAV Development at UM

Evolution of the MICOR MAV



1st Gen. 2nd Gen. 3rd Gen. 4nd Gen.

1999

1st Generation

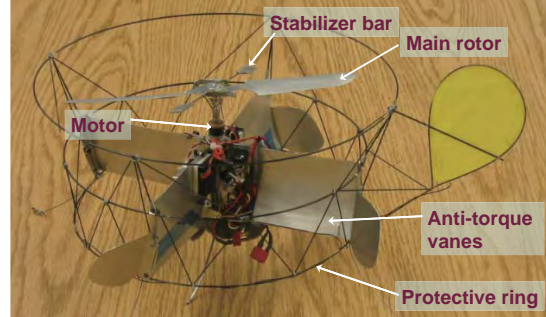
- 100 g Weight
- Maximum Single Rotor FM - 0.4
- No Payload Capacity
- No Lateral Control - Unstable
- 3 Minute Hover Endurance

2008

4th Generation

- Two bladed teetering rotors
- 135 gr. Single rotor max FM - 0.65
- Swashplate for cyclic control
- 20 minute hover endurance
- 25 g payload

MAV: Single Rotor & Anti-Torque Vanes



MAV: Single Rotor & Anti-Torque Vanes

Evolution of the Giant MAV



1st Gen. 2nd Gen. 3rd Gen. 4nd Gen.

1999

1st Generation

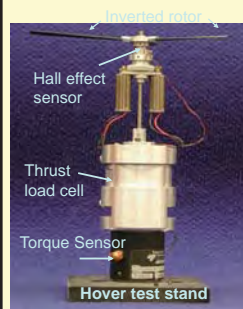
- 27 cm diameter
- 310 gm gross weight
- Aluminum construction
- Basic RC Components

2008

4th Generation

- 20 cm rotor diameter
- 200 gm gross weight
- Carbon fiber construction
- Refined spider-type swashplate
- On-board stability augmentation

Rotor Hover Test



Measurement of Hover Performance:

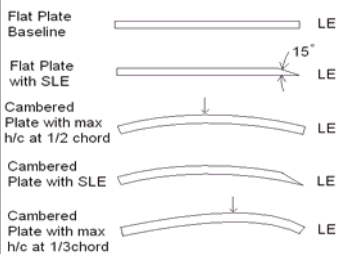
- Thrust
- Torque
- Rotational speed

FM
C_T
C_P

Figure of Merit

$$FM = \frac{\text{Ideal Power required to hover}}{\text{Actual Power required to hover}}$$

Blade Airfoil Variations



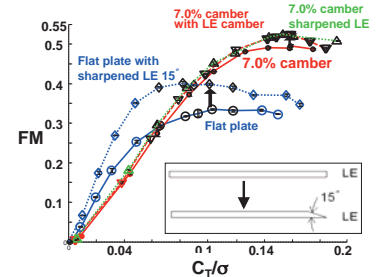
Camber Distribution



Planform Distribution

Sharpened Leading-Edge Airfoils

- Sharp leading-edge increases FM
- Smaller rise in FM for cambered airfoil



Sharpened LE can improve airfoil performance

Flow Visualization

7% camber, 2.75% thickness with sharpened LE
D=6" 2-bladed rotor, 3600 RPM, $Re=36.8 \cdot 10^3$

Strong tip vortices

High induced velocities in tip region

Vortical shed wake obstruction increases DL and lowers FM

Rotor Plane, Main Vortex, Vortex Sheet, Wake Obstruction

Rotating-Wing MAV Performance

Profile Effects

Airfoil section C_p / C_e , Rotor induced power factor, κ , Induced Effects

Better designs may come through careful aerodynamic optimization that minimizes both induced power and profile power

Shrouded Rotor System

Rotor Hover Efficiency

Figure of Merit M: Hover Efficiency is defined in terms thrust production per unit input power
For present designs: M is less than 0.6
Goal: Increase M over 0.8

Improvement of hover efficiency using duct around the rotor (plus safety protection of rotor)

Shrouded-Rotor Concept

Key Design Parameters

- **Expansion ratio/Diffuser angle**
 - Want this to be as large as possible for best performance
- **Inlet lip radius**
 - Incoming flow forms a suction peak on the inlet lip; cause of thrust augmentation
- **Blade tip clearance**
 - Proximity of shroud wall reduces strength of blade tip vortices; reduces blade tip losses

Experiment: Thrust Ratio vs. Total Power

Thrust Coefficient, C_T

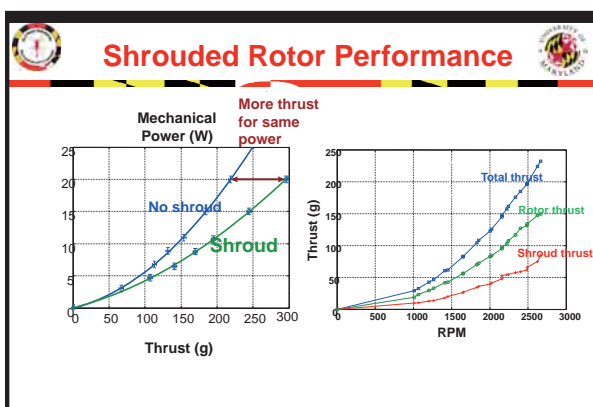
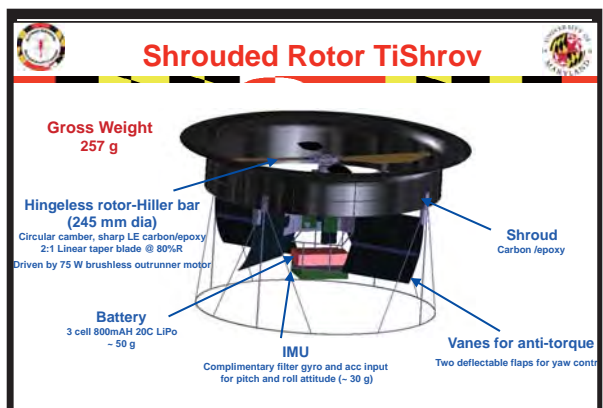
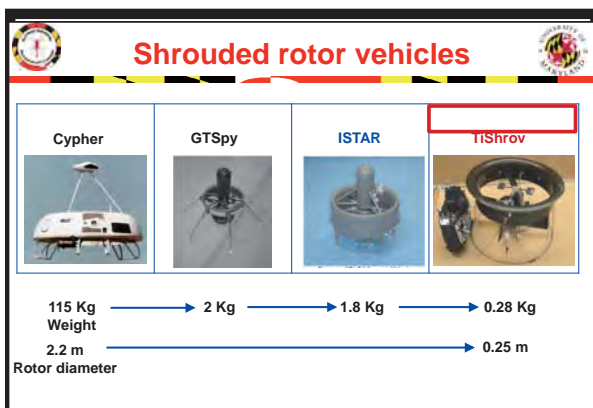
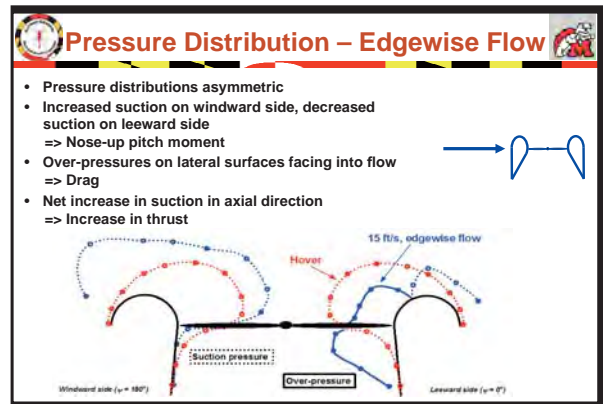
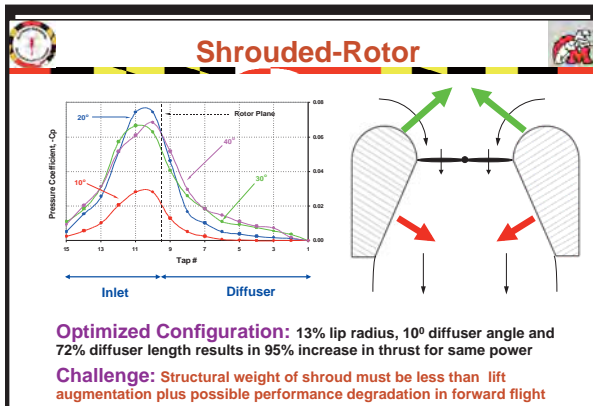
LR09-D20-4, LR13-D00, LR09-D20, LR06-D10, Free Rotor

Increase lip radius: Increase thrust
Decrease tip clearance: Increase thrust

Thrust Ratio, T_{total} / T_{free}

LR13-D00, LR09-D20-4, LR09-D20, LR06-D10

Diffuser angle: Thrust increases with small angle $< 10^\circ$

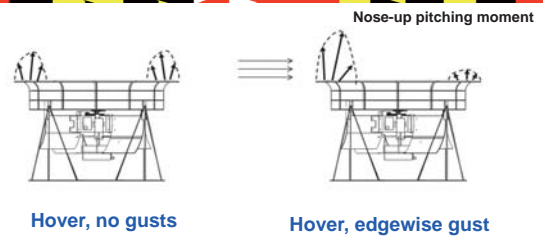


- ### Stability of Shrouded Rotor
- Shrouded rotor inherently unstable system
 - Instability due to asymmetric tip path plane movement more pronounced
 - Shroud should be incorporated only with a hingeless rotor
 - A feedback control system is required to stabilize shrouded vehicle in hover

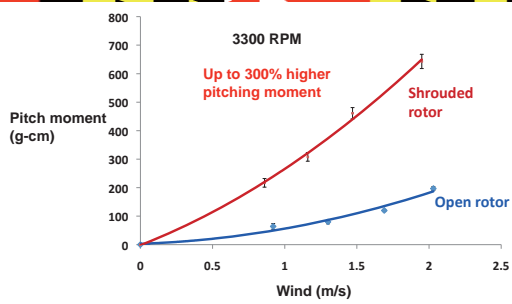
Hover flight testing in VICON



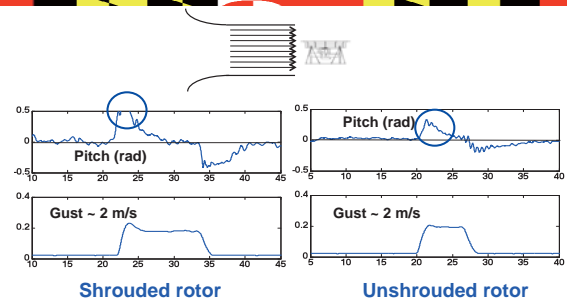
Edgewise gust disturbance response



Pitching Moment Comparison



Gust Disturbance Rejection (LQR controller)



Gust Disturbance Rejection (Free Flight)



Conclusions

- MAV shroud should be designed for high hover performance and low adverse pitching moment simultaneously
- Shrouded rotor
 - 30% higher power loading
 - 80% higher control authority (hingeless rotor, washplate)
 - can accept higher cyclic pitch range (stall delay)
 - 300% higher adverse pitching moment
- Adverse pitching moment of shrouded rotor not a function of operating RPM or rotor collective



Conclusions (2)

- Control authority varies quadratically with RPM, (linearly with operating thrust)
- Improve control authority
 - Increase cyclic pitch range
 - High operating RPM, high rotor solidity and low collective
- Gust tolerance increased from 2 m/s to 3 m/s with suggested changes (increased pitch and rectangular platform)



Shrouded rotor MAV viable platform for low gust environments

Micro Quad Rotor


185-g quadrotor with 10-cm rotor with off-the-shelf electronics

35-g quadrotor with 3-cm rotor with Berkeley's GINA

Quad-Rotor: 6-DOF Terrain Following + Centering Response using Optic Flow Sensor



**Rotary Wing Micro Air Vehicles:
Unconventional Configurations**

Cyclocopter


A set of blades rotate around an axis of rotation parallel to blades; pitch varies periodically once per revolution to produce thrust in desired direction

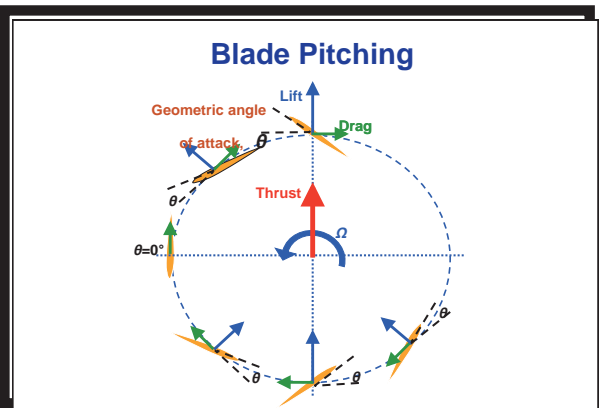
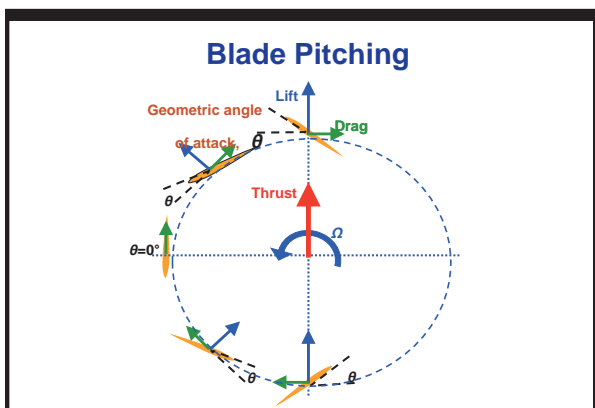
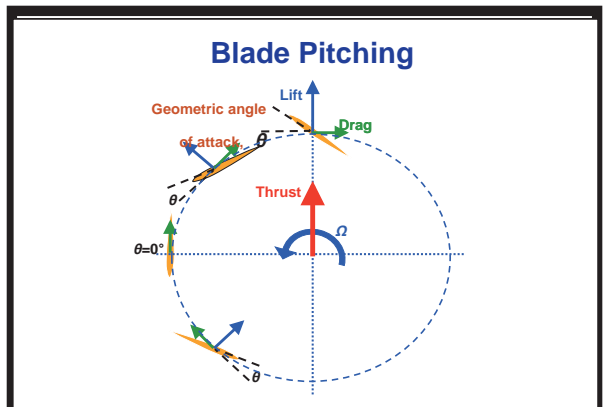
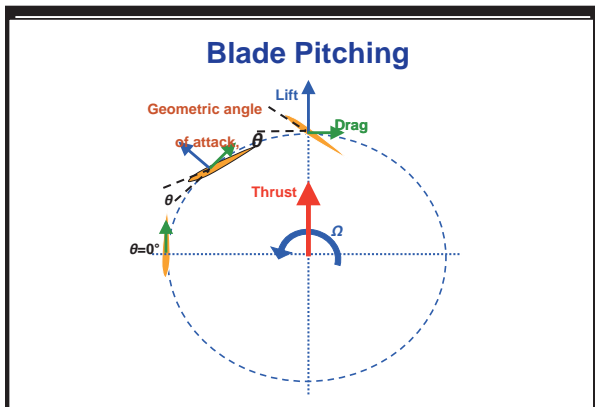
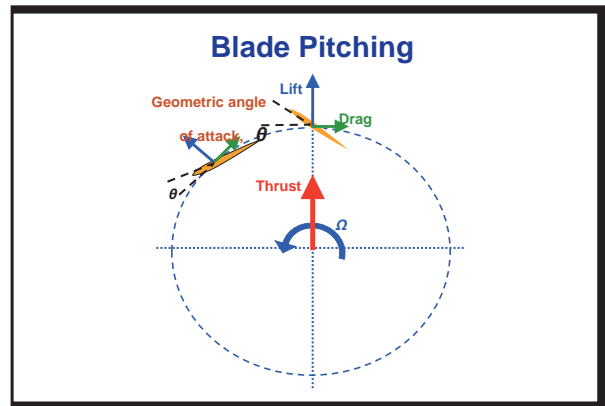
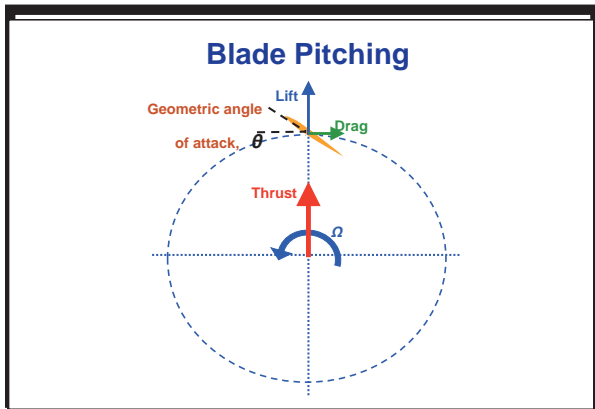
Advantages:

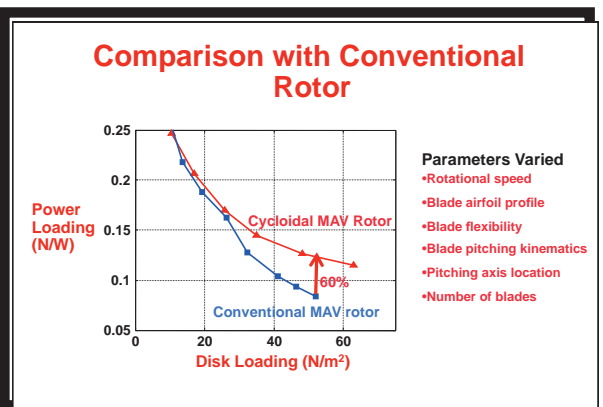
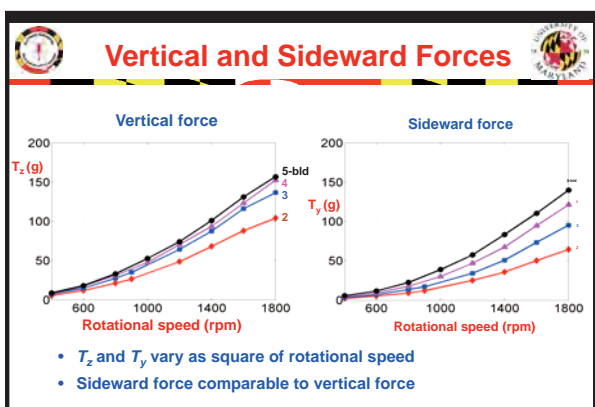
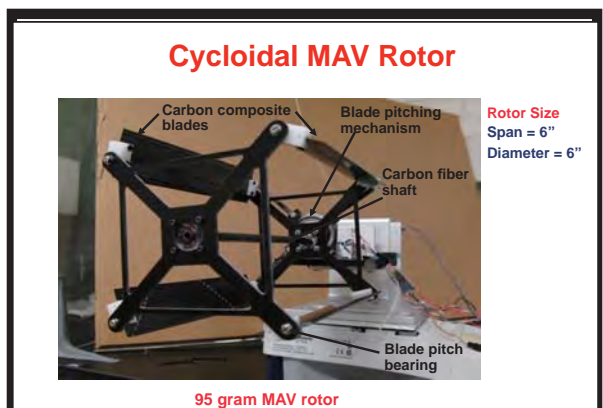
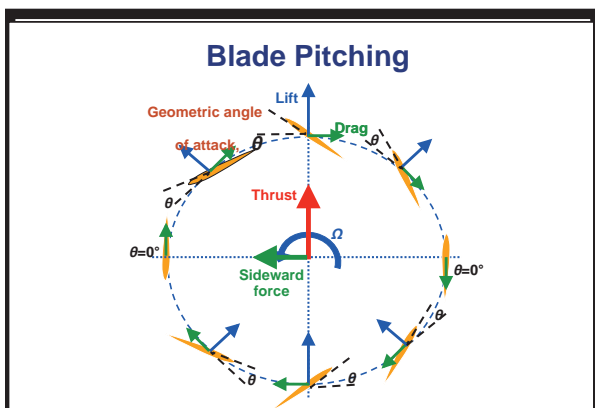
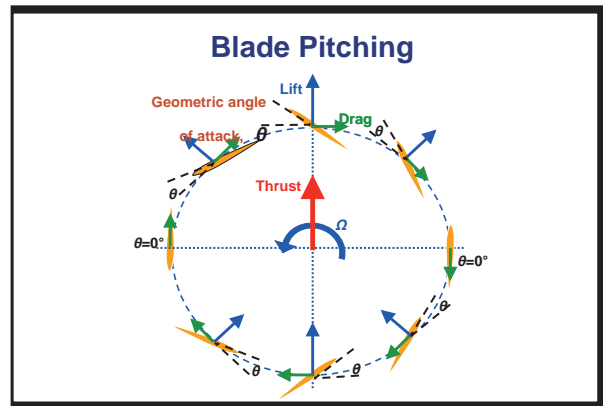
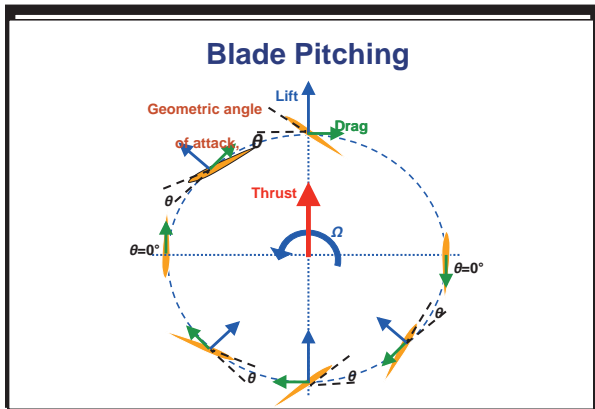
- High maneuverability: Instantaneous change of thrust vector
- All airfoils operate at maximum efficiency

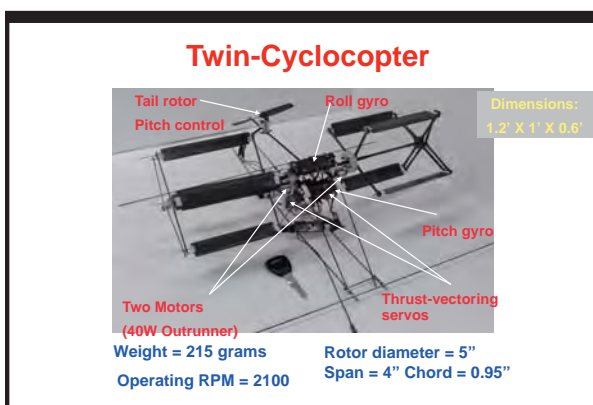
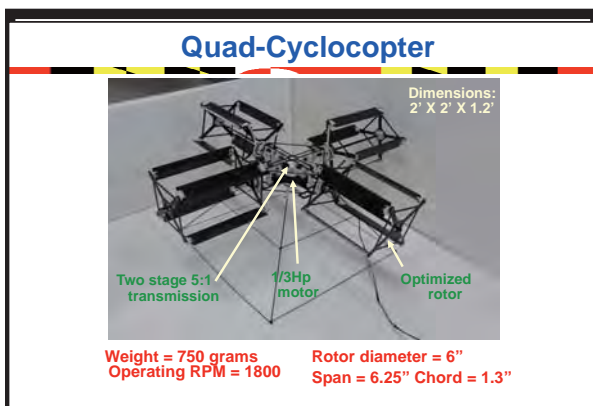
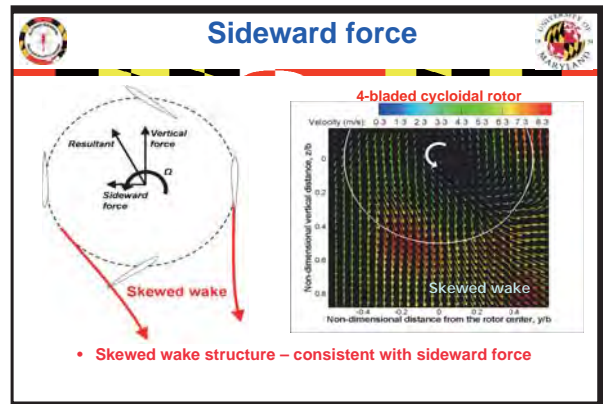
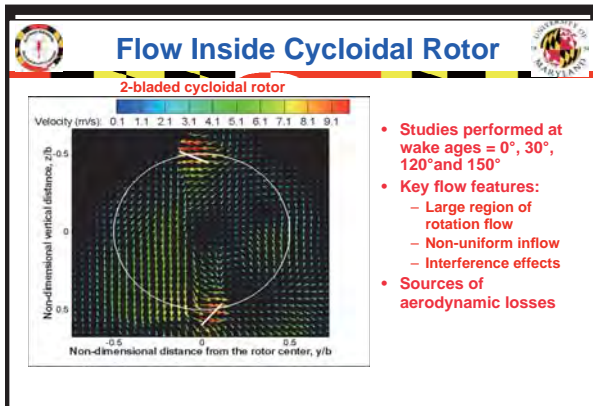
Major Concerns:

- Complex wake interaction
- Complexity of pitch change mechanism









Conclusions

- Power loading better than a conventional rotor
- Optimum cycloidal rotor based on parametric studies
 - 4-bladed, pitch amplitude = 40°, blade chord = 1.3"
- PIV measurements showed presence of a skewed wake
 - explaining side-force
- Absence of blade stall at high pitching amplitudes (45°)
 - high induced velocities in wake

Micro Hovering Air Vehicles: Flapping-Wing Based

Mechanism of Flapping-Wing Flight Insects vs Birds

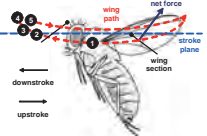



Birds vs Insects

Function	Bird	Insect
Weight	20g to 15 kg	Less than .2g
Size	0.15 to 3m	.1m and less
Aerodynamics	Quasi-steady Drag-reduction	Unsteady Lift enhancement
Morphing	Active wing morphing	Rigid wing, base motion
Wing frequency	Modest <10 Hz	High >50Hz
Hovering	Very rare	Quite common
Speed	High, wing morphing	Modest, tilting body and stroke plane
Reynolds No.	>10,000	<10,000

Insect Flight Fundamentals

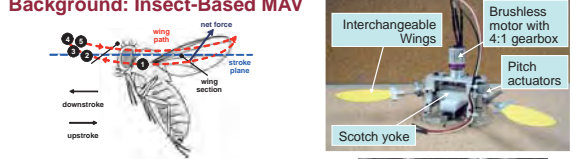
► The wing stroke of a hovering insect is divided into four kinematic stages:



1. **Upstroke** → **TRANSLATIONAL phase** – when the wings sweep through the air with a high pitch angle
2. **Downstroke** → **TRANSLATIONAL phase** – when the wings sweep through the air with a high pitch angle
3. **Pronation** → **ROTATIONAL phase** – when the wings rapidly rotate and reverse direction
4. **Supination** → **ROTATIONAL phase** – when the wings rapidly rotate and reverse direction

Flapping-Wing MAV


Background: Insect-Based MAV



- Examined insect-based flapping bio-mimetics.
- Hover-capable insect-based flapping causes delayed dynamic stall, rotational circulation and wake capture.
- A folded wake with the presence of multiple vortices on top and bottom surfaces.
- Key Parameters are: wing frequency, flap amplitude, pitch angle, aeroelastic couplings (flexibility)

Objective of Flapping-wing MAV

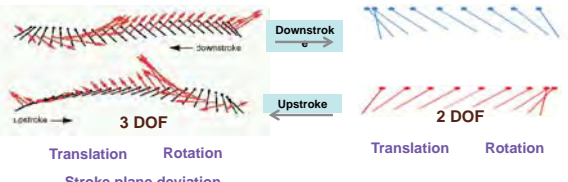
- Develop simplified flapping wing flight worthy system that can emulate insect kinematics
 - Simple and lightweight
- Exploit wing kinematics for control



CHALLENGE

- Heaviest hovering bird = 20 grams
- Flapping MAV with payload = 20 grams
- Gross Weight ~ 50 – 100 grams

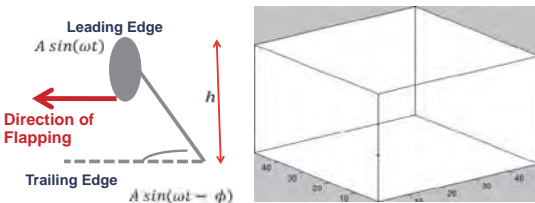
Flapping Mechanism



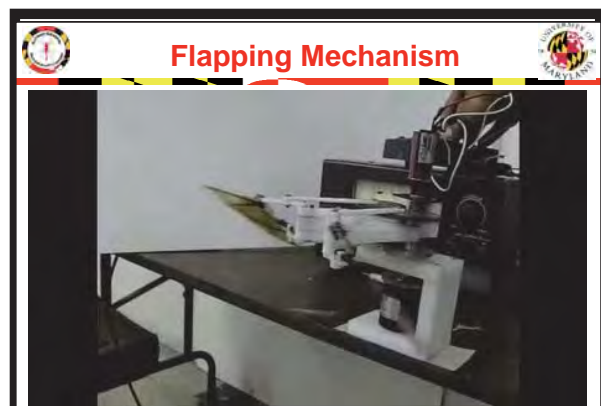
Insect Kinematics

Simplified Kinematics

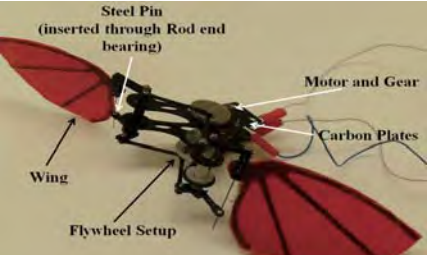
Flapping Mechanism Principle



$\theta = \tan^{-1} \left(\frac{A \sin(\omega t) - A \sin(\omega t - \phi)}{h} \right)$



Second Generation Flapping MAV



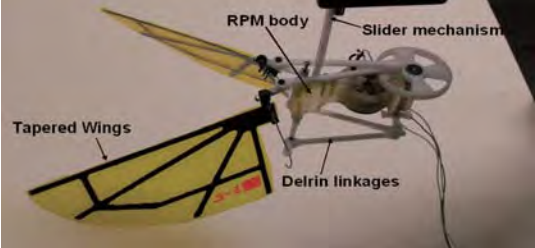
Wings hinged at different locations

Two carbon plates for increased stiffness

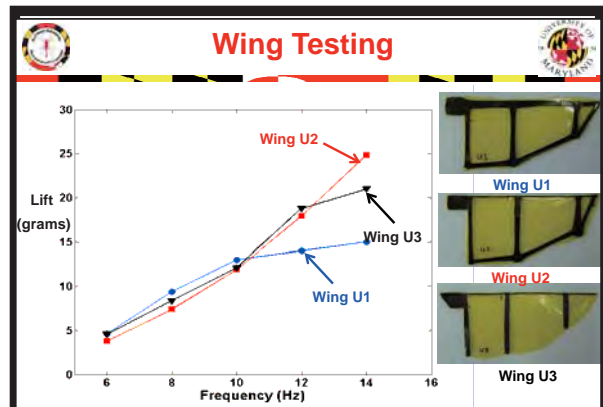
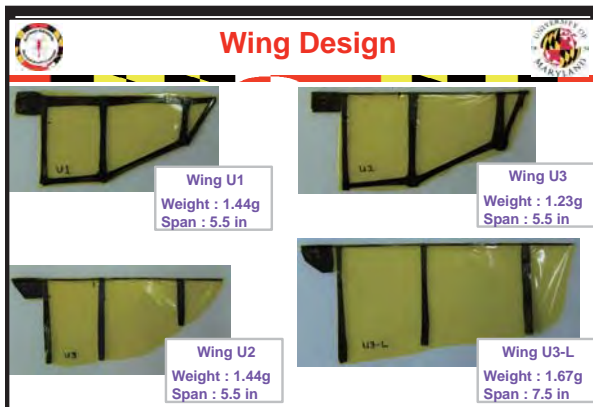
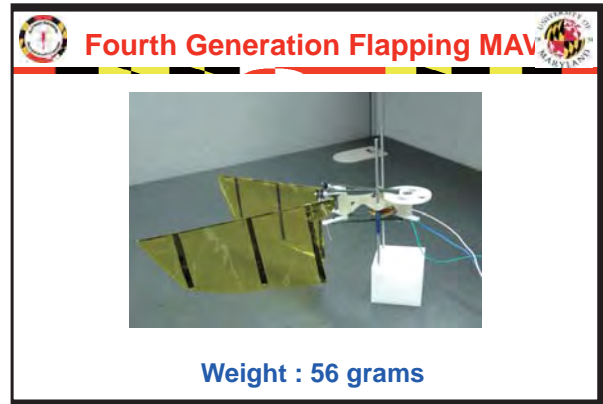
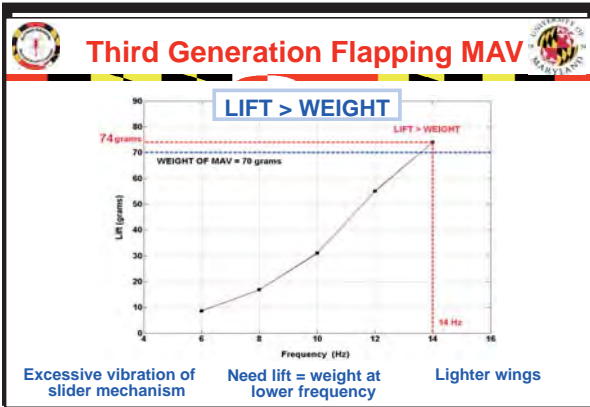
Total weight 130 grams

Motor power 140 W

Third Generation Flapping MAV



Weight : 70 grams



- ### Summary and Conclusions
- Demonstrated tethered hover capability of a 60 gram flapping MAV using insect kinematics
 - Active pitching improved MAV performance
 - Figure of merit 0.1 – 0.2
 - Wing design
 - Light – reduce power and inertial loads
 - Maintain bending stiffness and reduce torsional stiffness

Micro Flapper

Developed 10-g flapper and demonstrated yaw control in VICON and carried out detailed DPIV studies

Physics and Actuation of Flapping Flight

1) increase in stroke amplitude

2) tilt of stroke plane

Biomechanics / Control (Humbert)

0.25 1.0

Computational Fluids / Structures (Baeder / Chopra)

Particle Image Velocimetry (Leishman)

Conclusions

MAV is a multidisciplinary system and requires synthesis of:

- Aeromechanics (low Re)
- Micropropulsion
- Microelectronics
- Microprocessing
- Microfabrication

Many Challenges:

- Modeling and simulation
- Adaptive feedback controllers
- Communication and guidance
- Building and flight testing

Flight Inspired by Nature at Low Re

Propulsion and Power

- efficient batteries
- micro engines
- energy Storage/distribution

Sensing and Navigation

- miniature electronics
- Insect based guidance

Low Reynolds Number

- delayed Stall
- flow separation control
- wake capture

Biomimetic Kinematics

- actuation (thorax)
- efficiency
- frictionless

Lightweight Wing Structures

- active shape deformation
- wing morphing

Maneuvering Capability

- distributed control surfaces
- gust prone






Alfred Gessow Rotorcraft Center
 UNIVERSITY OF MARYLAND



Review of Rotorcraft Aeromechanics and Advanced Designs

Inderjit Chopra
 Director Alfred Gessow Rotorcraft Center &
 Alfred Gessow Professor of Aerospace Engineering


Presentation At: Korea Aerospace Research Institute (KARI), Daejeon
 June 27-30, 2011


Definition of Rotorcraft


An air vehicle whose primary means of vertical lift is a rotating airfoil

Is This Air Vehicle a Rotorcraft?


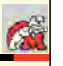
Yes Maybe No








Swashplateless Rotor with Integrated Flaps



MR RPM : 375 rpm
 Empty Weight: 1100 kg
 Fuel Weight: 150 kg
 Payload: 500 kg
 MTOW 1750 kg


Rotorcraft Aeromechanics Research


Today's Technology Drivers

- All round desire to increase performance & efficiency SFC, Figure of merit, power loading, L/D etc 
- Explosion of IT & wireless technology 
- Maturation of composite technology & upcoming smart structures technology 
- Availability of sophisticated prediction tools 
- Availability of miniaturized sensors & reliable measurement techniques 


Rotorcraft Aeromechanics Research


Today's Non-Technology Drivers

- All-round desire to reduce Cost! & Cost!! (Acquisition, maintenance and Operating: life cycle) 
- More Safety & ease of flying 
- Green legislations!!! Noise! & CO₂ level 
- More autonomy requirements 
- Runway saturation & terminal area gridlock 
- Asymmetric & urban warfare 



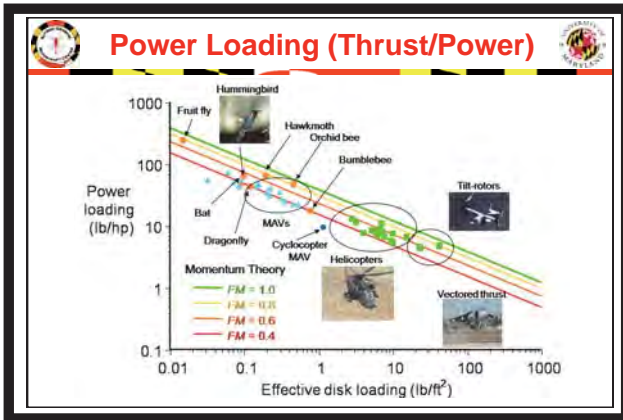

Index of Efficiency


Figure of Merit

$$FM = \frac{\text{Ideal Power required to hover}}{\text{Actual Power required to hover}}$$

Power Loading

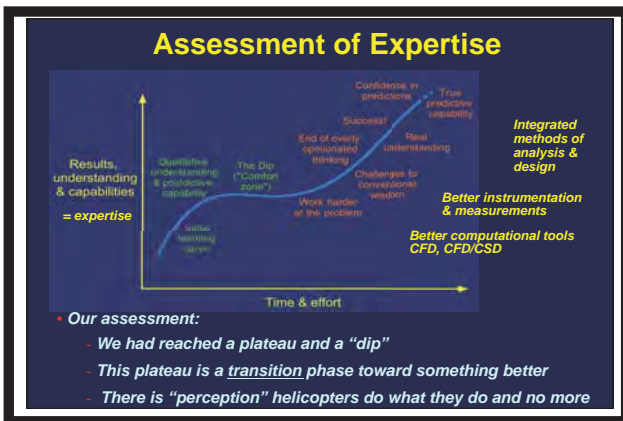
$$PL = \frac{\text{Thrust Produced}}{\text{Actual Power required}}$$



State-of-Art of Helicopter Technology

Speed	~150 Knots	Airplane of 1920's
Range	<500 nm	low
Payload	<40,000 lbs	low
Ceiling	<15,000 ft	low
Figure of merit	<0.8	Up from 0.6 in 1940
Lift-to-drag ratio	5-6	Up from 4-5 in 30 years
Productivity	Low c.f. of airplane	Small increase in 30 years
Vibration levels	High "	Uncomfortable
Noise levels	High "	Obtrusive

Despite all of the understanding of aeromechanics, why has the helicopter apparently reached a peak in its capabilities?
 By our estimate, it HASN'T!!
 But, we need to get better at implementing solutions to the problems!



- ### Postdictive Versus Predictive Capabilities
- **POSTDICTIVE modeling capability:**
 - Significant simplification of physics
 - Too many empirical "constants"
 - Usually operate on the "top" level
 - Calibrated to specific or "favorite" data sets
 - Cannot "predict" outside bounds of validation
 - **PREDICTIVE modeling capability:**
 - Requires in-depth understanding
 - Need very detailed experiments for proper validation
 - Built from upward from governing equations (first principle)
 - Appropriate predictive capability (especially for new configurations)
 - More expensive but needed for getting over the dip

- ### Why Does the "Dip" Happen?
- We reach our "comfort zone"
 - Rooted in "postdictive" capabilities
 - As methods are brought to bear on new problems, limitations realized
 - Priorities change or low (or no) funding for apparently "well-studied" problems
 - "Cultural barriers"
 - We close our wind tunnels!
 - Helicopter has "reached its peak"!
 - Expertise also slowly lost in time:
 - People move on, retire, etc.
 - We forget the fundamentals!
 - Fewer people with "sense of physics"
 - Experience not passed on effectively
 - Information hard to find (rediscovery!)
 - Work not written down in archival literature

- ### Continuation of "Dip"?
- **R&D Funds**
 - Erratic flow of funds
 - Following of milestones (creativity secondary)
 - Too much bureaucracy
 - **Future Rotorcraft**
 - Overindulgence in upgrades
 - Pursuing infeasible projects
 - Industry: too short sighted
 - **Government Laboratories (Buyers)**
 - Becoming weak in talent and facilities

Rotorcraft Aeromechanics



Coverage

Aeromechanics involves coupled, multi-, inter-disciplinary

- Dynamics (Aeroelasticity)
- Aerodynamics & Performance
- CFD
- Acoustics
- Flight Dynamics & Controls
- Composite Structures
- Transmission & Power-Trains
- Smart & Adaptive Structures

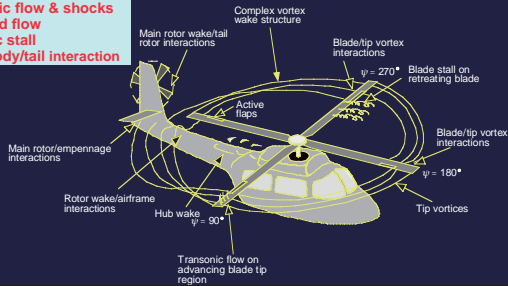


Aerodynamics

Aerodynamics: Challenges

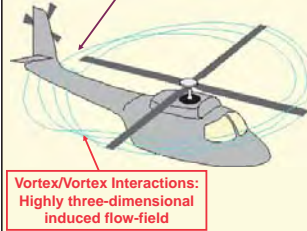
- Nonsteady and complex aerodynamics and rotor wakes

Transonic flow & shocks
Reversed flow
Dynamic stall
Rotor/body/tail interaction



Rotor Wakes

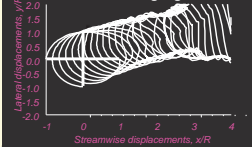
Main rotor wake interactions with fuselage, empennage, tail-rotor



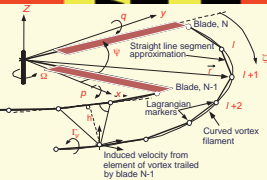
Free Vortex Wake Model

- Rotor wake modeled using vortex filaments
- Blade modeled by lifting lines (Weissinger L)
- Vortex filaments discretized into segments

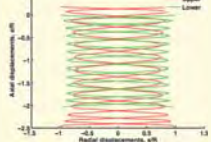
Rotor in maneuvering flight



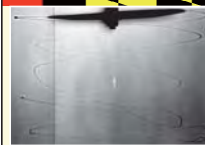
Rotor in Vortex Ring State



Coaxial rotor in hover



Rotor Wakes: Measurement



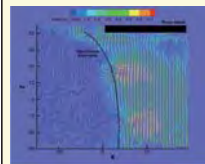
Wide-Field Shadowgraphy



Laser Doppler Velocimetry



Schlieren System



Particle Image Velocimetry

Future: DPS-DPIV (Dual-Plane Stereoscopic Digital Particle Image Velocimetry) can measure 3 velocity and 9 velocity gradients using 3 pair of lasers and 3 synchronized cameras.

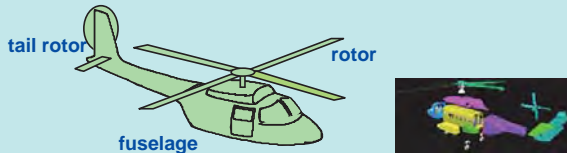
Aerodynamic Modeling: State-of-Art

	Past	Present	Future
Blade Aero	Lifting line Table-lookup Empirical stall	Indicial response functions for unsteady and dynamic stall	CFD/CSD tight coupling
Rotor Wake	Linear inflow Prescribed	Free wake Frequency & time-domain	CFD- generated wake capture
Airframe	Flat plate area	Table lookup Panel method	CFD rotor/ body coupled
CFD Modeling	Euler Uncoupled	Navier-Stokes CFD/CSD loose coupling	CFD/CSD tight coupling

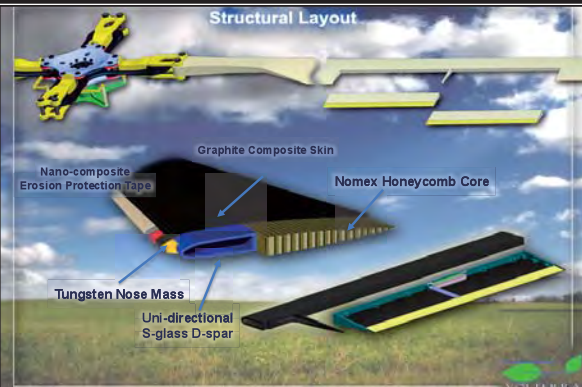
Structural Modeling

Structural Modeling: Challenges

- Coupled and nonlinear phenomena involving complex Coriolis/Gyroscopic forces
- Blade undergoing moderately large deformation involving coupled flap and lag bending, torsion and axial deformation
- Airframe 3-D structure with complex joints and nonuniformities



Structural Layout



Airframe Assembly



Composite Structures

Rotor and airframe are now increasingly being built out of composites

Key Issues:

- Modeling of composite blades and airframe (coupled, nonlinear, non-classical structural effects important)
- Structural integrity including ply delamination (flexbeam undergoing large dynamic twisting)
- Energy absorption due to landing and ballistic impact (off-axis landing, damaged blades)
- Repair of composites (field, depot and factory)

FEM vs Multibody

Classical FEM

- Typically uses single body coordinate frame
 - Deformations and loads in body coordinates
 - Topology dependent

Multibody

- Body and element coordinates
 - Deformation and loads in element coordinates
 - Increased scope of modeling

Multibody Analysis

- Increased scope of structural modeling
- Detailed modeling of control system and hub assembly
 - Exact pitch link, damper kinematics
 - Swashplate servo dynamics
- Large blade deformations
 - Moderate deformation within element frame
 - Large deformations accommodated by finite rotation of frames (important for maneuvering flight)

Structural Modeling: State-of-Art

	Past	Present	Future
Deflections	Moderate large Ordering scheme	Moderate/large	Large (no ordering)
Blade Modeling	FEM/modal	FEM/Multibody	Multibody
Airframe	Stick model	3-D FEM/modal	Multibody
Materials	Small strain Isotropic	Small strain Anisotropic	Large strain Coupled laminates

Rotorcraft Analysis

Rotorcraft Analysis: Challenges

- Governing Equations:** Coupled and nonlinear equations with periodic coefficients
- Solutions:** Trim and rotor response, aeroelastic stability, flight stability, transient response
- Steady Level Flight Analysis:** Periodic response analysis
- Non-Steady Maneuvering Analysis:** Time marching analysis

$$[A(\psi, y, \dot{y})]\{y\} = \{G(\psi, y, \dot{y})\}$$

Comprehensive rotorcraft codes: CAMRAD, RCAS, UMAC

Analyses: State-of-Art

	Past	Present	Future
Trim/Steady Response	Modal method/ Harmonic Balance	Modal/ Complete FEM time	Time integration coupled equations
CFD/CSD Coupling	Iteratively	Loose	Tight
Stability	Linear Modal/ Floquet	Linear Modal/ Full Floquet	Time marching Prony method
Maneuver Analysis	Modal/Time integration	Modal/Time integration	Fully coupled time marching

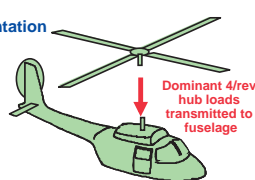
Dynamics

Dynamics

Interaction of structural, aerodynamics and inertial forces (aeroelasticity)

Issues:

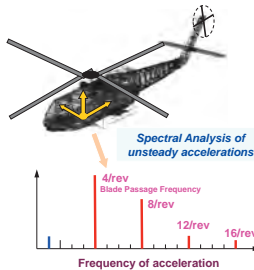
- Vibration & Loads:** prediction, measurement & suppression (level flight, maneuvering flight and gusty environment)
- Aeromechanical Stability:** augmentation (flap-lag flutter, pitch-flap flutter, ground/air resonance)



Dominant 4/rev hub loads transmitted to fuselage

Helicopter Vibration: Definition

Vibration : Accelerations in fuselage



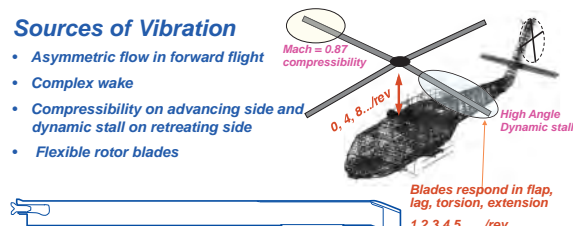
Spectral Analysis of unsteady accelerations

- Intrusion Index:** weighted mean of 4 largest frequencies in vertical, lateral and longitudinal directions up to 60 Hz
- Vibratory Forces:** Rotor blades are excited at all harmonics, only harmonics consisting integer multiples of blade number, pN_b/rev are filtered through hub
- 1/rev due to rotor asymmetry

Rotor Dynamics in Forward Flight

Sources of Vibration

- Asymmetric flow in forward flight
- Complex wake
- Compressibility on advancing side and dynamic stall on retreating side
- Flexible rotor blades



Mach = 0.87 compressibility

0, 4, 8, ... /rev

High Angle Dynamic stall

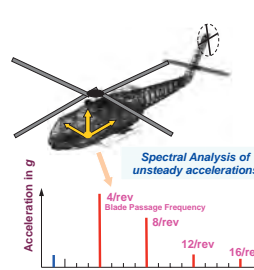
Blades respond in flap, lag, torsion, extension

1, 2, 3, 4, 5, ... /rev

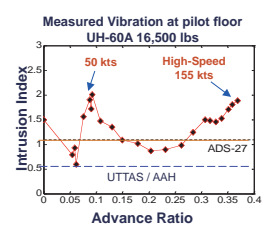
- Blades undergo moderately large deformations involving coupled flap, Lag, torsion and axial motion, nonlinear inertial couplings
- Airframe 3-D structure with complex joints and cutouts, Gyroscopic nonlinear couplings in vehicle dynamics

High Vibration: Flight Conditions

Vibration : Accelerations in fuselage



Spectral Analysis of unsteady accelerations



Measured Vibration at pilot floor UH-60A 16,500 lbs

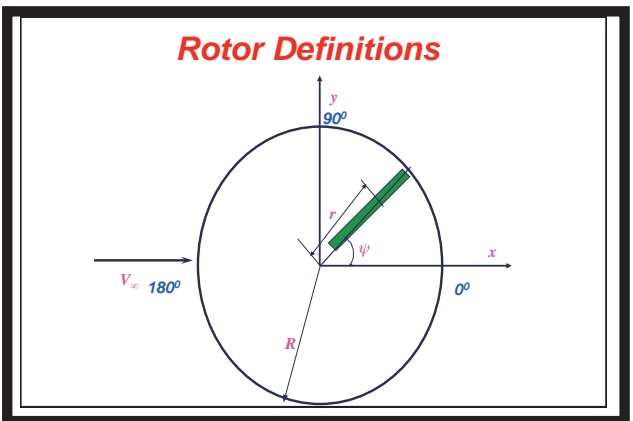
50 kts High-Speed 155 kts

Intrusion Index

Advance Ratio

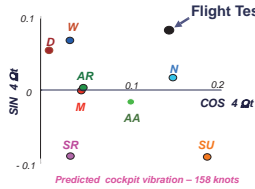
UTTAS / AAH ADS-27

- 3 Critical regimes : low speed transition, high speed, and high altitude-high thrust
- Enormous vibration: High operating cost, Reduced crew / system performance



Vibratory Loads at High Speed: Prediction vs. Flight Data in 1998

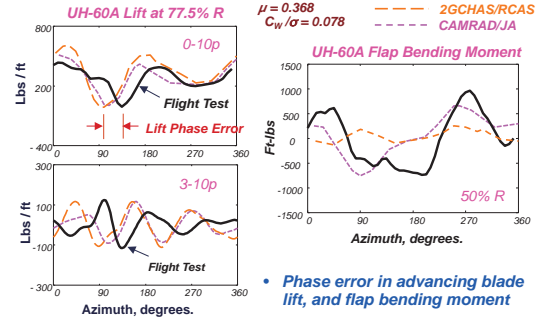
Predicted 4/rev vibratory hub load at high speed from 8 different rotor codes for LYNX



- None of predictions agreed with flight test data
- No two predictions agreed with each other
- LYNX Blades were not pressure instrumented, hence systematic correlation study with air loads and blade loads could not be possible

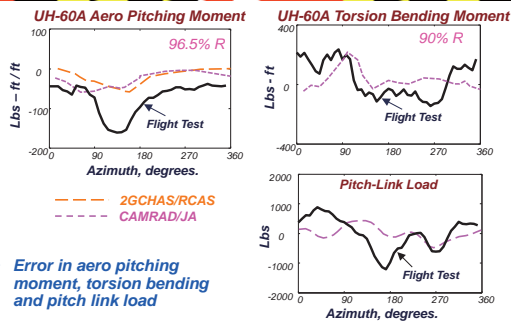
AA - 2GCHAS AR - Flightlab D - CRFM
M - UMARC (Maryland) N - CAMRAD1
SR - RDYNE SU - UMARC (Sikorsky)
W - R150

Vibratory Loads at High Speed: Prediction vs. Flight in 2000



- Phase error in advancing blade lift, and flap bending moment

Vibratory Loads at High Speed: Prediction vs Flight in 2000



- Error in aero pitching moment, torsion bending and pitch link load

Vibration Validation Study

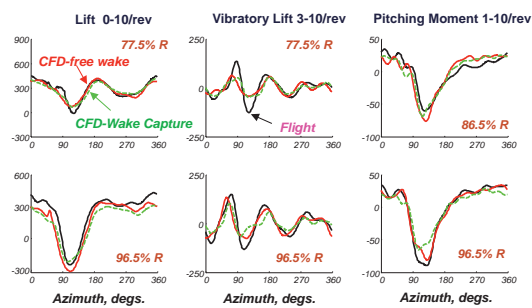
Major undertaking in 2001: Team involving industry, academia, NASA/ Army to resolve vibration barrier issues. Loads Workshop: Meet every 6 months since 2001

Vehicle: UH-60A Black Hawk, extensive flight test data with pressure instrumented blades

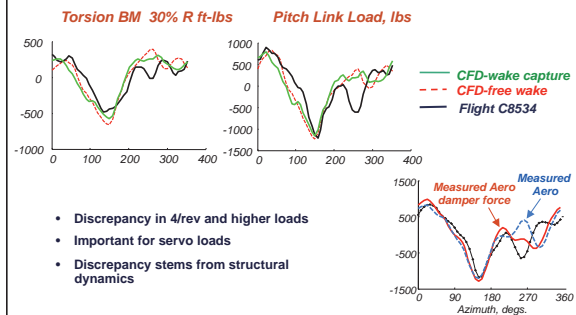
Identified 4 critical flight conditions:

- Level Flight:**
1. High speed $\mu = 0.37$ UH-60A flight 8534
 2. Low speed transition $\mu = 0.15$ UH-60A flight 8513
 3. High altitude dynamic stall $\mu = 0.24$ UH-60A flight 9017
- Maneuver:**
4. Severe UTTAS pull-up Maneuver $\mu = 0.341$ UH-60A flight 11029 (load factor = 2.09)

High Speed: CFD/CSD coupled Solution: First barrier problem resolved

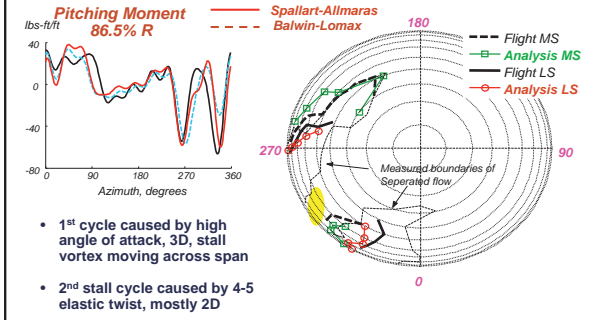


Pitch Link Load at high speed: CFD/CSD Second barrier problem resolved



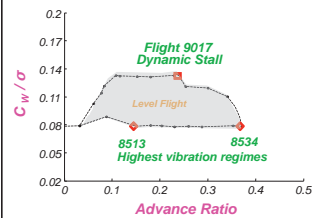
- Discrepancy in 4/rev and higher loads
- Important for servo loads
- Discrepancy stems from structural dynamics

Predicted Pitching Moment and Stall Map at High Altitude & High Thrust



- 1st cycle caused by high angle of attack, 3D, stall vortex moving across span
- 2nd stall cycle caused by 4-5 elastic twist, mostly 2D

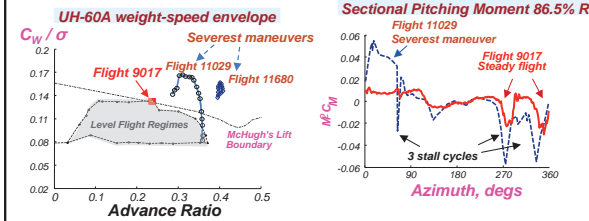
3 Critical Flight Conditions: Level Flight



- CFD challenges:**
- Low Speed : Grid for wake capture
 - High speed : 3D transonic effects on pitching moment
 - High altitude: turbulence modeling for dynamic stall
- CSD challenges:**
- Low Speed : 3/rev flap bending
 - High speed : Elastic twist low frequency
 - High altitude : Elastic twist high frequency

Separate mechanisms: wake, transonic effect, and dynamic stall

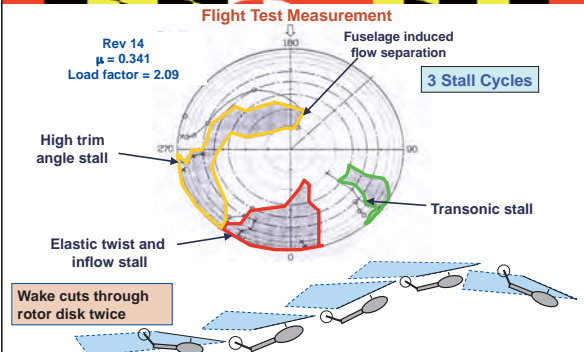
4th Critical Flight: Pull-Up Maneuvering Flight



- Design loads set by severe maneuvers under stall
- C11029 : 2.12 g pull up at 139 kts, highest flap bending, and Pitch-Link (PL) load, severest maneuver

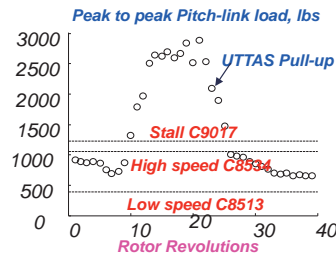
- C9017 stall similar to severest maneuver
- Compressibility, dynamic stall and wake all occur simultaneously in maneuvering flight

Flight 11029, Severest UH-60A Maneuver: Stall Map



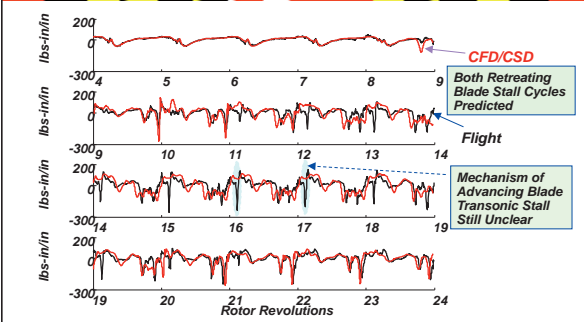
UTTAS Pull-up Maneuver

- Flight 11029**
- Based on Utility Tactical Transport Aerial System (UTTAS)
 - Third highest pitch link load (2.5 times steady flight)
 - Highest root flap bending moment

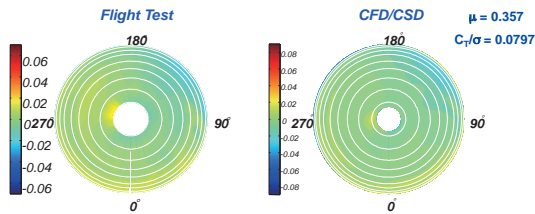


High Loads: Dynamic stall, vortex loading, transonic effects can occur simultaneously

Pitching Moment: 86.5%R

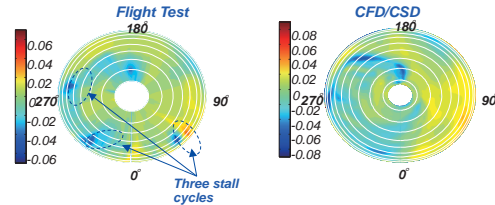


Pitching Moment: Level Flight Rev 1



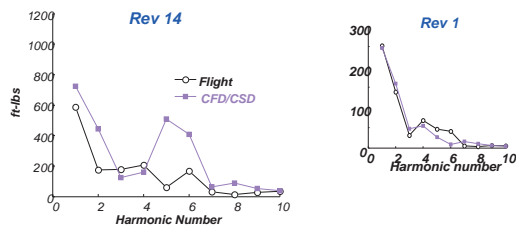
- Pitching moment variation during steady flight regime benign
 - shows no steep gradients across the rotor disk
- Prediction show good correlation with flight test

Pitching Moment: Maneuver Rev 14



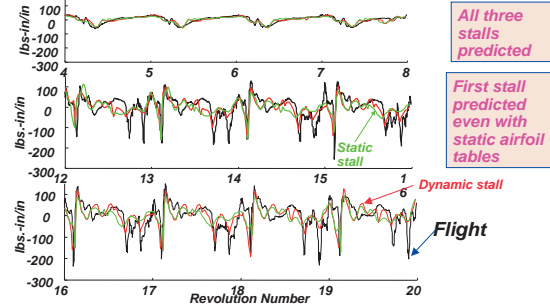
- Pitching moment variation during maneuver shows steep gradients
 - Three stall cycles
- Prediction show good correlation for two stall cycles on retreating side – **advancing blade stall not predicted**

Torsion Moment Harmonics: 30%R

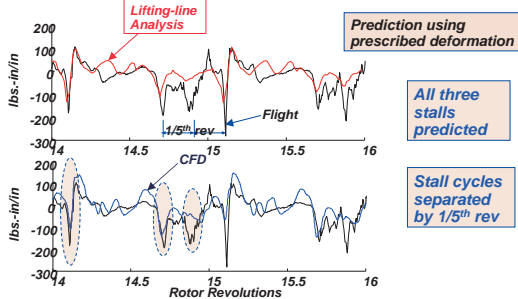


- Over-prediction of 40%–60% in the peak-to-peak magnitude
 - over-prediction of 5 and 6 rev torsional moment stemming from over-prediction of pitching moment stall peaks

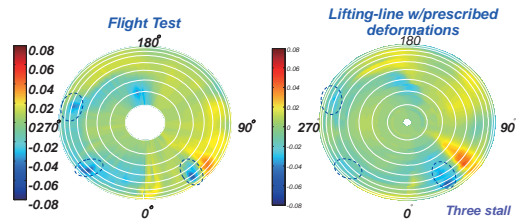
Pitching Moment Using Prescribed Deformation (From Measured Airloads): 86.5%R



Pitching Moment Using Prescribed Deformation: 86.5%R



Pitching Moment C11029: Rev 18



Advancing blade stall predicted accurately

Prediction of Vibratory Loads

Critical Flight Conditions:

- High speed forward flight: vibration
- Low speed transition flight: vibration
- High altitude dynamic stall: loads
- Severe maneuvers: pitch link loads

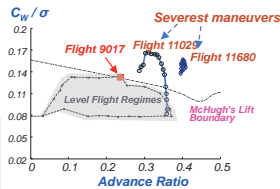
Key Conclusions:

CFD provides fundamental capability

- At high speed: 3D unsteady transonic pitching moment

- At low speed: capturing of inter-twinning of wakes

- For dynamic stall flight: capturing of second cycle due to 4 and 5P twist, placement depends upon wake and turbulence model



Pull-Up Maneuver:

3 dynamic stall cycles, Advancing-side stall triggered by 5rev twist. Two dynamic stall cycles on retreating side separated by 1/5th cycle excites 5/rev twist deformation

Vibration and Loads

Suppression

Currently: passive devices such as absorbers and isolators routinely used, also avoid rotor harmonics coupling with airframe modes

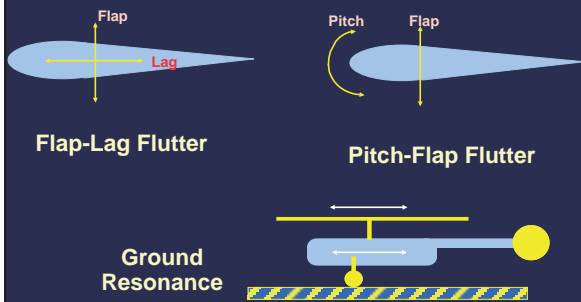
- mostly ad-hoc approaches
- extensive weight penalty (up to 3% of gross weight)



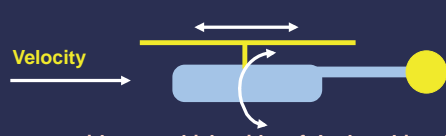
Future: towards active vibration control and structural optimization of rotor and airframe using robust prediction methodology

Goal: Reduction in vibratory loads by one-third from current values, weight penalty less than 1% of gross weight

Aeromechanical Stability



Air Resonance



- Occurs on airborne vehicle with soft-Inplane hingeless and bearingless rotors
- Caused by coupling of low frequency flap & lag modes and body airframe modes (aerodynamics very important)
- Soft Instability: To stabilize, needs mechanical damping in lag mode or negative pitch-lag coupling

Aeromechanical Stability

Prediction: For hover & forward flight with normal loading, current analyses predict satisfactorily for hingeless & bearingless rotors

- Needs robust aerodynamic modeling (dynamic stall) for highly loaded rotors (maneuvers)
- Needs refined structural model for complex hubs (bearingless rotors)

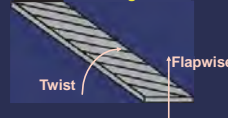
Measurement: Challenging to measure high damping modes

Stability Augmentation: Mechanical dampers routinely used
Possibility of using composite couplings to increase stability

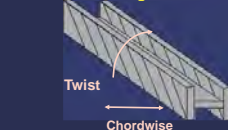
Goal: Build a damperless rotor

Stability Augmentation: Tailored Composite Rotor

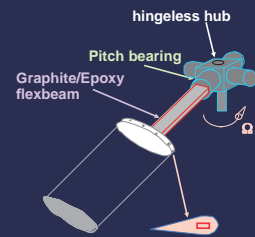
Flapwise bending-torsion

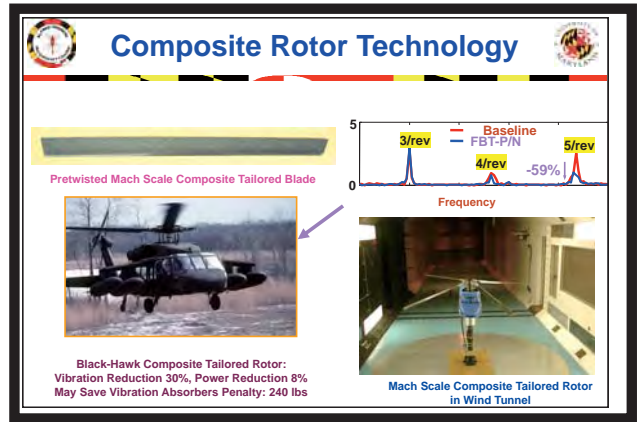
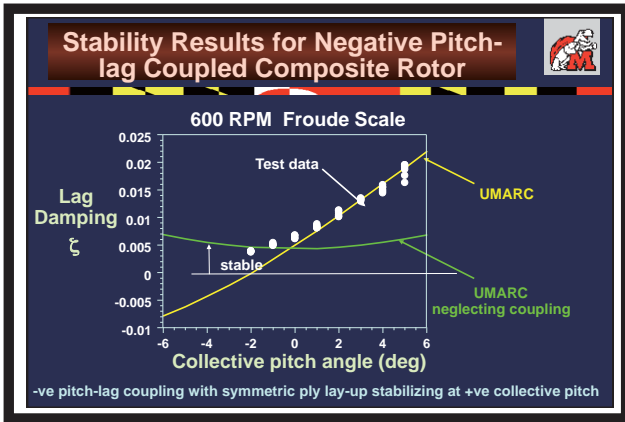


Chordwise bending-torsion



Stability Testing





Dynamics: State-of-Art

	Past	Present	Future
Vibration Prediction (normal flight) Prediction (Maneuvering) Suppression	>50% error Not reliable Passive Penalty 3% GW	~ 20% error Inadequate tools Passive/active (few) 1-3% penalty	<10% desirable ~10% desirable Active/passive/Optimized <1% penalty
Composites Couplings	Tools development	Showed potential to improve vibration and stability, but no implementation	Composite tailoring Full-scale implementation for performance and stability
Aeromechanical Stability Prediction (Normal flight) Prediction (Maneuvering) Suppression	Adequate for conventional rotors Inadequate Hydraulic/Elastomeric	Adequate for advanced rotors Tools development Elastomeric	Exploit couplings Reliable tools needed Damperness

Acoustics

External/Internal Acoustics

Rotorcraft suffer from too much noise

External Aeroacoustics:

- Blade Vortex Interaction (BVI) low speed noise
- High speed impulsive (HSI) noise (transonic waves)
- Low frequency noise (thickness and loading)

Internal Airframe Acoustics:
Rotors, transmission and gear boxes

Rotor Aeroacoustics

Predictive capability
CFD/CSD coupled analysis to predict noise source (unsteady pressure) and apply in acoustic propagation scheme (Fflowcs-Williams-Hawkin) Prediction less than satisfactory.

Noise Control

Passive Blade Design: Tip shape, aspect ratio, number of blades and tip speed using CFD tools, uneven blade spacing in fenestron (tail rotor).

Flight Path Management: Optic-based tip-path-plane tracking system to direct flight trajectory for minimum noise.

Active noise control: Using trailing-edge and leading-edge slats, actively control phasing and miss distance of vortices, and low frequency detection noise.

Goal: 5-10 db reduction of noise

Blade-Vortex Interaction Noise

When a trailing tip vortex intersects another blade, dramatic aerodynamic changes occur which generate noise

Results - Sweep Effect

Hover Tip Mach No. = 0.90; In-Plane Mach Contours

Forward Swept

Not Delocalized
Shock Bends Forward & Weakens

Rectangular

Backward Swept

- Large noise reduction for forward swept rotor
- Strong phasing effects with sweep

Results - Individual Parameter

Hover Tip Mach No. = 0.90; In-Plane Mach Contours

Forward Dogleg

Thin

Taper

- Greater noise reduction for thin and swept rotors
- Shock bends forward for swept blade

Flight Path Management for Noise Control

Technology Goal: Control External Noise by Control of Main Rotor Tip-Path-Plane (TPP) Angle using high-resolution camera. Successfully flight tested on Bell 206 & 407.

In-Flight Laser/Optical Measurement System

Rotorcraft Internal Acoustics

Motivation: Undesirable interior noise levels
Main/tail rotors & gas turbines (40-500 Hz), gears (500-6000Hz)

Passive means for noise reduction: Constrained layer damping and piezo shunting for high frequency suppression

Active noise control: Using piezo patches on fuselage frame and trim panels and with adaptive control strategies for low frequency suppression, active transmission mounts and constrained layer damping for high frequency noise

Goal: 20 db reduction of noise

Acoustics: State-of-Art

	Past	Present	Future
Exterior Noise Prediction	Lifting-line & Ffowcs-Williams-Hawkins (FWH) Not satisfactory	CFD & FWH loose coupling Not satisfactory	CFD/CSD & FWH tight coupling Validations
Exterior Noise Suppression	Passive	Passive	Passive/Active/ Flight path management
Interior Noise Suppression	Passive	Passive	Passive/Active

Flight Mechanics and Controls



Key Issues:

- System identification for coupled rotor-fuselage system for a wide frequency band
- Flight control systems for mission tailored handling qualities
- High quality simulations, real and non-real time

Barriers:

- Free wake modeling for maneuvering flight
- Robust system ID tools
- Modeling of multidisciplinary phenomena

Advanced Rotor Systems

Swashplateless Rotor

Conventional Helicopter Primary Flight Control



- Conventional helicopter flight control system via swashplate mechanism
 - Main rotor collective system (controls thrust)
 - Main rotor cyclic system (controls direction of thrust)
- Swashplate system involves pitch links, pushrods, and fixed frame hydraulic actuators
 - Weight & drag penalty
 - Mechanical complexity

Bo105M

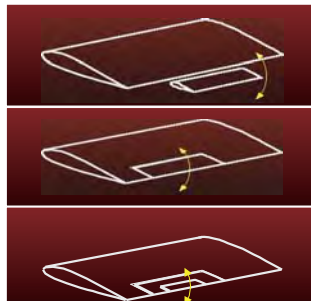


Swashplate System

Flap Configurations



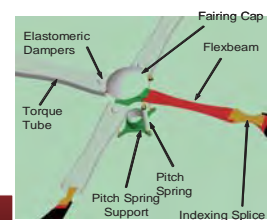
- **Servo Flap**
 - ▶ Large pitch moments
 - ▶ Exposed linkages, large drag
 - ▶ Hinge gaps reduce effectiveness
- **Integrated flap**
 - Modify lift & pitching moment
 - Internally mounted actuator and linkages (smart actuation)
- **Tab-actuated flap**
 - Tab moves flap
 - Modify lift & pitching moment
 - Least actuation power



Swashplateless Rotor System



- Swashplateless flight control via smart trailing-edge flaps
 - ▶ Flap deflections: collective and cyclic: in turn induce collective and cyclic blade pitch motion
 - ▶ Requires torsionally soft blade with blade pitch indexing
 - ▶ Potential of low drag and lightweight primary control
 - ▶ Hydraulicless system



Swashplateless System

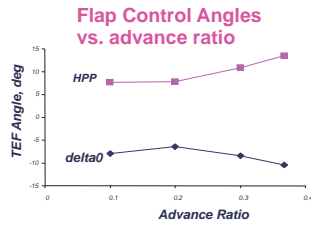


Primary Flight Control Requirements

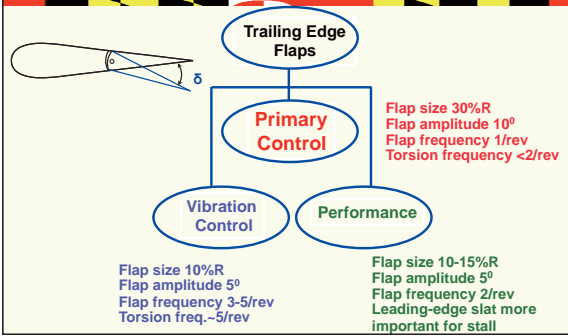


- Black Hawk
- $C_W/\sigma = 0.0783$ (16500 lb)
- $V_\theta = 2.0$ /rev
- $\theta_{dx} = 15^\circ$

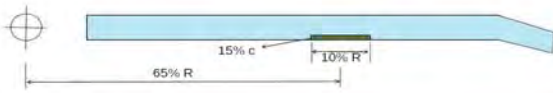
Primary control requires greater flap angles and hinge moments



Trailing Edge Flaps Rotor

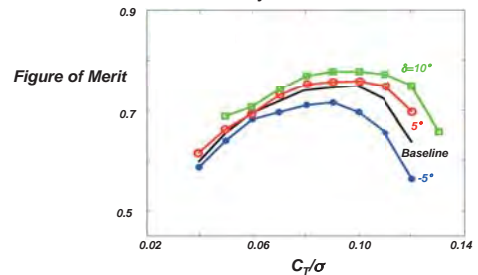


- **TEF geometry**
 - 10% span, 15% chord, midspan at 65%R
- **TEF operation**
 - Primarily moment flap
 - Alters section pitching moment and induces blade twist
 - Effect of reducing blade torsional stiffness on TE flap effectiveness



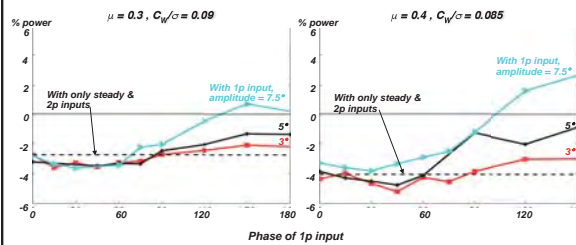
Hover Performance

Effect of steady TEF deflections



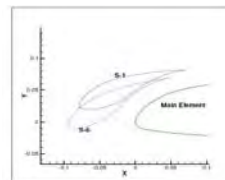
TEF geometry : 10%R, 15%c, mid-span at 65%R

Rotor Performance with Trailing-Edge Flaps

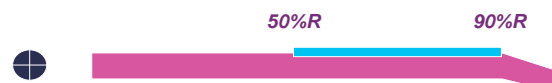


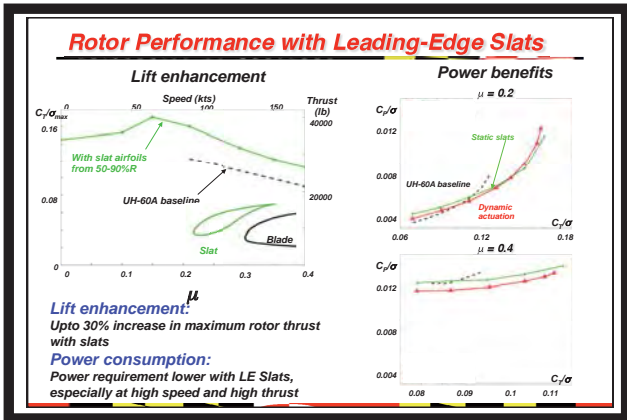
- Over 5% power reduction possible:
- Using a combination of steady, 1/rev and 2/rev flap inputs
 - Flap geometry : 10% span, 15% chord, midspan at 65% blade span

Leading Edge Slat Geometry



- S1 – Baseline position
- S6 – High Lift position
- Slat is ~15% of baseline chord





Trailing Edge Flaps Rotor

Past: Kaman SH-2 servo-flap rotor operational since 60s, servo-flaps for primary controls (collective & cyclic)

Present: Feasibility studies of integrated flaps to minimize vibration and noise using IBC (individual blade control)
Flight test: Eurocopter-Germany: BK117
Full-scale tunnel tests: Boeing-Mesa: MD900

Future: Development of full-scale integrated smart flap rotors for primary control (Eurocopter, Sikorsky, Boeing)

SH-2

Bo105

MD 900

Smart Rotor

Smart Rotor

Application of smart structures technology to actively control vibration, noise, stability and performance
Concepts: Flaps, blade twist, active tips

Present: Feasibility studies: Smart flaps
 UM: successfully tested Mach-scaled models
 Boeing: full-scale tests in 40x80 tunnel (April 08)
 Eurocopter: successfully flight tested Sept 2006

Future: Full-scale smart rotor for primary and noise control and performance enhancement: Sikorsky, Eurocopter & Boeing

Challenges: actuators stroke, integrity

Smart Structures Activities at Maryland

6-ft dia Froude scale rotor model in Glenn Martin Wind tunnel: active twist with embedded piezoelectric elements

6-ft dia Mach scale rotor model in Glenn Martin Wind tunnel: trailing edge flaps actuated with multi-layered piezobimorphs

6-ft dia Mach scale rotor model on hover tower: tip actuated with embedded piezos in conjunctions with bending-torsion composite couplings

Example: Technology Transfer

Smart Structures Technology

Smart Actuator Development:
Piezostacks with L-L Amplification

Smart Rotor Development:
Mach-Scale with Piezo Actuated Flap

Boeing: Full-Scale Smart Rotor Development:
 MD-900 Rotor with Smart Flaps, Ready for Flight Testing for Active Vibration Control (expects >80%)

Smart Structures: Enormous Potential to Minimize Vibration & Noise and improve performance

Smart Rotor Test in Glenn Martin Tunnel Mach-Scale with Smart Flaps

Eurocopter: Trailing Edge Flaps

trailing edge flaps

piezoelectric actuators

Flaps sized for vibration control
Must be scaled up for primary flight control

- BK 117 rotor blade with piezoactuated trailing edge flaps
- Successfully flight tested September 2006

Boeing: Trailing Edge Flaps

trailing edge flaps

MD900 rotor blade with piezoactuated trailing edge flaps
Successfully hover tested in May 2004
Successfully tested in 40x80 wind tunnel in April 2008

Flaps sized for vibration control
Must be scaled up for primary flight control

Tiltrotor Aircraft

Tiltrotor Dynamics Issues

- **Aeroelastic instabilities**
 - Rotor instabilities
 - Fixed-wing instabilities
 - Tiltrotor whirl flutter
- **Loads & Vibration**
 - Rotor-wing-body-tail interactional aerodynamics
 - Fountain effect
 - Gust loading
 - Tail buffeting
 - Conversion flight mode

Tiltrotor Aircraft

Past: Bell XV-15 flight tested successfully Whirl flutter stability and tail buffeting were major issues; Bell-Boeing V-22 fully operational and large descent speed a major concern (flight stability).

Present: Bell-Agusta 609 Civil tiltrotor under development, dynamics problems and performance.

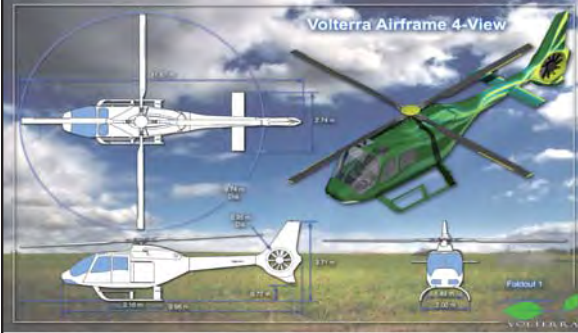
Future: High speed heavy-lift tiltrotor with variable speed morphing rotor; and Quad-rotor

Challenges: Complexity and cost, variable speed engine, high speed dynamic instability

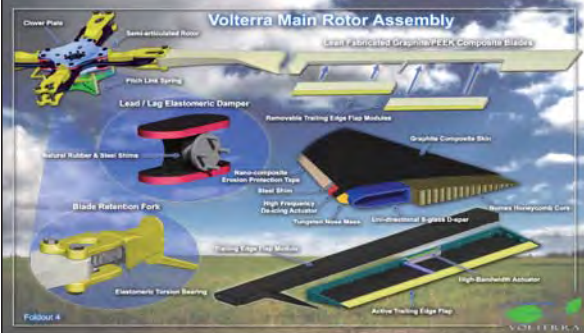
Challenges

- Whirl Flutter instability in high speed flight
- Interactional Aerodynamics Modeling
- Detailed Drive-shaft Dynamics
- Tail Buffeting
- Gust Response
- Detailed Hub and Gimbal Modeling
- Multi-rotor Wake Geometry

UM Winning Designs (2008): Green Helicopter



Volterra: Rotor Hub Assembly

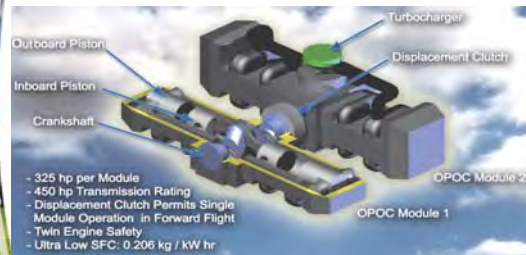


Volterra Performance Summary

	Volterra	EC-120B	Bell 206B3
Standard Accommodation	1 + 4	2 + 3	1 + 4
Design Gross Weight	1750 kg (3858 lb)	1715 kg (3780 lb)	1451 kg (3198 lb)
Useful load	500 kg (1102 lb)	404 kg (891 lb)	393 kg (866 lb)
Fuel Capacity	150 kg (43.5 gal)	321 kg (107 gal)	281 kg (91 gal)
Speed for best range	198 km/hr (107 knots)	204 km/hr (110 knots)	213 km/hr (115 knots)
Speed for best endurance	124 km/hr (67 knots)	120 km/hr (65 knots)	96 km/hr (52 knots)
Fast cruise speed	222 km/hr (120 knots)	222 km/hr (120 knots)	223 km/hr (121 knots)
HIGE Ceiling (ISA+20 deg C)	2238 m (7343 ft)	518 m (1700 ft)	914 m (2998 ft)
Maximum range	708 km (382 n.m.)	710 km (383 n.m.)	693 km (374 n.m.)
Maximum endurance	3 hr 34 min	4 hr 19 min	4 hr 30 min
Specific fuel consumption (SFC)	0.206 kg/kw-hr	0.26 kg/kw-hr	0.33 kg/kw-hr
Acquisition price	\$0.9 million	\$1.45 million	\$1.3 million
Direct operating costs (DOC) \$ / FH	\$ 104 / FH	\$ 231 / FH	\$ 235 / FH

Powerplant - OPOC Engine

Opposed-Piston/Opposed-Cylinder

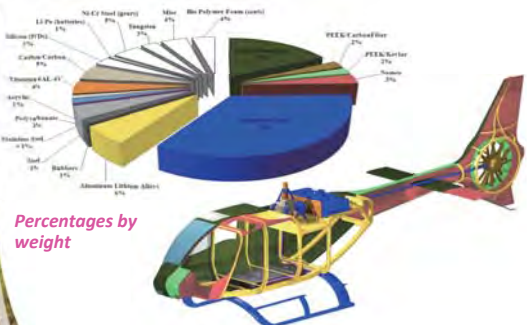
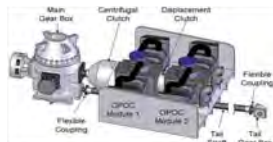


Powerplant - OPOC Engine

Engine	Type	Specific Power (kW/kg)	SFC (lb/hp-hr)	SFC (kg/kW-hr)
Teledyne Brown Engine	Piston	1.2	0.550	0.335
Rolls-Royce 250-C30P	Turbine	2.5	0.592	0.36
Turbomeca TM-333	Turbine	2.8	0.513	0.312
OPOC Engine	Piston	1.96	0.339	0.206

In summary the OPOC is:

- Cost effective
- Highly efficient
- Cleaner burning
- Multi-module versatile
- Multi-fuel versatile



Percentages by weight

AHS Design 2009 - The Griffin

- 2009 AHS Student Design Competition: Design of a non-conventional rotor/drive system with improved speed, range, payload and noise signature over a baseline in-service design
- University of Maryland designed the Griffin and its VERITAS: Variable Energy Rotor and Innovative Transmission ArchitectureS, improving on the EC-145



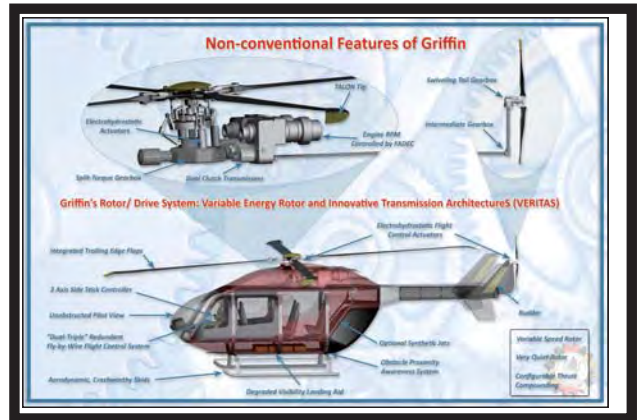
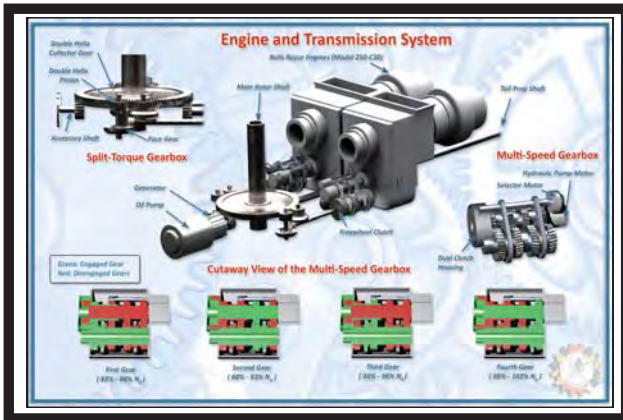
Core Features

- Main Rotor**
 - Innovative TALON blade tip: incorporates sweep, taper, anhedral and leading edge notch: reduced compressibility and blade stall penalties and increased figure of merit
 - Integrated trailing edge flaps: near 100% vibration suppression. Driven by lightweight electric DC motors rather than expensive smart actuators
- Swiveling Tail-Prop**
 - Dual-functional tail prop: anti-torque in hover and propulsion in forward flight
 - Conversion from anti-torque to thrust compounding mode performed automatically
 - Vertical stabilizers: sufficient anti-torque in the propeller configuration



VERITAS - Engine and Drivetrain

- Baseline Turbomeca Arriel 1E2 engines replaced with Rolls Royce 250-C30 engines: Lower specific fuel consumption (SFC), greener than the baseline
- Multi-speed main rotor gearbox: continuous and efficient rotor speed modulation over a 20% range of rotational speed
- Innovative dual-clutch mechanism: smooth and uninterrupted power delivery at all flight and rotor speeds
- Superior corrosion resistance and significant weight reduction
- Drivetrain Safety Features: automatic start-up, engine re-light, surge detection and recovery
- Extensive Health and Usage Monitoring System (HUMS)



Conclusions

- ✓ 77% increase in payload delivery efficiency
- ✓ 22% increase in productivity
- ✓ Total cost of ownership over an assumed 20 year service life: \$18.6 million for *Griffin* - nearly a 5% savings over EC-145
- ✓ *Griffin's* performance meets, and in some cases exceeds, the requirements of the DARPA Mission Adaptive Rotor (MAR) Program

Aerodynamics and Dynamics of High Speed Coaxial Rotor Systems

Objective: Develop comprehensive aeromechanics analysis of coaxial rotor system.

Advantages: Compact size (lower foot print), no tail rotor, lower aerodynamic asymmetry in forward flight

Disadvantages: Aerodynamic interference between rotors, complex hub and swashplate (more drag), poor yaw control

Challenges: Limited aeromechanics analysis, aerodynamic interference, trim complexity, variable speed impact (power train, performance and rotor separation)

Future: Sikorsky has built X2 high speed coaxial rotor with proprotor to achieve 250 knots, Sikorsky is also building X2 crane as a heavy lifter. Coaxial UAVs possible.

Rotorcraft Brownout

Brownout: Loose dust, sand, snow, etc. blown up by rotor flow in ground effect (IGE) Cloud of visually restrictive material causes pilot to lose outside visual references and situational awareness. Significant number of accidents caused by brownout.

Objective: Develop comprehensive understanding and mitigation of "brownout" of rotorcraft

Challenges: Interdisciplinary phenomenon involving rotor wake near ground effect and sediment (dust) particle dynamics (particles mass, size and shape, and uplift process)

- highly unsteady 3-D "jet-like" flow
- Embedded vortices near the ground
- 2-Phase fluids with fluid particle and particle/particle collisions

Airforce-MURI: Rotorcraft Brownout: Advanced Understanding, Control, and Mitigation

Objective: Develop a design methodology that will capture physical mechanisms of potential mitigation solutions of rotorcraft brownouts

Team: UM (lead), Arizona State University, Iowa State, Dartmouth College
5 years program (2008-13)

Task-1	Fundamental of Rotor and Airframe Aerodynamics in Ground Effect Operations
Task-2	Fundamentals of Particle Suspension
Task-3	Brownout Synthesis Mitigation and Validation

Flight Dynamics and Stabilization with Suspended Loads in High-Speed Flight

Objective: Study aerodynamics, dynamics and flight stability of a suspended load in hover and forward flight, examine role of unsteady aerodynamics and nonlinearities.

Background & Challenges: In high speed, possibility of dynamic instabilities of suspended loads, but would increase radius of action and productivity index, predictions poor; unsteady aero of sling load important, aero nonlinear, stabilizing challenging, lock-in phenomenon of large amplitude motion

Technical Approach:

1. CFD based model of containers and bluff body
2. Develop transfer function type aerodynamic models
3. Develop dynamic model of rotorcraft with suspended load
4. Investigate trim, aeromechanical stability, handling qualities and dynamic loads
5. Suspended load model tests in GLM Tunnel and validations
6. Stabilization of suspended loads using static and active controls

Major Outcome: Increase speed of rotorcraft with suspended load, improve handling qualities and reduce pilot work load, increase load carrying productivity index

Rotorcraft Technology Needs

Technology Needs

- **High Performance index**
 - Low airframe drag (exploit CFD)
 - Modular engine, high SFC
 - Variable speed transmission (exploit automotive technology)
- **Ultralight Structures**
 - Next generation composites
 - Multidisciplinary optimization
- **Mission Adaptive Rotors**
 - Active morphing for "quantum jump" in performance
 - Composite couplings for performance and loads
- **HUMS**
 - Beyond transmission & drivetrains (rotor head, servo failures, etc)

Technology Needs

- **Increased level of autonomy**
 - Collision avoidance
 - Embedded miniaturized sensors and transmitters
- **Green rotorcraft**
 - High SFC
 - Hybrid Engines
 - Re-cycling composite materials
 - All electric rotorcraft (swashplateless, hydraulicless)
- **Rapid Prototyping**
 - Numerical milling and rapid prototyping
- **Jet Smooth Rotorcraft**
 - Active controls using smart materials

Recommendations

- **For competitiveness of rotorcraft industry, seek new state-of-art production rotorcraft (not upgrades!!!).**
- **Nurture rotorcraft centers of excellence (not fragmentations!!!!)**
- **Reward creativity and depth in research (let us not create a culture of milestones!!!!)**
- **Experimental facilities are key to methodology robustness, product refinements and revolutionary designs (let us not close wind tunnels!!!)**
- **Use creativity to reduce life cycle cost (real not fake!!)**
- **Discourage infeasible designs (too many paper studies!!!)**

Crossing the Dip?

- **Advances in aeromechanics appear poised for enormous potential in rotorcraft, especially towards the development of a mission adaptive rotor with a quantum leap in performance**

Wonderful World of Rotorcraft Aeromechanics



Research frontiers are expanding and moving up rapidly

- Rotor designs are tending towards low vibration and low noise rotors (jet-smooth goal)
- Performance (speed, endurance, range) improving
 - Variable rotational speed morphing rotor in future
- Increasing pay-load/gross weight fraction
- Cost: Manufacturing and maintenance costs going down
- Product reliability and survivability increasing
- Autonomy is increasing by leaps and bounds
- Future vehicles tending towards "Green"
 - Fuel efficiency, CO₂ emission and recycling material
- *How about all electric or hybrid helicopter?*

